

Department of Precision and Microsystems Engineering

Low-Cost Benchtop Equipment and Procedures for Organ-on-Chip Prototyping

S.P. Aalbers

Report no : 2021.024
Coach : Prof. dr. U. Stauer
Professor : Prof. dr. U. Stauer
Specialisation : Micro and Nano Engineering
Type of report : Master Thesis
Date : 06/04/2021

Low-Cost Benchtop Equipment and Procedures for Organ-on-Chip Prototyping

by

S.P. Aalbers

to obtain the degree of Master of Science
at the Delft University of Technology,
to be defended publicly on April, Friday 23, 2021 at 16:00 AM.

Student number: 4044657
Project duration: February, 2016 – April, 2021
Thesis committee: Prof. dr. U. Staufer, TU Delft
Dr. ir. L. Sasso, TU Delft
Dr. ir. A. Denkova, TU Delft
Dr. A. Hunt, TU Delft

An electronic version of this thesis is available at <http://repository.tudelft.nl/>.

Preface

The initial aim of this project was to fabricate a Blood-Brain Barrier on Chip (BBB-on-Chip) which could be used for drug testing at the TNW department. During my literature review I found that multiple research groups are working on BBB-on-Chip models. The challenge of producing a realistic BBB-on-Chip model lays mainly in the biomedical field: relatively small changes to the design, material, cell line, cell culture etc., are followed by labour intensive cell culturing experiments executed by experienced (bio)medical professionals. For this reason I decided to focus on a different aspect of the research on BBB-on-Chip and Organ-on-Chip models in general: the fitness of prototypes for scale-up to enable the production of chips for the pharmaceutical industry.

Quite some time has past since I started working on this thesis and in that time many people came along whom I owe gratitude. First of all I would like to thank Luigi, Antonia and Urs for their supervision, in which they were very supportive and understanding. Antonia invited me to various talks and meetings with people with backgrounds different from mechanical engineering, which was inspiring. Luigi, thank you for your positivity and the fun polymers meetings. Halfway through the project Urs took over the supervision and came with creative insights during our meetings which motivated me to continue.

I would like to thank the technical support of PME, Jos, Rob, Patrick, Harry, Spiridon, Gideon and Bradley, for their help during my experimental work and fabrication of the press and Wim Velt for his support in the workshop. Jia Wei from the Else Kooi Laboratory helped me out with the measurements on the laser microscope, for which I am very thankful. Jan, thanks a lot for your calm instructions on milling and turning.

Daniel provided me with constructive criticism and discussion after thoroughly reading my thesis and also the feedback from Stefan, Roel and Joris after proofreading parts of my thesis was very useful. Last but not least, I'm very grateful for the support from my parents, my sisters and Emiel.

*S.P. Aalbers
Delft, March 2021*

Contents

1	Introduction	1
1.1	Blood-Brain-Barrier on Chip	2
1.1.1	The Blood Brain Barrier and the treatment of glioblastoma	2
1.1.2	In vitro drug assays	3
1.1.3	Requirements on the BBB-on-Chip	4
1.2	BBB-on-Chip fabrication	6
1.2.1	State of the art techniques and materials.	6
1.2.2	Alternatives suitable for mass production	6
1.3	Process plan for BBB-on-Chip prototypes.	9
1.3.1	Cyclic olefin copolymer	9
1.3.2	Soft embossing of COC.	10
1.3.3	Thermal fusion bonding and spin coating	11
1.3.4	Mold fabrication: 3D-printing and soft lithography	12
1.4	Easy-manufacturable benchtop press for embossing and bonding	12
1.5	Project aims and outline	13
1.6	Structure of this thesis	14
2	An easily-manufacturable low-cost benchtop press for embossing and bonding of microfluidic chip prototypes	15
3	Substrate preparation	31
3.1	Spin coating in theory.	31
3.2	Spin coating in practice.	32
3.2.1	Methods	32
3.2.2	Results and discussion - Solvent choice	35
3.2.3	Results and discussion - Film thickness	35
3.3	Conclusions.	40
4	Temperature Control	43
4.1	Introduction	43
4.2	Requirements.	43
4.3	LabView control layout	44
4.3.1	Temperature measurement	44
4.3.2	Computing.	44
4.3.3	Output.	46
4.4	Tuning of PID controller	47
4.4.1	Ziegler-Nichols' step response method.	47
4.4.2	Results.	47
4.5	Discussion and conclusions.	48
5	Conclusion	51
	Bibliography	53
I	Part 1	61
A	Literature study	63
B	Procedures	131
B.1	Mold fabrication	131
B.2	Spin coating.	132
B.2.1	Spin coating solution	132

B.2.2	Spincoating	133
B.2.3	Sputter coating.	135
B.2.4	Thin film reflectance.	135
B.3	Soft embossing	135
B.4	Benchtop press	137
B.4.1	Machining of the separate parts	137
B.4.2	Assembly of the parts	137
B.4.3	Calibration of force control	137
B.4.4	Calibration of temperature control.	138
B.4.5	Emissivity of Kapton foil	138
C	LabView control layout	141
D	Measurement data	149
D.1	Calibration of embossing tool.	149
D.1.1	Force calibration using torque wrench.	149
D.1.2	Calibration of blue spring before and after experiments	149
D.1.3	Emissivity of Kapton foil	150
D.2	Substrate preparation.	150
E	Design drawings	153
E.1	Embossing and bonding press	153
E.2	Soft lithography and soft embossing molds	172
E.3	BBB-on-Chip	175
II	Part 2	179
F	BioDay Poster	181
G	Risk mitigation plan	183



Introduction

Developing drugs comes with high costs which can be reduced if more accurate models of the human body would be available. At the moment, large-scale drug tests are performed in setups with cells cultured in petri dish like devices. These setups do not represent the in vivo situation of the cells adequately. As a consequence, a large amount of drugs that pass the in vitro developmental phase fail in clinical trials [34]. More realistic and cheaper models for testing in an early stage would decrease the amount of failed candidates in the clinical trials and drastically reduce the costs of drug development. This could be achieved by using Organ-on-Chips (OoCs). OoCs are microfluidic chips in which cells are cultured and in which hydrostatic pressure, shear stress, and medium composition can be mimicked more accurately than in conventional in vitro test platforms.

At the Radiation Science & Technology department (RST) of the faculty TNW at the Delft University of Technology nanocarriers are developed for the treatment of glioblastomas, which is an aggressive type of brain cancer. One of the major challenges in the treatment of brain diseases in general is the development of drugs that are able to cross the blood-brain barrier (BBB). The BBB is formed by the cells that form the walls of the capillaries in the brain. It acts as a barrier between the brain and blood to protect the brain against harmful substances. This protective barrier function of the BBB restricts the delivery of drugs to the brain. The RST asked to develop a BBB-on-Chip, a specific type of an OoC, for testing the ability of developed nanocarriers to cross the BBB and reach a glioblastoma spheroid in the brain, and to test the effect of the nanocarriers on the growth of the glioblastoma spheroid.

A literature study on BBB-on-Chip development showed that the development of a complete, functional BBB-on-Chip prototype was neither very novel, nor realistic within the scope of an MSc thesis, without thorough (bio-)medical training and or without collaboration with a biomedical research group. The main challenge of producing a realistic BBB-on-Chip prototype namely lays in the biomedical field: relatively small changes to the design, material, cell line, cell culture etc., are followed by labour intensive cell culturing experiments that have to be executed by experienced (bio)medical professionals.

Multiple research groups are engaged in developing BBB-on-Chips, employing materials and techniques workable for the production of prototypes, but unsuited for mass production. However, the necessary reduction of the high costs accompanying drug development requires the use of realistic models of the BBB for high-throughput drug testing. For this reason it was decided to focus on a different aspect of the research on BBB-on-Chip and Organ-on-Chip models in general: the fitness of prototypes for scale-up to enable the production of chips for the pharmaceutical industry.

The following contributions are the result of this thesis: Firstly, a process plan is designed for the production of BBB-on-Chip prototypes, consisting of a mold fabrication step, a spin coating step, a soft embossing step and a bonding step. All processes are low-cost, time-efficient, simple, and executable in basic labs. The resulting prototypes are fit for mass production. Secondly, a force and temperature controlled press which is required for the process plan is designed, fabricated, calibrated and tested. The press is low-cost, usable on a benchtop, easy and time-efficient in use, and enables experiments with high repeatability. Thirdly, for all steps preceding the bonding step protocols are developed and performed.

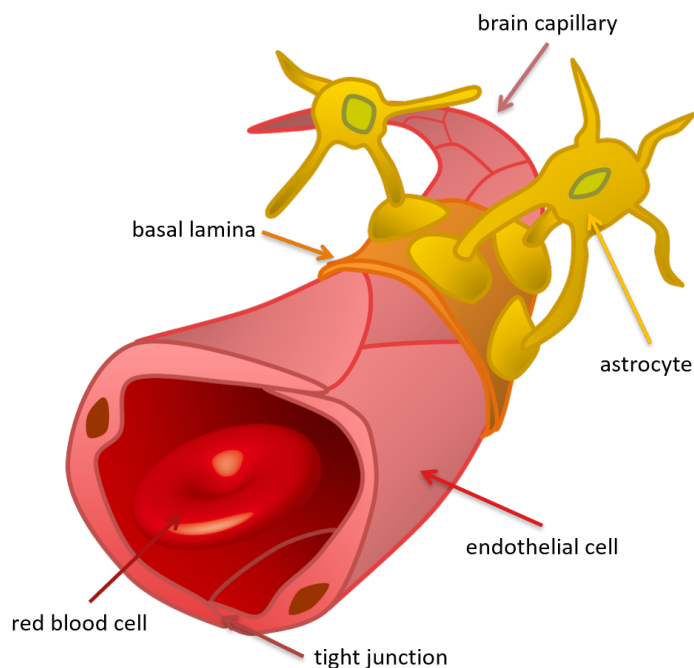


Figure 1.1: Schematic of a brain capillary with the most important elements forming the Blood Brain Barrier. A single layer of endothelial cells (ECs) form the walls of the capillaries. The basal lamina acts as a support structure for the ECs, which are attached to each other and the basal lamina with adherens junctions. Tight junctions seal the pores between ECs. Permeability of the ECs is affected by the interaction between ECs, astrocytes and pericytes (not shown in figure).

In the following chapter first a short background on the BBB-on-Chip and the drugs developed at the RST department is given. This information leads to the requirements on the chip in terms of functioning and fabrication. Next, the conventional and some alternative fabrication techniques and materials are discussed. Furthermore, from the alternatives a selection is made to design the process plan for BBB-on-Chip prototypes. The selected methods require the design and fabrication of a temperature and force controlled press for which the requirements are presented in the following section. Thereafter, the conclusions from this chapter are summarized and the milestones and deliverables are listed. Finally, the structure of this thesis is explained.

1.1. Blood-Brain-Barrier on Chip

1.1.1. The Blood Brain Barrier and the treatment of glioblastoma

The cells of interest in this thesis are the cells that form the Blood Brain Barrier (BBB). Exchange of substances, such as nutrients and oxygen, between the blood and the cerebrospinal fluid in the brain occurs across the walls of capillaries. Neurons are very sensitive to changes in concentrations of compounds in the extracellular fluid and to many different compounds that should not enter the brain. The BBB protects the brain by making sure the exchange of compounds between the blood and cerebrospinal fluid occurs very selectively. The BBB is formed by the walls of the capillaries and consists of specialized endothelial cells, astrocytes, pericytes and the basal lamina [72], see Figure 1.1. A capillary measures less than 1 mm in length and about 10 μm in diameter [28]. The walls are lined with a single layer of endothelial cells which adhere to the basal lamina, a support structure. The endothelial cells are connected to each other with adherens junctions and the pores between the cells are sealed with tight junctions. The permeability of the endothelial cells is affected by the interaction between the astrocytes, pericytes and endothelial cells. Also neurons, microglia and blood-borne immune cells are possible regulators of the functioning of the endothelial cells [77].

One of the major challenges in the treatment of brain diseases is the development of drugs that are able to cross the BBB: the protective barrier function of the BBB also restricts the delivery of drugs to the brain. At the RST nanocarriers in the form of polymersomes and polymeric micelles are developed for the treatment of glioblastomas, which are brain tumours developed from astrocytes. The surface of these nanocarriers will

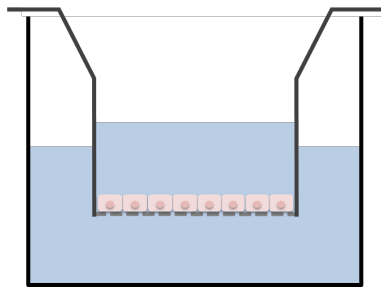


Figure 1.2: Transwell platform consisting of a Transwell insert hanging in a well plate. The bottom of the insert consists of a semi-permeable membrane with cells growing on top of the membrane. Both compartments are filled with culture medium

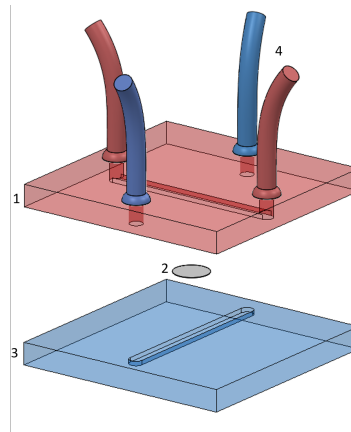


Figure 1.3: Schematic representation of a typical BBB-on-Chip. In both the top (1) and the bottom part (3) an open channel is produced. The two crossing channels are separated by a membrane (2) and connected to inlets and outlets (4). Some chips are also equipped with electrodes for trans endothelial electrical resistance (TEER) measurements, see Appendix A section 2.

be equipped with targeting agents, namely glutathione and lactoferrin, to enable the crossing of the BBB. The nanocarriers are largely 80-100 nm in diameter, with outliers up to 200 nm. Both targeting agents are naturally transported using a mechanism called *receptor-mediated transcytosis*. Various radionuclides and/or radiosensitizers will be encapsulated in the nanocarriers, which are released when reaching the glioblastoma cells for the treatment and imaging of the cells.

1.1.2. In vitro drug assays

An important part of drug discovery and development occurs in in vitro drug assays, meaning with cells or tissues cultured outside of their normal biological environment. The behaviour of cells is regulated by genetic information inside the cell and by signals, e.g. hormones and mechanical stress, from outside the cell. The way cells react on external signals is dependent on the genetic information in the cell. Changing the microenvironment of the cell changes the behaviour of the cell accordingly. To obtain a representative model of the BBB, the cells need to behave as in vivo and therefore the microenvironment needs to be mimicked as well as possible.

Conventional in vitro models In vitro models that are mostly used at the moment and which are commercially available are Transwell® platforms [87]. The Transwell platform consists of a Transwell insert with a porous, semi-permeable membrane, hanging in a well plate, see Figure 1.2. Cells are cultured on top of the membrane. More complex models are used as well: different cell types are cultured at the opposite site of the membrane, at the bottom of the system and different types are mixed on the same membrane. Cells take up nutrients and excrete waste via the culture medium in the well plates and inserts. The culture medium is therefore refreshed at fixed times. However, in Transwell platforms many factors cannot be represented very well. The medium for example is static, whereas many cell types in the human body are subjected to flow. Signalling agents are diluted strongly in Transwell models, because of the high ratio of medium-to-cell volume [13].

BBB-on-chip models In order to make a better representation of the microenvironment of the cell, microfluidic models are in development. In microfluidic models a representative flow can be applied, small culture medium volumes are used, nutrient concentrations remain constant and numerous other relevant factors can be applied. For the BBB for example, a sufficiently high shear stress induced by flow is necessary to trigger the barrier function. A typical BBB-on-chip device consists of two crossing channels separated by a porous mem-

brane, see Figure 1.3. The mostly rectangular channels typically measure 100-300 μm in height, 200 μm up to a few millimetres in width and up to a couple centimetres in length [10, 32, 64, 85]. The upper channel represents a capillary, the bottom channel the cerebrospinal fluid. In the blood channel endothelial cells are cultured. The cerebrospinal channel is either left without cell cultures [32], or multicultures are established by filling the chamber with astrocyte conditioned gel [64] or medium [22, 59] or by seeding astrocytes [10, 11, 22, 93], pericytes, neural cells, glial cells, or a combination of gels and/or different cells is used [2, 13, 85]. Before the cells are seeded the channels are coated with one or more proteins found in the extracellular matrix, such that the cells are able to adhere to the device. The chips are fabricated in polydimethylsiloxane (PDMS) and have channels with rectangular cross sections, separated by polycarbonate (PC) [2, 10, 11, 32], polyethylene (PE) [64], polytetrafluoroethylene (PTFE) [64] or polyethylene terephthalate (PET) [85] membranes with constant pore sizes ranging from 0.4 μm to 8 μm . Different methods are used to characterize the functioning of the cells: most used are immunohistofluorescence staining to visualise various (parts of) cells [2, 10, 11, 13, 22, 32, 64, 85, 93], permeability assays using fluorescently marked substances [2, 10, 11, 13, 22, 59, 63, 85, 93] and trans endothelial electrical resistance (TEER) measurements [10, 11, 13, 22, 32, 85], which give quantitative information on the functioning of the cells. For TEER measurements electrodes need to be incorporated in the design. Currently, research is focused on the influence of different aspects on endothelial cell function: the composition of cell culture medium and protein coatings [74, 91], membrane material [64] and pore size [90], shear stress induced by flow [4, 11, 21, 53, 82], the interaction with device materials [83], and on incorporating electrodes for TEER measurements to retrieve reliable measurement data [56]. See table 2.1 and 2.2 of Appendix A for an overview of the currently reported BBB-on-Chip models and their characteristics, advantages and disadvantages.

1.1.3. Requirements on the BBB-on-Chip

In this section the requirements on the BBB-on-Chip and on the fabrication process are presented. They originate from the requirements of the intended user, the RST department, and from a literature study on the BBB and BBB-on-Chip, see Appendix A.

Layout of the BBB-on-Chip Drug transport from the bloodstream to a tumour in the brain and tumour growth are to be studied with the BBB-on-Chip. The nanocarriers will be tracked using fluorescent labels. Hereto the BBB-on-Chip should consist of:

<i>Blood channel</i>	Represents a capillary in the brain, cell culture medium replaces blood
<i>Brain channel</i>	Represents the brain and can hold a glioblastoma spheroid, cell culture medium replaces the cerebrospinal fluid
<i>Permeable membrane</i>	A permeable membrane on which endothelial cells will be cultured should separate the two channels to construct the blood-brain barrier
<i>Fluidic inlets and outlets</i>	Both channels should have an inlet and outlet: the blood channel to administer medium with nutrients and fluorescently labelled nanocarriers and the brain channel to collect medium to evaluate transport through the blood-brain barrier using a fluorometer.

Cell culturing The cell culturing conditions should be as close as possible to the in vivo situation to achieve a monolayer of endothelial cells which function as similar as possible as in vivo.

<i>Biocompatibility</i>	Device and membrane materials should be suited for long term (two weeks) cell culturing and have no significant interaction with cells and medium compounds.
<i>Wall shear stress (WSS)</i>	The WSS exerted on the endothelial cells should be between 1.5 and 6.4 Pa. WSS should be uniform along the membrane width, to ensure similar culture conditions along the membrane width.
<i>Hydrostatic pressure</i>	A pressure of 30 mmHg in the blood channel of the device should be withstood
<i>Permeable membrane</i>	Membrane pore diameter cannot be bigger than 0.4 μm , to avoid penetration of the endothelial cells into the pores. The membrane should be coatable with proteins, e.g. laminin and fibronectin, to stimulate cell adhesion and proliferation.

<i>Permeability</i>	Oxygen and carbon-dioxide levels should be maintained as in vivo. This could be accomplished by controlling the concentration of the gases in the medium or, when the permeability of gases through the material is high enough, by controlling the concentration of the gases in the atmosphere where the device is placed. The permeability to water vapour should be low enough to avoid high fluctuations in medium osmolarity and volume.
<i>Sterilization</i>	Before culturing, the device needs to be sterilized to avoid contamination of the cells. For example using an autoclave, UV-light or radiation.

Testing barrier function The endothelial cells will be seeded and once grown to confluency (i.e. the cells formed a monolayer covering the whole culture surface) drug testing is possible. To efficiently evaluate confluency and functioning of the endothelial cells, TEER measurement should be performed intermittently. Next to that, it should be possible to check the endothelial cells visually. Electrodes will not be incorporated in this project, but it should be possible to extend the model later on with electrodes.

<i>Electrodes</i>	Space should be available to integrate electrodes directly above the membrane in the blood channel and below the membrane in the brain channel. Electrode material should be transparent to allow for visual inspection of the cells.
<i>Transparent material</i>	Transparent device material to allow for visual inspection of the cells

Testing drug transport Drug transport can be tested in different ways, quantitatively, by counting labelled nanocarriers in the brain channel using a fluorometer, and qualitatively, by fluorescent imaging of the device to locate the nanocarriers in the device. The size of the to be tested nanocarriers is 80-100 nm. Exceptionally they could be 200 nm. The nanocarriers are hydrophilic.

<i>Permeability membrane</i>	Permeability of the empty membrane to the nanocarriers should be high to minimally influence transport through the blood-brain barrier.
<i>Autofluorescence materials</i>	Low autofluorescence of the materials used to avoid noise during fluorescent imaging

Testing the effect of drugs on tumor growth The glioblastoma spheroids to be tested need to be cultured for five to seven days before the drugs are added, either inside or outside the device. The diameter of the spheroid at the start of the experiments is 400-500 μm . The therapeutic effect of the drugs on the spheroids will be tested up to two weeks. The diameter of the spheroids will then be maximally 600 μm . The spheroids are very brittle and should not fall apart before experiments are finished. After two weeks the spheroids are sliced to inspect the necrotic core. Hereto the spheroids need to be removed from the device either by disassembling the device or cutting out the spheroid. Since the experiments inside the device take more than two weeks (first culturing endothelial cells, next two weeks of tests) the endothelial cell culture should last for more than two weeks on the membrane.

<i>Dimensions brain channel</i>	Minimum width and height of the brain channel below the membrane is 700 μm , such that a maximally grown spheroid can be reached by the drugs from above and from the sides.
<i>Flow in brain channel</i>	No high flow around the spheroid is allowed to prevent the spheroid from falling apart
<i>Spheroid removable</i>	Glioblastoma spheroid should be removable from the device after experiments

Fabrication The BBB-on-Chip model is intended to be used for high throughput drug testing. However, first different prototypes need to be fabricated to come to an optimal design. For this reason production should be efficient for small quantities. In prototyping the use of molds is not desirable if fabrication of the mold is not very efficient, since small changes need complete new molds. The fabrication of the prototype should be possible at the Delft Technical University (DUT) or partners. Eventually the device is to be fabricated in high quantities, hence the prototype should be fit for mass production, without the need for redesigning and

retesting.

<i>Fabrication technique</i>	The material should be suitable for machining with the available microfabrication methods. A low surface roughness for optical imaging should be obtainable with the technique used.
<i>Bonding</i>	The different parts of the device (microfluidic channels, membrane, electrodes and in and outlet tubes) should be bonded leak-proof and without compromising bio-compatibility.
<i>Efficient prototyping</i>	Production for single devices should be efficient, since iterations are assumed to be needed to come to an optimal design.
<i>Scale-up possible</i>	The design should be suitable for scale-up to mass production

1.2. BBB-on-Chip fabrication

1.2.1. State of the art techniques and materials

Current BBB-on-Chip models [2, 10, 11, 13, 32, 59, 64, 85, 93] are fabricated out of PDMS, sometimes in combination with glass. The PDMS BBB-on-Chip models are fabricated using soft lithography: Hereto first a mold is made, typically by etching in SU-8 photoresist on silicon. PDMS pre-polymer, obtained by mixing a base and curing agent, is then poured over the mold and cured to obtain the PDMS chip. Curing at 25° C will take approximately 48 h, at higher temperature curing will be faster. At 150° C for example it takes about 10 minutes [18]. However, the higher the curing temperature, the higher the percentage of shrinkage when cooling to room temperature, which should be taken into account when designing a mold [46].

The use of PDMS comes with many advantages. Soft lithography is a simple process without the need of special equipment that is not already present in most laboratories. For PDMS no complex molds or expensive equipment is needed, which makes the fabrication of prototypes economically and time efficient. The material is transparent and has a low autofluorescence, which makes it suitable for optical and fluorescent imaging. Procedures for adequate bonding of PDMS with another PDMS surface and many other materials are available. PDMS is highly permeable to O₂ and CO₂, which makes the control of the concentration of these gases in the medium during cell culturing very simple.

Nevertheless, the following disadvantages are reasons to search for alternative techniques and materials: Soft lithography of PDMS is especially useful for the production of prototypes, but PDMS in combination with soft lithography is not suited for high-throughput fabrication, because of the long curing times inside a mold. The PDMS surface is hydrophobic, which could be reduced with plasma treatments or coatings with extra cellular matrix (ECM) proteins [74]. However, after plasma treatment hydrophobicity recovers almost completely within hours to days [29, 83], which makes it unfit for storage, and coatings might be unwanted in some cases. The bio-compatibility of PDMS is controversial [8, 62]: In general PDMS is assumed to be bio-compatible, but might leak irritants such as xylene and ethylbenzene [33], uncrosslinked oligomers can be found in cells cultured on PDMS [60] and hydrophobic compounds in cell culture medium or excreted by cells are absorbed by the material, which influences cell culture experiments [60, 86]. Where the high permeability to O₂ and CO₂ could be beneficial, the high permeability to water vapour could adversely affect cell culture experiments, since it causes fluctuations in medium osmolarity and volume. Treatments exist to limit the absorption of hydrophobic compounds and water vapour permeability, but these cause extra production steps with unknown effect on cell for some treatments [1, 8, 33, 58, 75].

To conclude, PDMS, the state-of-the-art material, and the corresponding fabrication technique, soft lithography, lend itself well for prototyping. However, they are less suited for the production of large amounts of chips, which is one of the requirements. For more detailed considerations of the advantages and disadvantages of PDMS and soft lithography the reader is referred to Appendix A section 5.2.

1.2.2. Alternatives suitable for mass production

To allow for faster prototyping and to enable scaling up the production, alternative materials and fabrication techniques are required. An extensive literature review on alternatives is performed and the considerations for the selection of the best alternative are described extensively in Appendix A section 5.3-5.5. Here the alternative fabrication techniques and materials are summarized.

Table 1.1: Properties and manufacturing possibilities of PS, PC and COPs.

	PS	PC	COC
Injection molding	Common practice [8]	Common practice [89]	Often reported for microscale structures [55]
Hot embossing	Often used for microfluidic device fabrication [8]. Molds are made of metals using CNC machining or laser ablation or made of PDMS or an epoxy cast on PDMS. Small structures in the order of tens of micrometers [31, 49, 78] have been produced and also 200 μm deep rectangular channels [49].	Becker and Heim [7] fabricated channels with a width of 20 μm and a depth of 140 μm .	Many studies report on hot embossing of COC with different mold materials and different feature sizes, e.g. 100 μm wide, 50 μm deep channels. Good temperature control required to avoid crazing.
Laser ablation	Few studies reported, results are unsatisfactory [43, 44]	Structures with widths down to 50 μm and aspect ratios up to 10 have been fabricated [89].	Few studies performed with varying results, none with a laser comparable to the one available [24, 42, 47, 61, 66, 70].
Milling	Microchannels of $276 \pm 3 \mu\text{m}$ wide and $223 \pm 9 \mu\text{m}$ to $452 \pm 5 \mu\text{m}$ deep have been fabricated, but did not yield transparent surfaces [17].	Microchannels with widths down to 250 μm and a precision of $< 28 \mu\text{m}$ have been fabricated, but needed surface treatments, sandpapering and vapor polishing, to obtain surfaces suitable for optical imaging [92].	Structures down to 25 μm have been fabricated [15]. Marginal information available about surface quality. Issues with surface roughness and burr formation are reported [15].
Bonding	Solvent, thermal, lamination film and surface treatment bonding. Thermal fusion bonding is prone to result in deformed channels and increases autofluorescence. Solvent bonding requires adequate removal of solvents [8, 94].	Solvent, thermal, adhesive, surface treatment and lamination film bonding. The risk of adhesive bonding is channel clogging. Thermal bonding could result in channel deformation, which could be limited by using solvents in the process [57, 80].	Thermal bonding, solvent bonding and surface treatment bonding are possible techniques. Thermal bonding with lower glass transition temperature layer to avoid channel deformation has been demonstrated (3.2 Mpa burst strength [36]).

Many polymers suitable for microfabrication are available. A smaller amount is used for lab- and organ-on-chips: cyclic olefin (co)polymer (COP), parylene C, PDMS, PC, PE, PET, poly(methyl methacrylate) (PMMA), polyimide, polystyrene (PS) and polyurethane (PU). PS and PC have been used for cell culturing for decades, meaning biologists have a lot of experience with these polymers already. COP is a newer class of polymers, but has very good optical quality, is biocompatible and the many different grades give various opportunities in microfabrication. Table 1.2 summarizes relevant properties of these materials.

The most common fabrication techniques suitable for the fabrication of microfluidic devices to be used in combination with PS, PC and COP are injection molding, hot embossing, laser ablation, and micromilling. Injection molding is only suitable for higher production quantities, since relatively complex molds are needed. For commercial production quantities the use of injection molding is the most economic choice. Although injection molding will not be used in this project, being able to produce the device with injection molding as well would be beneficial. Eventually it could then be produced in large quantities efficiently. For the production of the prototypes hot embossing, laser ablation and micromilling are considered for all three materials separately, Table 1.1 gives a summary of the findings.

Table 1.2: Comparison of relevant material properties of PS, PC and COC. Unless otherwise indicated the information on COC is true for all formulations.

	PS	PC	COC
Biocompatibility	ISO 10993 compliant Often used in lab equipment and culture wells Leaching of xenobiotic compounds [48]	ISO 10993 compliant Often used in lab equipment and culture wells Leaching of BPA (xenoe-strogen) [73]	ISO 10993 compliant Possible leaching of additives affecting cell viability from certain formulas (TOPAS) [55]
Chemical inertia	poor	concentrated acids, ether, hydrocarbons, most organic solvents	Nonpolar solvents, hydrocarbon oil [96]
	good	Bases, alcohols	Alcohols, acids Acids, bases, DMSO, hydrogen peroxide, ethylene oxide, polar solvents, fluorinated oil, silicone oil [96]
Adsorption and absorption of hydrophobic substances [83]	low	low	low
Water vapor permeability [54, 76]	low	low	very low
Water absorption [80]	very low - low	low	very low
Gas permeability	O ₂ [54]	low	very low
	CO ₂ [30]	low	no data found
Contact angle [23, 35]	high	high	high
Hydrophobic recovery	UV-ozone [83]	very low	very low
	O ₂ -plasma [83]	low	moderate
CTE [80]	10-150 · 10 ⁻⁶ m/mC	60-70 · 10 ⁻⁶ m/mC	60-80 · 10 ⁻⁶ m/mC
Youngs modulus [5, 89]	3600 MPa	2200 MPa	3000 MPa
Tensile strength [5, 89]	~ 57 MPa	65 MPa	60 MPa
Glass transition temperature [80, 95]	92-100°C	145-148°C	30-180°C (adaptable)
Melting temperature [80]	240-260°C	260-270°C	190-320°C
Heat distortion temperature [6]	70°C	125°C	140-170°C
Transparency [5, 20, 55, 73]	400-800 nm: very high	400-1100 nm: very high	300-1200 nm: very high
Refractive index [5, 20, 55]	1.59	1.57-1.64	1.53
Birefringence [55]	no data found	no data found	low
Abbé number [5, 20, 55]	low	low	high

1.3. Process plan for BBB-on-Chip prototypes

For this project soft embossing and thermal fusion bonding of cyclic olefin copolymer (COC) for chip fabrication in combination with soft lithography and 3D-printing for the fabrication of molds are selected as the best option, and will be discussed in this section. For thermal fusion bonding of COC a spin coating step is required. Soft lithography and the versatile 3D-printing process are time-efficient and relatively cheap for the fabrication of molds. Thermoplastic polymers can be efficiently molded using soft or hot embossing in small as well as large quantities. The thermoplastic polymer COC is biocompatible, has a low autofluorescence, good optical properties and can be efficiently bonded using thermal fusion bonding. See Figure 1.4 for an overview of the proposed process plan.

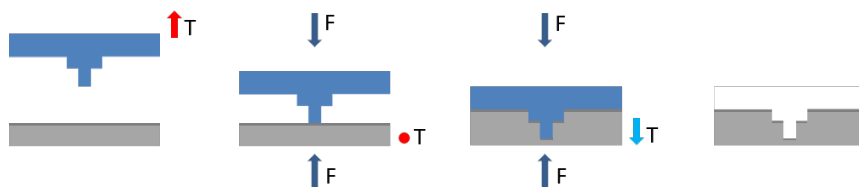
PDMS mold fabrication



Spincoating thermal bonding layer



Soft embossing



Thermal fusion bonding

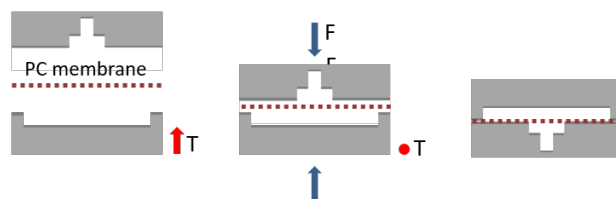


Figure 1.4: Proposed process steps for the fabrication of the BBB-on-Chip. First a PDMS mold is fabricated by printing a positive mold in HTM-140 and next creating a negative PDMS mold using soft lithography. In the next step a thermal bonding layer of TOPAS® 5013 is spin coated on a TOPAS 6015 substrate. Finally, channels are created in the TOPAS 6015 substrate with the spin coated layer of TOPAS 5013 using the soft embossing technique. In the thermal fusion bonding step, which will not be investigated in this thesis, two embossed substrates are bonded to each other while sandwiching a porous membrane.

1.3.1. Cyclic olefin copolymer

Cyclic olefin polymers are a class of amorphous thermoplastic polymers. Various brands offer COPs, which differ from each other depending on the cyclic monomer and polymerisation process used. Two different methods are used: Chain polymerisation of cyclic monomers with ethene (TOPAS and APEL™), and ring-opening metathesis polymerisation of cyclic monomers followed by hydrogenation (ARTON®, ZEONEX® and ZEONOR®) [55], see Figure 1.5. The first process yields a material that is referred to as a cyclic olefin copolymer (COC), since two different types of monomers are used. COP (and COC) is available in pellet form,

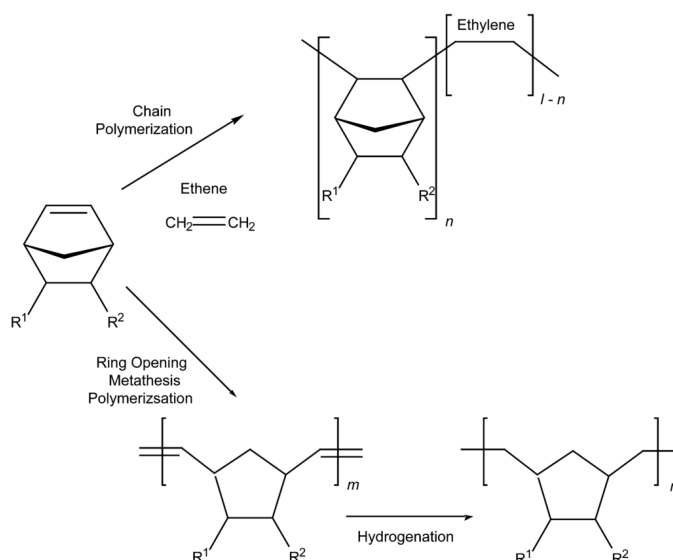


Figure 1.5: Two different polymerisation reactions for the synthesis of cyclic olefin polymer. Reproduced from Shin et al. [65]

solution or in sheets [55].

Various grades of COPs are biocompatible according to ISO 10993 tests and are often used for biomedical applications already [69]. Untreated COP is hydrophobic, which could result in protein adsorption, i.e. the accumulation and adhesion of proteins in the culture medium on the surface of the material. However, after UV-ozone treatment COC was shown to be resistant to adsorption of 7-ethoxycoumarin and testosterone and their metabolites, which are often used when testing metabolic activity of liver cells and tissue [83]. The adsorption of proteins can be reduced by photografting poly(ethylene glycol) methacrylate, by means of a dynamic coating of hydroxyethyl cellulose [55] or by reducing the hydrophobicity by means of UV-ozone treatments [83].

One of the advantages of COP is the low water absorption (<0.01%), since absorption of water causes dimensional changes and could influence other mechanical and chemical properties [55]. The water vapour permeability is relatively low, which confines the evaporation of water from the culture medium.

The optical quality of COP is high: it has a high optical transparency from 300 – 1200 nm, a high refractive index ($n = 1.53$ for TOPAS 5013), low birefringence and a large Abbé number (56.4 for TOPAS 5013). The transmittance of UV light is higher than for other polymers like PMMA, PC and PS. The autofluorescence is in the same order of magnitude as PMMA and PC, sufficiently low for fluorescent imaging.

The glass transition temperature T_g can be influenced by the fraction of norbornene molecules. A higher norbornene content makes the polymers chains more rigid resulting in less chain entanglement, increasing T_g , but also making the polymer more brittle [95]. COPs with T_g values between 30 and 180°C are available. The availability of one material with different glass transition temperatures makes the clean thermal fusion bonding very applicable, see Section 1.3.3.

1.3.2. Soft embossing of COC

In soft (and hot) embossing a negative mold is pressed onto a substrate at elevated temperature, see Figure 1.6, following the steps:

- A sheet of polymer, the substrate, is heated to a temperature slightly above T_g in a vacuum. The mold to be replicated is heated to the same temperature or slightly warmer.
- The mold is gradually pressed into the polymer substrate. The force is kept constant for a couple of minutes. Force, temperature and time depend on the mold design, the polymer to be embossed and the mold material.

- (c) The mold and substrate are cooled down at equal rates to just below T_g to avoid deformation during demolding.
- (d) Mold and substrate are separated.

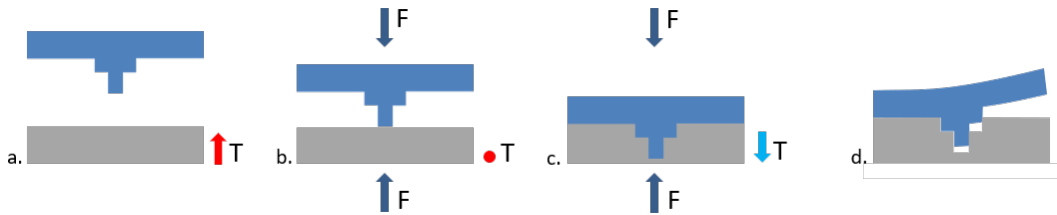


Figure 1.6: Soft embossing process. a. Mold and substrate are heated to a temperature above T_g , the embossing temperature T_e . b. Embossing force is applied gradually while keeping the temperature constant at T_e . c. Embossing force is kept constant while cooling mold and substrate to the demolding temperature. d. Substrate is released from mold.

The soft embossing procedure takes about 10-30 minutes [79] per product, which is very reasonable for prototyping. Hot embossing essentially follows the same steps. The difference lies in the mold material: soft embossing uses soft mold materials like PDMS, in hot embossing molds are made of hard materials like metals. The difference in mold material makes hot embossing somewhat faster. Not much literature was found on soft embossing of COP. Hot embossing of COP is reported more often. In view of the similarities between the techniques, general findings in literature on hot embossing of COP are summarized here.

Replication accuracy depends on the uniformity of the temperature across the mold, the vacuum quality to prevent air bubbles in the substrate, the surface quality of the mold and the chemical compatibility between mold and substrate [6]. The difference in temperature during the compression step and demolding step should be as small as possible to minimize thermal stresses and 'replication errors due to the different thermal expansion coefficients of tool and substrate' [7].

The resolution is predominantly determined by the resolution reached in fabricating the mold. Replication accuracies of tens of nanometers have been reached.

Surface quality mainly depends on the surface quality of the mold, but can worsen due to shrinkage, which can produce sink marks. The surface roughness could be deteriorated during the demolding process. For example, if there is a relative motion between the mold and the replicate during demolding, small defects can scratch the demolded structure [88, 89]. Residual mechanical stresses typically remain small in hot embossed parts, since no phase transitions take place during the process. This has the advantage that birefringence and warpage remain small, which is beneficial for the optical quality of the product [6].

1.3.3. Thermal fusion bonding and spin coating

COC can be bonded using thermal fusion bonding, solvent bonding, surface treatment bonding and adhesive bonding [80]. The possibility of tweaking the T_g of COCs allows to use a grade with low T_g as a sealant. Layers with microchannels which are prone to deform during thermal bonding can be fabricated out of COC with a high T_g and a cover plate out of COC with a lower T_g . The thermal bonding temperature can now be higher than the T_g of the cover plate and lower than the T_g of the microchannel layer, such that the microchannels will not deform. Jena et al. [36] accomplished a burst strength of 3.2MPa for their device with two crossing channels of 100 μm wide and about 15 and 10 mm long respectively. However, bonding two crossing channels separated by a membrane has not been done before.

In this process plan it is proposed to apply the thermal bonding layer by spin coating. For the spin coating process the to be spin coated material is dissolved in a solvent, e.g. toluene in the case of COC. The solution is then deposited on the substrate, after which the substrate is rotated around the vertical axes with a high rotation speed to spread the solution evenly while the solvent evaporates. Spin coating COC with a lower T_g

on top of a substrate with a higher T_g has been done before [15, 68]. However, a satisfyingly accurate method to determine the thickness of the spin coated layer has not been reported to the knowledge of the writer and needs to be experimented with.

1.3.4. Mold fabrication: 3D-printing and soft lithography

The mold should have sufficient surface quality and should sustain high temperatures. The mold will be heated to a temperature around the glass temperature of the COP used. The TOPAS grades available and their glass transition temperatures are given in Table 1.3.

In 3D-printing a structure is built layer by layer. A suitable printer available at the department is the Micro Plus Hi-Res printer from EnvisionTEC. This printer produces the layers by curing a resin through UV exposure on the x-y-plane. The cured material is then lifted in z-direction, such that the next layer can be cured. The resolution in the xy-plane is 30 μm , in z direction 25 μm . Especially in the direction of added layers the surface is not smooth, but a visual interface between the different layers remains present.

Table 1.3: Glass transition temperature of different TOPAS grades

Grade	9903	9506	8007	7010
T_g	33°C	65°C	78°C	110°C
Grade	5013	6013	6015	6017
T_g	134°C	138°C	158°C	178°C

Table 1.4: Properties of HTM 140 M

Tensile Strength	56	MPa
Elongation at Break	3.5	%
Flexural Strength	115	MPa
Flexural Modulus	3350	MPa
Heat Deflection Temperature	140	°C

For high temperature molding the material HTM140 M is available for this printer. Properties of this material are given in Table 1.4. The heat deflection temperature of HTM140 M is quite low compared to the T_g of the first four grades listed in Table 1.3, so when using HTM140 M as mold material the mold could deform during the embossing process when using TOPAS 5013 or a grade with an even higher T_g . Instead of turning to Topas grades with low T_g , a positive mold will be created using 3D-printing and next soft lithography is used to fabricate the negative mold out of PDMS, which is able to endure high temperatures.

1.4. Easy-manufacturable benchtop press for embossing and bonding

Producing a prototype of the BBB-on-Chip with the materials and methods described in the previous section, namely embossing and thermal fusion bonding of COC, require a device which can exert a calibrated force at a controlled high temperature. A readily available press for embossing relatively large-scale structures and thermal fusion bonding is not present at the department. Therefore an easy-manufacturable benchtop press is designed, manufactured, calibrated and tested in this thesis. The basic requirements on a press needed for this project are explained in this section.

During the embossing and bonding process substrates are pressed together under elevated temperature. The substrates need to stay parallel to each other and flat during the complete process: bending or tilting will yield deformed parts. The temperature of the substrates and the temperature of the parts in direct contact with the substrates need to be at about the same temperature to avoid thermal stresses.

The substrates will be placed between two heated plates which need to stay as parallel as possible while exerting a pressure. The temperature of the plates needs to be measurable, controlled and uniform. Also the force exerted on the substrates needs to be controllable and measurable. The press should withstand temperatures up to 200 °C, determined by taking the expected maximum temperature of 180°C needed for embossing plus a safety factor of 20 °C. The experiments will be performed in the chemical lab, hence the materials need to have a high resistance to different chemical vapours to prevent corrosion. Forces upto 3 kN are used for similar experiments in literature. Preliminary experiments showed that forces higher than 3 kN are not necessary. The press should therefore withstand a force of at least 3 kN.

Additionally, ease of use is an important requirement since a large amount of experiments needs to be performed. Placing and removing the substrates and mold in the press, applying the desired force and controlling the temperature should be quick and easy.

Next to these process imposed requirements the press should be manufacturable. Preferably in the workshop of the faculty of 3ME where lathes, milling machines, laser cutters and some auxiliary machines are available. The press should be manufacturable by a person with little metalworking experience in a foreseeable time, about 4 ECTS.

To summarize, the requirements are as follows:

<i>Compression force</i>	The plates applying compression force move parallel to each other A maximum compression force of 3 kN can be exerted The compression force can be controlled and measured
<i>Heating of substrates</i>	The plates have a uniform temperature distribution A maximum temperature of 200 °C can be withstood The temperature can be controlled and measured
<i>Environment</i>	The materials have a high chemical resistance for use in a chemical lab
<i>Usability</i>	The press is easy to use in terms of substrate handling and force application
<i>Fabrication</i>	The press is manufacturable by lathing, milling or laser cutting and by a person with no metalworking experience in maximally 4 ECTS.

1.5. Project aims and outline

High throughput drug testing is currently still performed in setups with cells cultured in petri dish like devices. The culture conditions in these setups are very different from the *in vivo* situation. More realistic testing of drugs will reduce the high costs accompanying drug development and the need for animal testing and can be achieved by using BBB-on-Chips, where i.a. hydrostatic pressure, shear stress, and medium composition can be mimicked more accurately. Different research groups are developing BBB-on-Chips. The chips consist typically of two channels separated by a permeable membrane on which cells are cultured and are mostly produced from PDMS. PDMS is a rewarding material to prototype with, but it is less suitable for mass production. Therefore a different prototyping strategy is necessary.

The aim of this thesis is to deliver a process plan for the production of BBB-on-Chip prototypes and to deliver the required equipment and protocols for this process plan. The prototypes must be fit for mass production, without redesign and subsequent retesting. The processes need to be low-cost, time-efficient, simple, and executable in basic labs. Two of the processes in the proposed plan, embossing and bonding, require the use of a temperature and force controlled press. The requirements imposed on the processes also apply to (the use of) the press. However, a press which matches these requirements is not available. Therefore, an easily-manufacturable low-cost benchtop press for experiments with high repeatability is designed, fabricated, calibrated, and tested in this thesis. The mold manufacturing steps, spin coating step, and soft embossing step are performed and developed.

The BBB-on-Chip will have the typical layout of two substrates with an open channel, sandwiching a permeable membrane. The channels will be produced by soft embossing of COC. COC is a biocompatible polymer with low autofluorescence and good optical qualities. Good results have been obtained in literature for hot and soft embossing of COC. Molds needed for soft embossing will be fabricated using rapid prototyping techniques: Soft lithography will be employed to produce a negative PDMS mold. The positive mold needed for soft lithography will be produced by additive manufacturing.

COC is available with different glass transition temperatures which makes it a suitable product for thermal bonding of patterned substrates. Hereto, the COC substrates require a thin layer of COC with a lower glass transition temperature. The substrates can then be bonded at a temperature below the glass transition temperature of the embossed substrate, preventing damage to the embossed structures. The bonding process itself will not be performed in this project.

The thin COC layer with low glass transition temperature and specific thickness will be applied on the substrates before the soft embossing procedure by spin coating. The relation between spin coating parameters and the thickness needs to be determined experimentally.

Machines for soft embossing and bonding experiments are not present at the department. Therefore, a device capable of embossing and bonding at temperatures up to 200°C and forces up to 3kN will be fabricated.

Table 1.5 summarizes the goals listed above in the form of milestones and deliverables. To reach the set of milestones and produce the deliverables a number of process steps are needed. Figure 1.4 gives an overview of the proposed process steps for the fabrication of the BBB-on-Chip. The risks concerning the different process steps are considered in Appendix G, in which also a risk mitigation plan is proposed when needed.

Table 1.5: Milestones and the corresponding deliverables.

Milestones	Deliverables
Functioning, calibrated, temperature and force controlled benchtop press	Functioning press Calibrated force control of the press Calibrated temperature control of the press Successful embossing experiments to illustrate functioning of the press
Substrates prepared for embossing	Spin coating protocol to obtain a specific TOPAS 5013 layer thickness on a TOPAS 5016 substrate Simplified design of a BBB-on-Chip device Fabrication of HTM140 mold for soft lithography Fabrication of a PDMS mold for soft embossing
Substrates prepared for bonding	Soft embossing of a TOPAS 5016 substrate Soft embossing of a TOPAS 5016 substrate with a TOPAS 5013 bonding layer (out of scope for this project)

1.6. Structure of this thesis

The embossing and bonding press is the subject of the first following chapter: Chapter 2 contains a paper presenting the design and capabilities of an easily-manufacturable low-cost benchtop press, with which embossing and bonding experiments can be performed with high repeatability. Chapter 3 covers the development of a protocol to obtain a COC substrate with a layer of COC with a different glass transition temperature and a specific thickness. In Chapter 4 the design of the heater of the press and the control loop to regulate the temperature of the press is described. Finally, in Chapter 5 a conclusion of this thesis is given.

2

An easily-manufacturable low-cost
benchtop press for embossing and bonding
of microfluidic chip prototypes

An easily-manufacturable low-cost benchtop press for embossing and bonding of microfluidic chip prototypes

A benchtop press for fast and easy prototyping of microfluidic chips fit for mass production

Sarah Aalbers

Received: April 6, 2021/ Accepted: date

Abstract A benchtop press is presented for low-cost and time-efficient soft embossing and thermal fusion bonding experiments with high repeatability. The press enables the production of microfluidic chip prototypes in small labs, after which scaling-up the production is straight-forward because of the nature of soft embossing and thermal fusion bonding. Heating elements and PID control are integrated in the press to facilitate temperature control up to a maximum calibrated temperature of 180°C with a precision of $\pm 0.25^{\circ}\text{C}$. A maximum calibrated force of 2000 N can be exerted with an accuracy of ± 80 N, for a maximum calibrated force of 1330 N an accuracy of ± 32 N can be reached. Microfluidic chips up to $30 \times 40 \text{ mm}^2$ can be produced. The press is fabricated in a standard machine shop using a lathe, mill and hand press and standard materials and parts are used. Soft embossing experiments demonstrate the performance of the press: $1000 \times 100 \mu\text{m}^2$ channels of $170 \mu\text{m}$ deep are soft embossed in cyclic olefin copolymer (COC) using a polydimethylsiloxane (PDMS) mold, with a replication accuracy similar to previously reported numbers for soft embossing. Embossing of smaller channels with depths between 140 and 560 nm is demonstrated with a mold made of MD700 on a glass wafer.

Keywords Soft embossing · Benchtop press · Cyclic olefin copolymer · Polydimethylsiloxane · Microfluidics · Organ on Chip · Prototyping · Mass production

S.P. Aalbers
Department of Precision and Microsystem Engineering (PME), Delft University of Technology,
Mekelweg 2, 2628 CD Delft, The Netherlands
E-mail: s.p.aalbers@student.tudelft.nl

1 Introduction

In 2017 the Organ-on-Chip (OoC) market was estimated to grow from \$7.5M in 2016 to \$60M - \$117M in 2022 by the Yolé market report (Mastrangeli et al., 2019). The OoC market is currently mainly made up of relatively small companies. The difference between the upper and lower boundary of the estimation lays in the ability of these small companies to scale-up from prototyping and small scale production to mass production and in the conservative nature of the pharmaceutical industry (Mastrangeli et al., 2019). The process of industrializing production requires the redesign of already extensively tested OoC models. The redesign process is currently inherent to the conventional method of prototyping, namely soft lithography of PDMS, making it costly.

1.1 Downsides of current fabrication techniques and materials

Microfluidic devices, including OoC models, are predominantly fabricated using soft lithography of PDMS or photolithography in glass. Photolithography requires costly equipment, labour and time and is, although well suited for mass-production, not efficient for prototyping. In contrast, soft lithography itself is a lot more cost- and time-effective for prototyping and can be performed in a benchtop lab. However, the long curing times make it a time consuming method when fabricating slightly larger quantities, let alone high amounts for commercial use.

Currently, OoCs are optimized and tested for PDMS. Materials suited for mass-production have dissimilar

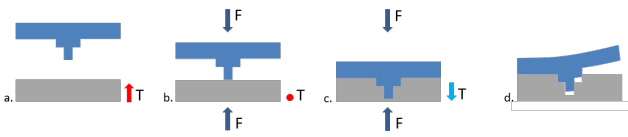


Fig. 1 Soft and hot embossing process. a. Mold and substrate are heated to a temperature above T_g . b. Embossing force is applied gradually while keeping the temperature constant. c. Embossing force is kept constant while cooling mold and substrate to the demolding temperature. d. Substrate is released from mold.

material properties, such that optimizing and testing needs to be redone when scaling-up.

Furthermore, PDMS itself comes with disadvantages when used in biomedical devices as well. Cell culturing experiments are obscured by the high water vapour permeability of PDMS, leaking oligomers (Regehr et al., 2009) and absorption of hydrophobic compounds (Van Midwoud et al., 2012).

To conclude, eliminating the step of redesigning and retesting would speed up commercialisation of OoC prototypes. This could be accomplished by using a method which is both available for benchtop laboratory settings and directly translatable to mass-production. Additionally, the method should support the use of biocompatible materials with low hydrophobic adsorption and high optical quality.

1.2 Soft and hot embossing

Two methods that meet the requirements set above are soft and hot embossing. Both are fast replication techniques when more than one device is needed: producing one replica takes 10-30 minutes and a submicron process resolution can be reached (Tsao, 2016). In soft embossing a mold of soft material, for example PDMS, is pressed in a polymer substrate at a temperature around the glass transition of the polymer. The soft mold can be reused multiple times. The mold used in hot embossing is made of a hard material and usually lasts longer than a soft mold. Substrate and mold are typically heated to a temperature of $\sim T_g - 20^\circ\text{C}$ to $T_g + 20^\circ\text{C}$, where T_g is the glass transition temperature, and consequently pressed together with a force of typically $0.5\text{-}2.0\text{ kN/cm}^2$ for a few seconds to minutes. Figure 1 illustrates the process of hot and soft embossing.

A multitude of polymers can be used as hot or soft embossing substrate: for example polystyrene, which has been used in the biomedical field for decades,

PMMA, polycarbonate, and cyclic olefin (co)polymer. Compared to PDMS, these polymers have a better optical quality, are less vulnerable to mechanical damage, show less swelling, have lower water vapour permeability and lower absorption and adsorption of hydrophobic compounds. Additionally, material costs are 6-75 times lower (Tsao, 2016). Polymers used for embossing are suitable for injection moulding and roller imprinting, both taking 10-30 sec/cycle, making embossed prototypes directly fit for mass-production (Tsao, 2016). The favourable low Young's modulus of PDMS is not met by polymers, but can be matched by applying gels or coatings.

1.3 Cyclic Olefin Copolymer

Cyclic olefin copolymer (COC) is used in this work both as a substrate and as a bonding layer. COC has a high optical quality, is biocompatible, inert to many chemical substances including polar solvents, has a low absorption of water and hydrophobic compounds (Van Midwoud et al., 2012), low water vapor permeability and low autofluorescence. The glass transition temperature, T_g , of COC can be altered by varying the norbornene content. This feature can be utilized for thermal fusion bonding (Jena et al., 2012; Steigert et al., 2007). Hereto a thin layer of COC with a T_g lower than that of the substrate is applied on the COC substrate as a thermal bonding layer. Thermal fusion bonding can then take place at a temperature lower than the T_g of the substrate, avoiding deformations of the structures embossed in the substrates.

1.4 Easily-manufacturable low-cost benchtop press

In this study we propose the fabrication of OoCs by embossing in COC with a benchtop press for prototyping purposes. Hot embossing systems with precise temperature and force control are available, but might not always be affordable or practical. For this reason a benchtop press device is produced which is easily-manufacturable and inexpensive. Both temperature and force are controlled. The press can be used in a benchtop lab and can be operated by hand to emboss and bond substrates of maximally $30 \times 40\text{ mm}^2$. In this work the design, fabrication, capabilities and functioning of this easily-manufacturable low-cost benchtop press is presented. Functioning of the press is validated by embossing various channel sizes in a COC substrate.

For the design of this press the following factors of influence regarding the hot embossing machine are

considered: stiffness of the device, parallel movement of the embossing plates, rate of force increase, uniformity of temperature, rate of heating and cooling, and heat conductivity. Worgull (2009) extensively discusses in chapter 4.4 and 5.4 why these factors are relevant, as is summarized below:

- The device should have a high stiffness to avoid significant bending of the embossing plates during molding. Bending of the plates results in a non-uniform distribution of force and a non-uniform thickness of the substrate, risking warping of the substrate. In extreme cases a hard mold could damage a bended substrate during demolding.
- A non parallel motion of the embossing plates results in a non-uniform force distribution, which could cause damage during demolding, a non-uniform substrate thickness and warpage of the substrate.
- The molding force should be applied slowly to avoid damaging the mold and control internal stresses in the polymer.
- A non-uniform temperature distribution during heating, molding and cooling causes the polymer to soften, flow and solidify non-uniformly. Non uniform flow results in an uneven substrate thickness. Non-uniform solidification causes anisotropic shrinkage, and hence warping of the substrate.
- The grade of crystallization of semi-crystalline polymers depends on the temperature and cooling rate. To increase reproducibility the cooling process should be reproducible.
- Surface roughness of the embossing plates of professional machines is optimized to be low enough for sufficient surface quality of the mold (e.g. when needed for optical purposes) and high enough to provide for a high adhesion force to overcome the demolding force, needed to separate mold and substrate. When demolding by hand, the movement of the mold will not be parallel to the substrate, raising the risk of damaging the structures on the substrate. PDMS however, is softer than COC. Damaging the substrate with the mold is therefore unlikely. Also in terms of pressure distribution soft embossing is more forgiving than hot embossing.

Finally, for this work a number of quantitative requirements on the table-top press is set, as summarized in Table 1.

Table 1 Quantitative requirements on the table-top press.

	Value	Motivation
F_{max}	2.0kN	Maximum embossing force needed. Successfully used embossing pressures, defined as the embossing force divided by the area of the mold, found in literature for COC with $T_g = 158^\circ\text{C}$ and comparable polymers are in the range of 27-97 N/mm ² (Fanzio et al., 2017a; Lee et al., 2005; Narasimhan and Papautsky, 2003; Steigert et al., 2007; Zhou and Papautsky, 2007). For the maximum chip size of 50x30 mm the embossing force will thus not exceed 1.5kN, which is rounded to 2 kN for the sake of a process margin.
e_F	5%	Error in applied force. The sensitivity of replication accuracy appears to be relatively low to force variation (Zhou and Papautsky, 2007). A minimum force is required to obtain sufficient filling of the cavities. Within a relatively large range above this minimum force similar results will be obtained, until compression of the soft mold opposes replication accuracy. However, for bonding only a small force range can be used. If the force is too low, thermal bonding will not take place. A too high force could result in deformed structures.
T_{max}	200°C	The expected embossing temperature needed lays 10-30°C above the T_g , translating to an embossing temperature of 170-190°C for COC with $T_g \approx 158^\circ\text{C}$ Fanzio et al. (2017a); Jena et al. (2012); Lee et al. (2005); Zhou and Papautsky (2007). A process margin of 10°C is taken into account.
M_p	1.0°C	Overshoot of the plate temperature when it is altered. Above the T_g the viscosity of the polymer decreases dramatically. The polymer will only be compressed after a stable temperature is reached, but to avoid excessive softening of the polymer and impose precise temperature control of the polymer a high overshoot is not desired.
error band	0.25°C	Band around the set point in which the plate temperature stays. The press will be used for both embossing and thermal bonding. Thermal bonding takes place above the T_g of the thermal bonding layer and below the T_g of the substrate to avoid deformations of the structures. This results in a small temperature gap. Therefore the errorband needs to be small and is set to 0.25°C.
t_s	5 min	Settling time of the plate temperature. The press is used for prototyping and thus does not need to be operated very efficiently. However, settling time is preferably not greater than the hold time for soft embossing, which is in the order of 5-15 min (Fanzio et al., 2017a,b; Lee et al., 2005; Steigert et al., 2007; Zhou and Papautsky, 2007).

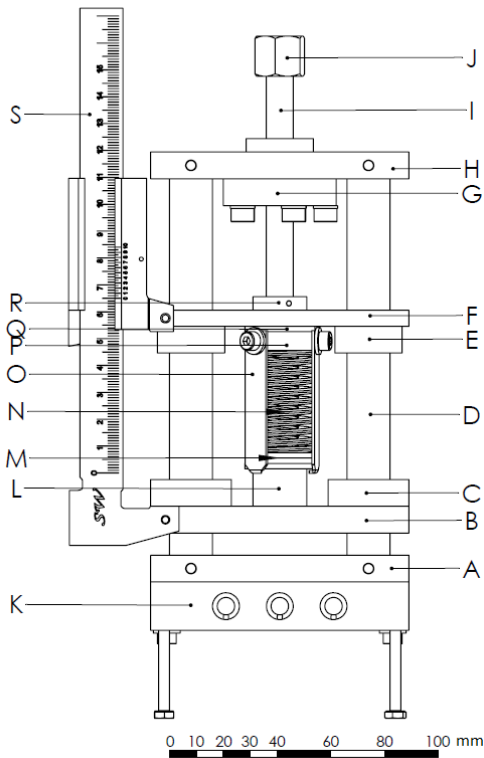


Fig. 2 Schematic representation of the hand-held table-top press with heater block. (A) Bottom embossing plate, fixed (B) Top embossing plate, sliding (C) Sliding bushings (D) Precision axes (E) Sliding bushings (F) Measurement plate moving with top of spring (G) Spindle flange nut (H) Fixed top plate (I) Spindle with (J) Bolt (K) Heater block (L) Part enabling lifting of the sliding plate (M) Washers (N) Spring (O) Hooks lifting part L (P) Steel ring fixed to spindle (Q) Bushing (R) Ring fixing the measurement plate to Q (S) Caliper indicating spring indentation.

2 Materials and methods

2.1 Benchtop press with temperature control

2.1.1 Design overview of the press

A schematic representation of the benchtop embossing and bonding press is given in Figure 2, with letters referring to the part described below, a picture of the press is shown in Figure 3 and a picture with the complete set-up is shown in Figure 4. The main structure of the press consists of two axes, D, and four plates (A,B,F,H). Plates A and H are fixed to the axis with a dowel pin, and plates B and F slide freely along the axes. Substrates to be embossed or bonded are placed between plates A and B. By tightening spindle I, which rotates in the spindle flange nut G, spring N is compressed and plate B is pushed down. Plate F is fixed on top of the spring and moves down with the top of the spring.

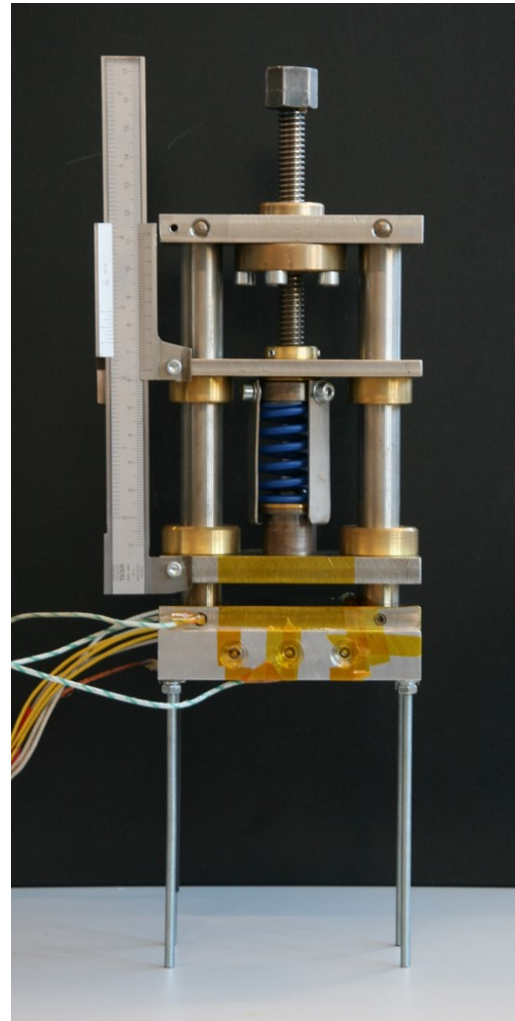


Fig. 3 Picture of the embossing press

The spring serves two goals: Firstly, the jaws of caliper S is fixed to plates B and F, such that the length of the spring can be measured and hence the force exerted on the substrate can be determined. Secondly, during embossing the mold will be pushed down slowly into the substrate, decreasing the thickness of the mold-substrate combination. Without the presence of the spring between the spindle I and plate B, there would not be any contact between the parts any more. Using a spring with a relatively low spring constant will make sure the decrease in force is negligible.

Vertical displacement of the spindle is transferred to the spring by steel ring P. The two washers M enable the spring to rotate along with the spindle. Part L holds the washers in place and passes the force through at the center of plate B.

Ring R is fixed on spindle I to press plate F on

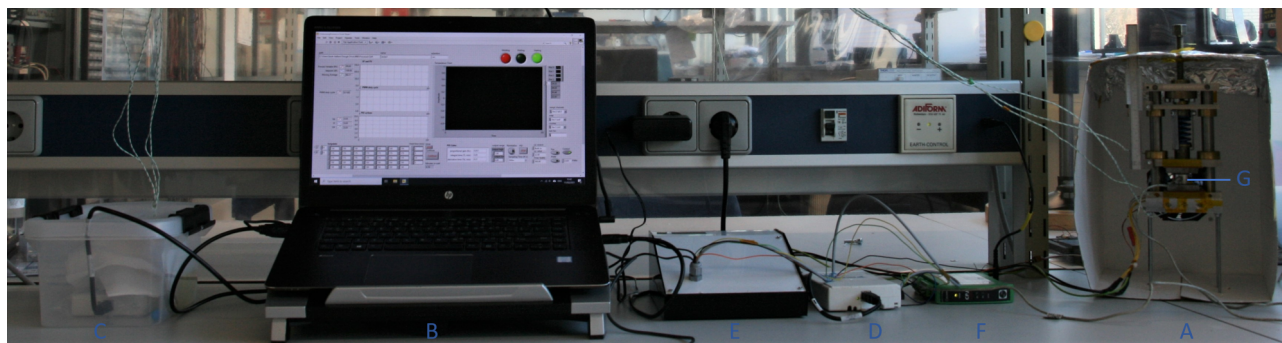


Fig. 4 Picture of the press with the complete setup as used in the soft embossing experiments and force calibration. A) Press B) Laptop computer with temperature control in LabView. C) Data acquisition (DAQ) device for signal condition of the thermocouples (NI USB-9211A, National Instruments Corporation, Austin, TX, USA) D) Multifunction DAQ device controlling fan and heater action (NI USB-6211, National Instruments Corporation, Austin, TX, USA) E) Control box containing PCBs for controlling the fan and heater. Extra in set up for the force calibration: F) Strain gage conditioner (CPJ, SCAIME S.A.S., Juvigny, France) G) Loadcell (Futek LCM300 2KN, Pimzos, Wierden, The Netherlands)

top of the spring. To allow ring R to rotate along with the spindle, ring R is fabricated out of brass and a brass flanged bushing Q is placed between parts P and R.

Plates B and F have a large thickness and are provided with high flanged bushings (C,E) to minimize wiggling of the plates during sliding. Parallel movement of the plates is promoted by applying the compression force in the centre of the plate and the high bushings. Surfaces of plates A and B in contact with the substrates are polished, to obtain substrates with an optical surface quality, and protected with easily replaceable Kapton foil or tape.

Substrates between the two embossing plates are heated indirectly by heating plate A with heater block K. To improve heat conduction the aluminium heater block is clamped to plate A with bolts. A type K thermocouple is applied to the top surface of plate A to measure temperature. Active convective cooling is enforced with a 5V case fan (not shown in Figure 2), placed horizontally at the height of the heater block.

2.1.2 Materials

To prevent degradation of the polished surfaces of plates A and B by chemical vapours these parts are made of stainless steel (AISI 316L). For the other two plates (E, H) the same material is used for consistency. All bushes and washers (C, E, M, Q, R) are made of brass. All less critical parts are made of steel (L, O, P). For the axes (D) silver steel precision shafts are used. Part L has a threaded end and is screwed on plate B. High temperature resistant adhesive (LOCTITE® 638™, Henkel AG & Co. KGaA, Düsseldorf, Ger-

many) is applied between part L and plate B to prevent loosening during demolding.

Standard die springs (N) with four different spring constants, but of equal lengths, are used to preload the press (natural length: 38 mm, inner diameter: 12.5 mm, outer diameter: 25 mm, spring constant: 62, 93, 219 and 346 N/mm respectively, Amatec Technische Veren, Alphen aan den Rijn). For a small molding or bonding force, a spring with low stiffness will be used, such that the indentation of the spring remains large. This makes the determination of the force as precise as possible, and the decrease in force during the process as small as possible.

A caliper (S) of hardened steel with a vernier constant of 0.02 mm is used. The heater block (K) is fabricated out of aluminium, which has a high thermal conductivity and allows for uniform temperature distribution of the block. Three cartridge heaters (\varnothing 6.5 mm, length 50 mm, 150W, 230V, Acim Jouanin, Évreux, France) are installed in the three holes with bore tolerance H7. Heat conduction and uniformity of the temperature is increased by applying boron nitride paste (Mosquito Boron Nitride Paste, Slice Engineering, Gainesville, FL, USA) between the cartridges and the holes. Two thermocouples (Type K (Nickel-Chromium / Nickel-Alumel)) with exposed bead are used. One is placed in an indentation in the top surface of plate A. At the bottom of the heater block a second thermocouple is installed to detect overheating of the cartridges. Thermocouple signal is processed using a thermocouple read-out module (NI 9211, National Instruments, Austin, TX, USA). Required heater power is calculated using PID control in LabView. Heater and fan are controlled with a

multifunction DAQ device (NI USB-6211, National Instruments, Austin, TX, USA).

2.1.3 Fabrication of the individual parts

The four stainless steel plates (A,B,F,H) are first milled to size in length and width, while being clamped together. Next, the large surfaces are milled to size in height by making multiple strokes with a relatively small mill, such that any error in the vertical alignment of the milling head is minimized. After the second surface is milled, the workpiece remains clamped and the holes are drilled directly. In this way the axis of the hole and the surface will be as close to perpendicular as the alignment of the milling machine allows.

The two surfaces in contact with the substrates (surfaces of plates A and B), are face milled last. For plates H and F the order of face milling is not important, here the bottom surface (for H) and top surface (for F) are face milled last.

The surfaces in contact with the substrates (A, B) are sanded and polished, since the surface profile will be transmitted to the substrates. Before sanding and polishing the bronze bushes are pressed in place, so that they do not stick out of the surface of the final product. After polishing the surfaces are protected from dust, chemicals and fingerprints to avoid scratching and etching of the surface using Kapton® tape.

All bushes and washers and parts P and L are made on a lathe.

2.1.4 Assembly of the press

The dowel hole through the steel ring (P) and spindle (I) is drilled through both parts simultaneously. All bushes (C,E,Q) are pressed into place with a hand press. The bolt (J) with inner spindle thread is welded on the spindle. The four plates (A,B,F,H) are slid on the axes (D). The whole press is now clamped in a milling machine to drill the dowel holes fixing plate A and H and the holes for caliper attachment. The holes in the caliper are drilled separately in a milling machine and drilled larger than the bolts that will be used to attach the caliper, to allow for some play and circumvent minor misalignment of the plates, which would block the caliper.

The plates will not slide smoothly along the axes right away, some misalignment is inevitable. Sliding the plates a few times up and down will wear out the

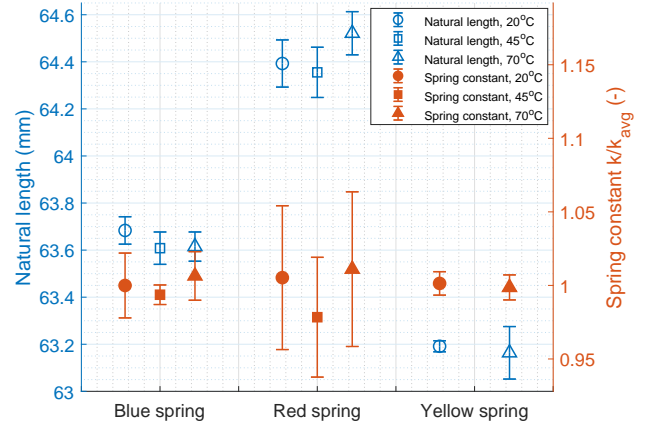


Fig. 5 Mean and standard deviation of the natural length and spring constant of different springs at varying temperature. For the blue and red spring $n = 10$ at $T = 20^\circ\text{C}$ and $n = 5$ for all other measurement points. $n = 3$ for the yellow spring. The blue and yellow spring are uniformly heated in the press in an oven. The yellow spring is heated in the press using the heater block.

bronze bushes and make the sliding smoother.

Alignment of the four plates would be better if all holes are drilled simultaneously while clamping the plates together. However, in this way it would not be possible to reach as much perpendicularity between the polished faces of the plates and the axes.

2.2 Error estimation and calibration of the press

2.2.1 Force control

Errors in force determination originate from, among other sources, read-out errors, resolution of the caliper, thermal expansion of the press and wear and play of the press. The resolution of the caliper equals 0.02 mm, translating to a fraction of $e_r = 0.01 \frac{k}{F}$ of random error on F , the force determined. Compliance of the parts between the caliper jaws, and therefore also the decrease in Young's modulus with increasing temperature of these parts, is negligible compared to the spring compliance. Thermal expansion introduces a systematic error in force determination dependent on temperature.

Random error By calibrating the press the uncertainty introduced by the total of random errors is determined. Natural length, l_0 , and spring constant, k , of the different springs combined with the parts between the caliper jaws is determined by noting caliper read-out for

Table 2 Spring stiffness, natural length and random uncertainty in force determination for a new observation. A sample size of respectively 100, 116 and 18 is used for the blue, red and yellow spring. Measurements are taken at 20°C, 45°C and 70°C and averaged.

Spring	k (N/mm)	l_0 (mm)	δF (95%) (N)
Blue	99.91	63.64	± 31.82
Red	216.87	64.43	± 96.48
Yellow	315.50	63.17	± 80.03

three loads, measured with a load cell (Futek LCM300 FSH03887, FUTEK Advanced Sensor Technology, Inc., Irvine, CA, USA), evenly distributed over the force range of the spring at room temperature, 45 °C and 70 °C, the maximum compensated temperature of the load cell. No significant temperature dependence was found in these measurements, see Figure 5. l_0 and k are therefore assumed constant for $20^\circ\text{C} < T_e < 70^\circ\text{C}$. See Table 2 for the calibration results.

Systematic error The systematic error originating from thermal expansion is estimated as follows: Expansion of the parts between the jaws of the caliper cause an over-estimation of the force on the substrate, countered by an underestimation of the force originating from the expansion of the caliper itself. The measured indentation is equal to:

$$u = \delta_s - \delta_T = \frac{F_s}{k} - \sum \alpha_i \Delta T_i l_i + \alpha_c \Delta T_c l_c \quad (1)$$

where:

- δ_s = Spring indentation following Hooke's law (m)
- δ_T = Thermal expansion (m)
- F_s = Force on spring (N)
- F = ku (N)
- k = Spring constant (N/m)
- l = Length of part (m)
- α = Coefficient of linear thermal expansion (m/mK)
- ΔT = Difference in temperature during force measurement and calibration of spring ($^\circ\text{C}$)
- i = Indicating parts between caliper jaws
- c = Indicating main scale of the caliper

The fraction of systematic error on u induced by temperature effects then becomes:

$$e_T = \frac{F - F_s}{F} = \left(\sum \alpha_i \Delta T_i l_i - \alpha_c \Delta T_c l_c \right) \frac{k}{F} \quad (2)$$

Table 3 Temperature and thermal expansion of the different parts between the jaws of the caliper and the caliper itself at an embossing temperature of $T_e=180^\circ\text{C}$. A temperature difference of $\Delta T = T - 45^\circ\text{C}$ is used, since k and l_0 are determined at an average temperature of 45°C .

	$\alpha \times 10^{-6}$ ($^\circ\text{C}^{-1}$)	l (mm)	T ($^\circ\text{C}$)	δ_T (mm)
Ring	12.0	7	100	0.0046
Spring	12.2	38	110	0.0301
Ring	21.0	2	120	0.0032
Stop	12.0	16	140	0.0182
Plate 2	15.9	5	150	0.0083
Plate 3	15.9	3	100	0.0026
Ring	21.0	2	90	0.0019
Caliper	15.9	73	87	-0.0487
Total				0.0203

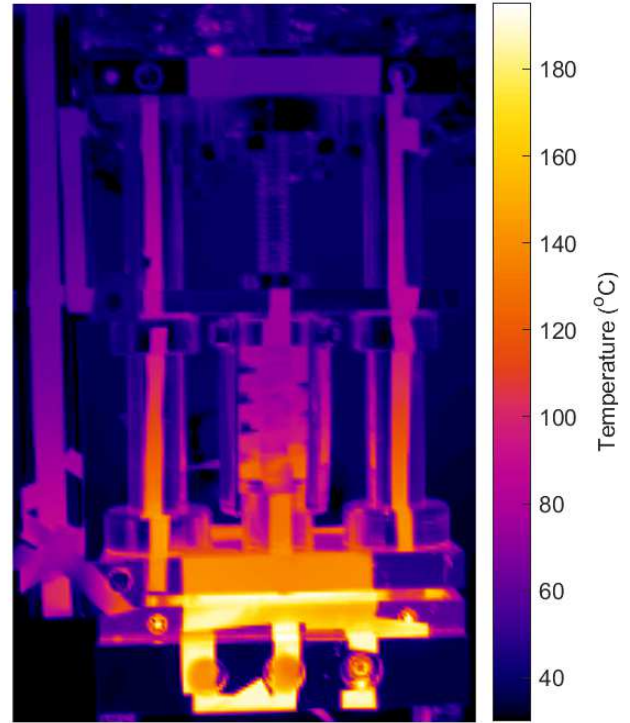


Fig. 6 Temperature distribution of the press at $T_e = 180^\circ\text{C}$, imaged using thermography (FLIR E74, FLIR® systems, Inc., Wilsonville, OR, USA). On all relevant parts a strip of Kapton tape with $\epsilon \approx 0.925$ is applied.

The systematic error is estimated as function of force at $T_e = 180^\circ\text{C}$, the expected maximum temperature needed for embossing of many polymers, and will from here decrease to zero monotonically with the temperature decreasing to the calibration temperature. The temperatures of the parts are measured at $T_e=180^\circ\text{C}$ using a heat camera (FLIR E74, FLIR® systems, Inc., Wilsonville, OR, USA), to determine the fraction of error. Figure 6 shows the thermogram of the heated press,

Table 4 Overshoot and settling time for cooling and heating of the press and an error band of $\pm 0.25^\circ\text{C}$. Measured for different set-point changes: 140 to 155, 160 and 165°C and vice versa. Settling time for cooling strongly depends on the decrease in set-point and the temperature difference with the environment, since it is governed by the convective cooling rate.

Mode	M_p ($^\circ\text{C}$)	t_s (min)
Heating	0.83 ± 0.08	1.97 ± 0.04
Cooling	0.39 ± 0.03	2.61 ± 0.40

Table 3 lists the temperatures found from the thermogram and the corresponding thermal expansion of the parts. The fraction of systematic error at $T_e = 180^\circ\text{C}$ follows from Table 3 and eq. 2 and equals $e_T = 0.02 \frac{k}{F}$. At temperatures around $T = 180^\circ\text{C}$ this value is to be subtracted from the force determined using the calibration values for k and l_0 , but is very small compared to the random errors listed in Table 2.

2.2.2 Temperature control

Temperature of the samples is controlled by regulating the temperature of the heating plate. Using PID control and pulse width modulation the cartridge heaters are controlled. Temperature of the heating plate is measured using a type K thermocouple, whose accuracy is determined by a systematic error of $\pm 2.2^\circ\text{C}$. This is larger than is allowed per the requirements, but since all experiments are performed while keeping the environment constant and with relatively small changes in temperature, this systematic error could be determined once using a more accurate temperature measurement if necessary. During embossing the temperature of the heating plate remains within an errorband of 0.25°C . Overshoot and settling time are given in Table 4 for different settings.

2.3 Functionality test method

Functioning of the benchtop soft embossing and bonding press is characterized by means of soft embossing experiments. The replication accuracy for a range of feature sizes is investigated. Hereto two different molds are used, one fabricated in PDMS and the second in perfluoropolyether-urethane dimethacrylate, or MD700 (Fluorolink® MD700, Solvay SA, Brussels, Belgium). The MD700 mold is fabricated as described by Fanzio et al. (2017a). The soft PDMS mold is produced by employing soft lithography in a 3D-printed mold. All procedures prior to the soft embossing experiments and the soft embossing experiments themselves are described in the following sections.



Fig. 7 Direction of writing and movement during printing of the mold. Hole for air escape in light grey.

2.3.1 Photopolymerisation

A positive mold is fabricated with a negative photoresist (HTM140 M V2, EnvisionTEC GmbH, Gladbeck, Germany) using the Micro Plus Hi-Res printer from EnvisionTEC, which makes use of UV photopolymerisation. The resolution in the xy-plane is $30 \mu\text{m}$, in z direction $25 \mu\text{m}$. Around the mold a container is printed, such that the mold can be used for soft lithography directly.

The printed layers are produced by curing a resin in the x-y-plane through UV exposure from below. The cured material is then lifted in z-direction to let in new resin and pushed back to touch the bottom of the resin container again, such that the next layer can be cured from below. The open side of the container is facing down during printing, to avoid trapping of liquid resin by the up and down movements during printing, see Figure 7. Trapped air can escape via the hole in the wall of the container.

2.3.2 Soft lithography

After the positive mold is produced the PDMS mold is fabricated. Base and curing agent are mixed in a 5:1 ratio (SYLGARD™ 184, Dow Chemical Company, Midland, MI, USA), poured in the HTM140M molds, degassed and cured overnight at 60°C . The cured PDMS molds are released using a scalpel and 99.9% ethanol, dried and stored in a petri dish. See Figure 8 for a drawing with the dimensions of the PDMS mold.

2.3.3 Soft embossing

The embossing process is summarized in Table 5 and 6 and visualised in Figure 10 and discussed in more detail in the following:

The PDMS mold is cleaned by applying Scotch tape (beschrijfbaar plakband, HEMA, Amsterdam, the Netherlands) and removing the tape again, hence picking up electrostatic dust particles from the mold, to avoid the use of solvents which cause swelling of PDMS. The substrates are cut to size ($36 \times 15 \times 1 \text{ mm}^3$) from a large TOPAS plate, which comes sealed with a protective foil on the top and bottom face

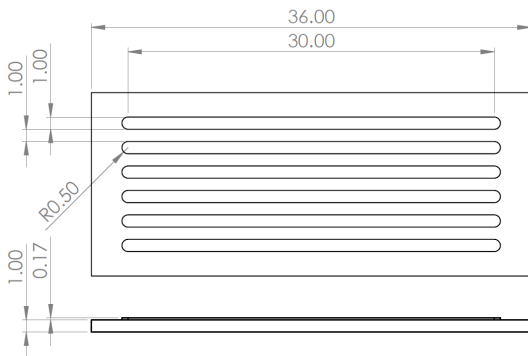


Fig. 8 Dimensions of the PDMS mold (mm)

(TOPAS® 6015, TOPAS Advanced Polymers, Inc., Florence, KY, USA). A substrate is placed on a clean piece of Kapton foil after removing the protective foil. The cleaned mold is placed on top of the substrate and covered with a piece of Kapton foil. The Kapton foil is used to prevent the substrate and mold to remain stuck to the press plates after embossing.

At t_0 , the substrate-mold-Kapton foil sandwich is placed in the centre of the bottom plate of the preheated press and pressed together lightly with a hold force F_h of a few Newtons to prevent in plane movement. The temperature of the press is kept constant at demolding temperature T_d , for 2 min to heat up the substrate and mold. Next, at t_1 the press is heated to the embossing temperature T_e . At t_2 the embossing force F_e is imposed slowly and kept constant during the embossing time t_e . At t_3 the press is cooled down to the demolding temperature T_d , the compression force remains at F_e . Finally at t_4 the compression force is removed slowly. The substrate and mold are removed from the press and separated from each other, during which the temperature of the mold and substrate drops quickly to room temperature.

The process times are set independently from the temperatures of the device, mold and substrate, but are chosen such that the temperatures of the device, mold and substrate settle completely before moving to the next step.

Embossing time, force and temperature are varied to investigate the effect on replication accuracy in terms of depth, width and straightness of the embossed channels. As a measure for straightness the angle of the channel borders with the horizontal and the area of the channel borders outside a linearly fitted line on the channels borders is determined, see Figure 9.

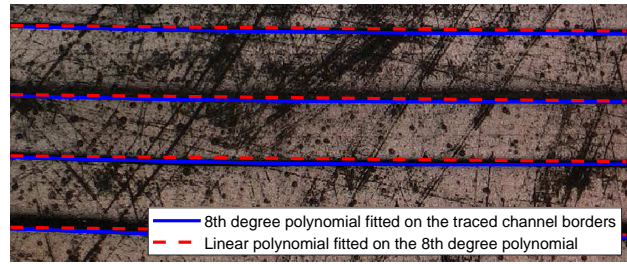


Fig. 9 Detail of sample 1 of set 4. Channel deformation is determined by first tracing the channel border (not shown in picture) and fitting a 8th degree polynomial on the tracing lines. A linear line is fitted through the 8th degree polynomial. The area between the linear fit and the 8th degree polynomial is divided by the area of the channel to obtain a relative value for the deviation from a straight channel border.

Table 5 Description of the embossing process

t	T	F	Actions
t_0	T_d	0	Mold and substrate are aligned by hand and placed on the bottom plate with the substrate facing down. A small holding force F_h is applied to hold mold and substrate in place.
t_1	T_d	F_h	Mold and substrate are heated to embossing temperature T_e .
t_2	T_e	F_e	Embossing force F_e is applied.
t_3	T_e	F_e	Mold and substrate are cooled down to demolding temperature T_d .
t_4	T_d	0	Substrate and mold are removed from the press and separated from each other. The temperature of the substrate drops quickly to room temperature, since it is not in contact any more with a heated element.

MD700 mold The embossing parameters from the experiments with the PDMS mold resulting in the best replication accuracies are used for embossing with the MD700 mold: $T_e = 175$ °C, $t_e = 20$ min. The embossing force is scaled with the surface area to $F_e = 400$ N. A piece of approximately one eighth of the original mold is used, such that it fits in the press. Prior to embossing the mold is cleaned in Liquinox 1% in an ultrasonic bath for 5 min, rinsed with DI water, cleaned in 99.9 % 2-propanol in an ultrasonic bath for 3 min and dried in a clean, dry air stream. Between the sliding plate and the MD700 mold a thin layer of PDMS ($t < 0.1$ mm) is placed to prevent breaking of the mold. Further embossing steps are as described above for the PDMS mold. Replication accuracy is evaluated in terms of channel depth.

Table 6 Embossing parameters used per sample set, with $t_e = t_3 - t_2$, $T_d = 150^\circ\text{C}$, $t_1 - t_0 = 2$ min, $t_2 - t_1 = 5$ min, $t_4 - t_3 = 5$ min. Where a is the maximum change in temperature during heating and cooling.

Set	t_e (min)	T_e ($^\circ\text{C}$)	F_e (N)	Mold	a_{heat} ($^\circ\text{C}/\text{s}$)	a_{cool} ($^\circ\text{C}/\text{s}$)
1	10	170	400	C	0.42	-0.25
2	10	175	400	B	0.50	-0.26
3	10	180	400	B	0.53	-0.30
4	20	175	200	A	0.50	-0.26
5	10	175	200	A	0.50	-0.26

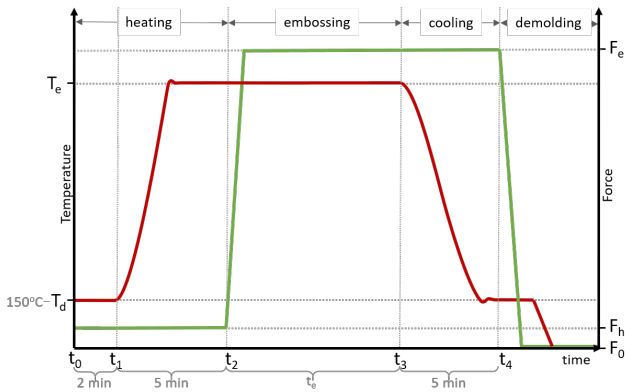


Fig. 10 Schematic of temperature (red) and force (green) during embossing as a function of time.

3 Results and discussion

3.1 Embossing with PDMS

Figure 11 shows the replication accuracy of the embossing process while independently varying embossing temperature, embossing time and embossing force.

Embossing temperature The difference between the thermal expansion coefficients of PDMS and TOPAS® introduces a replication error of:

$$\frac{d_m}{d_s} = (1 + \alpha_{PDMS}\Delta T)(1 - \alpha_{TOPAS}\Delta T) \quad (3)$$

This means that thermal expansion causes features to be 3.3%, 3.4% and 3.5% larger in the TOPAS® substrates than in the PDMS molds at molding temperatures of 170 $^\circ\text{C}$, 175 $^\circ\text{C}$ and 180 $^\circ\text{C}$ respectively, for $\alpha_{PDMS} = 284\text{ppm}/^\circ\text{C}$ (Müller et al., 2019) and $\alpha_{TOPAS} = 60\text{ppm}/^\circ\text{C}$ (Topas Advanced Polymers, 2015). The difference in thermal expansion between the different temperatures, 0.1%/ $^\circ\text{C}$, is insignificant compared to the uncertainty in replication accuracy. In vertical direction the compression of the mold counteracts the effect of thermal expansion. However, for the width of the channels the compression of the mold and

the thermal expansion both work in the same direction.

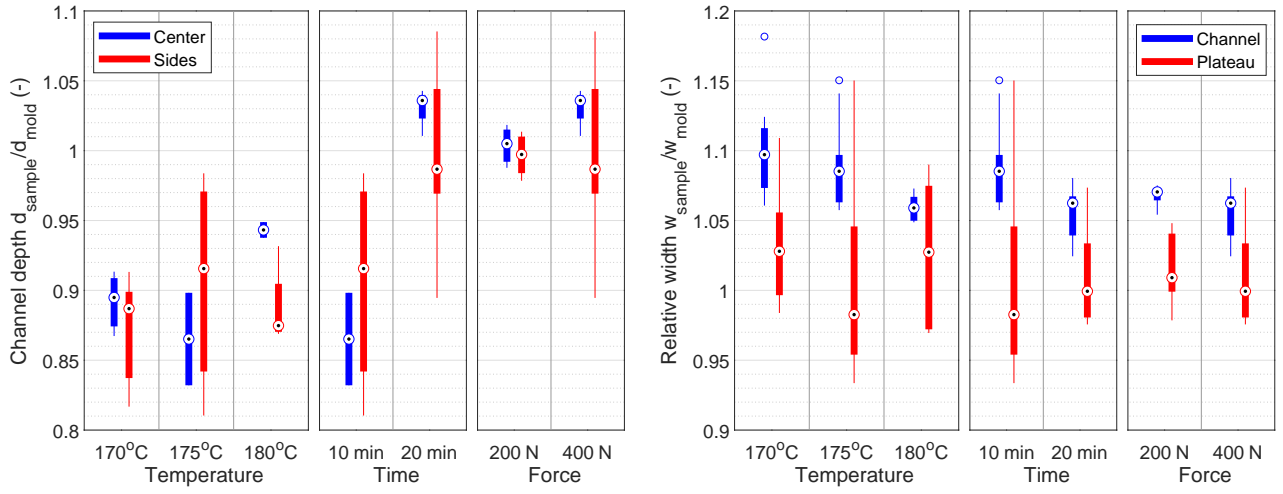
The variation of temperature does not have a clear influence on the replication of channel depth and deformation. The width of the channels and plateaus between the channels becomes more accurately replicated with higher temperature: the mold is less stretched in plane at higher temperature. The overall performance is best at 180 $^\circ\text{C}$: the relative channel depth is the nearest to 1, the relative channel and plateau widths are closest to each other, the angle of the channels does not show a significant difference from the lower temperatures, but the area deviating from the area of a straight channel is slightly larger than at 170 $^\circ\text{C}$. However, at 180 $^\circ\text{C}$ gas bubbles appeared at the edges of the TOPAS® substrates. Further experiments are therefore performed at 175 $^\circ\text{C}$.

Hold time Increasing the embossing time from 10 min to 20 min, with $T_m = 175^\circ\text{C}$ and $F_m = 400$ N, gives a clear improvement on the channel depth replication. Presumably because more time is available for the mold to decompress again. Also the replication of channel width is more accurate, especially the difference between channel and plateau width decreases. However, the directions of the channels diverge when increasing embossing time as indicated by the increased spread in angle.

Embossing force A reduction in force from 400 N to 200 N further lessens the spread in channel depth and channel width, while also decreasing the deformation of the channel in terms of both angle and area.

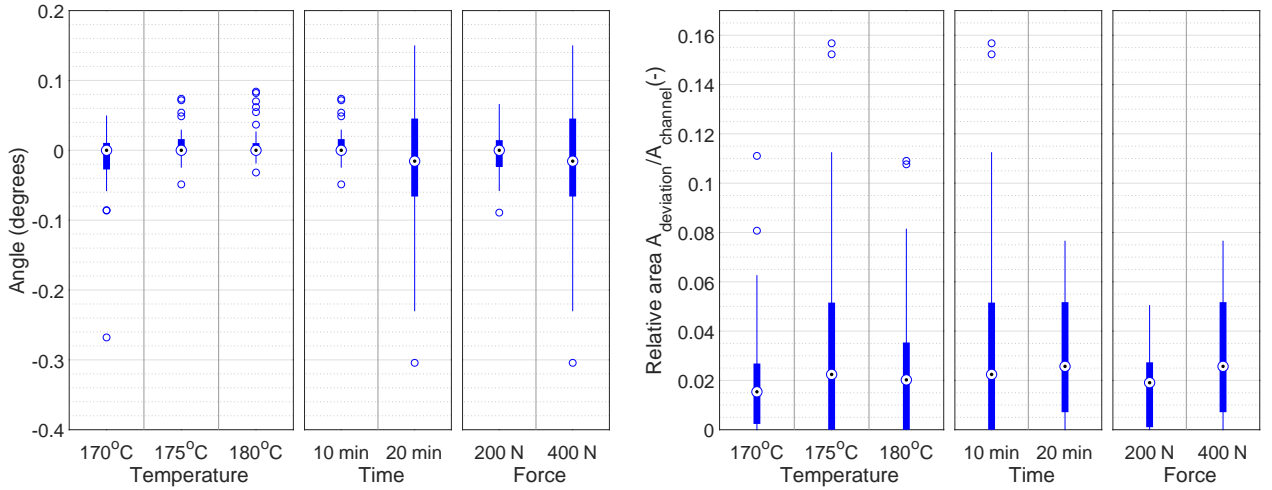
Optimal parameters The best embossing results are found for $T_e = 175^\circ\text{C}$, $t_e = 20$ min, $F_e = 200$ N. Hold time and embossing force have the strongest influence on the embossing result.

Source of deformations It is difficult to derive the exact origin of the deformations in the replicates since there are multiple sources. Firstly, the embossing plates might not be exactly parallel and polishing of the plates could have resulted in slightly convex surfaces. Secondly, the walls of the container of the printed mold are not perfectly parallel with the face on which the channels are printed, causing the thickness of the PMDS mold to vary. Thirdly, the PDMS might not have cured uniformly because of temperature fluctuations, causing variations in the stiffness of the mold and introducing internal stresses which warp the mold. Variations in thickness and stiffness cause a non-uniform embossing pressure, hence deforming the mold non-uniformly.



(a) Relative channel depth. Per substrate one channel in the center (red) and the two channels in the upper left and bottom right corner (blue) are considered.

(b) Relative width of the channels and the plateaus between the channels. Per substrate one channel in the center and the two channels in the upper left and bottom right corner are considered.



(c) Angle of the channel borders with the horizontal. For clarity the outlier at (200 N, 0.40°) is left out. Per sample 12 channel borders are considered.

(d) Area between the embossed channel border and the linear fit through the channel border divided by the area of the undeformed channel. Per sample 12 channel borders are considered.

Fig. 11 Replication accuracy of soft embossing experiments with the benchtop press device. A soft PDMS mold with six parallel channels of 100 μm deep, 1000 μm wide and 30 mm long is used to emboss in TOPAS® 6015 substrates. One embossing variable is varied per experiment, while the other two are kept constant. Varying temperature: $t_e = 10$ min, $F_e = 400$ N. Varying time: $T_e = 175$ °C, $F_e = 400$ N. Varying force: $t_e = 20$ min, $T_e = 175$ °C. 2 - 4 samples are used per setting.

Warping of the mold hinders accurate alignment with the substrate, which could deform the mold when pressure is applied. Lastly, in the current set up the mold and substrate are aligned and placed freely in the press. Combining this with the high elasticity of PDMS the deformation of the mold under load is considerable. However, the in plane deformation could be decreased

significantly by placing the mold in a holder to prevent the edges of the mold to expand to the sides.

3.2 Embossing with MD700

In Figure 12 the deviation of the depth of the embossed channels from the original depth of the channels in the

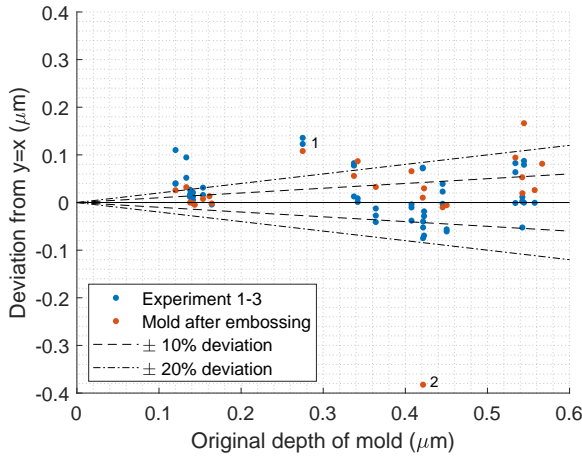


Fig. 12 Deviation of the embossed depth from the original depth of the channels in the mold. $T_e = 175^\circ\text{C}$, $t_e = 20$ min, $F_e = 400$ N. Remarkably, the channels in both the substrates and the mold after embossing are in some cases deeper than in the original mold. At location 1 the channel depth before embossing is measured with insufficient magnification, resulting in an inaccurate depth measurement. At location 2 the mold is presumably damaged during demolding in experiment 3. 82% of the measurements lays within the $\pm 20\%$ bounds, 49% lays within the $\pm 10\%$ bounds.

mold is plotted as function of the original depth of the channels in the mold. Roughly half of the data points show a deeper channel in the substrate than in the mold. Next to that, in some cases the mold has deeper channels after the embossing experiments than before use. This difference cannot be caused by a difference in α between TOPAS® and MD700, since it's in a different order of magnitude and would not explain the deformed mold. Where demolding the PDMS mold did not require any force, the demolding force necessary to separate the MD700 mold from the embossed TOPAS® substrate was considerable. During embossing the pressure is, at least initially, highest at the location of first contact: the bottom of the channels. A possible explanation of the deeper channels could be that during demolding a (thicker) layer of TOPAS® remains on the mold at these locations caused by the locally higher embossing pressure. This would make the channels of the substrates deeper, and the plateaus of the mold higher. Another explanation could be that the plateaus are overstretched during demolding: Adherence between mold and substrate and/or friction between the vertical parts of the mold and substrate are so high that the yield stress of the TOPAS® and MD700 are overcome. See Figure 13 for an illustration of the two principles.

Unfortunately the used imaging techniques are

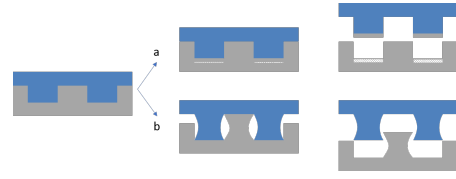


Fig. 13 Failure during demolding causing the channels of the substrate to be deeper than the channels of the original mold. a) A layer of TOPAS® remains stuck to the mold during demolding caused by a high adhesion force. b) Overstretched structures on both the mold and substrate caused by adhesion and/or friction forces exceeding the yield point (Worgull, 2009).

not precise enough to obtain reliable measurements for the width of the channels.

3.3 Design of the press

The springs used in this work are not certified for long term use on high temperatures. The springs were calibrated before and after use, but did not show significant stress relaxation. However, to ensure stable performance the springs could be replaced by springs designed for use at high temperatures.

The substrate is heated from below, the mold is not heated directly, but only via the substrate. Temperature is measured at the surface of the bottom plate, therefore the temperature of the interface between mold and substrate is not exactly known and will vary per material and thickness of the substrate and mold. A more accurate temperature control could be obtained when also the top plate, and hence the mold, is heated directly. It is advised to implement this for example when the results of various mold and substrate materials are compared or when a high reproducibility of the experiments on different equipment is needed.

The requirement on the maximum allowed error in force, $e_F \leq 5\%$, is not met for low press forces, $F < 600$ N, and a small range of intermediate press forces, $1330 < F < 1600$ N. If low embossing or bonding forces are needed with a high accuracy, a spring with lower spring stiffness could be used. Next to that, the measurement plate displays some play along its long axis. Increasing the thickness of both the plate and its bushes will decrease this play and increase the accuracy of the force measurement, permitting a higher accuracy for intermediate force measurements.

4 Conclusion

In this work an easily-manufacturable low-cost benchtop press is presented and its value for the production of microfluidic chip prototypes is demonstrated. The small size of the press and the necessary connection to a laptop computer and the mains allow operation on workbenches without the need for an external oven or a device to apply compression force. Using a lathe and a mill the press can be fabricated in about 2-3 days by a skilled metal worker costing no more than € 250,-. The temperature of the heated plate can be regulated within $\pm 0.25^\circ\text{C}$ up to a maximum calibrated temperature of 180°C . A maximum calibrated force of 2000 N can be applied with an error of ± 79.90 N (95%), a maximum force of 1330 N can be applied with an accuracy of ± 31.82 (95%). The maximum allowed force is 3500 N. One chip of maximally $30 \times 40 \text{ mm}^2$ or multiple smaller chips can be embossed at a time.

The above-mentioned characteristics make the benchtop press valuable for low-cost and time-efficient prototyping of microfluidic chips with high repeatability in basic labs. The production of the chips can be easily scaled-up after prototyping and testing: hot embossing is employed for prototyping as well as for mass production and for even larger quantities injection molding can be used without major changes to the chip design.

The embossing of TOPAS® with a T_g of $\sim 160^\circ\text{C}$ has been demonstrated to be successful for a channel depth of 170 μm . Replication accuracies of $0.37\% \pm 3.83\%$ (95%) (center of the mold) and $-0.33\% \pm 1.60\%$ (95%) (corners of the mold) in depth and $6.82\% \pm 0.50\%$ (95%) (channels) and $1.57\% \pm 1.85\%$ (95%) (plateaus) in width are achieved. The in plane replication accuracy lays in the order of magnitude of the in plane replication accuracies reported in literature.

Embossing smaller feature sizes, with depths between 140 and 560 nm, with a harder MD700 mold was also shown to be successful, but resulted in less accurate replication. The replication accuracy of more than 80% of the channels lays within $\pm 20\%$ and almost half of the channels deviate maximally $\pm 10\%$.

The usability of the press can be further evaluated by soft embossing with a PDMS mold in a container to prevent in plane deformation due to the Poisson effect. Embossing experiments with small feature sizes should be repeated with a smaller mold, which fits directly into the press and adequate equipment should be used

to evaluate the replication accuracy of the in plane dimensions.

Acknowledgements The TOPAS® 6015 substrates were kindly provided by Jörg Strack from TOPAS Advanced Polymers GmbH.

Conflict of interest

The authors declare that they have no conflict of interest.

References

- Fanzio P, Cagliani A, Peterffy KG, Sasso L (2017a) High throughput soft embossing process for micro-patterning of PEDOT thin films. *Microelectronic Engineering* 176:15–21, DOI 10.1016/j.mee.2017.01.011, URL <http://dx.doi.org/10.1016/j.mee.2017.01.011>
- Fanzio P, Chang CT, Skolimowski M, Tanzi S, Sasso L (2017b) Fully-Polymeric pH Sensor Realized by Means of a Single-Step Soft Embossing Technique. *Sensors* 17(6):1169, DOI 10.3390/s17051169, URL <http://www.mdpi.com/1424-8220/17/5/1169>
- Jena RK, Yue CY, Lam YC (2012) Micro fabrication of cyclic olefin copolymer (COC) based microfluidic devices. *Microsystem Technologies* 18(2):159–166, DOI 10.1007/s00542-011-1366-z
- Lee JH, Peterson ETK, Dagani G, Papautsky I (2005) Rapid prototyping of plastic microfluidic devices in cyclic olefin copolymer (COC). *Proc SPIE* 5718:82–91, DOI 10.1117/12.591852, URL <http://dx.doi.org/10.1117/12.591852>
- Mastrangeli M, Millet S, Raaij JVDEv (2019) Organ-on-Chip In Development : Towards a roadmap for Organs-on-Chip. *Preprints (March):1–37*, DOI 10.20944/preprints201903.0031.v1
- Müller A, Wapler MC, Wallrabe U (2019) A quick and accurate method to determine the Poisson's ratio and the coefficient of thermal expansion of PDMS. *Soft Matter* 15(4):779–784, DOI 10.1039/c8sm02105h
- Narasimhan J, Papautsky I (2003) Polymer embossing tools for rapid prototyping of plastic microfluidic devices. *Journal of Micromechanics and Microengineering* 14:96–103, DOI 10.1088/0960-1317/14/1/013
- Regehr KJ, Domenech M, Koepsel JT, Carver KC, Ellison-zelski J, Murphy WL, Schuler LA, Alarid ET, David J (2009) Biological implications of polydimethylsiloxane-based microfluidic cell culture. *Lab on a chip* 9(15):2132–2139, DOI 10.1039/b903043c.Biological

- Steigert J, Haeberle S, Brenner T, Müller C, Steinert CP, Koltay P, Gottschlich N, Reinecke H, Rühle J, Zengerle R, Ducleé J (2007) Rapid prototyping of microfluidic chips in COC. *Journal of Micromechanics and Microengineering* 17(2):333–341, DOI 10.1088/0960-1317/17/2/020
- Topas Advanced Polymers (2015) TOPAS- Cyclic Olefin Copolymers. URL [http://www.topas.com/sites/default/files/files/TOPAS_Brochure_E.2014.06\(1\).pdf](http://www.topas.com/sites/default/files/files/TOPAS_Brochure_E.2014.06(1).pdf)
- Tsao CW (2016) Polymer microfluidics: Simple, low-cost fabrication process bridging academic lab research to commercialized production. *Micromachines* 7(12), DOI 10.3390/mi7120225
- Van Midwoud P, Janse A, Merema M, Groothuis G, Verpoorte E (2012) Comparison of biocompatibility and adsorption properties of different plastics for advanced microfluidic cell and tissue culture models. *Analytical Chemistry* 84(9), DOI 10.1021/ac300771z
- Worgull M (2009) *Hot Embossing: Theory and Technology of Microreplication*. Elsevier Science, DOI 10.1016/B978-0-8155-1579-1.50001-X, ISBN:978-0-8155-1579-1
- Zhou K, Papautsky I (2007) Optimization of COC hot embossing with soft PDMS tools. *Microfluidics, BioMEMS, and Medical Microsystems* V 6465(January 2007):64650R, DOI 10.1117/12.701281

3

Substrate preparation

Before soft embossing, a layer of TOPAS 5013 is applied on the TOPAS 6015 substrates by spin coating to serve as a bonding layer. After soft embossing two substrates will be bonded with a membrane in between using thermal fusion bonding at a temperature lower than the soft embossing temperature to avoid deformations, as described in Section 1.3.1. The presence of the spin coated TOPAS 5013 makes bonding at low temperature possible.

In this chapter a protocol is determined to obtain a film of TOPAS 5013 on TOPAS 6015 with a tunable thickness. The thickness of the spin coated layer depends mainly on solvent choice, spin-speed and time. In the following, first the theory of spin coating is described followed by the spin coating experiments performed to determine a relation between spin speed and thickness.

3.1. Spin coating in theory

Spin coating is a technique used to produce thin films of several nanometers to tens of micrometers on flat substrates. The desired film material is dissolved in a solvent. The solution is applied on the usually circular substrate, which will be spinned to form a uniform layer of the solution. The solvent will evaporate, leaving behind a uniform thin film. The process is generally divided into four phases [81]:

1. Dispense of the solution. The solution can either be dispensed statically, the substrate having no angular velocity, or dynamically, the substrate rotating at a low speed, typically around 500-1000 rpm. Depending on the viscosity and substrate size typically a few millilitre of solution is deposited using a pipette. Dynamical deposition gives better reproducibility, since the time for the solution to evaporate before spinning is smaller. However, it is more difficult to wet the complete surface of the substrate, especially when the wettability is poor.
2. The substrate is accelerated at a constant rate to the desired rotational speed. During this phase the solution is spread out due to the centripetal force and a large amount is flung off of the edge of the substrate. Vortices might be present in the fluid caused by the faster moving substrate underneath, but while the film gets thinner the fluid will eventually move along with the substrate and the inhomogeneities will disappear.
3. The substrate spins at constant rate and film thinning is dominated by viscous forces. The fluid flows to the edges and flings off when the surface tension is overcome by the centripetal force. Along the edge of the substrate beads could form, depending mainly on surface tension, viscosity and rotational speed.
4. The substrate is still spinning at constant rate but the thin film thinning is now dominated by evaporation of the solvent. The evaporation rate depends, among others, on vapour pressure, boiling point, substrate temperature and rotational speed. As the solvent evaporates, the viscosity of the solution increases and the solution will stop flowing.

The processes in phase 3 and 4 will both occur at the same time, but the dominant phase will gradually change from phase 3 to phase 4. After the spin coating process the substrates are typically annealed at low temperature to force out the remaining solvent.

Film thickness Film thickness can be influenced by alternating the viscosity of the solution and the spin speed. Madou [45] proposes the following empirical relation to approach film thickness T :

$$T = \frac{K \cdot C^\beta \cdot \eta^\gamma}{\omega^\alpha} \quad (3.1)$$

With concentration (C) of the polymer in solvent (g/100ml), the intrinsic viscosity (η) of the polymer, the rotational speed (ω in rpm) and constants, (α, β, γ, K), to be determined empirically. In the case of TOPAS substrates the hydrophobicity can be varied to influence surface tension and hence film thickness.

3.2. Spin coating in practice

Bonding experiments were to be started with a target of 10 μm of TOPAS 5013 on both TOPAS 6015 substrates to be bonded. During the bonding experiments the thickness might need to be altered. Thickness as function of spin speed is plotted in the coming section to accommodate for this. The layers need to completely cover the substrates and to have an acceptable surface roughness. The solvent sec-butyl benzene appeared to be more suitable in this regard than toluene.

Measuring the thickness of a TOPAS layer spin coated on a TOPAS substrate brings along some complications. Starting with a good initial guess of the spin coating parameters will speed up the process of optimizing the film thickness. Hereto experiments are started by spin coating on a glass substrate. The parameters found to obtain the desired layer thickness then give a good indication how to set the parameters when experimenting with a TOPAS substrate. Different methods were tried to measure the thickness. In the first method a gold/palladium coating is used to create a visible interface and measure the thickness using white light interferometry. In the second method the thickness of the complete substrate is measured before and after spin coating with confocal laser scanning microscopy.

In the following sections first the methods are described. Hereafter the results and a motivation for the individual experiments will be given.

3.2.1. Methods

Table 3.1: Solution composition, substrates and measurement method used per experiment

Experiment	Solvent	TOPAS weight percentage wt%	Substrate material	Substrate size mm	Measurement method
1	Toluene	12.5	Borosilicate glass	$\emptyset 54$	scratch + WLI
2	Sec-butyl benzene	25.0	Borosilicate glass	26x76x1	scratch + WLI
3	Sec-butyl benzene	25.0	TOPAS 6015 + Au/Pd	15x36x1	step + WLI
4	Sec-butyl benzene	15.0	TOPAS 6015 + Au/Pd	15x36x1	step + WLI
5	Sec-butyl benzene	15.0	TOPAS 6015	15x36x1	CLSM
i	Sec-butyl benzene	25.0	Borosilicate glass	15x36x1	scratch + WLI

WLI: white light interferometry CLSM: confocal laser scanning microscopy

Table 3.2: Spin coating program used in experiments 1-5. All spin coating parameters are kept constant as indicated in this table, except for the spin speed in step 1, ω_1 , which is varied between 1000 and 5000 rpm.

	spin speed (rpm)	acceleration (rpm/s)	time (s)
Step 1	1000-5000	250	50
Step 2	100	250	30

Spin coating Prior to spin coating samples were cleaned in Liquinox 1% in an ultrasonic bath for 5 min, rinsed with DI water, cleaned in 99.9 % 2-propanol in an ultrasonic bath for 3 min and dried in a clean, dry air stream. After mounting a substrate on the spin coater, it is cleaned again by applying 2-propanol and removing it by spinning.

The spin coating solution consists of TOPAS 5013 granules (rinsed with Liquinox 1%, DI water and 2-propanol consecutively and dried) dissolved in the respective solvents. The TOPAS 5013 granules are dissolved in the solvent in a glass bottle with screw cap with PTFE inlay by placing the bottle on an orbital shaker at room temperature for ~ 3 hours until fully dissolved.

All relevant spin coating experiments performed are summarized in Section 3.2.1 and Table 3.2. Table 3.2 gives the used spin coating programs, derived from Kapel [38]. In step 1 a spin speed between 1000 and 5000 rpm is used. All other parameters are kept constant as in Table 3.2. The solution is dispensed statically, since dynamic dispense resulted in incomplete coverage of the substrate due to very low wettability.

After mounting the substrates on the vacuum chuck of the spin coater, the spin coating solution is applied statically using a glass pipette. Care was taken to wet the complete surface of the TOPAS substrates. After spin coating samples were left in the fume hood for ~ 3 days to let the solvent evaporate.

Substrates of experiment 5 were hard baked at ~ 70 °C for a few hours before thickness measurements were performed.

Sputter coating The TOPAS substrates of experiments 3 and 4 are sputter coated before spin coating: Masks (Figure 3.1) are cut from a layer of ~ 1 μm thick PDMS, cleaned in 2-propanol, dried and applied on the substrates. Three to four substrates at the same time are sputter coated at ~ 12.5 mA for 180 s using a Au/Pd target.



Figure 3.1: PDMS mask (17x38 mm) applied for sputter coating Au/Pd on TOPAS 6015 substrates.

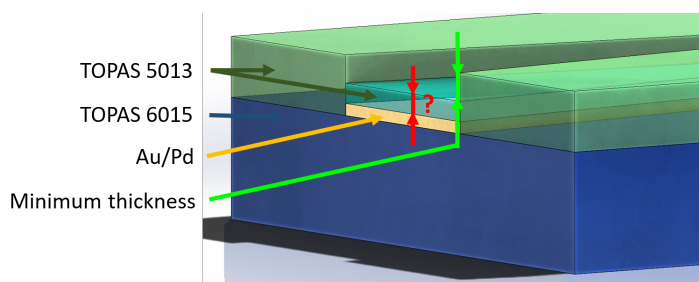


Figure 3.2: Schematic of the sputtered and spin coated substrate. The sputtered Au/Pd is transparent. Above the Au/Pd layer, the spin coated TOPAS 5013 layer is a lot thinner than at places where it is directly spin coated on the TOPAS 6015 substrate. The red dimension, indicated with a question mark, could not be determined because of the transparency of the Au/Pd layer. The green dimensions is a measure for the minimum thickness of the spin coated layer. Dimensions are not to scale.

Layer thickness measurement using white light interferometry Experiments on glass and experiments on TOPAS 6015 substrates with a Au-Pd coating where evaluated using the same method (experiments 1-4). After coating on glass, part of the coating is scratched away using a scalpel, revealing the glass surface and resulting in two areas with different surface heights. The step size determines the layer thickness of the TOPAS 5013 on glass. Complete removal of the TOPAS and leaving the glass surface unaffected is confirmed when white light interferometry shows a surface with very low surface roughness, similar to untreated microscope slides. The TOPAS 5013 layer on top of the Au-Pd coating, which only partly covers the substrate, is thinner than the layer on top of the rest of the substrate. This also results in two areas with different surface heights. See Figure 3.2 for a schematic of the substrate to illustrate the difference in surface height.

Using white light interferometry areas of 1.8 x 2.7 mm, containing both areas with different surface heights, are imaged. Processing of the image starts with levelling the images by linearly fitting the xy-plane to a horizontal

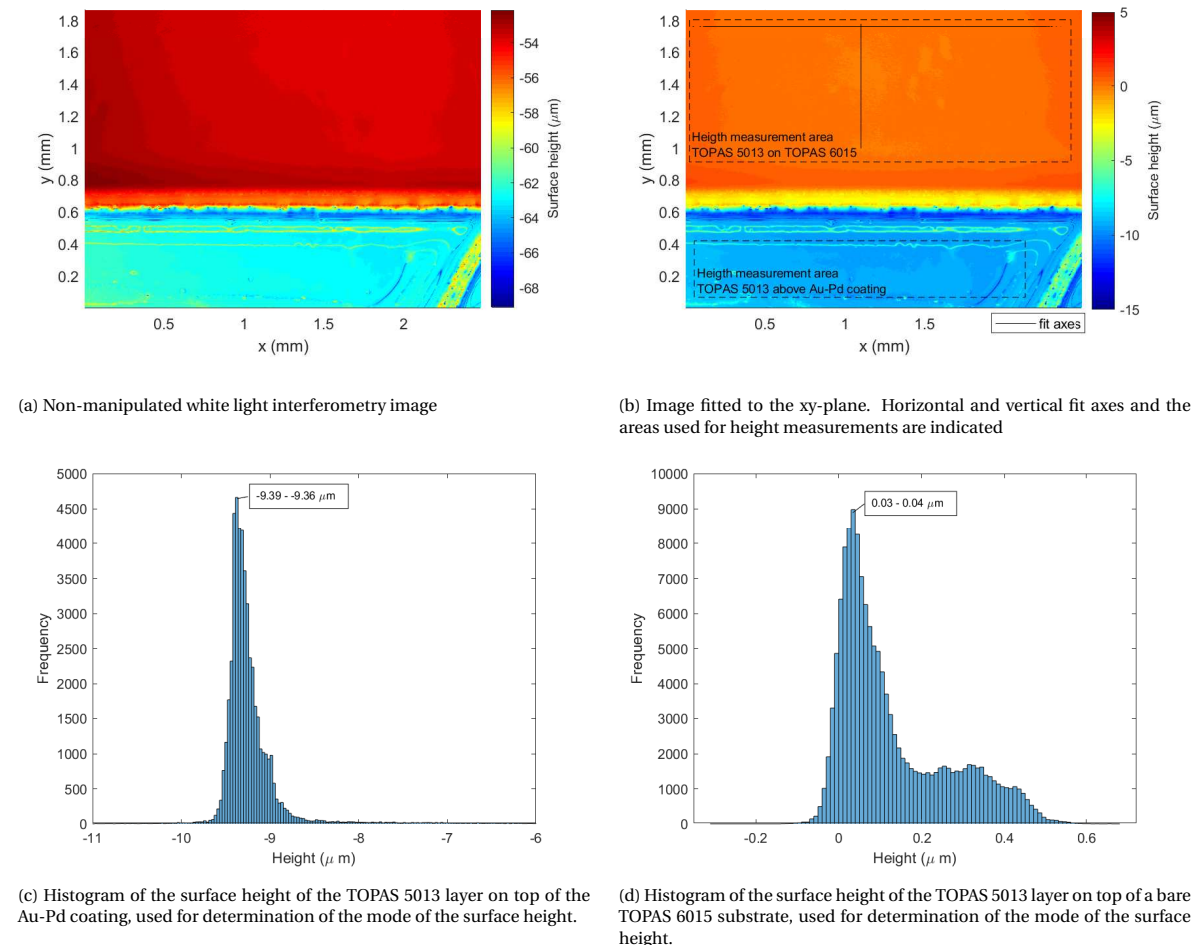


Figure 3.3: Determining the height of sample 1 of experiment 4. (15wt% TOPAS 5013 in sec-butylbenzene on TOPAS 6015 with Au-Pd coating, spin coated at 2500 rpm)

line ($y, z = c$) and a vertical line ($x, z = c$) consecutively. On both parts (small and large heights) an area is selected, avoiding major defects in the coating. In these areas the mode of the z -values (i.e. the height of the surface) is determined. The step size is calculated as the difference between the modes of the two areas. See Figure 3.3 for the consecutive steps.

Layer thickness measurement using laser microscopy The thickness of the sample is measured before and after spin coating, the difference determining the spin coated layer thickness. Samples are placed flat and suspended in air under a laser microscope. A depth image is made which captures both the top and bottom surface of the samples. The height of the top and bottom surface is determined by calculating the average height of respectively 10 and 20 lines of ~ 1 cm in an area close to the centre of the sample.

Experiment i Samples are spin coated according to the protocol in Table 3.2 with a spin speed of $\omega = 1500$ rpm in step 1. White light interferometry images of a strip of the substrate depicted in Figure 3.4 are levelled with the xy -plane as described above in *layer thickness measurements using white light interferometry*. The average height of the surface is determined at areas with constant width and increasing distance r to the centre of the substrate, see Figure 3.4. The layer thickness is determined for three samples at $|r| = 8$ mm by scratching part of the film and proceeding as in *layer thickness measurements using white light interferometry*.

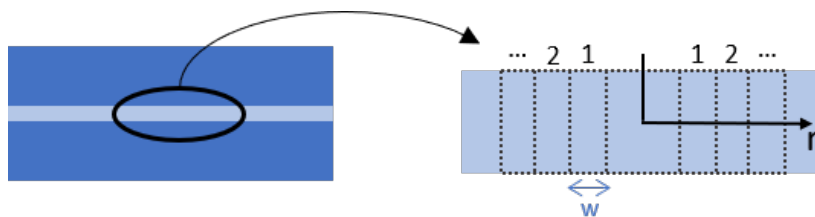


Figure 3.4: The light-blue strip is imaged using white light interferometry. The strip is divided in intervals of $w = 250 \mu\text{m}$. The average height of every interval is determined. Intervals on the left and right side of the centre with equal distance r to the centre are taken together.

Table 3.3: Properties of toluene and sec-butyl benzene. Reproduced from Bundgaard [15]

Substance	Boiling point	Vapor pressure @ 20 °C	Molecular formula	Structure formula
Toluene	110 °C	5.4 kPa	C_7H_8	
Sec-butyl benzene	174 °C	0.133 kPa	$\text{C}_{10}\text{H}_{14}$	

3.2.2. Results and discussion - Solvent choice

The first experiment is performed using toluene as a solvent in the spin coating solution, as was done before in the department. Visual inspection of the results of experiment 1 shows ripples in radial direction: see Figure 3.5 for a typical substrate, see remaining substrates in Appendix D.2. The ripples are suspected to be caused by the high evaporation rate of toluene. During the spin coating process, evaporative cooling causes temperature gradients. Concentration gradients occur when evaporation takes place at a higher rate than diffusion of solvent through the film. These gradients induce a gradient in surface tension, causing convective currents and hence variations in film thickness, visible as the radial striations in the spin coated film. This phenomenon is known as a subset of the *Marangoni effect* and can be diminished by decreasing the evaporation rate [9, 67].

Bundgaard et al. [14], who had similar difficulties with the use of toluene as solvent as described above, switched the solvent for sec-butylbenzene. Sec-butylbenzene has a higher boiling point and a lower vapour pressure, thus evaporating slower, see Table 3.3. Figure 3.6 is a typical result for experiment 2, where sec-butylbenzene is used. The surface of the TOPAS 5013 layer is indeed a lot smoother than when using toluene as in experiment 1. For this reason toluene is exchanged for sec-butyl benzene in all following experiments. However, the surface is still not smooth. Small holes are visible, which are also present in the first experiment but less visible because of the striations. This is a common issue in spin coating and is attributed to the use of solvents with high volatility. Lai [39] found that this *orange peel* effect disappears when using a solvent with lower volatility. The scale of the irregularities is low compared to the to be embossed feature sizes and will likely disappear during embossing. It is therefore decided to work with the result as is.

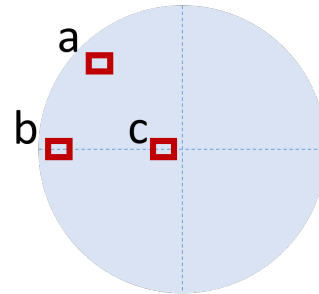
3.2.3. Results and discussion - Film thickness

Layer thickness is first determined on glass substrates. TOPAS coatings on glass are easier to measure than on TOPAS substrates and the measurements on glass make it possible to predict the parameters needed to obtain the desired layer thickness of $10 \mu\text{m}$ on TOPAS substrates. The experiments are started with a protocol that was set up at the department by Kapel [38] and altered step by step to get the desired result. Spin coating protocols sometimes contain two coating steps. Layer thickness is mainly determined by the first step. In the second step the rotational speed is mostly accelerated rapidly to remove edge and corner beads. In the protocol of Kapel [38] the second step has a very low velocity. The aim of this step is not very clear, but it is noted that this step was added to spread the solution ore slowly on the substrate. For this project the second step appeared useful to allow the solvent to evaporate sufficiently, such that the substrate can be removed without damaging the spin coated layer, while at the same time the low spin speed does not influence layer thickness significantly.

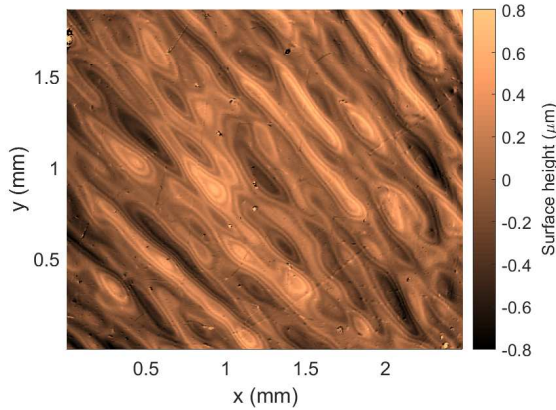
Figure 3.7 summarizes the results of experiments 1 to 5. The measurement data is fitted to the relation proposed by Madou [45], simplified to $T = a\omega^b$.



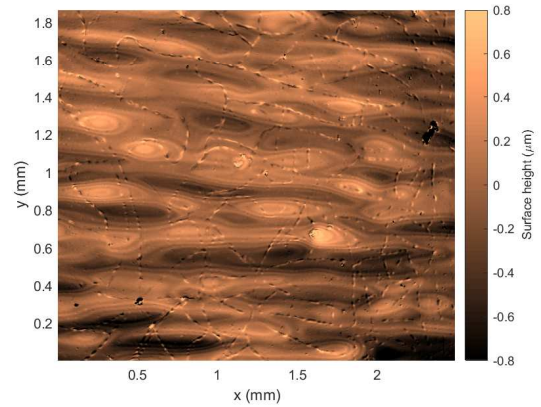
(a) Result of sample 6 from experiment 1, $\omega_1 = 3900$ rpm. Along the centre of the petri dish the TOPAS film is scratched away to allow for thickness measurements. The surface is not smooth but shows radial ripples.



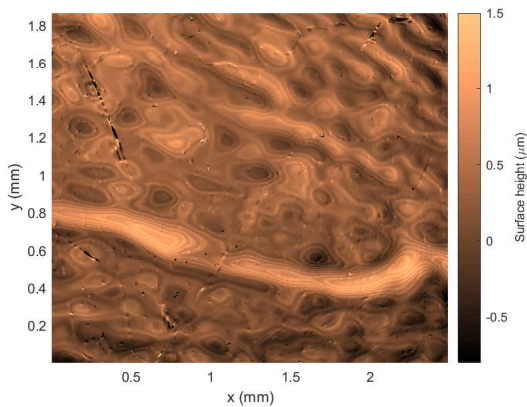
(b) Location of the images on the substrate. Dimensions not to scale



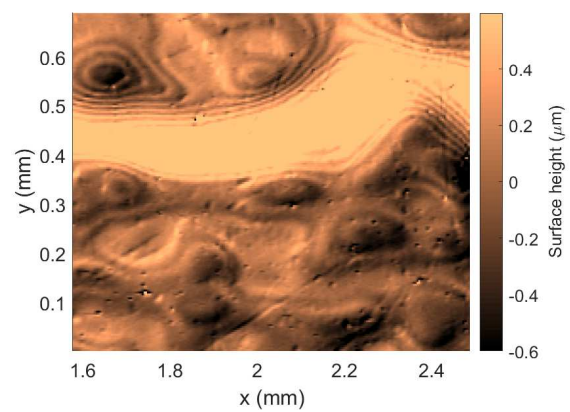
(c) Surface at location a. Ripples direct upward with an angle of ~ 45 degrees.



(d) Surface at location b. Ripples are parallel with the x-axis.

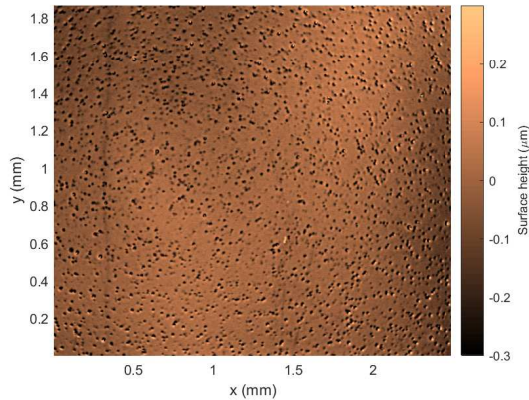


(e) Surface at location c. Direction of the ripples changes from parallel with the x-axis at the bottom, to slightly upwards. The ripples are higher, but less wide than further from the centre of the substrate (note the adjusted colorbar).



(f) Surface at location c. Small holes with diameters in the order of 10-20 μm are present.

Figure 3.5: Images of the surface of sample 6 of experiment 1 captured using white light interferometry. From the images at different locations it can be seen that the ripples are directed radially and decrease in height and increase in width further from the centre of the substrate. (Scratches are assumed to originate from manipulation for thickness measurements after spin coating).



(a) Image of the surface of sample 4 of experiment 2 captured using white light interferometry. No ripples are present, but small holes appear, a phenomenon called 'orange peel' by [39].



(b) Result of sample 4 of experiment 2, $\omega_1 = 3900$ rpm. The surface is smooth, no defects visible for the naked eye. Irregularities along the edges are caused by insufficient wetting of the surface.

Figure 3.6: Surface quality of sample 4 of experiment 2. The ripples seen in experiment 1 are not visible anymore for the naked eye or with white light interferometry. Smaller defects are however visible using white light interferometry.

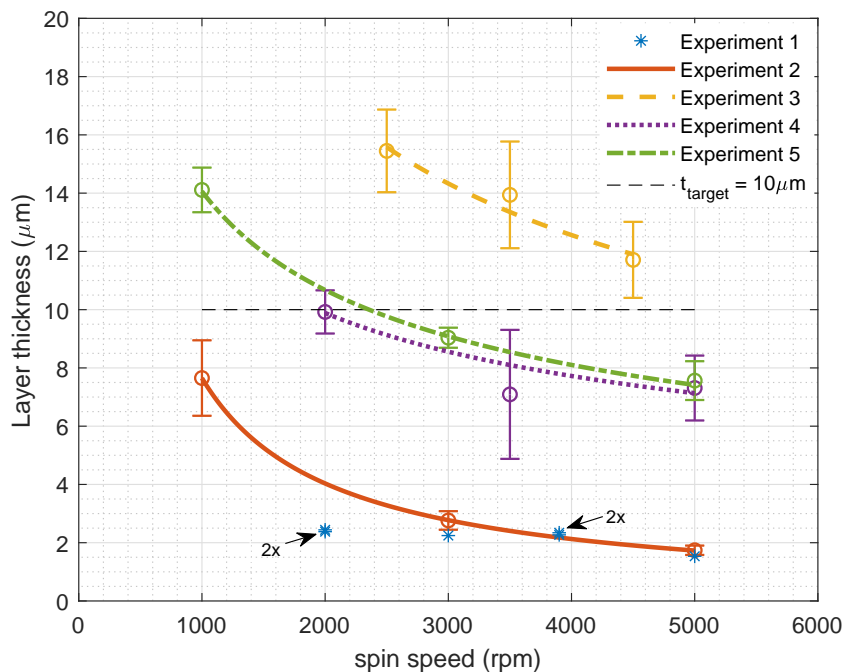


Figure 3.7: Layer thickness of a TOPAS 5013 spin coated on different substrates, for varying weight percentage, solvent and substrate size, see Section 3.2.1. Fitted curves of the form $T = a\omega^b$ are obtained with the Nelder-Mead Simplex Method. Every measurement point in experiment 1 to 5 indicates the average of the height of multiple samples. Three samples per spin speed are evaluated for experiment 4 and 5, three to seven for experiment 2 and 3. The error bars give the standard deviation.

Experiment 1 - Toluene 12.5 wt% on glass As a starting point, the protocol determined by Kapel [38] for spin coating TOPAS 8007 is used, since the same layer thickness is needed, namely $10 \mu\text{m}$. Kapel [38] used a solution of 20 wt% TOPAS 8007 in toluene to obtain a layer of $10 \mu\text{m}$ TOPAS 8007 on a glass petri dish of 54 mm with the protocol in Table 3.2, with a spin speed of 3900 rpm in the first step. With increasing T_g , the solubility of TOPAS in toluene appears to decrease and the viscosity of the solution appears to increase [15]. Therefore a solution with a lower weight percentage of TOPAS 5013 is used, namely 12.5 wt%, which gives a visually comparable viscosity.

Figure 3.7(*) shows the results of the thickness measurements. The layers are about $2 \mu\text{m}$ thick, a lot thinner than expected and than the desired $10 \mu\text{m}$.



Figure 3.8: Spherical defects in the spin coated TOPAS layer on top of the sputter coated Au/Pd line. Picture made with a confocal microscope, 300 \times magnified.

Experiment 2 - SSB 25.0 wt% on glass As described in Section 3.2.2 toluene is exchanged for sec-butylbenzene in experiment 2 due to rippling. The weight percentage needed to obtain comparable results with two different solvents can not be determined easily without experiments, since it depends on multiple adverse elements: evaporation rate, solubility, contact angle and viscosity among other things. It was decided to double the weight percentage to 25 wt% TOPAS 5013 in sec-butylbenzene. This resulted in layers of 2 - 7.5 μm , see Figure 3.7 (Φ). The desired 10 μm is not reached. Bundgaard [15] showed that spin coating solutions with high TOPAS 8007 content (20-30 %) on thin TOPAS 8007 layers yields 1.5-2 x thicker layers than when spin coating on silicon. Therefore in the next experiment, which is performed on TOPAS substrates instead of glass substrates, the same weight percentage is used to obtain a thicker layer in experiment 3 than in experiment 2.

Experiments 3 and 4 - SSB 25.0 and 15.0 wt% on TOPAS + Au/Pd A thin line is sputter coated on the substrate before spin coating to provide for an interface between the substrate and spin coated layer. The interface should be visible with white light interferometry, such that the height of both the sputter coated layer and the spin coated layer could be determined. Unfortunately, sputter coating programs which should yield layers of > 100 nm did not result in an interface visible with white light interferometry. This could be explained by the fact that the sputter coated layers could be thinner than expected from the sputter coating programs used. Next to that, the refractive index of the sputter coated Au-Pd layer could be a lot closer to the refractive index of Pd, $n = 1.6175 @ 540 \text{ nm}$ [37] than to that of Au, $n = 0.48899 @ 540 \text{ nm}$ [37], resulting in a layer with a high transparency at 100 nm thickness, see Appendix B.2.4. Recently Şenay [25] determined the refractive index of sputtered Au/Pd layers of 20 and 80 nm to be indeed $n \approx 1.74$ and $n \approx 1.63$ respectively.

Nevertheless, a minimum layer thickness could be determined: Above the sputtered lines the spin coated layers are a lot thinner, see Figure 3.2 for a schematic of the substrate. This is believed to be caused by the small contact angle of the solution on the sputtered Au-Pd and the physical barrier the Au-Pd layer forms between the solvent and the substrate. Edge effects influence the layer thickness in a small region along the Au-Pd line, see Figure 3.9. Edge effects are only significant up to 0.2 mm from the Au-Pd line. The thickness is determined by taking the mode of the height data from an area with a height of about 0.3 - 1.2 mm above the Au-Pd line. Edge effect will therefore not influence the layer thickness determination. The minimum thicknesses determined as in Section 3.2.1 show that 25 wt% is too high (12-16 μm), but 15 wt% looks promising (7-10 μm), see Figure 3.7 (Φ, Φ).

On top of the Au-Pd layer spherical defects appear in the TOPAS layer, see Figure 3.8. These defects are presumably caused by colloidal TOPAS particles in the spin coated solution which did not properly dissolve in the solvent. The defects are not visible in the thicker spin coated layers and might appear when the layer is thinner than the colloidal particles. Because the size of the particles is unknown, the layer thickness on top of the Au-Pd layer cannot be approximated using the size of the smallest spherical defects in the TOPAS layer.

Different strategies could be employed to determine the thickness of the TOPAS layer on top of the Au/Pd

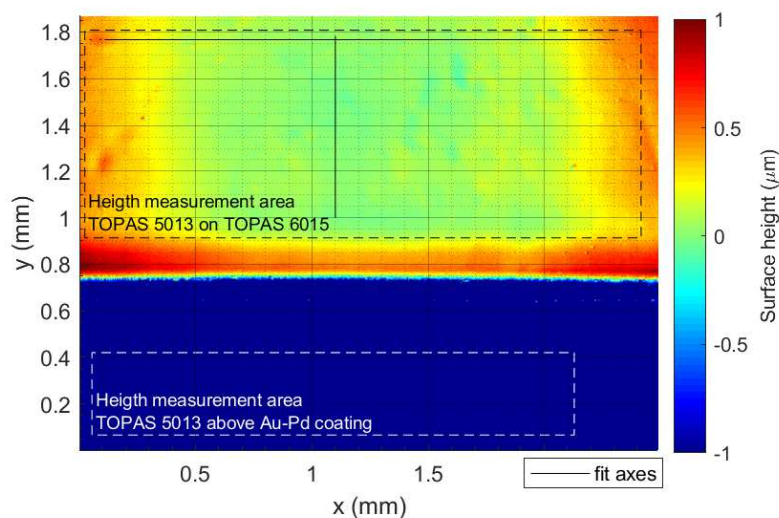


Figure 3.9: Height measurements areas of sample 1 (2000 rpm) of experiment 4. Edge effects cause a higher layer thickness along the Au-Pd line. The effect is visible up to 0.3 mm next to the Au-Pd line. The edge effect does not influence the layer thickness determination since the height measurement area is selected above this area with heightened layer thickness. Next to that, the layer thickness is determined by taking the mode of the height data, which further cancels out any errors in area selection.

layer. The TOPAS layer on top of the Au/Pd layer could be removed by plasma etching after partially masking the sample with a material less affected by plasma etching such as aluminium. Another method could be by depositing an extra Au/Pd layer on top of the spin coated TOPAS, making a cross section of the samples and determining the distance between the Au/Pd layers using electron microscopy. Attempts have been made to cut the samples to make a cross section. However, verifying if the cutting process did not affect the layer thicknesses was difficult. Hence, experiment 5 is performed to determine the thickness of the TOPAS films.

Experiment 5 - SSB 15.0 wt% on TOPAS In the last experiment samples are measured using confocal laser scanning microscopy. The previous experiments give a good approximation of the necessary weight percentage of TOPAS, such that the relative expensive laser microscopy measurements only need to be performed once. By using 15 wt% TOPAS 5013 in sec-butylbenzene for spin coating speeds between 1000 and 5000, layers of 7.5-14 μm can be obtained, see Figure 3.7(Φ).

In experiment 4 the minimum thickness obtained using the same settings is indeed slightly smaller (0.5-1 μm). However, the thickness measurements are not performed at the same location. In experiment 4 thickness measurements are performed as close to $|r|=8$ mm as the surface quality would allow (the surface quality is affected by presumably colloidal particles), in experiment 5 the measurements are taken close to $|r|=1$ mm. At $|r|=1.125$ mm, the thickness in experiment i is $(6.85 \pm 2.00)\%$ smaller than at $|r|=8$ mm. This difference dependent on measurement location exceeds the difference between experiment 4 and 5 at spin speeds ≥ 2500 rpm. Possible causes of this discrepancy might be the sputter coated layer influencing the layer thickness and the influence of spin speed and substrate material on the uniformity of the layer thickness.

The target thickness of 10 μm can be obtained by statically depositing a solution of 15.0 wt% TOPAS 5013 in sec-butylbenzene, spinning for 50 s at 2355 rpm, followed by 30 s at 100 rpm, using an acceleration of ± 250 rpm/s for both steps. The most accurate thickness measurements are obtained by measuring the thickness of the samples before and after spin coating using confocal laser scanning microscopy.

Experiment i - SSB 25.0 wt% on glass, height profile Experiment i is performed to determine the dependency of the layer thickness on the distance from the centre of the substrate. A spin speed of 1500 rpm is used in step 1 of the protocol in Table 3.2. It was found in experiment 4 and 5 that the spin coated substrates warp during or after spin coating and could therefore not be used to determine the thickness-distance relation. To

Table 3.4: Measurement locations per experiment expressed as r , the distance from the center of the substrate. All locations lay on the long axis (rectangular substrates) or diagonal (circular substrates) of the substrates.

Experiment	Measurement location r mm	Substrate size mm
1	Averaged at $r = 0, 10$ and 20	$\phi 54$
2	35	26 x 76 x 1
3	6-8	15 x 36 x 1
4	1.7- 12.9	15 x 36 x 1
5	0-2	15 x 36 x 1

reduce warping experiment i is performed on 1 mm thick glass microscope slides. For three different samples the layer thickness is determined along the long axis of the samples.

Thickness measurements are performed along the long axes of the substrates (rectangular substrates) or along an arbitrary diagonal (circular substrates). In experiment 1 the height of every sample was determined by taking the average of three points along the diagonal: at 0, 10 and 20 mm from the centre. Because of the amount of time it takes to image and process one measurement point it was decided to measure one point per sample only for the remaining experiments. In experiment 3 and 4 the location of the measurement is determined by the quality of the surface: Above the gold coated layer many spherical defects, presumably caused by colloidal particles, are present. Measurements are taken at spots with the least amount of defects. See Table 3.4 for the measurement locations per experiment.

Figure 3.10 shows the variation in layer thickness along the long axis of the samples. This variation depends on spin speed, viscosity of the solution, substrate material and size, and is therefore not one-to-one transferable to experiments 1 to 5. However, it gives an idea of the influence of the measurement location. No measurements in experiment 3-5 are taken at $r > 12.9$ mm, which is considered to be a safe limit, since only at $r > 14.72$ mm edge bead effects alter thickness drastically. In the range $1.16 \text{ mm} \leq |r| \leq 14.72 \text{ mm}$, the maximum deviation in layer thickness is $(0.24 \pm 0.15) \mu\text{m}$, which lays well within the error of the thickness measurements of experiment 1 to 5.

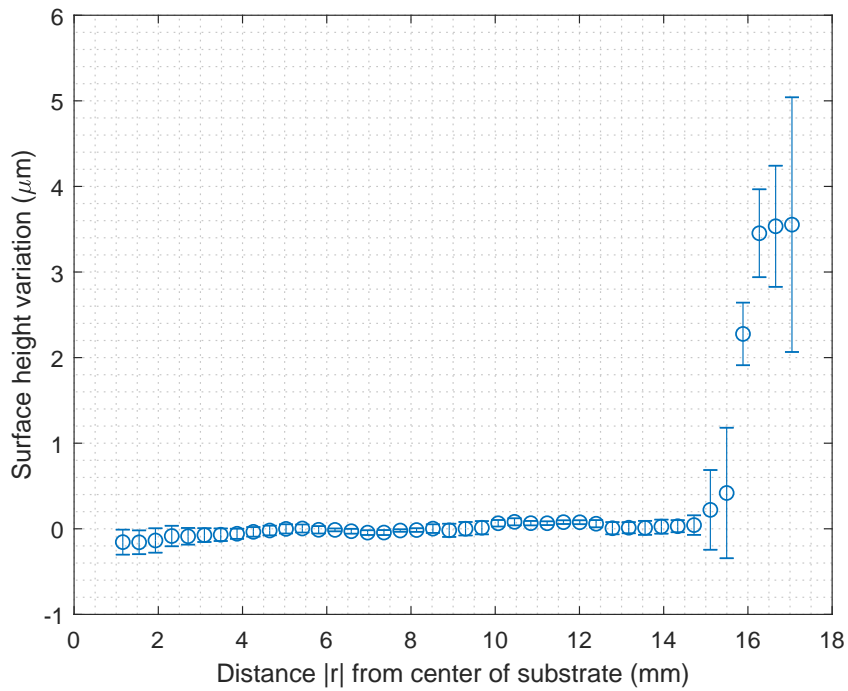
Substrate size The spin coating experiments are performed on substrates with different dimensions for practical reasons. The first series is performed on petridishes to first gain experience on a substrate with the relatively simple circular shape, giving the most uniform results. At the start of the second set of experiments the lab ran out of petridishes and standard microscope slide were used. For the remaining experiments TOPAS and glass substrates were cut to the target size of the microfluidic device to be embossed.

The dimensions of the substrate influence film thickness. A small increase in substrate size will result in a smaller film thickness, since the centrifugal force that needs to overcome the surface tension at the edges, increases when the rotational speed remains constant. Since also the fluid-air interface increases with increasing substrate size, viscosity of the solution will increase faster and slow down film thinning. The effect of increasing substrate size on film thickness is therefore not straightforward. However, experiment 3 to 5 and i are performed on the target substrate size on which the film thickness needs to be determined, so the substrate size does not have a relevant influence on the final result.

3.3. Conclusions

Surface quality of the spin coated layer is strongly influenced by the solvent used. When the evaporation rate of the solvent is too high, gradients in temperature and viscosity cause ripples in the film. The use of toluene, a solvent with a very high evaporation rate, results in non uniform films. Using sec-butyl benzene, which has a lower evaporation rate, results in films with a better surface quality.

The thickness of the TOPAS 5013 layer on the TOPAS 6015 substrate is measured with two different methods, resulting in similar outcomes. For the first method a Au/Pd line was sputter coated on the substrate before spin coating. The line acts as a physical barrier between the substrate and the spin coating solution, such that the substrate could not be dissolved by the solvent, and the Au/Pd layer has a higher wettability. The film



4

Temperature Control

4.1. Introduction

In commercial hot embossing machines sample temperature is controlled by actively heating and cooling thin plates in contact with the sample. The initial plan for controlling the temperature of the device in this thesis was to place the complete device in an oven with precise temperature control. The thick stainless steel plates needed for structural strength of the device would then benefit another cause: The high heat capacity of the tool would make sure that the temperature of the steel plates would remain relatively stable during fluctuations in temperature in the oven caused by opening the oven door. After fabricating the device and testing its embossing performance in the oven, it became clear that this setup was not optimal. Handling the device to load and unload a sample and applying a force while standing in the oven appeared inconvenient. The temperature of the device dropped more than expected and even more limitative: The temperature control of the oven appeared very unstable when opening the door. The temperature sensor in the cooled down door would register a much lower temperature than that of the bulk material of the oven, causing the temperature to overshoot dramatically when closing the door.

After some tests on a rotary knob controlled hot plate it was decided to fabricate a controllable heater on which the table-top press can be placed. Heating the sample directly instead of indirectly by heating the whole device would be faster and more precise. However, affordable, sufficiently flat heaters which can sustain high amounts of pressure, without inducing unwanted deformation or imprints of the samples, could not be found.

The following chapters describes the steps that were taken to obtain control of the temperature of the bottom stainless steel plate within 0.25°C precise, and with a settling time of 2 minutes for heating and 3 minutes for cooling. First an overview of the control scheme made in LabView is given. A description of how the PID gains are predicted and tuned to reach the requirements of the temperature control follows next. Finally, some recommendations are given for the design of the complete device to gain faster temperature control of the device.

4.2. Requirements

The largest part of the embossing or bonding experiments should not consist of waiting for the temperature of the device and substrate to settle to a desired value. Therefore, a maximum settling time equal to the holding time is aimed for. Typical holding times in hot embossing are in the order of seconds to minutes. During soft embossing the PDMS mold will deform initially when the embossing force is applied and slowly decompress again while displacing the material of the substrate [41]. To allow the PDMS mold to return to its original shape and obtain high replication accuracies, holding times for soft embossing will be higher, in the order of 5 to 15 minutes [26, 27, 41, 68, 97]. This leads to the requirement on the settling time $t_s \leq 5$ minutes.

The embossing force will only be applied when the device and sample are heated to the desired temperature. It is therefore not necessary to eliminate all overshoot, but an overshoot of $M_p \leq 1$ °C is permitted to avoid too much softening of the material when operating in the proximity of the glass transition temperature.

During the embossing and bonding steps, when the force is applied, a higher accuracy is desired. In the bonding step the spin coated TOPAS 5013 layer should be soft enough to allow for thermal fusion bonding, but low enough to prevent deformations in the Topas 6015 substrate. The T_g of Topas 5013 and Topas 6015 are

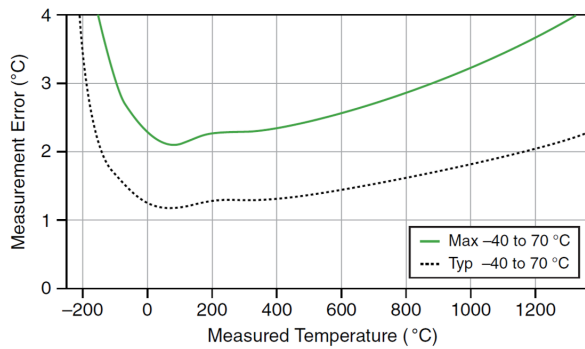


Figure 4.1: Typical and maximum errors for thermocouple type K when used with the NI 9211 over the full temperature range and auto zero on. The figures account for gain errors, offset errors, differential and integral non linearity, quantization errors, noise errors, and isothermal errors. The figure does not account for the accuracy of the thermocouple itself. Figure and description adapted from National Instruments [52].

Table 4.1: Design requirements of the temperature control

t_s	5 min
M_p	1 °C
error band	0.25 °C

Table 4.2: Thermocouple Type K accuracy[50]

Systematic uncertainty	max(± 2.2 °C or 0.75%)
Random uncertainty	0 °C

134°C and 158°C respectively; a difference of 14°C only. Thermal fusion bonding takes place at temperatures above the T_g , from where the shear modulus decreases dramatically with increasing temperature. The TOPAS 5013 bonding layer will be heated indirectly via the TOPAS 6015 substrate, so the substrate will be slightly warmer than the TOPAS 5013 bonding layer. This means that the window in which thermal fusion bonding could be possible without deforming the substrate, will be a small fraction of the difference between the T_g of the two TOPAS grades. The error band therefore needs to be low and is set to ± 0.25 °C. To accomplish this the temperature measurements need to have a high precision and sensitivity. To be able to repeat the experiments using a different setup, a high accuracy is needed. Table 4.1 summarises the requirements on the design of the temperature control.

4.3. LabView control layout

4.3.1. Temperature measurement

Measuring the temperature of the stainless steel plate is done by applying a standard type K thermocouple with exposed bead to the surface of the plate. The bead is electrically isolated by applying Kapton tape as a shield between the thermocouple bead and the steel plate. Another thermocouple is attached to the heater block to be able to register overheating of the heater. Characteristics of the used thermocouples are shown in Table 4.2.

The signals of the thermocouples are processed with a NI 9211 thermocouple readout module from National Instruments, which has a maximum sample rate of 14 samples per second. Figure 4.1 shows the typical and maximum errors for temperature measurements with the NI 9211 module when using type K thermocouples, when gain-, offset-, quantization-, noise-, and isothermal errors, and differential and integral non linearity are considered. The overall error is obtained by taking the root of the sum of squares of the thermocouple and the NI9211 module errors: At 175°C this gives a typical overall error of ± 2.53 °C and a maximum overall error of ± 3.11 °C.

4.3.2. Computing

The PID controller that is used is a modified version of the basic built-in LabView PID controller, see Appendix C for an overview of the LabView program. In Figure 4.2 the block diagram of the control scheme for the heater is given.

The PID algorithm implemented by LabView is in standard form:

$$u(t) = K_c \left(e(t) + \frac{1}{T_i} \int_0^t e(\tau) d\tau + T_d \frac{d}{dt} e(t) \right) \quad (4.1)$$

where:

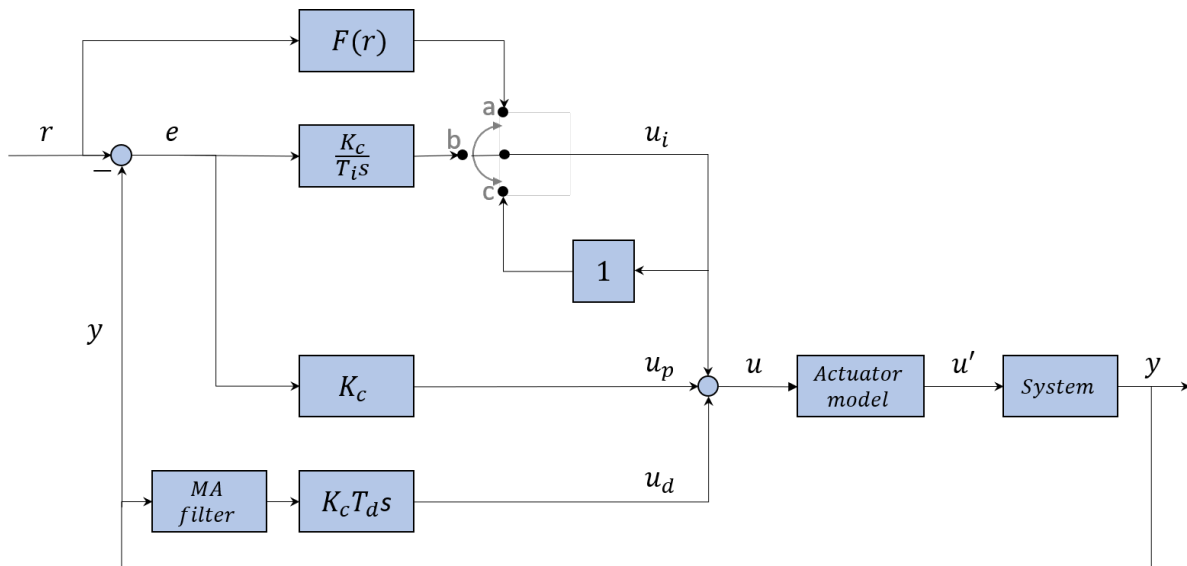


Figure 4.2: Block diagram of the heating action control. Proportional control and integral control are calculated using the error. Derivative control is based on the measured process variable y only. Before calculating the derivative action, the process variable is filtered by taking the arithmetic mean of the 7 most recent measured values to filter out measurement noise. Determination of integral action depends on the error and set-point change: normally the switch is in position b , if the error is larger than the maximum set error ($e(k) \geq 2^\circ\text{C}$) the switch is in position c , at set-point changes ($S(k) \neq S(k-1)$) the switch is in position a . The actuator model encompasses coercion of the output signal u to the limits of the actuator. Active cooling using the fan is not represented in this block diagram.

$e(t)$ = Error
 K_c = Gain factor
 T_i = Integral time
 T_d = Derivative time

The modification is applied to the anti-windup algorithm, which affects the integral action. Integral action is calculated using trapezoidal integration:

$$u_I(k) = u_I(k-1) + \frac{K_c}{T_i} \left(\frac{e(k) - e(k-1)}{2} \right) \Delta T \quad (4.2)$$

where:

ΔT = sampling time
 k = time step

The PID action indicates the desired fraction of power the heater should deliver. This fraction cannot be lower than zero or higher than one, since the heater cannot deliver negative power or more than its maximum. When the set-point and process variable differ greatly, the calculated PID action will exceed the physical bounds of the heater. Calculated PID actions exceeding these bounds will therefore be coerced to its limits:

$$u(k) = \begin{cases} u_{max} & \text{if } u(k) \geq u_{max} \\ u_{min} & \text{if } u(k) \leq u_{min} \end{cases} \quad (4.3)$$

In the case the calculated PID actions exceed the output limits the integral error will build up, while less action is provided to the setup than expected from the calculated PID actions. Eventually the set-point will be reached, but it takes time before the integral error is reduced again, resulting in a large overshoot. To avoid this *wind-up* LabView implemented the following anti-windup algorithm:

$$u_I(k) = \begin{cases} u_{max} - u_p(k) & \text{if } u_p(k) + u_I(k) \geq u_{max} \\ u_{min} - u_p(k) & \text{if } u_p(k) + u_I(k) \leq u_{min} \end{cases} \quad (4.4)$$

This implementation appeared to impede fast control action, see Figure 4.3. The bump in the temperature graph prior to reaching the set-point is caused by the integral action. After a set-point increase of 20°C u_p

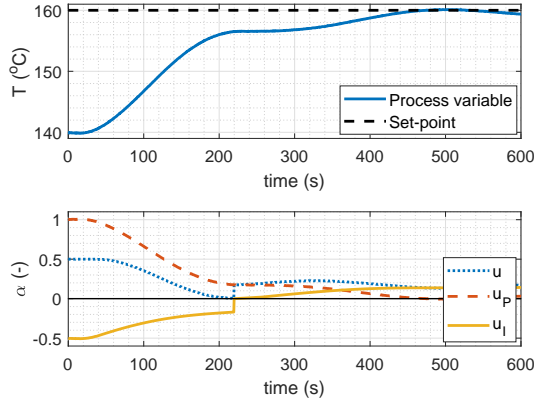


Figure 4.3: The LabView anti-windup algorithm counteracts fast control action in its attempt to avoid overshoot. *Settings*: control output is coerced to $0 \leq u \leq 0.5$, $K_c = 0.05$, $T_i = 3$ min and no derivative control is used. The set-point is changed from 140 to 160 °C and strip heater 1 is used. At $t = 0$ s the proportional control alone is already larger than u_{max} : $u_p = 1.003$. u_I therefore takes the value $u_{max} - u_p = -0.503$. The anti-windup action causes integral wind-up in the opposite direction from what it was meant to prevent. At $t \approx 220$ s, u_I is 'unwound', which is indicated by the jump in both u_I and u .

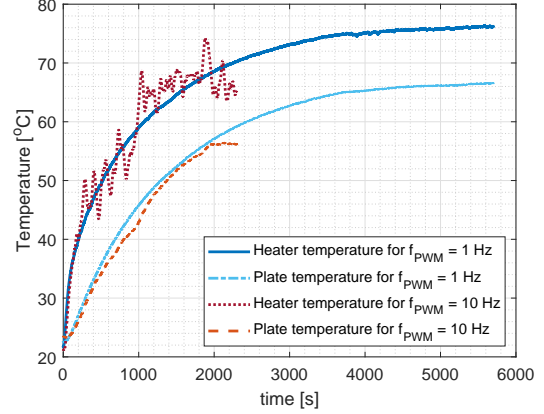


Figure 4.4: Step response from room temperature with varying PWM frequency and $\alpha = 0.05$. Heater temperature shows oscillating behaviour for high PWM frequency, which causes an inconsistent heater power. Strip heater 1 is used.

would become so large that, when using this anti-windup algorithm, the integral error would wind-up in opposite direction. For $K_c = 0.057$, the gain obtained after tuning, this results in $u_I = -0.14$:

$$\begin{aligned} u_p(k) &= K_c e(k) \\ u_I(k) &= u_{max} - u_p(k) \\ &= 1 - 0.057 \times 20 \\ &= -0.14 \end{aligned} \quad (4.5)$$

The choice is therefore made to replace the anti-windup algorithm of LabView and to keep the integral error constant during large set-point changes, a strategy called *conditional integration* or *integrator clamping*[84]. The condition when to use this algorithm is changed. It replaces the summation of integral action if the error becomes larger than 2:

$$u_I(k) = \begin{cases} u_I(k-1) + \frac{K_c}{T_i} \left(\frac{e(k) - e(k-1)}{2} \right) \Delta T & \text{if } |e(k)| \leq 2 \\ u_I(k-1) & \text{if } |e(k)| > 2 \end{cases} \quad (4.6)$$

Next to that, a form of *preloading* [84] is used when changing the set-point to shorten the settling time: u_I will be given the steady state value of u at the applied set-point. At steady state the value of $u_I(k)$ will be equal to the steady state action of the heater, since u_p and u_D will approach zero. The table-top press will be used many times at temperatures very close to each other. Determining the steady state heater action for a few relevant temperatures and recording them in a look-up table will cost relatively little work and can be used to speed up settling time. When changing the set-point, $u_I(k)$ will then be obtained by linear interpolation of the values in the look-up table:

$$u_I(k) = \begin{cases} u_I(k-1) + \frac{K_p}{T_i} \left(\frac{e(k) - e(k-1)}{2} \right) \Delta T & \text{if } S(k) = S(k-1) \\ f(S(k)) & \text{if } S(k) \neq S(k-1) \end{cases} \quad (4.7)$$

4.3.3. Output

Pulse Width Modulation (PWM) in combination with a solid state relay is used to convert the output signal of the PID controller to be able to operate the heater. Hereto a suitable PWM switching frequency has to be chosen. If the frequency is high and combined with a low duty cycle, α , the fraction of time the heater is switched on is small, the power delivered becomes unpredictable. The heater will be switched on for a period

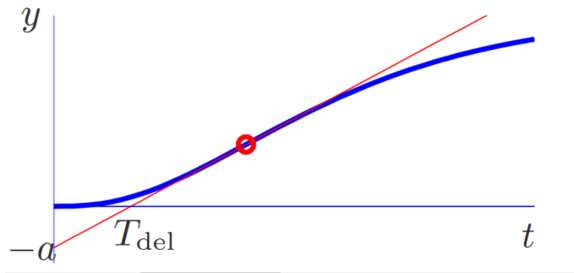


Figure 4.5: Extracting the parameters L (here T_{del}), the delay time of the system, and a from the step response to obtain good starting values for the PID parameters. The circle indicates the point of inflection, with the tangent line in red. Figure reproduced from [3].

Controller	K_c	T_i	T_d
P	$\frac{1}{a}$		
PI	$\frac{0.9}{a}$	$3L$	
PID	$\frac{1.2}{a}$	$2L$	$0.5L$

Table 4.3: PID parameters obtained with the Ziegler-Nichols step response method. Table modified from Åström and Murray [3].

of $\frac{\alpha}{f_{PWM}}$. The main supply has a period of $\frac{1}{50}$ s. So for $\alpha = 0.01$ and $f_{PWM} = 10$ Hz, the heater is switched on for only a fraction of the period T_M of the main supply:

$$\frac{\alpha \frac{1}{f_{PWM}}}{\frac{1}{f_M}} = \frac{0.05 \times \frac{1}{10}}{\frac{1}{50}} = 0.25 \quad (4.8)$$

The power delivered thus depends significantly on the moment the heater is switched on. However, the lower f_{PWM} is set, the slower the heater power can be modified. Therefore, a trade-off has to be made. A f_{PWM} of 2 Hz is chosen, which is still high compared to the lag and delay times determined in Section 4.4. Figure 4.4 shows the temperature of the heater and stainless steel plate for a step response at 5% heater power using two different PWM frequencies.

4.4. Tuning of PID controller

4.4.1. Ziegler-Nichols' step response method

Many different PID-tuning methods have been developed for various types of systems. Two of the most well-known and most used methods are the Ziegler-Nichols methods. One of the reasons of their popularity is the ease of application [3]. Tuning the PID controller of the heater is done by using the step response method from Ziegler and Nichols. In this method an open-loop step response of the system needs to be recorded. From this response the parameters L , the delay time of the system, and a are extracted to define K_c , T_i and T_d from Equation (4.1). At the point of steepest descent of the step response the tangent is drawn. The parameters a and L are defined as the intersections of the tangent and the coordinate axes, see Figure 4.5. The PID parameters are then defined as in Table 4.3.

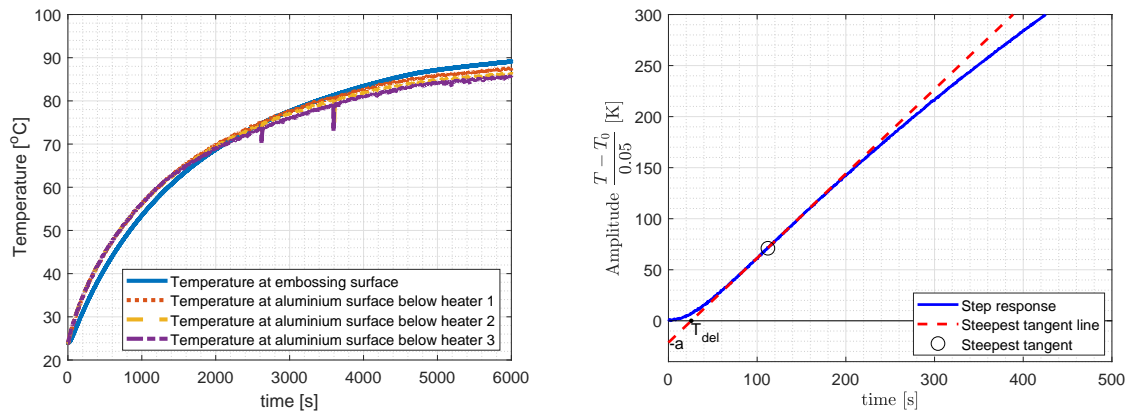
4.4.2. Results

The open-loop step response of the system is recorded for a heater power of 22.5 W, 5% of the total heater power, see Figure 4.6. The systems consists of the heater and the press, placed in a closed box to prevent perturbations caused by air flow. The press is clamping a representative load: a TOPAS substrate and a PDMS mold. Recording the step response is time consuming and only an estimation of the PID parameters are retrieved: afterwards they can be tuned further. Therefore, the open-loop step response is recorded once only.

Using the parameters a and L , obtained from the open-loop step response as in Figure 4.6b, gives the parameters for the PID controller in Table 4.4.

Table 4.4: PID parameters obtained with the Ziegler-Nichols step response method

$$\begin{aligned} K_c &= 0.057 \\ T_i &= 0.85 \text{ min} \\ T_d &= 0.21 \text{ min} \end{aligned}$$



(a) Temperature of the press and the bottom side of the aluminium heater block. The strong dips in temperature are caused by loosening of the thermocouples from the measured surfaces.

(b) First part of the step response, with the point of inclination and the parameters a and T_{del} . Temperature is scaled with the power used.

Figure 4.6: Open-loop step response of the heater and press combination. The press is closed with a representative load (TOPAS 6015 substrate with PDMS mold).

The closed-loop response with the values for K_c , T_i and T_d as in Table 4.4 is recorded for typical set-point changes for the embossing experiments. To fill out the look-up table described in Section 4.3.2, the steady-state heater power at every set-point is determined. Next, the response to every set-point change is recorded three times, see Figure 4.7. The responses are evaluated in terms of overshoot and settling time, see Table 4.5. For all these set-point changes the requirements of Table 4.1 are met. The settling time could be decreased further by increasing the damping of the system, such that the undershoot during heating would be decreased to maximally 0.25 °C. Since the requirements are met already, further tuning is not carried out.

4.5. Discussion and conclusions

The requirements in terms of precision of the temperature control are met: Overshoot, settling time and error band are well below the demanded values, see Table 4.6. The high precision ensures a high reproducibility if the experiments were to be repeated on the same equipment.

Accuracy of the temperature measurements is limited by the used temperature sensors. The K-type thermocouples introduce a systematic error of typically 1.28°C and maximally 2.28°C. A higher reproducibility when switching to a different setup could be achieved by using a different temperature sensor. For example, a DIN/IEC 751 class A RTD, a Resistance Temperature Detector, has an accuracy of $\pm 0.55^\circ\text{C}$ at 200°C and, depending on the size of the sensor, a sufficiently low response time.

The press was originally designed to use in an oven, on a later moment it was decided to apply heat directly. Therefore, the heating block is not integrated in the press, but is clamped to the thick stainless steel bottom plate. The thermal resistance between the bottom plate and the cartridge heaters could be removed by integrating the heaters directly in to the press. The bending stiffness of the stainless steel bottom plate is still needed. Durability of the cartridge heaters is ensured when mounted in a material with a high conductivity. Also temperature uniformity is higher for a material with high conductivity. Therefore, a good option would be to place an aluminium heating block with cartridge heaters on top of the bottom plate, heating the substrate directly.

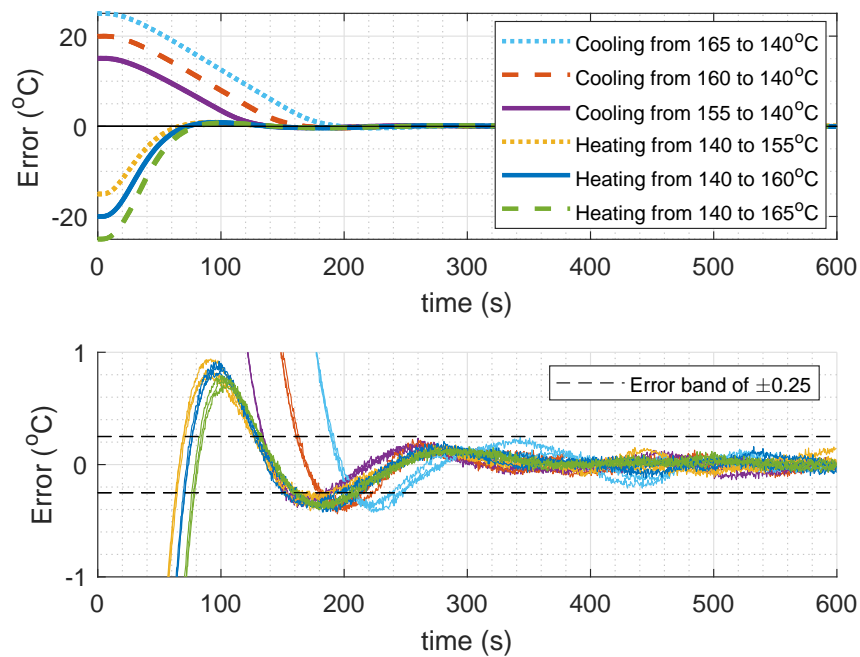


Figure 4.7: Closed-loop responses for different set-point changes, using the parameters of Table 4.4. Temperature is measured at the top surface of the bottom plate of the press. The response for every set-point change is recorded three times. The three individual measurements are partly visible in the lower plot only, because of the very similar responses.

Table 4.5: Overshoot and settling time per set-point change. Settling time and overshoot do not show a dependency on temperature change for increasing set-point. Decreasing the set-point shows a strong dependency of settling time on the temperature difference of the set-point, caused by the low cooling rate.

Set-point change (°C)	M_p (°C)	t_s (min)
140 - 155	0.86 ± 0.08	1.93 ± 0.03
140 - 160	0.88 ± 0.05	1.98 ± 0.01
140 - 165	0.76 ± 0.04	2.01 ± 0.02
155 - 140	0.36 ± 0.02	2.15 ± 0.00
160 - 140	0.40 ± 0.05	2.61 ± 0.02
165 - 140	0.40 ± 0.02	3.08 ± 0.02

Table 4.6: Overview of the requirements and results in terms of precision of the temperature control.

	Required	Accomplished	
		Heating	Cooling
t_s (min)	5	1.97 ± 0.04	2.61 ± 0.40^1
M_p (°C)	1.0	0.83 ± 0.08	0.39 ± 0.03
error band (°C)	0.25	0.25	0.25

¹ Highly dependent on temperature difference, see Table 4.5.

5

Conclusion

The Organ on Chip market is fast-growing with the promise to drastically reduce the cost of drug development and the need for animal testing. The promise lays in the ability to more realistically mimic the microenvironment of the cell than conventional cell culture platforms are capable of. However, the growth could be obstructed by difficulties in the production scale-up of organ on chip prototypes. Most Organ on Chip prototypes are fabricated out of polydimethylsiloxane (PDMS), which cannot be used for the mass production of these microfluidic devices. This indicates the need for a change in the state-of-the-art prototyping procedure for Organ on Chip models. In this thesis, three steps are taken towards a new prototyping procedure. First of all a prototyping process plan is designed, which enables fast, simple, and low-cost prototyping of Blood-Brain barrier-on-Chips (BBB-on-Chips), while the resulting prototypes are fit for mass production. Secondly, an easily-manufacturable, low-cost table-top press is developed with precise force and temperature control, hence enabling embossing and bonding experiments, both part of the prototyping process, with high repeatability. Thirdly, the mold fabrication steps are performed, a spin coating protocol is produced to deposit a cyclic olefin copolymer (COC) film with controllable thickness on top of a COC substrate, and the soft embossing protocol is optimized.

First, a BBB-on-Chip prototyping process is developed which can be carried out in smaller labs without expensive equipment and can be directly scaled up to mass production. Like the conventional BBB-on-Chips the chips will consist of a bottom plate with a channel, a top plate with a channel perpendicular to the bottom channel, and a membrane which is sandwiched between the two plates. The polymer COC is used instead of PDMS, which is suitable for mass production. The designed prototyping process consists of four main components: First a mold is fabricated using 3D printing and soft lithography, which are cheaper, faster and less complicated processes for the production of small quantities than the conventional etching processes for mold fabrication. Second, a layer of COC is spincoated on top of a COC substrate. Third, the substrate with spincoated COC film is soft embossed using the mold. Finally the parts are assembled using thermal fusion bonding. These steps require relatively simple equipment, namely a 3D printer, spin coater, fume hood, and basic lab ware. Next to that, a press for embossing and bonding is required.

In the second part, a press for embossing and bonding experiments is designed, fabricated, calibrated and tested. The press enables embossing and bonding experiments with high repeatability on a simple desktop and can be fabricated in roughly 2 - 3 days in a workshop with standard materials costing no more than €250. Temperature of the compression platens can be controlled up to 180°C and precise within 0.25°C. Hereto a program is made in LabView using PID control. Compression forces up to 3.5 kN can be applied and an accuracy of ± 32 N (95%) and ± 80 N (95%) for forces up to 1.3 kN and 2.0 kN respectively can be reached. The design and the fabrication process of the press ensure parallel movement of the platens relative to each other to facilitate uniform pressure distribution. The performance of the press is tested by carrying out embossing experiments, which yielded replication accuracies comparable with literature for channels of 170 μm deep.

Lastly, all necessary steps for prototype production preceding the bonding experiments are developed and performed. First, designs and strategies for mold fabrication are delivered using 3D printing and soft lithography. Secondly, for the proposed bonding procedure a COC substrate is required with an additional thin

film of COC with a lower glass transition temperature. The thin film is applied by spin coating a solution of COC in sec-butylbenzene. For this, a protocol is delivered to spin coat layers of COC with a specific thickness between 7.5 - 14 μm . Furthermore, different methods are studied to measure the thickness of the film on top of the visually similar material of the substrate. Eventually the film thickness is determined by measuring the substrate thickness before and after spin coating by using laser microscopy. Thirdly, the soft embossing process of COC substrates with the fabricated mold is optimized for the embossing and bonding press.

The steps taken in this thesis cleared the way for investigation of the proposed bonding procedure, fabrication of a complete Organ on Chip model, and for quick and easy embossing experiments at the department without the need for clean room access.

Bibliography

- [1] Adam R. Abate, Daeyeon Lee, Thao Do, Christian Holtze, and David A. Weitz. Glass coating for PDMS microfluidic channels by sol-gel methods. *Lab on a Chip*, 8(4):516, 2008. ISSN 1473-0197. doi: 10.1039/b800001h. URL <http://xlink.rsc.org/?DOI=b800001h>.
- [2] Anil Kumar H. Achyuta, Amy J. Conway, Richard B. Crouse, Emilee C. Bannister, Robin N. Lee, Christopher P. Katnik, Adam a. Behensky, Javier Cuevas, and Shivshankar S. Sundaram. A modular approach to create a neurovascular unit-on-a-chip. *Lab on a Chip*, pages 542–553, 2013. ISSN 1473-0197. doi: 10.1039/c2lc41033h.
- [3] Karl Johan Åström and Richard M. Murray. PID Tuning. In *Feedback Systems*, chapter 10, pages 302–303. Princeton University Press, 2008. URL http://www.cds.caltech.edu/~murray/books/AM05/pdf/am08-complete{}_22Feb09.pdf.
- [4] B J Ballermann, a Dardik, E Eng, and a Liu. Shear stress and the endothelium. *Kidney international. Supplement*, 67:S100–S108, 1998. ISSN 0085-2538. doi: 10.1046/j.1523-1755.1998.06720.x.
- [5] BASF. Polystyrene and Styrolux, 2010.
- [6] Holger Becker and Claudia Gärtner. Polymer microfabrication technologies for microfluidic systems. *Analytical and Bioanalytical Chemistry*, 390(1):89–111, 2008. ISSN 16182642. doi: 10.1007/s00216-007-1692-2.
- [7] Holger Becker and Ulf Heim. Hot embossing as a method for the fabrication of polymer high aspect ratio structures. *Sensors and Actuators, A:Physical*, 83:130–135, 2000.
- [8] Erwin Berthier, Edmond W. K. Young, and David Beebe. Engineers are from PDMS-land, Biologists are from Polystyrenia. *Lab on a Chip*, 12(7):1224, 2012. ISSN 1473-0197. doi: 10.1039/c2lc20982a. URL <http://xlink.rsc.org/?DOI=c2lc20982a>.
- [9] Dunbar P. Birnie. A model for drying control cosolvent selection for spin-coating uniformity: The thin film. *Langmuir*, 29(29):9072–9078, 2013. ISSN 07437463. doi: 10.1021/la401106z.
- [10] Ross Booth and Hanseup Kim. Characterization of a microfluidic in vitro model of the blood-brain barrier (μ BBB). *Lab on a Chip*, 12(10):1784, 2012. ISSN 1473-0197. doi: 10.1039/c2lc40094d.
- [11] Ross Booth and Hanseup Kim. Permeability Analysis of Neuroactive Drugs Through a Dynamic Microfluidic In Vitro Blood-Brain Barrier Model. *Annals of Biomedical Engineering*, 42(12):2379–2391, 2014. ISSN 15739686. doi: 10.1007/s10439-014-1086-5.
- [12] T Brenner, C Müller, H Reinecke, Roland Zengerle, and J. Dacrée. Fabrication chain for prototyping of microfluidic chips in polymers. *Proceedings of the*, (C):1–4, 2005. URL http://www.4m-net.org/files/papers/4M2005/01{}_12/01{}_12.PDF.
- [13] Jacquelyn A. Brown, Virginia Pensabene, Dmitry A. Markov, Vanessa Allwardt, M. Diana Neely, Mingjian Shi, Clayton M. Britt, Orlando S. Hoilett, Qing Yang, Bryson M. Brewer, Philip C. Samson, Lisa J. McCawley, James M. May, Donna J. Webb, Deyu Li, Aaron B. Bowman, Ronald S. Reiserer, and John P. Wikswo. Recreating blood-brain barrier physiology and structure on chip: A novel neurovascular microfluidic bioreactor. *Biomicrofluidics*, 9(5), 2015. ISSN 19321058. doi: 10.1063/1.4934713. URL <http://dx.doi.org/10.1063/1.4934713>.
- [14] F Bundgaard, G Perozziello, and O Geschke. Rapid prototyping tools and methods for all-Topas® cyclic olefin copolymer fluidic microsystems. *Proceedings of the Institution of Mechanical Engineers, Part C: Journal of Mechanical Engineering Science*, 220(11):1625–1632, 2006. ISSN 0954-4062. doi: 10.1243/09544062JMES295. URL <http://pic.sagepub.com/content/220/11/1625.abstract{}%}5Cnhttp://pic.sagepub.com/lookup/doi/10.1243/09544062JMES295>.

- [15] Frederik Bundgaard. *Prototyping of Microfluidic Systems with Integrated Waveguides in Cyclic Olefin Copolymer (COC)*. PhD thesis, Technical University of Denmark, 2006.
- [16] Zhi Chen, Luyan Zhang, and Gang Chen. A spring-driven press device for hot embossing and thermal bonding of PMMA microfluidic chips. *Electrophoresis*, 31(15):2512–2519, 2010. ISSN 01730835. doi: 10.1002/elps.201000084.
- [17] Kv Christ, Bb Smith, Fe Pfefferkorn, and Kt Turner. Micro End Milling Polystyrene for Microfluidic Applications ICOMM/4M. *Core.Kmi.Open.Ac.Uk*, pages 423–430, 2010. URL <http://core.kmi.open.ac.uk/download/pdf/10597915.pdf>.
- [18] Dow Corning. Electronics Sylgard® 184 Silicone Elastomer, 2013. ISSN 1098-6596.
- [19] KLA Corporation. Spectral Reflectance Calculator, 2020. URL <https://www.filmetrics.com/reflectance-calculator>.
- [20] Covestro Deutschland AG. Optical properties of Makrolon and apec for non-imaging optics, 2016.
- [21] Luca Cucullo, Mohammed Hossain, Vikram Puvanna, Nicola Marchi, and Damir Janigro. The role of shear stress in Blood-Brain Barrier endothelial physiology. *BMC neuroscience*, 12:40, 2011. ISSN 1471-2202. doi: 10.1186/1471-2202-12-40. URL <http://www.pubmedcentral.nih.gov/articlerender.fcgi?artid=3103473&tool=pmcentrez&rendertype=abstract>.
- [22] Sudhir P. Deosarkar, Balabhaskar Prabhakarpandian, Bin Wang, Joel B. Sheffield, Barbara Krynska, and Mohammad F. Kiani. A novel dynamic neonatal blood-brain barrier on a chip. *PLoS ONE*, 10(11):1–21, 2015. ISSN 19326203. doi: 10.1371/journal.pone.0142725.
- [23] Diversified Enterprises. Critical Surface Tension and Contact Angle with Water for Various Polymers. URL https://www.accudynetest.com/polytable_{_}03.html?sortBy=contact_{_}angle{#}branding.
- [24] Shane M. Eaton, Carmela De Marco, Rebeca Martinez-Vazquez, Roberta Ramponi, Stefano Turri, Giulio Cerullo, and Roberto Osellame. Femtosecond laser microstructuring for polymeric lab-on-chips. *Journal of Biophotonics*, 5(8-9):687–702, 2012. ISSN 1864-0648. doi: 10.1002/jbio.201200048. URL <http://dx.doi.org/10.1002/jbio.201200048>.
- [25] Volkan Şenay. Gold/palladium (Au/Pd) Bimetallic Thin Film Deposition by Radio Frequency Magnetron Sputtering Technique. *Journal of the Institute of Science and Technology*, 9(3):1377–1384, 2019. ISSN 2146-0574. doi: 10.21597/jist.513363.
- [26] Paola Fanzio, Alberto Cagliani, Kristof G. Peterffy, and Luigi Sasso. High throughput soft embossing process for micro-patterning of PEDOT thin films. *Microelectronic Engineering*, 176:15–21, 2017. ISSN 01679317. doi: 10.1016/j.mee.2017.01.011. URL <http://dx.doi.org/10.1016/j.mee.2017.01.011>.
- [27] Paola Fanzio, Chi-Tung Chang, Maciej Skolimowski, Simone Tanzi, and Luigi Sasso. Fully-Polymeric pH Sensor Realized by Means of a Single-Step Soft Embossing Technique. *Sensors*, 17(6):1169, 2017. ISSN 1424-8220. doi: 10.3390/s17051169. URL <http://www.mdpi.com/1424-8220/17/5/1169>.
- [28] Ronald L. Fournier. *Basic transport phenomena in biomedical engineering*. Francis & Taylor, 1999.
- [29] Jennifer L. Fritz and Michael J. Owen. Hydrophobic Recovery of Plasma-Treated Polydimethylsiloxane. *The Journal of Adhesion*, 54(1-4):33–45, 1995. ISSN 0021-8464. doi: 10.1080/00218469508014379. URL <http://www.tandfonline.com/doi/abs/10.1080/00218469508014379>.
- [30] Goodfellow. Goodfellow On-line Interactive Catalogue. URL <http://www.goodfellow.com/catalogue/GFCatalogue.php?Language=E>.
- [31] V.N. Goral, Y.-C. Hsieh, O.N. Petzold, R.A. Faris, and P.K. Yuen. Hot embossing of plastic microfluidic devices using poly (dimethylsiloxane) molds. In *14th International Conference on Miniaturized Systems for Chemistry and Life Sciences*, pages 1214–1216, 2010. ISBN 9780979806438. doi: 10.1088/0960-1317/21/1/017002. URL <http://iopscience.iop.org/0960-1317/21/1/017002>.

- [32] L. M. Griep, F. Wolbers, B. De Wagenaar, P. M. Ter Braak, Babette Weksler, Ignacio a Romero, Pierre Oliver Couraud, I. Vermes, Andries D van der Meer, and Albert van den Berg. BBB on CHIP: Microfluidic platform to mechanically and biochemically modulate blood-brain barrier function. *Biomedical Microdevices*, 15(1):145–150, 2013. ISSN 13872176. doi: 10.1007/s10544-012-9699-7.
- [33] Skarphedinn Halldorsson, Edinson Lucumi, Rafael Gómez-sjöberg, and Ronan M T Fleming. Biosensors and Bioelectronics Advantages and challenges of micro fluidic cell culture in polydimethylsiloxane devices. *Biosensors and Bioelectronic*, 63:218–231, 2015. ISSN 0956-5663. doi: 10.1016/j.bios.2014.07.029. URL <http://dx.doi.org/10.1016/j.bios.2014.07.029>.
- [34] Amy M. Hopkins, Elise DeSimone, Karolina Chwalek, and David L. Kaplan. 3D in vitro modeling of the central nervous system. *Progress in Neurobiology*, 125:1–25, 2015. ISSN 18735118. doi: 10.1016/j.pneurobio.2014.11.003. URL <http://dx.doi.org/10.1016/j.pneurobio.2014.11.003>.
- [35] Rajeeb K. Jena and C. Y. Yue. Cyclic olefin copolymer based microfluidic devices for biochip applications: Ultraviolet surface grafting using 2-methacryloyloxyethyl phosphorylcholine. *Biomicrofluidics*, 6(1):1–12, 2012. ISSN 19321058. doi: 10.1063/1.3682098.
- [36] Rajeeb K. Jena, C. Y. Yue, and Y. C. Lam. Micro fabrication of cyclic olefin copolymer (COC) based microfluidic devices. *Microsystem Technologies*, 18(2):159–166, 2012. ISSN 09467076. doi: 10.1007/s00542-011-1366-z.
- [37] P. B. Johnson and R. W. Christy. Optical constants of the noble metals. *Physical Review B*, 6(12):4370–4379, 1972. ISSN 01631829. doi: 10.1103/PhysRevB.6.4370.
- [38] Pieter Kapel. *Manufacturing of a polymeric membrane with integrated porous electrode*. PhD thesis, TU Delft, 2018.
- [39] Juey H. Lai. An investigation of spin coating of electron resists. *Polymer Engineering & Science*, 19(15):1117–1121, 1979. ISSN 15482634. doi: 10.1002/pen.760191509.
- [40] Jessamine Ng Lee, Cheolmin Park, and George M. Whitesides. Solvent Compatibility of Poly(dimethylsiloxane)-Based Microfluidic Devices. *Analytical Chemistry*, 75(23):6544–6554, 2003. ISSN 00032700. doi: 10.1021/ac0346712.
- [41] Jin-Hwan Lee, Erik T K Peterson, Gabriel Dagani, and Ian Papautsky. Rapid prototyping of plastic microfluidic devices in cyclic olefin copolymer (COC). *Proc. SPIE*, 5718:82–91, 2005. ISSN 0277786X. doi: 10.1117/12.591852. URL <http://dx.doi.org/10.1117/12.591852>.
- [42] Patrick W. Leech, Xiaoqing Zhang, and Yonggang Zhu. Effect of norbornene content on deformation properties and hot embossing of cyclic olefin copolymers. *Journal of Materials Science*, 45(19):5364–5369, 2010. ISSN 00222461. doi: 10.1007/s10853-010-4585-2.
- [43] Huawei Li, Yiqiang Fan, Rimantas Kodzius, and Ian G. Foulds. Fabrication of polystyrene microfluidic devices using a pulsed CO₂ laser system. *Microsystem Technologies*, 18(3):373–379, 2011. ISSN 0946-7076. doi: 10.1007/s00542-011-1410-z. URL <http://www.springerlink.com/index/10.1007/s00542-011-1410-z>.
- [44] L E Locascio, D J Ross, P B Howell, and M Gaitan. Fabrication of polymer microfluidic systems by hot embossing and laser ablation. *Methods Mol Biol*, 339(1):37–46, 2006. ISSN 1064-3745. doi: 10.1385/1-59745-076-6:37. URL <http://www.ncbi.nlm.nih.gov/pubmed/16790865>{%}5Cnhttp://download.springer.com/static/pdf/651/chp{%}253A10.1385{%}252F1-59745-076-6{%}253A37.pdf?auth66=1406187205_{_}ae134393429ee70c3496cd5bc576e5ec{%}&ext=.pdf.
- [45] Marc J. Madou. *Fundamentals of microfabrication : the science of miniaturization*. Boca Raton: CRC Press, 2 edition.
- [46] Morten Hannibal Madsen, Nikolaj A. Feidenhans'l, Poul Erik Hansen, Jørgen Garnæs, and Kai Dirscherl. Accounting for PDMS shrinkage when replicating structures. *Journal of Micromechanics and Microengineering*, 24(12), 2014. ISSN 13616439. doi: 10.1088/0960-1317/24/12/127002.

- [47] Ronan McCann, Komal Bagga, Apryll Stalcup, Mercedes Vázquez, and Dermot Brabazon. Laser micro-engineering of functionalised cyclic olefin polymers for microfluidic applications. *Laser-based Micro- and Nanoprocessing IX*, 9351(February):93511N, 2015. ISSN 1996756X. doi: 10.1117/12.2076916.
- [48] J C McDonald, D C Duffy, J R Anderson, D T Chiu, H Wu, O J Schueller, and G M Whitesides. Fabrication of microfluidic systems in poly(dimethylsiloxane). *Electrophoresis*, 21(1):27–40, 2000. ISSN 01730835 (ISSN). doi: 10.1002/(SICI)1522-2683(20000101)21:1<27::AID-ELPS27>3.0.CO;2-C.
- [49] G Mehta, J Lee, W Cha, Y C Tung, J J Linderman, and S Takayama. Hard top soft bottom microfluidic devices for cell culture and chemical analysis. *Anal Chem*, 81(10):3714–3722, 2009. ISSN 1520-6882. doi: 10.1021/ac802178u[doi].
- [50] JT Nakos. Uncertainty analysis of thermocouple measurements used in normal and abnormal thermal environment experiments at Sandia's Radiant Heat Facility and Lurance Canyon Burn Site. Technical Report April, Sandia National Laboratories, 2004. URL <http://infoserve.sandia.gov/sand{ }doc/2004/041023.pdf>.
- [51] Jagannathan Narasimhan and Ian Papautsky. Polymer embossing tools for rapid prototyping of plastic microfluidic devices. *Journal of Micromechanics and Microengineering*, 14:96–103, 2003. ISSN 0960-1317. doi: 10.1088/0960-1317/14/1/013.
- [52] National Instruments. NI 9211 Datasheet, 2015.
- [53] Winfried Neuhaus, Regina Lauer, Silvester Oelzant, Urs P. Fringeli, Gerhard F. Ecker, and Christian R. Noe. A novel flow based hollow-fiber blood-brain barrier in vitro model with immortalised cell line PBMEC/C1-2. *Journal of Biotechnology*, 125(1):127–141, 2006. ISSN 01681656. doi: 10.1016/j.jbiotec.2006.02.019.
- [54] Walter D. Niles and Peter J. Coassin. Cyclic Olefin Polymers: Innovative Materials for High-Density Multiwell Plates. *ASSAY and Drug Development Technologies*, 6(4):577–590, 2008. ISSN 1540-658X. doi: 10.1089/adt.2008.134. URL <http://www.liebertonline.com/doi/abs/10.1089/adt.2008.134>.
- [55] Pedro S. Nunes, Pelle D. Ohlsson, Olga Ordeig, and Jörg P. Kutter. Cyclic olefin polymers: Emerging materials for lab-on-a-chip applications. *Microfluidics and Nanofluidics*, 9(2-3):145–161, 2010. ISSN 16134982. doi: 10.1007/s10404-010-0605-4.
- [56] Mathieu Odijk, Andries D van der Meer, Daniel Levner, Hyun Jung Kim, Marinke van der Helm, Loes I Segerink, Jean-Phillipe Frimat, Geraldine A Hamilton, Donald E Ingber, and Albert van den Berg. Measuring direct current trans-epithelial electrical resistance in organ-on-a-chip microsystems. *Lab on a chip*, 15(3):745–52, 2015. ISSN 1473-0189. doi: 10.1039/c4lc01219d. URL <http://pubs.rsc.org/en/content/articlehtml/2015/lc/c4lc01219d>.
- [57] D. Ogonczyk, J. Wegrzyn, P Jankowski, B Dabrowski, and P Garstecki. Bonding of microfluidic devices fabricated in polycarbonate. *Lab on a Chip*, 10:1324–1327, 2010. doi: 10.1039/b924439e.
- [58] J. B. Orhan, V. K. Parashar, J. Flueckiger, and M. A M Gijs. Internal modification of poly(dimethylsiloxane) microchannels with a borosilicate glass coating. *Langmuir*, 24(16):9154–9161, 2008. ISSN 07437463. doi: 10.1021/la801317x.
- [59] Balabhaskar Prabhakarandian, Ming-Che Shen, Joseph B Nichols, Ivy R Mills, Marta Sidoryk-Wegrzynowicz, Michael Aschner, and Kapil Pant. SyM-BBB: a microfluidic blood brain barrier model. *Lab on a Chip*, 13(6):1093–1101, 2013. ISSN 1473-0189 (Electronic). doi: 10.1039/c2lc41208j. URL <http://dx.doi.org/10.1039/C2LC41208J>.
- [60] Keil J Regehr, Maribella Domenech, Justin T Koepsel, Kristopher C Carver, J Ellison-zelski, William L Murphy, Linda A Schuler, Elaine T Alarid, and J David. Biological implications of polydimethylsiloxane-based microfluidic cell culture. *Lab on a chip*, 9(15):2132–2139, 2009. doi: 10.1039/b903043c.Biological.
- [61] Dirk Sabbert, Jörg Landsiedel, Hans Dieter Bauer, and Wolfgang Ehrfeld. ArF-excimer laser ablation experiments on Cycloolefin Copolymer (COC). *Applied Surface Science*, 150(1):185–189, 1999. ISSN 01694332. doi: 10.1016/S0169-4332(98)00334-1.

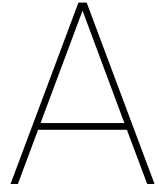
- [62] Eric K. Sackmann, Anna L. Fulton, and David J. Beebe. The present and future role of microfluidics in biomedical research. *Nature*, 507(7491):181–189, 2014. ISSN 0028-0836. doi: 10.1038/nature13118. URL <http://www.nature.com/doifinder/10.1038/nature13118>.
- [63] Katelyn L Sellgren, Elizabeth J Butala, Brian P Gilmour, Scott H Randell, and Sonia Grego. A biomimetic multicellular model of the airways using primary human cells. *Lab on a chip*, pages 3349–3358, 2014. ISSN 1473-0189. doi: 10.1039/c4lc00552j. URL <http://www.ncbi.nlm.nih.gov/pubmed/25000964>.
- [64] Katelyn L. Sellgren, Brian T. Hawkins, and Sonia Grego. An optically transparent membrane supports shear stress studies in a three-dimensional microfluidic neurovascular unit model. *Biomicrofluidics*, 9(6): 48–52, 2015. ISSN 19321058. doi: 10.1063/1.4935594. URL <http://dx.doi.org/10.1063/1.4935594>.
- [65] Ju Young Shin, Ji Yong Park, Chenyang Liu, Jiasong He, and Sung Chul Kim. Chemical structure and physical properties of cyclic olefin copolymers. *Pure and Applied Chemistry*, 77(5):801–814, 2005. ISSN 0033-4545. doi: 10.1351/pac200577050801. URL <http://www.degruyter.com/dg/viewarticle.fullcontentlink:pdfeventlink/{\protect\T1\textdollar}002fj{\protect\T1\textdollar}002fpac.2005.77.issue-5{\protect\T1\textdollar}002fpac200577050801{\protect\T1\textdollar}002fpac200577050801.pdf?t:ac=j{\protect\T1\textdollar}002fpac.2005.77.issue-5{\protect\T1\textdollar}002fpac200577050801{\protect\T1\textdollar}002fpac200577050801.xml>.
- [66] S. Singaravelu, J. M. Klopff, K. E. Schriver, H. K. Park, M. J. Kelley, and R. F. Haglund. Resonant infrared pulsed laser deposition of cyclic olefin copolymer films. *Applied Physics A*, 114(4):1285–1293, Mar 2014. ISSN 1432-0630. doi: 10.1007/s00339-013-7933-7. URL <https://doi.org/10.1007/s00339-013-7933-7>.
- [67] Emma Spooner. Spin Coating: Guide to Coating Difficult Solutions. URL <https://www.ossila.com/pages/spin-coating-difficult-solutions{#}ExtremeVolatility>.
- [68] J Steigert, S Haeberle, T Brenner, C Müller, C P Steinert, P Koltay, N Gottschlich, H Reinecke, J Rühle, R Zengerle, and J Ducleé. Rapid prototyping of microfluidic chips in COC. *Journal of Micromechanics and Microengineering*, 17(2):333–341, 2007. ISSN 0960-1317. doi: 10.1088/0960-1317/17/2/020.
- [69] Serguei Stoukatch. Low-Temperature Microassembly Methods and Integration Techniques for Biomedical Application. In *Wireless Medical Systems and Algorithms*, pages 21–42. CRC Press - Taylor & Francis Group, 2016.
- [70] Raffaella Suriano, Arseniy Kuznetsov, Shane M. Eaton, Roman Kiyan, Giulio Cerullo, Roberto Osellame, Boris N. Chichkov, Marinella Levi, and Stefano Turri. Femtosecond laser ablation of polymeric substrates for the fabrication of microfluidic channels. *Applied Surface Science*, 257(14):6243 – 6250, 2011. ISSN 0169-4332. doi: <http://dx.doi.org/10.1016/j.apsusc.2011.02.053>. URL <http://www.sciencedirect.com/science/article/pii/S0169433211002443>.
- [71] FLIR systems Inc. User’s Manual FLIR Exx series, 2011. URL <https://www.flir.eu/support/products/e75/{#}Resources>.
- [72] Marta Tajés, Eva Ramos-Fernández, Xian Weng-Jiang, Mònica Bosch-Morató, Biuse Guivernau, Abel Eraso-Pichot, Bertrán Salvador, Xavier Fernández-Busquets, Jaume Roquer, and Francisco J Muñoz. The blood-brain barrier: Structure, function and therapeutic approaches to cross it. *Molecular membrane biology*, 31(5):152–67, 2014. ISSN 1464-5203. doi: 10.3109/09687688.2014.937468. URL <http://www.ncbi.nlm.nih.gov/pubmed/25046533>.
- [73] Vijay Kumar Thakur and Kumari Manju Thakur. *Handbook of Polymers for Pharmaceutical Technologies Volume 2 Processing and Applications*. Wiley Scrivener, 2015. ISBN 9781119041382.
- [74] T Tilling, D Korte, D Hoheisel, and H J Galla. Basement membrane proteins influence brain capillary endothelial barrier function in vitro. *Journal of neurochemistry*, 71(3):1151–1157, 1998. ISSN 0022-3042. doi: 10.1046/j.1471-4159.1998.71031151.x.
- [75] Michael W. Toepke and David J. Beebe. PDMS absorption of small molecules and consequences in microfluidic applications. *Lab on a Chip*, 6(12):1484, 2006. ISSN 1473-0197. doi: 10.1039/b612140c. URL <http://xlink.rsc.org/?DOI=b612140c>.

- [76] Topas Advanced Polymers. TOPAS- Cyclic Olefin Copolymers, 2015. URL [http://www.topas.com/sites/default/files/files/TOPAS_{_}Brochure_{_}E{_}2014{_}06\(1\).pdf](http://www.topas.com/sites/default/files/files/TOPAS_{_}Brochure_{_}E{_}2014{_}06(1).pdf).
- [77] Erica Tornabene and Birger Brodin. Stroke and Drug Delivery - In Vitro Models of the Ischemic Blood-Brain Barrier. *Journal of Pharmaceutical Sciences*, 105(2):398–405, 2016. ISSN 0022-3549. doi: 10.1016/j.xphs.2015.11.041. URL <http://dx.doi.org/10.1016/j.xphs.2015.11.041>.
- [78] Reginald Tran, Byungwook Ahn, David R Myers, Yongzhi Qiu, Yumiko Sakurai, Robert Moot, Emma Mihevc, H Trent Spencer, Christopher Doering, and Wilbur A Lam. Simplified prototyping of perfusable polystyrene microfluidics. *Biomicrofluidics*, 8(4):046501, 2014. ISSN 1932-1058. doi: 10.1063/1.4892035. URL <http://www.ncbi.nlm.nih.gov/pubmed/25379106>{%}5Cn<http://www.pubmedcentral.nih.gov/articlerender.fcgi?artid=PMC4189295>.
- [79] Chia Wen Tsao. Polymer microfluidics: Simple, low-cost fabrication process bridging academic lab research to commercialized production. *Micromachines*, 7(12), 2016. ISSN 2072666X. doi: 10.3390/mi7120225.
- [80] Chia-Wen Tsao and Don L. DeVoe. Bonding of thermoplastic polymer microfluidics. *Microfluidics Nanofluidics*, 6(1):1–16, 2009. doi: 10.1007/s10404-008-0361-x.
- [81] M.D. Tyona. Key stages in spin coating process. *Advances in Material Research*, 2(4):181–193, 2013. ISSN 2234-0912.
- [82] Marinke van der Helm, Andries van der Meer, Jan Eijkel, Albert van den Berg, and Loes Segerink. Microfluidic organ-on-chip technology for blood-brain barrier research. *Tissue Barriers*, 8370(May):00–00, 2016. ISSN 2168-8370. doi: 10.1080/21688370.2016.1142493. URL <http://www.tandfonline.com/doi/full/10.1080/21688370.2016.1142493>.
- [83] P.M. Van Midwoud, A. Janse, M.T. Merema, G.M.M. Groothuis, and E. Verpoorte. Comparison of biocompatibility and adsorption properties of different plastics for advanced microfluidic cell and tissue culture models. *Analytical Chemistry*, 84(9), 2012. ISSN 00032700. doi: 10.1021/ac300771z.
- [84] Antonio Visioli. *Practical PID Control*. Number 9781846285851. Springer-Verlag London Limited, London, 2006. ISBN 9781846285851. doi: 10.1007/1-84628-586-0_3. URL <https://doi-org.tudelft.idm.oclc.org/10.1007/1-84628-586-0>.
- [85] Fzsina R. Walter, Sándor Valkai, András Kincses, András Petneházi, Tamás Czeller, Szilvia Veszelka, Pál Ormos, Mária A. Deli, and András Dér. A versatile lab-on-a-chip tool for modeling biological barriersru. *Sensors and Actuators, B: Chemical*, 222:1209–1219, 2016. ISSN 09254005. doi: 10.1016/j.snb.2015.07.110. URL <http://dx.doi.org/10.1016/j.snb.2015.07.110>.
- [86] Jack D. Wang, Nicholas J. Douville, Shuichi Takayama, and Mohamed Elsayed. Quantitative analysis of molecular absorption into PDMS microfluidic channels. *Annals of Biomedical Engineering*, 40(9):1862–1873, 2012. ISSN 00906964. doi: 10.1007/s10439-012-0562-z.
- [87] Anette Wolff, Maria Antfolk, Birger Brodin, and Maria Tenje. In Vitro Blood-Brain Barrier Models-An Overview of Established Models and New Microfluidic Approaches. *Journal of Pharmaceutical Sciences*, 104(9):2727–2746, 2015. ISSN 15206017. doi: 10.1002/jps.24329. URL <http://dx.doi.org/10.1002/jps.24329>.
- [88] Matthias Worgull. *Hot Embossing: Theory and Technology of Microreplication*. Elsevier Science, 2009. ISBN 0815515790. doi: 10.1016/B978-0-8155-1579-1.50001-X.
- [89] W.I. Wu, P. Rezai, H.H. Hsu, and P.R. Selvaganapathy. Materials and methods for the microfabrication of microfluidic biomedical devices. In Xiujun James Li and Yu Zhou, editors, *Microfluidic Devices for Biomedical Applications*, pages 3–62. Woodhead Publishing, 2013. ISBN 9780857096975. doi: 10.1533/9780857097040.1.3. URL <http://linkinghub.elsevier.com/retrieve/pii/B9780857096975500013>.
- [90] Diane M. Wuest, Allison M. Wing, and Kelvin H. Lee. Membrane configuration optimization for a murine in vitro blood-brain barrier model. *Journal of Neuroscience Methods*, 212(2):211–221, 2013. ISSN 01650270. doi: 10.1016/j.jneumeth.2012.10.016. URL <http://dx.doi.org/10.1016/j.jneumeth.2012.10.016>.

- [91] Yao Yao, Zu Lin Chen, Erin H. Norris, and Sidney Strickland. Astrocytic laminin regulates pericyte differentiation and maintains blood brain barrier integrity. *Nature Communications*, 5:1–12, 2014. ISSN 20411723. doi: 10.1038/ncomms4413.
- [92] Daniel P Yen, Yuta Ando, and Keyue Shen. A cost-effective micromilling platform for rapid prototyping of microdevices. *Technology*, 4(4), 2016. doi: 10.1142/S2339547816200041.
- [93] Ju Hun Yeon, Dokyun Na, Kyungsun Choi, Seung Wook Ryu, Chulhee Choi, and Je Kyun Park. Reliable permeability assay system in a microfluidic device mimicking cerebral vasculatures. *Biomedical Microdevices*, 14(6):1141–1148, 2012. ISSN 13872176. doi: 10.1007/s10544-012-9680-5.
- [94] Edmond W K Young, Erwin Berthier, and David J. Beebe. Assessment of enhanced autofluorescence and impact on cell microscopy for microfabricated thermoplastic devices. *Analytical Chemistry*, 85(1):44–49, 2013. ISSN 00032700. doi: 10.1021/ac3034773.
- [95] Seung Tack Yu, Sung Jae Na, Tae Sun Lim, and Bun Yeoul Lee. Preparation of a bulky cycloolefin/ethylene copolymer and its tensile properties. *Macromolecules*, 43(2):725–730, 2010. ISSN 00249297. doi: 10.1021/ma902334d.
- [96] Zeon Specialty Materials. The Lowest Autofluorescent Injection-Moldable Plastic, 2016. URL <https://www.zeonex.com/life-sciences.aspx.html>.
- [97] Kaichang Zhou and Ian Papautsky. Optimization of COC hot embossing with soft PDMS tools. *Microfluidics, BioMEMS, and Medical Microsystems V*, 6465(January 2007):64650R, 2007. doi: 10.1117/12.701281.

I

Part 1



Literature study

The literature study as submitted for the first part of this thesis is presented in this appendix. Some parts have been adapted with advancing insights and reused in the main part of the thesis.

Department of Precision and Microsystems Engineering

Design and fabrication of a Blood-Brain Barrier on Chip for high-throughput production

Sarah Aalbers

Coaches : Dr.ir L. Sasso
: Dr.ir. A. Denkova
Specialisation : Micro and Nanosystems Engineering
Type of report : Literature review
Date : 7 November 2017

Contents

1	Blood Brain Barrier and the treatment of glioblastoma	2
2	In vitro BBB models	4
2.1	Transwell models	4
2.1.1	Characterisation techniques	4
2.2	Microfluidic models	7
2.2.1	Characterisation techniques	14
2.3	Conclusion	15
3	Mechanical factors influencing the BBB	16
3.1	Shear stress	16
3.1.1	Influence of shear stress in in vitro experiments	16
3.1.2	Shear stress in vivo	17
3.2	Intraluminal pressure and pulsatile flow	18
3.2.1	Intraluminal pulsatile pressure in vivo	18
3.2.2	Intraluminal pressure in in vitro experiments	18
3.2.3	Intraluminal pressure and shear stress combined in in vitro experiments	19
3.2.4	Intraluminal pulsatile pressure in in vitro BBB models	19
3.2.5	Conclusion	20
3.3	Flow pattern in rectangular channels	20
3.4	Curvature	21
3.5	Permeable membrane	21
3.5.1	Protein coating	21
3.5.2	Membrane material and pore size	22
3.6	Conclusion	22
4	Requirements	24
4.1	Layout of the BBB-on-Chip	24
4.2	Cell culturing	24
4.3	Testing barrier function	25
4.4	Testing drug transport	25
4.5	Testing the effect of drugs on tumor growth	25
4.6	Fabrication	26
5	Fabrication techniques and material	27
5.1	Introduction to polymers	27
5.2	State of the art: PDMS and soft lithography	28
5.2.1	Fabrication throughput	29
5.2.2	Bonding and hydrophobicity	29
5.2.3	Bio-compatibility	29
5.2.4	Permeability	30
5.2.5	Optical properties	30
5.2.6	Conclusion	30
5.3	Alternative fabrication techniques	31
5.3.1	Injection molding	31
5.3.2	Hot embossing	31
5.3.3	Laser ablation	32
5.3.4	Micro milling	32
5.4	Alternative materials	33
5.4.1	Polystyrene	33

5.4.2	Polycarbonate	34
5.4.3	Cyclic Olefin Polymers	35
5.5	Choice of material and fabrication method	37
5.6	Mold fabrication	39
5.6.1	3D-printing	39
5.6.2	Laser ablation	43
5.6.3	Conclusion	43
5.7	Electrode fabrication by hot embossing COC with a conductive polymer layer	43
6	Project proposal	46
6.1	Research question	46
6.2	Milestones and deliverables	46
6.3	Activities and risk mitigation	46
6.3.1	Design and simulation	48
6.3.2	Mold fabrication	48
6.3.3	Substrate preparation	49
6.3.4	Soft embossing	50
6.3.5	Thermal fusion bonding	51
6.3.6	Characterization	52
6.4	Timeline	53

1. Blood Brain Barrier and the treatment of glioblastoma

In 1885 Paul Ehrlich, a microbiologist, injected various laboratory animals with a blue dye and found out that in mammals all organs were stained to a certain degree, except for the brain. Ehrlich thought this was because cells in the brain had no affinity for the dye. However in 1913 his student Edwin Goldmann injected trypan blue into the brain of a young rabbit and saw that now parts of the brain were stained, but no other organs. This phenomenon is attributed to the blood-brain-barrier.¹¹⁰

Exchange of substances, such as nutrients and oxygen, between the blood and the cerebrospinal fluid in the brain occurs across the capillaries' walls. Neurons are very sensitive to changes in concentrations and to many different compounds that should not enter the brain. The Blood Brain Barrier (BBB) protects the brain by making sure the exchange of compounds between the blood and cerebrospinal fluid occurs very selectively. This barrier is formed by the walls of the capillaries and consists of specialized endothelial cells, astrocytes, pericytes and the basal lamina, see fig. 1.1.¹²¹ A capillary measures less than 1 mm in length and about 10 μm in diameter.⁴⁵ The walls are lined with a single layer of endothelial cells which adhere to the basal lamina, which acts as a support structure. The endothelial cells are connected to each other with adherens junctions, the pores between the cells are sealed with tight junctions. The permeability of the endothelial cells is affected by the interaction between the astrocytes, pericytes and endothelial cells. Also neurons, microglia and blood-borne immune cells might regulate the functioning of the endothelial cells.¹²⁷

Molecules cross the blood brain barrier via the paracellular pathway or the transcellular pathway. Transport via the paracellular pathway is the passive diffusion of small water soluble compounds through the pores between the endothelial cells. The transport is driven by electrochemical, osmotic and hydrostatic gradient. Adherens junctions and in particular tight junctions restrict the rate of passive paracellular diffusion.

Other compounds, such as hormones, high molecular mass proteins and amino acids, cross the blood brain barrier via the transcellular pathway. The compounds are transported actively or passively through the endothelial cells. Different mechanisms take care of the transport.¹²¹

One of these mechanisms is called receptor mediated transcytosis, see fig. 1.2 for a schematic representation. Receptor-mediated transcytosis is the mechanism which is used to transport hormones and high molecular mass proteins to the brain. In this mechanism a ligand (the to be transported hormone or protein) binds to a receptor present on the luminal side of the cell membrane. Inside of the cell a protein coat forms over the cell membrane at the location of the receptor. This coating enables the formation of a vesicle, called endocytic vesicle, formed out of the cell membrane and enclosing the ligand-receptor complex¹⁰⁴. Inside the cell the ligand is dissociated from the receptor after fusion with an endosome. Next the ligand is delivered to the abluminal side of the endothelial cell by exocytosis. Not all ligands reach the abluminal side since some vesicles fuse with lysosomes, which break down the ligand. The mechanism of receptor-mediated transport does not depend on size or lipophilicity of the compound that is transported.¹²¹ Once compounds reach the cerebrospinal fluid, they can again be transported back to the blood by efflux transporters.

One of the challenges in the treatment of brain diseases is the development of drugs that are able to cross the BBB. At the Radiation Science & Technology department of the faculty TNW at the Delft University of Technology nano-carriers (polymersomes and polymeric micelles) are developed for the treatment of glioblastomas, brain tumors arisen from astrocytes. These nano-carriers can be equipped with targeting agents, namely glutathione and lactoferrin. Both are naturally transported using receptor-mediated transcytosis, and bind to receptors on the cell membrane.

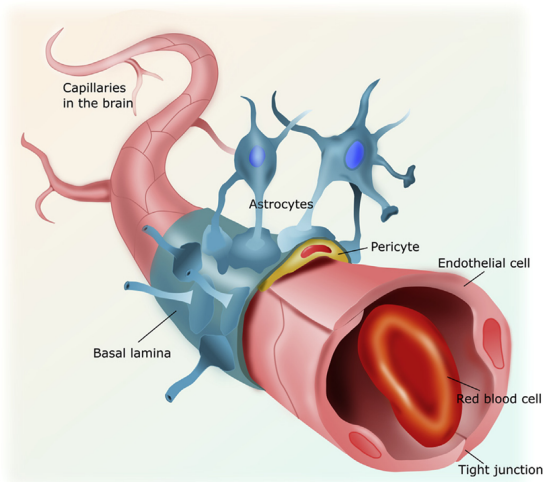
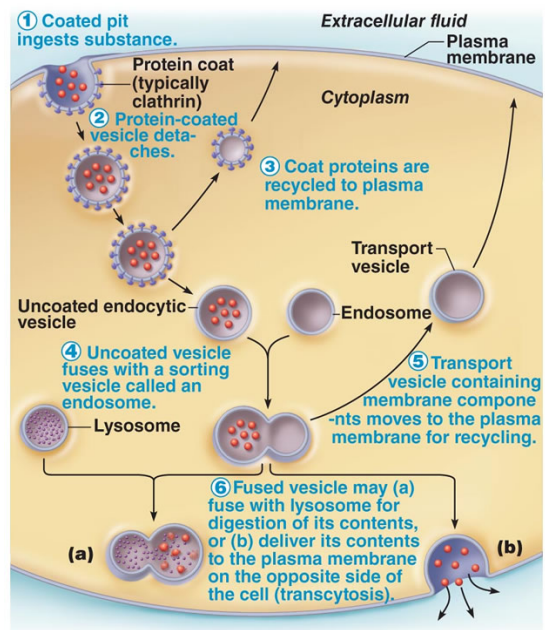


Figure 1.1: Figure from Tornabene and Brodin¹²⁷.
Capillary in the brain.



© 2013 Pearson Education, Inc.

Figure 1.2: Figure from Marieb et al.⁸⁰ permission.
Receptor-mediated transcytosis

Next to these targeting agents also radionuclides and/or radiosensitizers will be encapsulated in the nano-carriers. Different radionuclides will be used: ^{111}In , emitting gamma radiation which can be used for diagnosis using SPECT; ^{177}Lu , emitting gamma and beta radiation which makes it suitable for both diagnosis and therapy; ^{225}Ac and ^{213}Bi , both emitting alpha radiation suitable for therapy. Radiosensitizers increase the effect of radiation therapy on tumour cells, for example by inhibiting DNA repair.

2. In vitro BBB models

Developing drugs for brain diseases comes with high costs, which could be reduced when more accurate models of the BBB are available. At the moment a large amount of drugs that passed the developmental phase fail in clinical trials⁵⁷. The costs of developing drugs could be reduced when better and cheaper models are present to use for testing in an early stage, such that fewer candidates fail in the clinical trials.

The Radiation Science & Technology department of the faculty TNW at the Delft University of Technology asked to develop such a model. In this model it should be possible to test the ability of the nanocarriers in development to cross the blood brain barrier and reach a glioblastoma spheroid in the brain. Next to that it should be possible to study the effect of the nanocarriers transported through the blood-brain barrier on the growth of the glioblastoma spheroid. In the following chapter the models that are currently available and how their performance can be tested will be discussed.

2.1 Transwell models

In vitro models that are mostly used at the moment for drug assays and which are commercially available are Transwell® platforms¹⁴¹. The Transwell® platform consists of a Transwell® insert with a porous semi-permeable membrane, hanging in a well plate, see fig. 2.1. The now formed upper chamber typically represents the lumen of the capillary and the bottom chamber the abluminal side of the endothelial cells. The simplest model is a monoculture, as in fig. 2.1, here only endothelial cells are cultured on the membrane.

The endothelial cells are obtained by isolating endothelial cells from for example isolated brain microvessels. These primary cells are modified such that they can proliferate indefinitely, creating a cell line. Different primary cells and cell lines, from different animals or from humans can be used. See for example the reviews of Wolff et al.¹⁴¹, Abbott et al.⁵, Bicker et al.¹⁶ and Wilhelm and Krizbai¹³⁸ for overviews of primary cells and cell lines used in BBB models with their characteristics.

Astrocytes, pericytes and microglia interact with the endothelial cells and thereby influence the permeability of the BBB. To make a better representation of the in vivo situation and to maintain or induce the barrier properties of the endothelial cells, also coculture models and multicultures are developed, see fig. 2.2 for some examples.

2.1.1 Characterisation techniques

The barrier properties of the endothelial cells can be characterized in two ways, by measuring the *Transendothelial Electrical Resistance* (TEER) and by determining the permeability to different compounds.

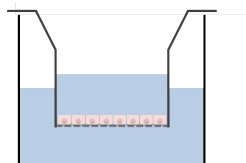


Figure 2.1: Transwell platform.

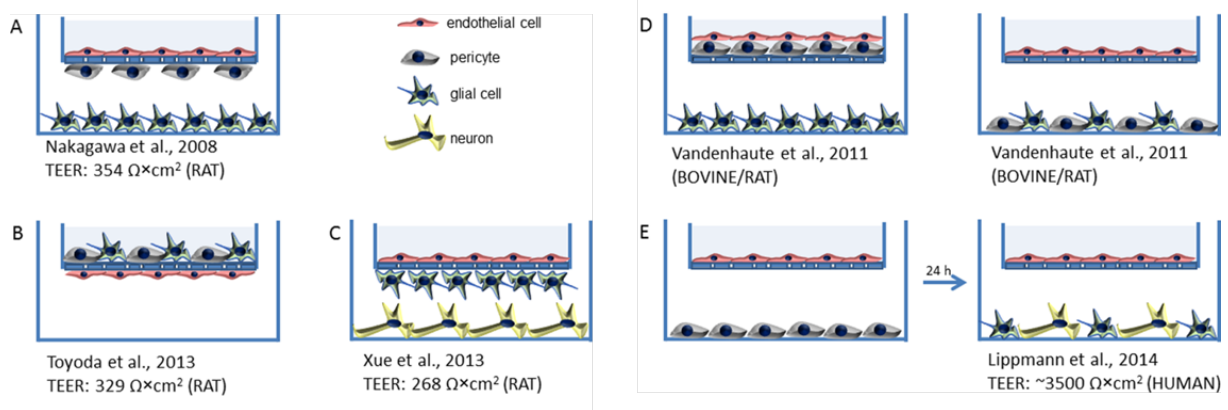


Figure 2.2: Figure adapted from Wilhelm and Krizbai¹³⁸. Different multicultures in Transwell systems. Astrocytes, a type of glial cells, are noted here as glial cells

TEER measurements

The TEER is the electrical resistance of the endothelial cells from the luminal to abluminal side. It is mainly defined by the tight junctions, which prevent the transport of ions through the paracellular pathway.¹³⁸ TEER measurements are non-destructive, label-free and enable real-time characterization of the barrier function⁹⁴.

Voltohmmeter

Determining the TEER in a Transwell platform is mostly done by applying a potential difference over the membrane and measuring the electric current, see fig. 2.3. Mostly a 'chopstick' electrode is placed in both chambers. The instruments to perform such measurements are called volt-ohmmeters. The membrane with the endothelial cells and the rest of the Transwell model is represented by an equivalent circuit with the resistance of the endothelial cells and the combined resistance of the medium, the membrane and the electrode-medium interface resistance connected in series. By performing measurements on empty models and models with endothelial cells cultured, the resistance of the endothelial cells and the combined resistance of the rest of the models follows from Ohm's law. The resistance of the endothelial cells is then multiplied by the surface area of the membrane, which gives the TEER in Ωcm^2 .⁵

Benson et al.¹⁴ note that a DC voltage source could charge the electrodes and the cell layer. A commonly used system, the EVOM², World Precision Instruments, Sarasota, USA, uses an AC square wave at 12.5 HZ to avoid this. An amplitude of $10\ \mu\text{A}$ is used.

The measurements are dependent on temperature and electrode placement. For accurate results a uniform current distribution over the membrane is needed. For larger membranes, $>12\ \text{mm}$, the manufacturer of EVOM² recommends to place the to be measured culture insert in their Endohm chamber. The location of the electrodes relative to the culture inserts is fixed and the shape of the electrodes is concentric, to enhance a more uniform current density through the membrane.^{117,42}

Medium conductivity and diffusion coefficient depend on temperature.¹²⁸ Therefore it is desirable to measure TEER at a steady state temperature, for example in an incubator. If it is not possible to perform the measurements inside an incubator (37°C) and TEER is measured outside the incubator at room temperature (20°C), the device needs about 20 minutes to cool down to room temperature completely. Blume et al.¹⁷ To overcome this problem Blume et al.¹⁷ developed a numerical method to calculate TEER from measurements during heating and cooling.

Impedance Spectroscopy

Another method to measure the TEER can be applied using an Impedance Spectroscopy System, for example the cellZscope system from nanoAnalytics. The set-up is the same as for voltohmmeters, but now the amplitude and phase of the current is measured over a range of AC frequencies. From the acquired data the TEER and the transendothelial electrical capacitance is calculated. In the cellZscope system hereto it is assumed that the equivalent circuit of fig. 2.4 is valid⁸⁸. The tight-junctions are responsible

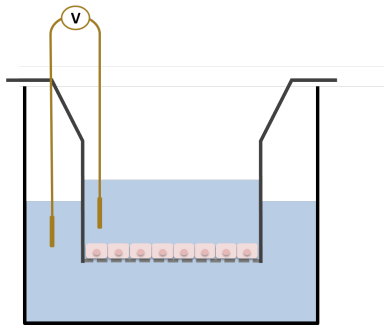


Figure 2.3: Characterization of the barrier function by measuring the TEER

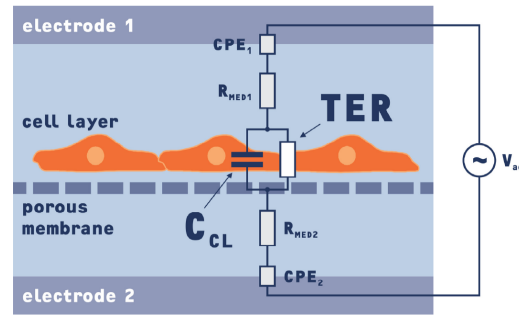


Figure 2.4: Equivalent circuit used in impedance spectroscopy to calculate the TEER (TER in figure), defined by the paracellular pathway, and the transendothelial electrical capacitance (C_{cl}), defined by the transcellular pathway. Other contributions to the total impedance of the cell layer, for example the ohmic resistance of the cell membrane, can be neglected in first approximation⁸⁸.

for an ohmic resistance, TER in the figure. The impedance of the transcellular pathway is represented by an electrical capacitance, C_{cl} , resulting from the cell-membranes on apical and basolateral side. Other contributions to the impedance of the cell layers are neglected. For example the ohmic resistance of the cell-membrane parallel to the capacitance C_{cl} is very high, which results in the current flowing mainly across the capacitor and allowing to neglect this resistance¹⁴. Furthermore, the medium on both sides of the membrane can be modeled as a simple ohmic resistance, R_{med} . The electrodes and the interface between the electrodes and the medium introduce a constant phase element, CPE. A capacitor like element with a phase shift between 0° and 90° . The impedance of the constant phase element depends on the parameters A_{cpe} and n_{cpe} . The phase shift of the CPE is equal to $90^\circ \cdot n_{cpe}$.

With the equivalent circuit the total impedance of the device can be described with an analytical function depending on TER, C_{cl} , R_{med} , A_{cpe} and n_{cpe} . The impedance and phase shift of the system is measured over a range of frequencies. The five parameters are then obtained by non-linear least-square fitting of the analytical expression to the experimental data.⁸⁸

Impedance spectroscopy yields more accurate TEER values than measurements with the voltohmmeter, since also the capacitive effects of the cell membranes and the electrode-medium interface are taken into account.

Permeability assays

Two characteristics of the barrier function can be quantified using permeability assays: barrier tightness and transporter function.

Permeability

The permeability of the layer of endothelial cells can be quantified by adding marker molecules to one side of the membrane and monitoring the amount which reaches the other side of the membrane. The permeability to these molecules is a measure for the tightness of the barrier.

For characterizing the paracellular permeability small molecules such as radiolabelled sucrose and mannitol or fluorescent markers such as Lucifer Yellow and sodium fluorescein can be used. For less tight barriers larger molecules such as inulin, dextrans, and serum albumin can be used.⁴

Transporter function

The efflux ratio of a compound is equal to the permeability from apical to basolateral (AB) side of the cell layer divided by the permeability from basolateral to apical (BA) side of the cell layer. It is the ratio at which compounds are actively transported from one side of the cell layer to the other side. Transport

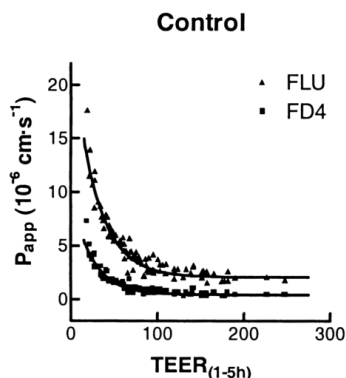


Figure 2.5: Dependency of the permeability to sodium fluorescein (FLU) and FITC-labeled dextran (FD4) on TEER in bovine brain endothelial cells in coculture with murine astrocytes. Figure reproduced from Gaillard and De Boer⁴⁸

of a substance is said to be active when the efflux ratio of this substance is greater than 1.5-2.0 or smaller than 0.5.¹³⁹

According to Abbott et al.⁵ permeability assays are labour-intensive and time-consuming, the time-resolution is low and additional assays and analytical delays can not be avoided. When the permeability assays are for instance performed at the same moment as the permeability of fluorescent labelled drugs are tested the tests could interfere with each other.

Relation TEER and permeability assays

For low TEER values, the permeability decreases, but when a certain threshold in TEER is reached the permeability becomes independent on TEER. Gaillard and De Boer⁴⁸ showed this by culturing brain endothelial cells from calves on Transwell filters and measuring TEER across the filter insert and the permeability to sodium fluorescein and FITC-labeled dextran, see fig. 2.5. This means that the TEER should be high enough to obtain reliable permeability assays, but may not need to be as high as the in vivo TEER value. Gaillard and De Boer⁴⁸ found that the permeability became independent of TEER upward of $\sim 150 \Omega\text{cm}^2$ in their experiments. This value depends on cell type and culture conditions.

Fluorescence staining

Fluorescence microscopy is often used to visualize tight junction and adherens junction proteins. Also cell viability, cytoskeleton, transporters, vesicular trafficking and more can be visualized.²⁵ Staining tight junctions and adherens junctions gives a good insight into the functioning of the endothelial cells, since it shows the intensity and orientation of the junctions.

Mostly fluorescence imaging of the BBB is done after fixating the cells. It is also possible to use fluorescence staining in live cells. However, the intense illumination of the cells needed in fluorescence microscopy is phototoxic. Fluorescence microscopy of live cells could therefore influence the behaviour of the cells and can not be performed for an extended time period.⁴¹

2.2 Microfluidic models

The behaviour of cells is regulated by genetic information inside the cell and by signals from outside the cell. The way cells react on external signals is dependent on the genetic information in the cell. When the microenvironment of the cell changes, external signals and therefore the behaviour of the cell changes. To be able to get a representative model of the blood-brain-barrier, the cells need to behave as in vivo and therefore the microenvironment needs to be mimicked as good as possible. In Transwell platforms many factors cannot be represented well. The medium for example is static, whereas the blood flows and the

dimensions of the blood chamber do not comply with those of a capillary. Brown et al.²² points out that the ratio of medium-to-cell volume in Transwell models is high, which causes signalling agents to dilute strongly. In order to make a better representation of the microenvironment of the brain endothelial cell, microfluidic models are in development. In microfluidic models a representative flow and other relevant factors can be applied. This section gives an overview of the microfluidic models currently in development.

Two main groups of microfluidic devices can be distinguished: *hollow fiber models* and *BBB-on-chip models*. A typical BBB-on-chip model consists of two chambers separated by a porous membrane. The upper chamber represents a capillary, the bottom chamber the cerebrospinal fluid. In the blood chamber endothelial cells are cultured. The cerebrospinal chamber is left empty, or multicultures can be established by filling the chamber with astrocyte conditioned gel or medium or by seeding astrocytes, pericytes and/or glial cells. The blood chamber and upper part of the membrane are coated with one or more proteins found in the extracellular matrix, such that the cells are able to adhere to the device.

Three papers present a completely different layout, Prabhakarpanthian et al.⁹⁹, Deosarkar et al.³⁷ (continuation on Prabhakarpanthian et al.⁹⁹) and Yeon et al.¹⁴⁹. In these devices the blood and brain compartments are placed side by side instead of on top of each other. A membrane is not used, but microholes are fabricated in the PDMS wall separating the brain and blood compartment. The first two devices are coated such that a monolayer of endothelial cells is formed in the whole channel. In the device of Yeon et al.¹⁴⁹ coating is not reported, but cells get trapped in the microholes and then form a monolayer.

Hollow fiber models are presented by Cucullo et al.³⁴ and Neuhaus et al.⁹¹. They consist of a hollow fiber made of polypropylene, with a relatively large wall thickness (150 μm for Neuhaus' model). Endothelial cells are cultured on the luminal side of the fiber wall, on the abluminal side for example astrocytes can be cultured. The design does not allow for visualization during cell culture and cell characterization requires removal of the cells from the hollow fiber.⁸⁶ It is therefore chosen to focus on the BBB-on-Chip devices.

In table 2.1 devices with used dimensions, materials and fabrication procedures are noted. Not all information in this overview will be discussed in this chapter, but throughout this literature review this overview will be used. Table 2.2 gives an overview of the methods used to characterize the function of the BBB grown in the devices.

Dimensions and shear stress

The cross-sections of the chambers all have rectangular shapes, for the blood chamber the width x height ranges from 200x100 μm to 62000x100 μm . This means the cross-section in the devices is a lot larger than the cross-sections of capillaries in the brain (10 μm). The ratio width/height determines the flow pattern and thus the variation in wall shear stress over the width of the channel. Shear stress is an important factor in BBB function. In section 3.1 and section 3.3 more information can be found about the shear stress in capillaries and its influence and the flow pattern of media in a rectangular channel.

Materials and fabrication

The main structure of all devices is fabricated out of polydimethylsiloxane (PDMS). PDMS has many properties that make the material suitable for the fabrication of organ-on-chip models, but also some drawbacks. It is for example inexpensive and transparent, but deposition for electrode integration is difficult. Transparency is practical for real time optical monitoring of the cell culture.

To overcome the problem of electrode integration some groups use loose electrodes that are inserted by hand (Griep et al.⁵¹, Deosarkar et al.³⁷, Brown et al.²², Prabhakarpanthian et al.⁹⁹), others by using a glass slide cover on which the electrodes are sputtered (Booth and Kim¹⁹²⁰, Walter et al.¹³⁶). The devices are all fabricated using molds and soft lithography. These molds are almost all fabricated using photolithography processes, which are time consuming fabrication steps. Fabrication techniques for which molds are not needed would be more practical to produce these prototypes, since minor changes to the design require complete new molds. Next to that, soft lithography can not be scaled up efficiently for

Table 2.1: Characteristics BBB-on-Chip devices

Reference	Description	Fabrication * techniques	Fore size (μm)	Membrane Material	Thickness (μm)	Area (mm^2)	Device Material	Coating	Dimensions	Shear stress
Achyuta et al. ⁶	Bottom layer with oval vascular channel containing pillars to support the porous membrane. On top a neural layer on which neural cells are cultured prior to assembly. The neural layer is covered with a glass slide. Flow through both channels.	17, 11, 12, 18, 22, 16, 8	8	PC	NA	78	PDMS	V: bovine plasma fibronectin $2\mu\text{g}/\text{cm}^2$ C: poly-D-lysine $50\mu\text{g}/\text{mL}$	V: 100 μm h: 30 mm w: 3-10 mm	NA
Booth and Kim ¹⁹	A membrane is sandwiched between two PDMS layers both containing a channel. The channels cross perpendicular. The PDMS layers are sandwiched between two PDMS layers which contain an embedded glass layer with sputtered electrodes. Endothelial cells grow on top of the membrane in the vascular channel, astrocytes on the bottom side of the membrane in the cerebral chamber to allow endfeet contact. Flow through both channels.	9, 19, 4, 6, 12, 17, 10, 2	0.4	PC	10	10	PDMS	fibronectin mg/ml	V: h: 200 μm w: 2 mm C: h: 200 μm w: 5 mm	2.2 mPa
Booth and Kim ²⁰	<i>Differences from Booth and Kim¹⁹ are given only</i>					16			V and C: w: 4 mm	1.5 Pa
Brown et al. ²²	At the bottom a vascular channel is made in PDMS. This PDMS layer is mounted on a glass slide. On top of the vascular channel a brain compartment filled with gel is placed. In between the two layers a membrane is placed. On top of the brain compartment a PDMS layer with multiple small channels makes perfusion, loading and sampling of the brain compartment possible.	18, 16(2), 19, 11, 12, 1, 12, 11	0.2	PC	NG	18.6	PDMS	laminin at $\mu\text{g}/\text{ml}$	V: h: 100 μm w: 6.2 mm l: 3 mm	2.3 mPa
Deosankar et al. ³⁷	A circular basolateral compartment, apical channels run around it. Apical and basolateral sides separated by an interface with 3 mm gaps. Apical channels contain endothelial cells while basolateral side contains astrocytes conditioned media.	5, 16, 12, 11, 13	3x3	PDMS	100	~ 0.55	PDMS	rat fibronectin	V: w: 200 μm h: 100 μm l: 2762 μm	0.38 mPa (2 hours) 7.6 mPa
Griep et al. ⁵¹	Two PDMS layers with two chambers and two platinum electrodes. Chambers run perpendicular to each other. In between the two layers a membrane is placed.	18, 16, 22, 18, 12, 2	0.4	PC	10	0.25	PDMS	150 $\mu\text{g}/\text{ml}$ rat collagen type 1	V and C: l: 1 cm w: 500 μm h: 100 μm electrodes: d: 200 μm channels: l: 1cm w: 200 μm h: 300 μm	0.58 Pa (18 h, after 3 days static culture)

* See table 2.3 for the fabrication techniques corresponding to the numbers

Reference	Description	Fabrication techniques	Membrane Pore size (μm) Material	Thickness (μm) Area (mm^2) Device material	Coating	Dimensions	Shear stress
Prabhakarpan- dian et al. ⁹⁹	A basolateral compartment with pentagonal shape, apical channels run around it. Apical and basolateral sides separated by an interface with 3x3 mm gaps formed by microfabricated duct of 100 mm in length. Apical channels contain endothelial cells while basolateral side contains astrocytes conditioned media.	5, 16, 12, 11, 13	3x3 PDMS	50 ~0.5 PDMS	rat fibronectin	V: w: 200 μm h: 100 μm	3.4 mPa
Sellgren et al. ¹¹¹	Two-compartment microfluidic devices were obtained by sandwiching a nanoporous membrane between two PDMS micromolded channels. Performance of PE and PTFE membranes are compared. Astrocytes cultured in 3D collagen matrix.	5, 4, 22, 16, 12, 11, 15, 8, 11, 15	0.40 PE 0.40 PTFE	10 PDMS 10 PDMS 40	PE: collagen IV-fibronectin 1.8 $\mu\text{g}/\text{cm}^2$ PTFE: collagen I 1.6 $\mu\text{g}/\text{cm}^2$	C: h: 100 μm V: w: 1 mm h: 150 μm l: 10 mm C: w: 1 mm h: 150-300 μm l: 10 mm	0.5 Pa (24 h) Monolayers were peeled off with flow
Walter et al. ¹³⁶	Membrane is sandwiched by PDMS layers with parallel channels, PDMS layers are sandwiched by glass slides with electrodes. Device can be attached to peristaltic pump.	3, 16, 11, 14, 21, 7, 14, 11, 4	0.45 PET	23 PDMS and glass	V: rat tail collagen C: collagen type IV	V: l: 3.7 cm w: 0.2 cm h: 0.2 cm C: l: 4.2 cm w: 0.2 cm h: 0.2 cm	1.5 mPa (48 h, after 3 days static culture)
Yeon et al. ¹⁴⁹	Channels with connecting microholes, in which endothelial cells get trapped to form a monolayer.	18 (2), 16	area: PDMS 12 μm^2	25 NG PDMS	no coating		2.8-81.9 mPa (questionable calculation)

* See table 2.3 for the fabrication techniques corresponding to the numbers

Table 2.2: Characterization methods BBB-on-Chip devices

Reference	Cells	Permeability assays	Immunohisto-fluorescence	Other	TEER measuring method	TEER Stimulation (Ωcm^2)	Pro/Con
Achyuta et al. ⁶	RBE4 (rat) E-18 cortical (rat)	FITC Dextran 3 kDa	ZO-1 staining GFAP (astrocytes) MAP-2 (neurons) OX-42 (microglia) vWF ICAM-1 (EC function)	Western blots to distinguish dead from living cells.	NA	NA TNF-alpha response	+ Neural layer consists of astrocytes, neurons and glial cells. + Neurovascular communication, shown by response to TNF-alpha + circulating immune cells and choroid plexus - Labour intensive device construction - Before assembly neural layer needs to be cultured - No TEER measurements - Not tightly sealable - Undesirable flow pattern + Uniform ion flow density + Recovery from exposure to 150 microM histamine solution + Real time TEER measurements - No imaging possible with electrode pads - Shear stress (2.3E-2 dyne/cm ²) significantly lower than in vivo
Booth and Kim ¹⁹	b.End3 CSD1A (astrocytes)	FITC Dextran 4 kDa FITC Dextran 20 kDa FITC Dextran 70 kDa	ZO-1 staining GFAP	NA	EVOM2 system Two sets of two AgCl thin film electrodes. Electrode area: 75% of cell culture area EVOM2 system	>250 Recovery from histamine exposure	
Booth and Kim ²⁰	b.End3 C6 (glial cells)	Drugs with molecular weights between 141.17 Da and 489.65 Da	ZO-1 staining DAPI	Cytotoxicity of drugs with LDH assay	EVOM2 system	mono: NA 223 co: 280	
Brown et al. ²²	hBMVEC Primary astrocytes Primary pericytes Human cortical glutamatergic neurons differentiated from hiPSCs suspended in collagen I matrix	FITC Dextran 10 kDa FITC Dextran 70 kDa Ascorbate	ZO-1 staining Actin filaments (phalloidin)	NA	Four-probe approach Measured with frequencies between 3 and 100 kHz	864.9 - cold shock - glutamate exposure - ascorbate exposure	+ Culture with ECs, astrocytes, pericytes and neurons - Very short vascular channel, entrance effects might influence shear stress - TEER only used for comparison within the experiments of the writers, not to compare with others. - Electrodes inserted at channels entrances, causes a not uniform ion flow.

Reference	Cells	Permeability assays	Immunohisto- fluorescence	Other	Method	max TEER	Stimulation	Pro/Con
Deosankar et al. ³⁷	Primary cultures of neonatal rat brain capillary endothelial cells (RBEC) Primary cultures of neonatal rat astrocytes Primary cultures of neonatal rat astrocytes for conditioned medium	Texas Red dextran 40kDa	ZO-1 staining Astrocytes (GFAP) Microglia (CD11F) Nuclei (Hoechst 33342) Actin filaments (phalloidin) Nuclei (Draq5)	NA	EVOM2 with chop- sticks	NG	NA	+ Side-by-side placement of channels permits simultaneous real-time visualization of both compartments + Contact between astrocytes and endothelial cells - Low shear stress - Microgaps in corners of channel - Shear stress not uniform?
Griep et al. ⁵¹	HCMEC/D3	NA	ZO-1 staining Actin filaments (phalloidin) Nuclei (PI)	NA	Impedance spectro- scopy (0.2 V, 100 - 10M Hz)	36.9 (with SS)	TNF-alpha (with SS)	+ Easy accessible chambers + optical clarity + Real time TEER measurements + Simplicity of device and fabrication - Small surface area electrodes causes noise, will be replaced by sputtered electrodes in future. - No optical inspection possible at location of crossing channels, because of electrodes + Side-by-side placement of channels permits simultaneous real-time visualization of both compartments + Efflux transporter system characterisation - Low shear stress - Microgaps in corners of channel - No uniform shear stress
Prabhakarpan-RBE4 dian et al. ⁹⁹	ACM	FITC-dextran (3-5 kDa)	-	Efflux transporter function: Rhodamine 123 verapamil Western blots: ZO-1 Claudin-1 P-gp (efflux transporter system)	NA	NA	NA	+ Easy accessible chambers + optical clarity + Real time TEER measurements + Simplicity of device and fabrication - Small surface area electrodes causes noise, will be replaced by sputtered electrodes in future. - No optical inspection possible at location of crossing channels, because of electrodes + Side-by-side placement of channels permits simultaneous real-time visualization of both compartments + Efflux transporter system characterisation - Low shear stress - Microgaps in corners of channel - No uniform shear stress

Reference	Cells	Permeability assays	Immunohisto-fluorescence	Other	Method	max TEER	Stimulation	Pro/Con
Sellgren et al. ¹¹¹	b.End3 CSD1A (astrocytes) in collagen hydrogels	70 kDa FITC-dextran	Actin filaments (phalloidin) claudin-5	NA	NA	NA	NA	+ Comparison of PE and PTFE membranes - PE: No claudin-5 expression - Cells were peeled off at 5 dyne/cm ²
Walter et al. ¹³⁶	hCMEC/D3 Primary rat brain endothelial cells, -pericytes, and -astroglia cells	Sodium fluorescein 376 Da FITC Dextran 4.4 kDa Albumin 67 kDa	Ecs: ZO-1 Beta-catenin Pericytes (Alpha-SM) Astroglial cells (GFAP) Cell viability (Ethidium homodimer-1, Bis-benzimide)	NA	Impedance spectra in a frequency range from 1 Hz to 20 MHz. Sheet electrodes directly above and underneath membrane	28.5±7.2	NA	+ Transparent electrodes + Uniform ion flow - Low shear stress
Yeon et al. ¹⁴⁹	HUVEC astrocytes	Propranolol Antipyrine Carbamazepine Verapamil Atenolol	ZO-1 staining	NA	NA	NA	NA	+ Permeability values comply with Transwell model from Nakagawa et al. ⁸⁷ + Presence of astrocytes * Shear stress on abluminal side of Ecs - No uniform shear stress - Astrocytes not cultured but in medium

Table 2.3: Fabrication techniques by number, used for the different BBB-on-Chip models

1	Bonding using APTES	12	Punching in PDMS
2	Bonding with PDMS mortar	13	Sealing by heating
3	Brass mold fabrication	14	Sealing with silicone
4	Dicing glass/silicium	15	Soaking membranes in APTMS and bonding
5	DRIE process	16	Soft lithography of PDMS
6	Embedding glass slide in PDMS	17	Spin coating of PDMS
7	Glueing of wires to electrodes	18	Standard photolithography using SU-8
8	Glueing PDMS parts, tubing and/or membrane together	19	Trimming PDMS
9	Laser patterning glass	20	Vapor deposition of metal on glass
10	laser patterning PDMS	21	Vapor deposition of metal on PDMS
11	Oxygen plasma bonding	22	Vapor deposition of release agent on mold

higher production quantities. The desired properties of the material of the device and the possibilities of processing different materials will be discussed in chapter 5.

Membrane

The most used membrane material is polycarbonate (PC), which is translucent. Translucency makes it possible to optically inspect both compartments at the same time. Also polyethylene (PE), polytetrafluoroethylene (PTFE)¹¹¹ and polyethylene terephthalate (PET)¹³⁶ are used, which are all transparent. In most devices the pores in the membrane have a diameter of 0.4μ . Only the pore size in the device of Achyuta et al.⁶ ($8\mu\text{m}$) and in the side-by-side models of Prabhakarparandian et al.⁹⁹ and Deosarkar et al.³⁷ ($3\times 3\mu\text{m}$) is much larger. Yeon et al.¹⁴⁹ do not note the dimensions of the pores. Different coatings of ECM proteins, fibronectin, collagen I, collagen IV and laminin are used to allow the endothelial cells to adhere to the PDMS and the membrane. A more comprehensive discussion on the performance of different membrane materials, pore sizes and coatings can be found in section 3.5.2.

2.2.1 Characterisation techniques

The techniques described in section 2.1.1 to characterise the quality of the BBB in Transwell models can be used for the characterisation of the BBB in the microfluidic devices as well. Permeability assays can be performed in the same way, but for TEER measurements some adjustments need to be made.

Teer measurements

TEER values reported in different papers vary greatly, also when the same experimental set up is used or even same cell lines. Odijk et al.⁹⁴ discuss the origin of these variations, focussing mainly on DC measurements in microfluidic organ-on-chips. See Odijk et al.⁹⁴ for an overview of various cell types and different reported TEER values.

In Transwell models chopstick electrodes can be inserted in the medium and the potential will be distributed evenly over the membrane. In microfluidic chips the electrodes are sometimes placed in the inlet of one channel and in the outlet of the other channel. Since the channels are narrow the medium in the channel will cause a significant resistance, which leads to a non-uniform potential distribution over the membrane. The current will flow mainly through the membrane at the beginning and end of the membrane and not in the middle, leading to a higher apparent TEER than in Transwell models. Odijk et al.⁹⁴ report a theoretical model and comparison method to correct for this. It would be best to not have to make the measurement errors, for instance by placing the electrodes above and underneath the channels, covering the whole membrane area. The electrodes of Booth and Kim¹⁹, Booth and Kim²⁰ and Walter et al.¹³⁶ are implemented this way using vapor deposition. In the model of Griep et al.⁵¹ loose platinum electrodes are inserted in a channel running up to above the membrane. They note that this resulted in a different position from batch to batch and that they will use vapor deposition in future as well. The use of transparent electrodes would be preferred, such that optical inspection of the membrane remains possible.

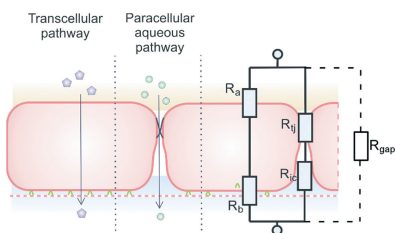


Figure 2.6: Equivalent circuit of an endothelial cell monolayer with gaps in the monolayer, with R_a : apical cell membrane resistance, R_b : basolateral cell membrane resistance, R_{tj} tight junction resistance, R_{ic} : intercellular resistance and R_{gap} the gap resistance. Reproduced from Odijk et al.⁹⁴

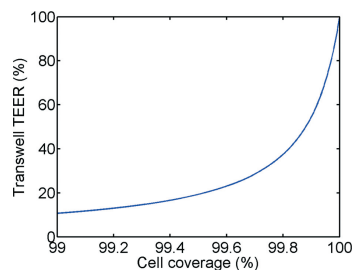


Figure 2.7: Calculated relative Transwell TEER vs. cell coverage. Figure and description reproduced from Odijk et al.⁹⁴

When performing and evaluating TEER measurements some factors of influence need to be considered. Odijk et al.⁹⁴ modelled the effect of gaps in the monolayer cultured in a Transwell system on the TEER value, by using the equivalent system in fig. 2.6. They found a dramatic decrease in TEER for only minor defects in the monolayer, expressed by percentage of coverage. For a coverage of 99.6% a decrease in TEER of 20% is found, see fig. 2.7.

Next to the above phenomenon, also temperature differences and material, quality and surface state of the electrodes have a significant influence on TEER measurements. Multicultures are known to increase the tightness of the BBB, however, care should be taken that the measured increase in TEER is not caused by the resistance of the extra layer of cells.⁹⁴

TEER measurements can thus not only be used to evaluate the performance of an intact monolayer, but are also quick and simple tests to check when a confluent monolayer, 100% coverage, is reached. At this moment drug assays can be performed. During these tests temperature differences should be avoided, or taken into account when determining the TEER value. Electrodes need to be fabricated adequately, to prevent high noise caused by bad electrode state and placement and to allow for optical inspection of the cells on the membrane.

2.3 Conclusion

The ability of drugs to cross the BBB *ex vivo* is tested in the pharmaceutical industry by using Transwell models. Unfortunately many drug candidates that looked promising in the developmental stage fail during clinical tests, which brings along high costs. Developing models that better represent the BBB is therefore necessary. Microfluidic chips have the capability of mimicking the microenvironment of the endothelial cells forming the BBB more closely than Transwell models. For example, the endothelial cells can be subjected to flow, like to blood also induces a flow in the capillaries. In microfluidic chips also smaller volumes of culture medium are needed than in Transwell models, which results in signaling agent excreted by the endothelial cells being diluted far less, complying better to the *in vivo* situation.

The *in vitro* BBB in both Transwell models and BBB-on-Chip models can be characterized using different methods: The resistivity of the cell monolayer (TEER) can be measured, permeability assays can be performed, and relevant structures of the endothelial cells can be visualised using fluorescence staining. Generally accepted guidelines for performing TEER measurements in microfluidic chips do not exist. This makes it difficult to make reliable comparisons between different models, but when performed correctly TEER measurements could give valuable information on boundary integrity.

In this section an overview was given of the currently published BBB-on-Chip models and important characteristics of these models. The influence on BBB function and consequences for the fabrication of different design choices made for these models will be discussed in the next chapter.

3. Mechanical factors influencing the BBB

External stimuli have a big influence on the behaviour of cells, as explained in section 2.2. The flow of blood for example causes the endothelial cells to be sheared and stretched, which influences both morphology and physiology of the endothelial cells. The specifications of a microfluidic device will define the microenvironment of the cells. For instance the dimensions of the blood chamber determine the flow pattern of the medium and therefore the shear stress on the cells. In this section an overview, as complete as possible, of the factors influencing the blood-brain-barrier in vivo and in vitro is given, in order to set up the requirements for a new model.

3.1 Shear stress

3.1.1 Influence of shear stress in in vitro experiments

Vascular endothelial cells are subjected to shear stress, caused by blood flow. In vitro experiments from different studies show that subjecting endothelial cells to shear stress affects function and morphology. Ballermann et al.¹⁰ report a difference in response to acute and chronic shear stress. Sudden exposure to shear stress during seconds or hours is referred to as exposure to acute shear stress. The term chronic shear stress is used when endothelial cells are cultured under shear stress during days or weeks. Under chronic shear stress the level of shear stress can have acute alterations. Chronic shear stress is the normal in vivo situation. Acute shear stress can occur in vivo for example when a new vessel is formed or after temporary vessel occlusion. Acute shear stress causes activation of ion channels, remodelling of the cytoskeleton and gene transcription. Under influence of chronic shear stress the endothelial cells align themselves in the direction of the flow, actin microfilaments rearrange and increase in amount, and cells become flatter. Cells become bigger (hypertrophy) and more focal adhesion-associated proteins (for adhesion of the cells to the extracellular matrix) are present.

Cucullo et al.³⁴ found ‘a significant upregulation of tight and adherens junctions proteins and genes’ in a study with a coculture of normal human brain microvascular endothelial cells (HBMEC) and human astrocytes (HA) in a hollow fiber model. Subjecting endothelial cells to a level of shear stress of 6.2 dyne/cm² (shear stress was gradually increased from static condition to 6.2 dyne/cm² within ten days) resulted in a more tight and more selective BBB. After 30 days of culture under the influence of shear stress a TEER of 700 cm² was reached, where the culture under static conditions reached a TEER of only 100 cm². Booth et al.²¹ studied the effect on permeability of propidium-iodide and FITC-Dextran and cell morphology by exposing bEnd.3 cells to shear levels in the range of 1-86 dyne/cm² for 24 h. The permeability of both substances decreased with increasing shear stress. With increasing shear stress cells elongate more and align closer to the flow direction. See Koutsiaris⁶⁵ for an extensive summary of the effects of shear stress on brain endothelial cells.

Whereas the morphology of endothelial cells throughout the body is found to change significantly under the influence of shear stress, Reinitz et al.¹⁰¹ find that HBMECs resist these morphological changes. The behaviour of human umbilical vein endothelial cells (HUVECs) and HBMECs under influence of a shear stress ranging from 4 to 16 dyne/cm² is compared. HUVECs aligned and elongated in the direction of flow, but HBMECs did not. Reinitz et al.¹⁰¹ state that this suggests that HBMECs are programmed to resist elongation and alignment under shear stress.

From current models it appears to be difficult to grow endothelial cells in microchips which form a tight in vivo like blood brain barrier. In vivo endothelial cells are chronically exposed to a level of shear stress. Applying shear stress in vitro changes the EC morphology and physiology. The tightness of the BBB depends on the tight- and adherens junctions. Shear stress increases the expression of the pro-

teins forming the tight and adherens junctions. The TEER increases when shear stress is applied and permeability decreases with increasing shear stress. Since shear stress has such a big influence on the behaviour of endothelial cells it is desirable to mimic the in vivo level of shear stress in an in vitro BBB model.

3.1.2 Shear stress in vivo

No consensus is reached about the in vivo level of shear stress in the capillaries of the brain. Most authors assume values around 0.3-2 Pa^{132,142,64} referring to an article of Kamiya and Togawa⁶³, in which data from different studies is compared. In the article wall shear stress in capillaries in different parts of a rat and cats is estimated from the measured gradient of the pressure drop along a capillary assuming Poiseuille flow. In different parts of the arterial tree of different animals the blood flow velocity and lumen diameter was measured and from that the wall shear stress and apparent blood viscosity was calculated, assuming laminar flow. The wall shear stress level estimated in the different parts of the arterial tree fell around 1.5 Pa within a range of $\pm 50\%$. Kamiya concludes that the wall shear stress in the entire arterial system and the capillary beds is controlled at a constant level. However, Tangelder et al.¹²² showed that the velocity profiles in arterioles of rabbit mesentery are flattened parabolas rather than fully developed parabolas, using fluorescently labelled nanoparticles as velocity tracers in vivo. Reneman et al.¹⁰² measured the velocity profile in vivo in large arteries by using ultrasound and also found a more flattened parabolic velocity profile. Cheng et al.²⁹ performed a literature study on wall shear stress levels in different parts of the arterial system in humans and in different animals. The study shows that the level of shear stress in all straight vessels of the arterial tree is not constant and not approximately 1.5 Pa. The shear stress level also varies largely between species.

The commonly accepted level of wall shear stress in human brain capillaries is estimated assuming a fully developed parabolic velocity profile, using measurements in capillaries in the rat cremaster muscle, cat tenuissimus muscle and the cat mesentery. The measurements are performed in capillaries in a different part of the artery tree and in different species. However, the velocity profile is not parabolic but more flattened and the shear stress level differs throughout the arterial tree and across species. Reneman et al.¹⁰² The in vivo value of wall shear stress in human brain capillaries could therefore be different from what is commonly used.

Koutsiaris et al.⁶⁷ quantified the wall shear stress in the human conjunctival pre-capillary arterioles in vivo. During the cardiac cycle velocity, volume flow, wall shear rate and wall shear stress changes. Peak systolic, end diastolic and average values are measured and calculated. The best fit power laws for wall shear stress levels give in arterioles of 10 μm a peak systolic value of 4.5 Pa, an end diastolic value of 2.0 Pa and an average value of 3.2 Pa.

In another study of Koutsiaris et al.⁶⁶ the wall shear stress in human conjunctival capillaries and post-capillary venules, with diameters ranging from 4 to 24 μm , is determined. In the smallest capillaries a maximum value of 9.55 Pa was observed and in the largest post-capillary venules a minimum value of 0.28 Pa was observed. A best power law fit on the WSS calculation in the human conjunctival capillaries and post-capillary venules gives for small capillaries, 4 μm in diameter, an average wall shear stress of 6.41 Pa, and for large capillaries, 10 μm in diameter, an average wall shear stress of 1.51 Pa.

Shear stress values applied in BBB-on-chip models mostly do not reach the average levels determined in even the larger capillaries of 10 μm ⁶⁶. Booth and Kim²⁰ applied a shear stress value of 1.5 Pa, in all other models the shear stress does not go higher than 0.6 Pa. Cucullo et al.³³ reach a level of 1.63 Pa in their hollow fiber model. See section 3.1.2 for an overview of applied shear stress values.

In the absence of measurements in the brain capillaries the measurements for the human conjunctival capillaries will be used as an estimation of the wall shear stress in the brain capillaries. Therefore the level of wall shear stress applied in the in vitro model should be at least 1.51 Pa, as encountered in large capillaries of 10 μm , and could be as high as 6.41 Pa, as encountered in small capillaries of 4 μm .

Table 3.1: Shear stress values in in vitro models

	Shear stress (Pa)	Pulse
Hollow fiber		
Cucullo et al. ³³	1.63	pulsatile
Neuhaus et al. ⁹¹	0.27 - 0.39	pulsatile
BBB-on-chip		
Sellgren et al. ¹¹¹	0.5	constant
Booth and Kim ²⁰	1.5	constant
Griep et al. ⁵¹	0.58	constant
Yeon et al. ¹⁴⁹	0.028 - 0.819	constant

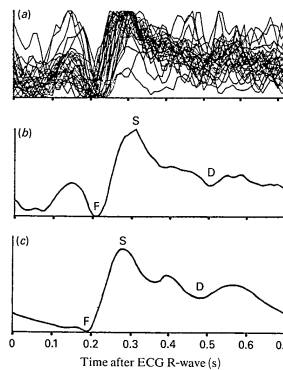


Figure 3.1: Figure and text from Williams et al.¹⁴⁰: Comparison between computerized superimposition (a) and averaging (b) of 34 capillary pulse waveforms and the radial artery pulse (c) in age-matched subjects. All timings are relative to the peak of the R-wave of the ECG. Capillary pressure = 32/25 mmHg; arterial pressure = 138/75 mm Hg. Abbreviations: F, foot of pulse wave; S, peak of systolic pulse; D, dicrotic notch

3.2 Intraluminal pressure and pulsatile flow

3.2.1 Intraluminal pulsatile pressure in vivo

Although blood pressure, blood flow and shear stress is pulsatile in vivo, no BBB-on-chip models, but only hollow fiber models, incorporate this pulsatile behaviour. No studies were found in which the pressure in the brain capillaries is calculated or measured. Williams et al.¹⁴⁰ and Shore et al.¹¹³ measured the capillary pressure in the finger nail fold, both using the same measuring technique. Williams et al. note that the mean capillary pressure differs per location, but found a pressure of 37.7 ± 3.7 mmHg in the arteriolar limb, 19.4 ± 1.0 mmHg in the apex limb and 14.6 ± 0.5 mmHg in the venular limb. In capillaries with high mean pressures also a high capillary pulse pressure amplitude (CPPA) was measured. The average CPPA was 3.6 ± 3.4 mmHg. The pulse wave form in 34 capillaries were superimposed and averaged, and compared to the blood pressure in the radial artery, see fig. 3.1. As can be seen, the shape of the capillary pressure waves and the shape of the pressure wave in the radial artery comply well. Shore et al. measure the capillary pressure (location at capillary is not specified) in men and women younger and older than 50 years. In these four groups capillary pressures between 15.0 ± 2.4 mmHg and 18.4 ± 2.0 mmHg and CPPA between 4.0 ± 3.0 mmHg and 6.4 ± 2.8 mmHg were measured. In this literature study the average intraluminal pressure in vivo is assumed to be 19.4 mmHg with a CPPA of 3.6 mmHg, the value found in the apex limb of a capillary in the nail fold¹⁴⁰.

3.2.2 Intraluminal pressure in in vitro experiments

Sato and Ohashi¹⁰⁸ reviewed research on the effect of shear stress and hydrostatic pressure on cell morphology and cytoskeletal structure. Under influence of shear stress it seems like first stress fibers, large bundles of actin filaments, appear along the cell long axis and then cells elongate and align in the direction of the flow. Sato et al.¹⁰⁹ reported that endothelial cells (ECs) become stiffer when fluid flow is applied. In both circumstances, shear stress and hydrostatic pressure, the area of the cells decreases. Under influence of hydrostatic pressure (100mmHg) cells show elongation and orientation, as when shear stress is applied, but in random directions. The tortuosity index of the cells (P/P' , where P is the cell perimeter and P' the equivalent ellipse perimeter of the cell) increases when exposed to pressure. ECs form multilayered structures with less VE-cadherin expression. Adherens junctions are mainly composed of VE-cadherin and other transmembrane glycoproteins of the cadherin superfamily¹²¹. In the control

cells VE-cadherin was found at the entire periphery of the cells, whereas under hydrostatic pressure only (100mmHg) VE-cadherin was found 'sparsely distributed' at the periphery. VE-cadherin simultaneously contributes to inhibition of cell growth and stimulation of cell proliferation. A decrease of VE-cadherin expression may cause morphological changes and the formation of stress fibers, which are important for cell adhesion, via the protein family Rho. See Sato and Ohashi¹⁰⁸ for the suggested underlying mechanism.

Multilayering has not been found to occur *in vivo*. Sato and Ohashi¹⁰⁸ suggest that multilayering under hydrostatic pressure is caused by vascular endothelial growth factor (VEGF). VEGF-2 expression is pressure sensitive and VEGF induces EC proliferation, migration and differentiation and also 'stimulates dephosphorylation of catenins, which is associated with vascular endothelial- (VE-)cadherin and localize to adherens junctions.' When a confluent monolayer is formed ECs do not grow further. Proliferative signals of VEGF influence confluent ECs marginally. Sato and Ohashi¹⁰⁸ conclude that the combined effect of shear stress and hydrostatic pressure alters the role of VEGF on ECs.

Vozzi et al.¹³⁵ measured the release of nitric oxide (NO) and endothelin-1 (ET-1) after subjecting endothelial cells to various levels of shear stress and hydrostatic pressure. In the pressure experiments a pressure of 70 mmHg was imposed and no flow, in the control experiment a pressure of 0 mmHg and no flow was imposed. Imposing pressure resulted in down-regulation of ET-1 production compared to the control experiment. No significant changes in NO level or cell morphology were observed.

Vozzi notes that NO and ET-1 act on the smooth muscle cells forming the outside of a vessel. These muscle cells are not present in capillaries, but not all functions of NO and ET-1 are known. Eibl et al.⁴⁰ administered ET-1 and ET-1 receptor antagonist to animals with induced pancreatitis (inflammation of the pancreas). The capillary permeability in the pancreas increased significantly in the group that received ET-1. ET-1 receptor blockade caused a significant decrease in capillary permeability. This effect might also be present in brain capillaries.

3.2.3 Intraluminal pressure and shear stress combined in *in vitro* experiments

Sato and Ohashi¹⁰⁸ compared cells exposed to hydrostatic pressure (100mmHg), shear stress (2 Pa), a control group with no pressure or shear stress exposure and the two factors combined (100 mmHg and 3 Pa). The ECs in the first three groups are described in section 3.2.2. Imposing both shear stress and hydrostatic pressure resulted in elongated cells aligned with the direction of the flow. The distribution of VE-cadherin at the periphery of the cells was uniform. The combination of shear stress and pressure did not result in multilayering.

3.2.4 Intraluminal pulsatile pressure in *in vitro* BBB models

Cucullo et al. and Neuhaus et al. mimic pulsatile behaviour in their hollow fiber models. In both studies the CellMax @QUAD Artificial Capillary Cell Culture System is used to generate a pulsatile flow. Neuhaus et al.⁹¹ do not specify the height of the intraluminal pressure over time, only an average flow rate of 14 ml/min and a shear stress between 2.7 and 3.9 dyne/cm² (written is dyne/m², but I assume dyne/cm² is meant). Cucullo et al.³⁵ show the shape of the blood pressure before entering a module of three hollow fibers, see figure, and note that the CellMax mimics 60 beats/min. The systolic like pressure before entering is approximately 70 mmHg, when leaving it amounts approximately 25 mmHg. The shape of the intraluminal pressure looks more damped after leaving compared to the shape before entering. Within the capillaries a pressure of 25.5 mmHg is noted. The pressure varies with about 75 mmHg before the capillaries and about 30 mmHg after the capillaries. It is noted that a pumping mechanism is used which allows to establish different pulsatile rates. However, experiments where different pulsatile rates are compared are not reported.

In the research of Neuhaus et al.⁹¹ the pulsatile rate and pressure is not specified. It is noted that an average flow rate of 14 ml/min is used, which causes a shear stress between 270 and 390 mN/m². No variations in pulsatile rate were made, but it is assumed that the pulsatile flow causes 'morphological

change of PBMEC/C12 from polygonal form in bi-dimensional models to an elongated form’.

From these papers the influence of pulsatile versus continuous flow can not be determined, since the different flow types are not studied separately.

3.2.5 Conclusion

From the studies mentioned above it becomes clear that hydrostatic pressure has a significant influence on the cell behaviour. Imposing hydrostatic pressure only and no shear stress causes the cells to elongate in random directions, the cells become more tortuous, multilayers are formed instead of monolayers, VE-cadherin expression, important for adherens junctions, becomes lower and ET-1 production, possibly influencing capillary permeability, is down-regulated. When hydrostatic pressure is applied in combination with shear stress, the cells align in the direction of the flow, which induces the shear stress, VE-cadherin is distributed uniformly and the endothelial cells form a monolayer.

Studies on the effect of pulsatility of the blood flow are not found. In two studies a pulsatile flow is imposed on the endothelial cells in a hollow fiber model. However, the results are not compared with the results from a model where a continuous flow is used. Therefore it is difficult to draw a conclusion about the role of pulsatility in cell behaviour.

In a new BBB model a physiological relevant level of hydrostatic pressure should be imposed in combination with shear stress, because of the influence it has on the cell behaviour. The flow will not be pulsatile, since no information is available on the influence of pulsatility of the medium flow and studying the influence is beyond the scope of this study.

3.3 Flow pattern in rectangular channels

Van der Helm et al.¹³² point out the relevance of the dimensions of the channels in which the fluid flows across the endothelial cells. Blood vessels have circular cross sections and therefore the wall shear stress will be uniform along the wall. Most BBB-on-chip models make use of rectangular channels, which causes a non-uniform shear stress along the wall. The shear stress at the edges will be lower than in the middle of the channel. Since shear stress has a major influence on the morphology and function of the endothelial cells, the behaviour of the cells will vary along the width of the channel. Next to that, medium with substances for permeability analyses will flow slower in the edges, which result in a longer retention time in the edges. The aspect ratio h/w defines the flow pattern of the fluid. The wall shear stress can be approximated for Newtonian fluids as a function of the width, w and height, h of the channel and flow rate, Q :^{115,132}

$$\tau_w = \frac{6\mu Q}{wh^2} \left(1 + \frac{h}{w}\right) f^* \left(\frac{h}{w}\right) \quad (3.1)$$

With μ the viscosity of the fluid and $f^*(\frac{h}{w})$ a function with a sum of infinite series. The function f^* approaches 1 when h/w approaches 0. This means when h/w approaches zero, the wall shear stress becomes: $\tau_w = \frac{6\mu Q}{wh^2}$. The fluid velocity profile of a rectangular channel can be approximated as follows¹³⁴:

$$\frac{u_{x,y}}{u_{max}} = \left[1 - \left(\frac{2x}{h}\right)^2\right] \left[1 - \left|\frac{2y}{w}\right|^m\right] \quad (3.2)$$

with u_{max} the maximum velocity and m according to:

$$m = \sqrt{2} \frac{h}{w} + 0.89 \frac{w}{h} \quad (3.3)$$

From eq. 3.2 we see that the smaller the ratio $\frac{h}{w}$ gets, the flatter the fluid velocity profile gets.¹³² Van der Helm et al.¹³² plotted the flow profiles for different aspect ratios and included the aspect ratios used in the models of Prabhakarbandian et al.⁹⁹ and Booth and Kim¹⁹, see fig. 3.2.

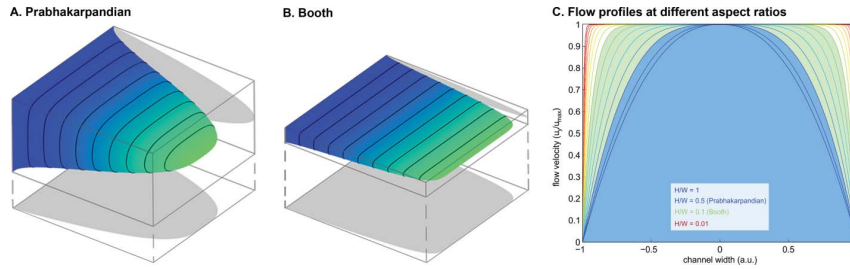


Figure 3.2: Flow profiles inside the BBB chip of Prabhakarparandian et al.⁹⁹ (A) and Booth and Kim¹⁹ and at different aspect ratios (C), modeled with `Matlab` R2013a. The endothelial cells are cultured at the bottom surface of the depicted channel. Figure and description reproduced from van der Helm et al.¹³²

It is clear that the variation in shear stress on the cells in the width of the channel in Prabhakarparandian's model is a lot higher than in Booth's model. To make sure the shear stress on the endothelial cells is distributed uniformly when using a rectangular channel, the channel should be sufficiently wide compared to the channel height.

3.4 Curvature

The endothelial cells in most microfluidic models are cultured on a flat surface, whereas in a capillary the endothelial cells are curved to form a tube. Ye et al.¹⁴⁷ investigated the effect of curvature on HBMECs and human umbilical vein endothelial cells (HUVECs) under the influence of shear stress by seeding the cells on glass rods with diameters ranging from 10 to 500 μm . The morphology of HUVECs appeared to depend on curvature a lot more than HBMECs. HUVECs elongate and align increasingly in opposite direction of curvature with decreasing diameter, i.e. with increasing curvature. HBMECs respond to increasing curvature only slightly with changing morphology. Ye et al.¹⁴⁷ suggest that HBMECs are programmed to resist elongation in response to curvature (and shear stress) and pose the hypothesis that the HBMECs 'evolved to minimize the length of tight junctions per unit length of capillary and hence minimize paracellular transport into the brain'.

To conclude: Publication on the influence of curvature on barrier function have not been found, but morphological changes and a difference in response to curvature between HBMECs and HUVECs has been shown. It could be interesting to design the device such that the membrane is curved, such that the influence of curvature on permeability and TEER could be studied. However, the focus of this project is not on studying different factors on endothelial cell function, so for the moment curvature will be neglected, but could be considered at a later time.

3.5 Permeable membrane

3.5.1 Protein coating

The basement membrane is a 30-40 nm thick⁸⁵ sheet of extracellular matrix, which consists of molecules secreted by cells. The basement membrane gives structural support to endothelial cells and regulates communication between different cells in the neurovascular unit. It consists of molecules secreted by endothelial cells and brain parenchyma cells, summarized by Baeten and Akassoglou⁹ as "structural elements (e.g., type IV collagens and elastin), specialized proteins (e.g., laminins, entactin/nidogen, fibronectin, and vitronectin), and proteoglycans (e.g., heparan sulfate proteoglycans (HSPG) perlecan and agrin". For an extensive overview of the functions and variations of these proteins, see Baeten and Akassoglou⁹. Endothelial cells are anchored to the basement membrane with focal adhesion points. Focal adhesion points mainly consist of integrins, which are, directly or indirectly via linker protein, connected to the proteins in the basement membrane.¹⁵²

To enhance cell adhesion, devices are coated with ECM proteins. In most models a fibronectin coating is used. However, other proteins or protein mixtures might result in tighter barriers.

Tilling et al.¹²⁴ investigated the influence of various ECM proteins on barrier function by culturing porcine brain capillary endothelial cells on filter inserts coated with laminin, fibronectin, collagen IV or 1:1 composition of these proteins. Different culture preparations were tested. Preparation yielding a low TEER ($\sim 350 \Omega\text{cm}^2$) on rat tail collagen used as reference yielded a 2.3 to 2.9 fold higher TEER, reference preparations yielding a higher TEER ($\sim 1000 \Omega\text{cm}^2$) on rat tail collagen yielded a 1.1-1.2 fold increase in TEER when using the different coatings. A 1:1 fibronectin/laminin coating performed best. Also SPARC, secreted protein acidic and rich in cysteine, was tested in combination with collagen IV, but here the presence of SPARC decreased the TEER value of the cell culture.

Yao et al.¹⁴⁶ found that the absence of astrocytic laminin (laminin-111 and -211) in mice induces pericyte function to change from BBB stabilizing to BBB compromising.

In short, different proteins in the basement membrane have a significant effect on BBB-function. Tilling et al.¹²⁴ found that from the coatings they tested, a 1:1 fibronectin/laminin coating performed best. The use of this coating is therefore desired in the BBB-glioblastoma device.

3.5.2 Membrane material and pore size

The models in table 2.1 mostly use polycarbonate (PC) membranes with small pore sizes, 0.4 microns or even smaller. Wuest et al.¹⁴⁵ compare membranes with different pore sizes (0.4, 1.0, 3.0 and 8.0 microns), materials (PC and polyethylene terephthalate (PET)) and manufacturers for culturing of primary murine BMEC, in monoculture and in contact and non-contact coculture with primary mouse astrocytes, and b.end3 monocultures. TEER measurements, permeability assays and tight junctions protein staining were used for characterization.

Membranes with a pore size of 0.4 μm , yielded a significant higher TEER and lower permeability than the membranes with larger pores. At 1.0 μm cytoplasm is observed in the pores, at 3.0 and 8.0 μm an extra monolayer was observed on the bottom side of the membrane. Using the three larger pore sizes, also overlapping cell growth was observed.

PET membranes from three manufacturers resulted in significant higher TEER values and lower permeability than PC membranes from Corning. For the BMEC cells a PET membrane from BD Falcon resulted in the highest TEER and lowest permeability, for b.End3 cells a PET membrane from Corning performed best in terms of TEER and permeability. Finally Wuest et al.¹⁴⁵ note that the translucent Corning and BD Falcon membranes made visualization of the the cells under light microscope possible as opposed to the transparent Corning PC and Millipore PET membranes.

Sellgren et al.¹¹¹ compared polyethylene (PE) and polytetrafluoroethylene (PTFE) membranes in a microfluidic device culturing b.End3 cells in coculture with C8D1A (astrocytes). The devices with both membranes withstood 4 days of shear stress without leaking. However, the cells on the PE membranes did not show claudin-5 expression and the cells were peeled off at 5 dyne/cm².

In summary, a PET membrane with 0.4 μm pores performs best compared to PC membranes and larger pore sizes. Literature about the performance of PTFE compared to PET or PC are not present, therefore a PET membrane with 0.4 μm pores will be the preferred material in terms of biocompatibility in this study. If needed because of fabrication limitations the material of the membrane could be changed to PC. However, the pores of the membrane should not exceed 0.4 μm , since membrane with larger pores will not result in endothelial cell monolayers.

3.6 Conclusion

To conclude, many factors influence endothelial cell functions. Some of these factors are known, other are not understood or known yet. Shear stress is a well known factor influencing endothelial cell function. In

some models therefore shear stress is applied. However, only in the BBB-on-Chip device of Booth and Kim²⁰ the lower limit of shear stress in large capillaries in vivo is reached, namely 1.5 Pa. In our model the goal in terms of wall shear stress applied will be 1.5-6.4 Pa, based on the levels of wall shear stress found in human conjunctival capillaries.⁶⁶

The effect of pulsatility of the flow is not known, the flow will therefore be kept constant. Applying hydrostatic pressure does have an effect on cell morphology and physiology. Barrier function of the endothelial cells is not investigated, but could be influenced by the morphological and physiological changes under hydrostatic pressure. It is therefore desirable to design the device such that a hydrostatic pressure level of 30 mmHg can be withstood. This value is based on the pressure in the apex limb of a capillary in the nail fold found by¹⁴⁰ and by taking a margin into account.

The ratio between the width and height of the channels should be high enough to prevent low shear stresses at the sides of the channel. Finally some requirements on the permeable membrane are found. To prevent endothelial cells to penetrate into the pores of the membrane, the diameter of the pores should be no larger than 0.4 μm . To stimulate cell adhesion and proliferation some materials in combination with protein coatings are preferred over other. Especially PET appears to perform well, but PC is also a good and often used candidate. Protein coatings are necessary to allow for cell adhesion, in a comparative study a 1:1 preparation of laminin and fibronectin performed superior to preparations with different ratios and proteins.

In chapter 4 the information found in this chapter and chapter 2 will be summarized by means of a list of requirements.

4. Requirements

In this chapter the demands on the BBB-on-Chip model of the Radiation Science & Technology department, the intended user, and the conclusions drawn in chapter 2 and chapter 3 are used to compile the requirements for the BBB-on-Chip model. Except for the first set, section 4.1, which are the initial questions of the user, the requirements are organized by the different functionalities it should fulfil.

4.1 Layout of the BBB-on-Chip

A model is desired to study drug transport from blood to a tumor in the brain and to study the effect of tumor growth. The drugs, nanocarriers, should be followed by fluorescently labelling them. Hereto a BBB-on-Chip model will be designed which should consist of:

<i>Blood channel</i>	Represents a capillary in the brain, medium replaces blood
<i>Brain channel</i>	Represents the brain and can hold a glioblastoma spheroid
<i>Permeable membrane</i>	A permeable membrane on which endothelial cells will be cultured should separate the two channels to construct the blood-brain barrier
<i>Fluidic inlets and outlets</i>	Both channels should have an inlet and outlet to administer medium with nutrients and fluorescently labelled nanocarriers to the blood channel and collect medium from the brain channel to evaluate transport through the blood-brain barrier using a fluorimeter.

4.2 Cell culturing

The cell culturing conditions should be as close as possible to the *in vivo* situation to achieve a monolayer of endothelial cells which function as similar as possible as *in vivo*. From chapter 3 the following requirements are added:

<i>Biocompatibility</i>	Since cells and medium come into contact with the device material, it should be bio-compatible to obtain good viability of the cells and no significant interaction between the material and the cells and medium compounds.
<i>Wall shear stress (WSS)</i>	The WSS exerted on the endothelial cells should be between 1.5 and 6.4 Pa WSS should be uniform along the membrane width, to ensure similar culture conditions along the membrane width
<i>Hydrostatic pressure</i>	A pressure of 30 mmHg in the blood channel of the device should be withstood
<i>Permeable membrane</i>	Membrane pore diameter cannot be bigger than 0.4 μm , to avoid penetration of the endothelial cells into the pores The membrane should be coatable with proteins, e.g. laminin and fibronectin to stimulate cell adhesion and proliferation
<i>Permeability</i>	Oxygen and carbon-dioxide levels should be maintained as <i>in vivo</i> . This could be accomplished by controlling the concentration of the gases in the medium or, when the permeability of gases through the material is high enough, by controlling the concentration of the gases in the atmosphere where the device is placed. The permeability to water vapor should be low enough to avoid high fluctuations in medium osmolarity and volume.

Sterilization Before culturing, the device needs to be sterilized to avoid contamination of the cells.

4.3 Testing barrier function

The endothelial cells will be seeded and grow to confluency, the moment when drug testing is possible. To efficiently evaluate confluency and functioning of the endothelial cells, TEER measurement should be performed intermittently. Next to that, it should be possible to check the endothelial cells visually. This gives the following requirements:

Electrodes Electrodes should be integrated directly above the membrane in the blood channel and below the membrane in the brain channel
Electrode material should be transparent to allow for visual inspection of the cells

Transparent material Transparent device material to allow for visual inspection of the cells

4.4 Testing drug transport

Drug transport can be tested in different ways, quantitatively, by counting labeled nanocarriers in the brain channel using a fluorimeter, and qualitatively, by fluorescent imaging of the device to locate the nanocarriers in the device. The size of the to be tested nanocarriers is 80-100 nm. Exceptionally they could be 200 nm. The nanocarriers are hydrophilic.

Permeability membrane Permeability of the empty membrane to the nanocarriers should be high to minimally influence transport through the blood-brain barrier

Autofluorescence materials Low autofluorescence of the materials used to avoid noise during fluorescent imaging

4.5 Testing the effect of drugs on tumor growth

The glioblastoma spheroids to be tested need to be cultured for five to seven days before the drugs are added, this can be inside or outside the device. The diameter of the spheroid at the start of the experiments is 400-500 μm . The therapeutic effect of the drugs on the spheroids will be tested for two weeks, after two weeks the diameter of the spheroids will be maximally 600 μm . The spheroids are very brittle and should not fall apart before experiments are finished. After two weeks the spheroids are sliced to inspect the necrotic core. Hereto the spheroids need to be removed from the device either by disassembling the device or cutting out the spheroid. Since the experiments inside the device take more than two weeks (first culturing endothelial cells, next two weeks of tests) the endothelial cell culture should last for more than two weeks on the membrane.

Dimensions brain channel Minimum width and height of the brain channel below the membrane is 700 μm , such that a maximally grown spheroid can be reached by the drugs from above and from the sides.

Flow in brain channel No high flow around the spheroid is allowed to prevent the spheroid from falling apart

Spheroid removable Glioblastoma spheroid should be removable from the device after experiments

Biocompatibility Device and membrane materials suitable for long term cell culturing (two weeks), which is not necessarily the case for all 'biocompatible' materials

4.6 Fabrication

The BBB-on-Chip model is intended to be used for high throughput drug testing. However, first different prototypes need to be fabricated to come to an optimal design. For this reason production should be efficient for small quantities. In prototyping the use of molds is not desirable if fabrication of the mold is not very efficient, since small changes need complete new molds. The fabrication of the prototype should be possible at the TU or partners. Eventually the device should be fabricated in high quantities, so production scale-up should be possible.

<i>Fabrication technique</i>	The material should be suitable for machining with the available micro-fabrication methods. A low surface roughness for optical imaging should be obtainable with the technique used.
<i>Bonding</i>	Techniques should be available to properly bond the different parts of the device, the microfluidic channels, membrane, electrodes and in and outlet tubes, to each other such that there will be no leakage. The bonding technique should not oppose the bio-compatibility of the device.
<i>Efficient prototyping</i>	Since iterations are assumed to be needed to come to an optimal design, efficient production for singular devices is desired.
<i>Scale-up possible</i>	The design should be suitable for scale-up to mass production

5. Fabrication techniques and material

In the following chapter it is determined which fabrication techniques and materials will be used for the production of the BBB-on-chip prototype. Hereto first a description of how current BBB-on-chip models are fabricated, using PDMS in combination with soft lithography, and what the advantages and disadvantages are of the fabrication method and material. Available alternative fabrication methods will then be described in section 5.3 and next in section 5.4 the advantages and disadvantages of three polymers in combination with the alternative methods will be investigated. Since the physical properties of polymers are important for the different fabrication techniques and polymer related terminology is used throughout this chapter, the chapter starts with an introduction to polymers.

5.1 Introduction to polymers

The main structures of microfluidic devices are mostly made out of polymer. A huge amount of different polymers exists, varying greatly in chemical, mechanical, electrical and optical properties and suitable for different fabrication methods. A polymer consists of chains of repeating smaller molecules, monomers. The chains are linked to each other with H-bonds, van der Waals bonds, covalent bonds or they are mechanically intertwined. The chains are linear, branched, cross-linked or form networks when the monomer can react with other monomers on three instead of two points.¹²

A way to classify polymers uses the characteristic temperatures T_g , the glass transition temperature, HDT, the heat distortion temperature and TD, the decomposition temperature. Below the glass transition temperature a polymer behaves like an amorphous solid. Above T_g the polymer shows rubbery behaviour, it softens and is flexible. Enough energy is present to overcome the forces between the polymer chains when a force is exerted, parts of the chains (20-50 atoms long) are able to slide along each other. The HDT is determined as the temperature at which a polymer will show a certain measure of distortion under a given load. Practically it describes the maximum temperature for structural use of the polymer. Heating even further the decomposition temperature TD will be reached, where the polymer chains are irreversibly broken.¹²

Using these characteristic temperatures, polymers can be divided in three classes^{12,90}:

Thermosets

Thermosets are formed out of resins, which are liquid or in soft solid state. When heated, exposed to radiation or mixed with a catalyst or hardener the polymer chains cross-link to form a network polymer, by forming covalent bonds. After curing thermosets are hard and brittle. Curing is irreversible, when heated the thermoset will not become soft and flexible. Thermosets have high glass temperatures, which lay close to their decomposition temperature. In microfabrication thermosets are used as resist material in lithography. For example SU-8 is used in photolithography.

Thermoplastics

Thermoplastics have few cross-links and soften when heated to T_g . The distortion temperature TD is a lot higher than T_g . The changes in material behaviour when cooling and heating are reversible, although every cycle the material will degrade to some degree. At temperatures between T_g and TD the material can be reshaped using for example injection molding or hot embossing. Thermoplastics often used in microfabrication are for example polycarbonate (PC) and poly(methyl methacrylate) (PMMA). In microfluidics often cycloolefin polymer (COP) and cycloolefin copolymer (COC).

Elastomers

Elastomers have long chains, which are mechanically entangled and have few cross-links. When a force

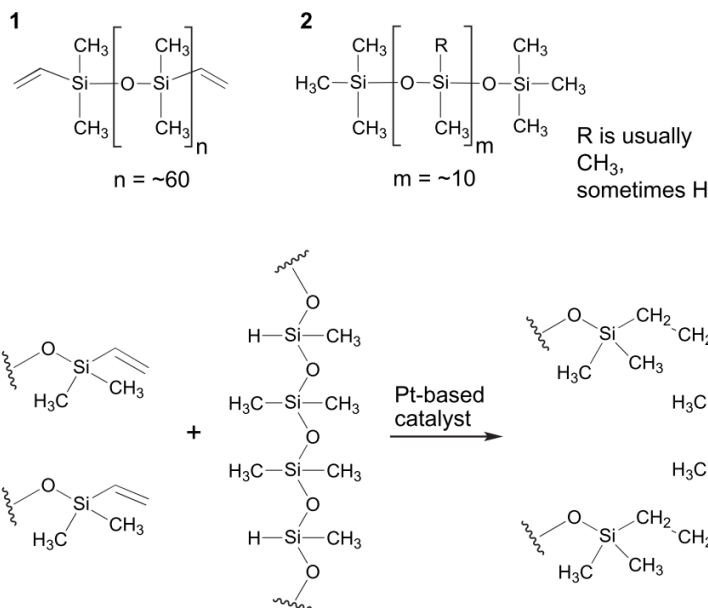


Figure 5.1: Cross-linking reaction. 1 Vinyl ended oligomers, 2 Cross-linking oligomers. Adapted from Campbell et al. ²⁴

is applied the chains which are coiled up and entangled randomly, align in the direction of the applied force, the material can elongate multiple times its original length. When the force is removed the chains get back to their equilibrium configurations by forming cross-links and the elastomer gets in its original shape immediately. Elastomers have a low rate of crystallinity and exist above their glass transition temperatures. An often used elastomer in microfluidic devices is poly(dimethylsiloxane) (PDMS).

Different properties are important for the selection of the materials to fabricate the microfluidic channels, which include:

5.2 State of the art: PDMS and soft lithography

Current BBB-on-Chip models are all fabricated out of PDMS, sometimes in combination with glass. Poly(dimethylsiloxane), $\text{CH}_3[\text{Si}(\text{CH}_3)_2\text{O}]_n\text{Si}(\text{CH}_3)_2$, exists in different forms, such as fluid, elastomer or resin. ¹⁴⁴ Microfluidic devices out of PDMS are typically fabricated using soft lithography. Hereto first a mold is made typically by etching in a layer of SU-8 photoresist on silicon. The PDMS is then poured on the obtained negative mold. Mostly the kit Sylgard 184 from Dow Corning is used, which consists of a base (resin) and a curing agent. The base contains vinyl ended oligomers, a platinum based catalyst and silica fillers, the agent contains the same vinyl ended oligomers and cross-linking oligomers. The cross-linking oligomers are shorter ($n = \sim 10$) than the vinyl ended oligomers ($n = \sim 60$) and have at least three silicon-hydride bonds instead of a silicon-methyl bond. ²⁴

Base and agent are typically mixed in a 10:1 ratio. The catalyst and the application of heat inhibit the addition of the silicon-hydride bond to the vinyl groups, which is called hydrosilation, see fig. 5.1. ²⁴ Curing at 25°C will take approximately 48 h, at higher temperature curing will be faster. At 150°C for example it takes about 10 minutes. ³¹

In the following section the most important advantages and drawbacks of PDMS will be discussed.

5.2.1 Fabrication throughput

The fabrication of PDMS microfluidic devices using soft lithography is especially useful for the production of prototypes. It is a fast and cheap method when small volumes of devices are being fabricated. As described above, curing PDMS at low temperatures can take up to two days, at high temperatures (150°C) it takes about 10 minutes. All this time the mold cannot be used for the next device. PDMS in combination with soft lithography is therefore not suitable for high-throughput fabrication.

5.2.2 Bonding and hydrophobicity

The surface of PDMS is hydrophobic. To make the surface suitable for bonding with different materials or to allow for cell attachment, the surface should be treated to become hydrophilic. One method is to expose the surface to oxygen plasma. During plasma treatment hydrophilic Si-CH₂OH and SiOH groups are formed at the surface at the place of Si-CH₃ groups. The hydrophilic surface is now ready for bonding with various materials. Wu et al.¹⁴⁴ sums up materials bonded in different studies: PDMS, glass, silicon, PSG, USG, Si₂NH₄ and SiO₂. In contact with another plasma treated PDMS surface, the hydroxyl groups will form Si-O-Si bonds. Plasma treatment using other gases enables bonding with even more materials: 1:2 Argon:Oxygen for bonding between PDMS and PETG, COC and PS, SF₆:N₂ for bonding with parylene. Many more bonding techniques are investigated with various materials, see Rezai et al.¹⁰³ for an extensive overview.

The PDMS surface will not remain hydrophilic permanently. Uncross-linked oligomers will diffuse to the surface and cause 'hydrophobic recovery' within a week.⁴⁷ When the surface of the microfluidic channels needs to be hydrophilic during cell culture, hydrophobic recovery restricts the duration of the experiments and causes a short shelf life.

Hydrophobicity of the surface is also greatly reduced by applying ECM coatings or with charged molecules like poly-D-lysine. The effect of different ECM coatings on cell behaviour is discussed in section 3.5.1.

5.2.3 Bio-compatibility

PDMS is mostly assumed to be bio-compatible. However, some studies raise objections.^{106,15} Sylgard 184, but also RTV-615 from Momentive Materials, also used for microfluidic devices, both contain irritants such as xylene and ethylbenzene. According to Halldorsson et al.⁵⁵ the effects of these irritants on cell cultures is unknown. Furthermore, after curing uncross-linked oligomers will still be present in the bulk material¹⁰⁰. The uncross-linked oligomers diffuse through the material to the surface. Regehr et al.¹⁰⁰ showed that the oligomers were present in water which was incubated for 24 hours in microfluidic channels made of PDMS. Also after Soxhlet extraction using ethanol, oligomers were still present. Normal mouse mammary epithelial cells were cultured in microfluidic devices with and without the Soxhlet extraction. In both cases oligomers were found in the cell membranes, but in a lesser extent in the channels that underwent the Soxhlet extraction before culturing. The effect of oligomers on cell behaviour is unknown. The leaching of oligomers can be reduced by first extracting the oligomers with a solvent. However, these solvents need to be removed before culturing as well. Lee et al.⁷⁰ tested the rate of extraction of various solvents.

PDMS is hydrophobic, very permeable and prone to absorb small hydrophobic molecules. Wang et al.¹³⁷ show a correlation between $\log P$ value and absorption by PDMS, by studying the absorption of five molecules with different $\log P$ values. Molecules with $\log P < 2.47$ show small absorption by PDMS and molecules with $\log P > 2.62$ extensive absorption. The absorption by PDMS of hydrophobic compounds in the culture media or cell signalling agents excreted by the cells in culture could influence cell behaviour. Indeed, Regehr et al.¹⁰⁰ found that estrogen signaling is inhibited in MCF-7 cells when cultured directly on PDMS, which could be explained by a reduced availability of estrogen, which is absorbed by the PDMS substrate. Also drugs could be absorbed by PDMS, which could cause inaccurate information

about the concentration of drugs, the nanocarriers in our case, provided to the cells. Predicting the absorption to compensate for the absorption is difficult according to Toepke and Beebe¹²⁵, since they found a pH dependence in the amount of absorption by PDMS in their study on the uptake of Nile red by PDMS.

So, if PDMS is used to fabricate the microfluidic channels, first it should be studied to what extent the nanocarriers will be absorbed by PDMS and if this could influence drug tests.

As a solution, Halldorsson et al.⁵⁵ list different studies (Gomez-Sjoberg et al.⁴⁹, Abate et al.³, Orhan et al.⁹⁷) which report on treatments to reduce the absorption of small molecules by PDMS. However, they also note that the effects of these treatments on cell cultures should still be tested first.

PDMS has a very low Young's

5.2.4 Permeability

High O₂ and CO₂ diffusion rates are often noted as beneficial characteristics of PDMS to achieve sufficient exchange of these gases between the medium inside the device and the environment in which the device is located. In our case, the medium inside the BBB-on-Chip model will continuously flow through the channels, so it might not be necessary to regulate the gas concentration in another way than by controlling the concentrations in the medium before it enters the device.

Besides to gases, the permeability of PDMS to water vapor ($\sim 1000 - 6000 \mu\text{m}^2/\text{s}$) is also very high. The amount of medium in a microfluidic device is very low, evaporation of water could therefore have a big influence on volumes, concentrations, chemical balance and other factors. This is mainly a problem in cultures under static conditions, such as in the tumor compartment in this study.¹⁵ These factors should be kept as stable as possible for accurate test results and steady cell cultures. To prevent evaporation, a parylene coating could be applied⁵⁶. Another method could be placing the device in an isoosmotic bath⁶⁹.

Surface modifications by plasma treatment, applying coatings and the adsorption of proteins changes the permeability of PDMS to gases and water vapor, but precisely to what extent is unknown.⁵⁵ Only the effect of plasma treatment on oxygen diffusivity has been studied before. Markov et al.⁸¹ This makes it difficult to predict what will happen to medium volume, osmolarity and gas concentrations during experiments and to anticipate during the design of the device.

In short, the high permeability of PDMS to gases makes it possible to control the gas concentrations within the medium via the concentrations in the surrounding air of the device, but this might not be relevant in our case because of the continuous refreshing of medium. However, the high permeability to water vapor could cause harmful fluctuation in medium osmolarity and volume. Different methods exist to prevent water evaporation, but induce extra steps in the production or experiments.

5.2.5 Optical properties

PDMS has a low autofluorescence and is optically transparent. The refractive index of PDMS is 1.41-1.43 in the visible light spectrum.⁹⁸ PDMS is therefore suitable for optical imaging and fluorescence microscopy.

5.2.6 Conclusion

The use of PDMS comes with many advantages. Soft lithography is a simple process without the need of special equipment that is not already present in most laboratories. To start with, different prototypes need to be fabricated. It is therefore practical if small changes to the design of the device can be easily made. For PDMS no complex molds or expensive equipment is needed, which makes the fabrication of prototypes economically and time efficient. The material is transparent and has a low autofluorescence,

which makes it suitable for optical and fluorescent imaging. Procedures for adequate bonding of PDMS with another PDMS surface and many other materials are available. PDMS is highly permeable to O_2 and CO_2 , which makes the control of the concentration of these gasses in the medium during cell culture very simple.

However, the following disadvantages direct to search for different techniques and materials: The PDMS surface is hydrophobic, treatments exist but the hydrophobicity of the surface recovers quickly, completely within a week, such that before use after storage treatments have to be performed to reduce hydrophobicity. The bio-compatibility of PDMS is controversial. In general PDMS is assumed to be bio-compatible, but uncrosslinked oligomers can be found in cells cultured on PDMS and hydrophobic compounds in medium or excreted by cells are absorbed by the material, which influences cell culture experiments. Where the high permeability to O_2 and CO_2 could be beneficial, the high permeability to water vapor could adversely affect cell culture experiments, since it causes fluctuations in medium osmolarity and volume. Treatments exist to limit the absorption of hydrophobic compounds and water vapor permeability, but these cause extra production steps and effects on cell cultures are not known for all treatments. Eventually the aim is to design a device which can be used for high-throughput testing. Therefore, the design should be suitable for scale up to bulk production, but this is not the case for PDMS in combination with soft lithography.

5.3 Alternative fabrication techniques

In the following section four fabrication techniques suitable for machining of thermoplastics are given. The advantages and disadvantages of these methods in combination with different materials are discussed in section 5.4. Injection molding is only suitable for higher production quantities, since relatively complex molds are needed. For commercial production quantities the use of injection molding is the best economic choice. Although injection molding will not be used in this project, it is desirable to produce a prototype which is suitable for injection molding as well, such that eventually it could be produced in large quantities efficiently. For the production of the prototypes hot embossing, laser ablation and micro-milling are considered.

5.3.1 Injection molding

Injection molding is a replication process which is cost effective for high production quantities. This process will not be used for the fabrication of prototypes, but scale-up could be desirable in a later stadium.

During injection molding polymer in granulate form is transported into a screw, in which the polymer is heated above the melting temperature and consequently compressed. The polymer is then injected into the mold by a translatory movement of the screw. The molding tool is designed such that demolding is an automated process. Because of this, the starting costs are relatively high, but the cycle times, between a few seconds to ten minutes, are very low.¹⁴³

5.3.2 Hot embossing

Hot embossing is a suitable method for thermoplastics only, since the replication process takes place above the glass transition temperature. The procedure of hot embossing consists of the following steps:

1. A sheet of polymer, the substrate, is heated to just above T_g in a vacuum.
2. The mold to be replicated is heated to the same temperature or slightly warmer.
3. The mold is pressed into the polymer substrate. For PMMA or PC the force used is about $500N/cm^2$ and is dependent on the design, the polymer to be embossed and the mold material.
4. The mold and substrate are cooled down at equal rates to just below T_g , such that the substrate can be peeled off the mold.

Table 5.1: Characteristics of the Talon 355-15 laser.¹¹⁶

Wavelength	355 nm
Power	4W @ 300 kHz (typical)
Repetition Rate	0-500 Hz
Pulse width	<25 ns @ 100 kHz

Replication results depend on the uniformity of the temperature distribution across the mold, the vacuum quality to prevent air bubbles in the substrate, the surface quality of the mold and the chemical compatibility between mold and substrate.¹² The difference in temperature during the compression step and demolding step should be as small as possible to minimize thermal stresses and the 'replication errors due to the different thermal expansion coefficients of tool and substrate'.¹³ The resolution mainly depends on the resolution reached in fabricating the mold. Replication accuracies of tens of nanometers have been reached.¹⁴⁴ Residual mechanical stresses typically remain small in hot embossed parts, since no phase transitions take place during the process. This has the advantage that birefringence and warpage remain small, which is beneficial for the optical quality of the product.¹² The hot embossing procedure takes about 10-30 minutes per product.¹³⁰ The surface quality mainly depends on the surface quality of the mold, but can be decreased due to shrinkage, which can produce sink marks. The surface roughness can be increased during the demolding process. For example, during demolding there is a relative motion between the mold and the replicate, small defects can scratch the demolded structure.¹⁴³

The fabrication of through-holes with hot embossing is possible, but needs an extra post processing step or the use of an extra layer during the embossing step.

5.3.3 Laser ablation

In laser ablation a high intensity laser causes decomposition of the polymer at the focal point of the laser. The polymer can be irradiated by direct writing or by applying a mask on the polymer and irradiating the mask. One laser shot will ablate about $1\mu\text{m}$ deep. For deeper cuts repeated laser shots are needed, which results in a typical surface roughness. Ablated material, debris, remains in the cutted structure and needs to be removed with suitable methods. The interaction of the laser with the polymer surface changes surface chemistry and surface charge to an extend difficult to predict.

The mechanism behind the decomposition is complex and controversial. Photochemical and photothermal reactions play an important role in ablation. The contribution of different mechanisms in the ablation process depends on the ablated polymer, the wavelength and pulse length of the laser and the substrate.⁷⁵Lippert⁷⁵ wrote an extensive review on the mechanisms and relevant parameters in UV laser ablation of polymers.

Lasers with different wavelengths and intensity and pulse length ranges are available. The laser available at the department is a Talon 355-15 laser, the output and beam characteristics are listed in table 5.1.

5.3.4 Micro milling

In micromilling material is removed mechanically from the workpiece using a rotating cutting tool. Production costs for small quantities are low, since no mold is needed. Milling is extensively characterised for large scale structures in many metals, producing micro scale structures in polymers is much less characterised.⁵³ note that 'devices with features ranging in size from several microns to several meters' can be fabricated using micromilling. The surface roughness, defining the optical quality, depends on the cutting tool and the operational parameters, spindle speed, feed rate and depth of cut.^{53,28,30}

Guckenberger et al.⁵³ published an extensive tutorial review on micromilling for microfluidic devices, in which they also compare micromilling with other fabrication techniques.

5.4 Alternative materials

Many polymers suitable for microfabrication are available. A smaller amount is used for lab- and organ-on-chip devices: COC, parylene C, PDMS, PC, PE, PET, PMMA, polyimide, PS and PU. In this section PS, PC and COC will be compared with PDMS. PS and PC have been used in cell culture for decades, so biologists have a lot of experience with these polymers already. COC is a newer class of polymers, but has very good optical quality, is biocompatible and the many different grades give various opportunities in microfabrication.

5.4.1 Polystyrene

Polystyrene, a thermoplastic synthesized from styrene, or ethenylbenzene, $C_6H_5CH=CH_2$, is one of the most used materials in products for cell culture parts and has been used since the 1960s. Polystyrene is manufactured by mixing styrene, with or without diluents with a free radical initiator and heating the mixture to $120^\circ C$. Unreacted monomer and diluent are removed by flashing under vacuum.¹⁰⁷ The fabrication of microfluidic devices out of polystyrene, and thermoplastics in general, is a more challenging task and more expensive than soft lithography of PDMS. Therefore, most of the time PDMS is chosen above PS for academic use.

Bio-compatibility

Since PS has been used for decades in cell culture ware, a lot of experience and knowledge from research has been gained by biologists and culture procedures are optimized for culturing on PS. Various grades of PS are available which meet the ISO 10993 biocompatibility standards. However, McDonald et al.⁸³ reported activation of human monoamine oxidase-B, an enzyme recognizing xenobiotic substrates, which indicates leaching of compounds out of PS well plates.

PS and all thermoplastics, including PC and COP, are only subject to surface adsorption of hydrophobic compounds, which stands in contrast to the bulk absorption seen in PDMS.¹⁵ The uptake of hydrophobic compounds in thermoplastics will therefore be a lot lower for thermoplastics than for PDMS in general.

A drawback of cell culture on PS is the high stiffness of the material, a property PS has in common with both PC and COP, which is not comparable to the in vivo situation and affects cell adhesion.

Fabrication methods

Challenges in the fabrication of PS microfluidic devices include the need for molds which resist the high temperatures and pressures occurring in the hot embossing process, creating inlets and outlets and bonding of thermoplastic materials.

Injection molding and hot embossing

The most used methods for PS microfluidic device fabrication are injection molding and hot embossing. For these methods the molds are often fabricated using CNC or laser ablation machining of metals, since the molds need to resist high temperatures. These methods bring along a significant surface roughness, which can have negative effects on bonding and optical microscopy results, or need an extra step polishing the device.¹⁵

To avoid the high surface roughness, devices have also been made by casting a high strength epoxy on a PDMS mold, which is obtained by soft-lithography of PDMS on a SU-8-silicon mold. The PS is then embossed using the epoxy mold. PS can also be directly embossed using a PDMS mold, making use of the flexibility of PDMS at the demolding step.¹⁵

Tran et al.¹²⁹ hot embossed $1.5\text{mm} \times 22\text{mm}$ channels with a second layer consisting of a checkerboard pattern of $15\ \mu\text{m}$ squares and circles $2\ \mu\text{m}$ high within the channels using a PDMS mold with silanized surface. Young et al.¹⁵⁰ produces arrays of channels of $150\ \mu\text{m}$ deep, $1.5\ \text{mm}$ wide and $22\ \text{mm}$ long using epoxy molds and used a sacrificial layer of COC underneath the PS to be able to produce through-holes. Mehta et al.⁸⁴ produced $30\ \mu\text{m}$ high bell shaped channels and $200\ \mu\text{m}$ high rectangular channels using epoxy molds. Goral et al.⁵⁰ produced holes with different shapes with cross sections of $5 - 10\ \mu\text{m}$ and $15\ \mu\text{m}$ deep by pressing PDMS molds on PS sheets with binder clips.

Laser ablation

Laser ablation is a suitable technique to produce polystyrene devices.⁷⁶ Only few studies report on laser ablating in polystyrene. Li et al.⁷³ report on the use of a CO_2 laser with a focal spot size of $0.127\ \text{mm}$ in diameter to produce bell shaped channels of about $250\ \mu\text{m}$ wide, without reporting on the surface roughness. These results would not be sufficient for this study, however, the spot size of the available laser can be as small as [size](#).

Micromilling

Christ et al.³⁰ studied the 'effects of tool speed, feed rate and depth of cut on finished channel width, bottom surface roughness, and burring along the channel sides', and produced channels of $276 \pm 3\ \mu\text{m}$ wide and $223 \pm 9\ \mu\text{m}$ to $452\ \mu\text{m}$ $5\ \mu\text{m}$ deep. The micromilling procedure did not result in optically transparent surfaces.

Bonding

Berthier et al.¹⁵ point out that bonding of PS has received less attention than other thermoplastics like PC and PMMA, partly because PS can deform below the T_g , making thermal bonding difficult. Next to that, thermal fusion bonding increases autofluorescence of polystyrene significantly at wavelengths of 350nm , 492nm and 572nm .¹⁵⁰

Tsao and DeVoe¹³¹ report the use of lamination film bonding and surface treatment bonding. Solvent bonding and thermal diffusion bonding are most often used. The organic solvents used in solvent bonding should be adequately removed, since even picomolar concentrations could 'affect culture cells and bias results'. Furthermore, solvent bonding brings along the risk of channel deformation, especially in the height of the channels. In low temperature bonding the surfaces are treated with UV or ozone prior to bonding. Also laser bonding and ultrasonic welding have been developed, but both need specialized equipment.¹⁵

Since PS is a lot stiffer than PDMS, connecting tubes tightly to the inlets and outlets is more difficult than with the more flexible PDMS.

5.4.2 Polycarbonate

Polycarbonate, PC, is a class of mainly amorphous thermoplastic polymers, named after the carbonate group ($\text{O}(\text{C}=\text{O})\text{O}$), present in the polymers. The most used polycarbonate is synthesized from the monomer bisphenol-A ($(\text{CH}_3)_2\text{C}(\text{C}_6\text{H}_4\text{OH})_2$) and phosgene (COCl_2).¹²³

Polycarbonates have a good optical quality and a high transparency from 400 to $1650\ \text{nm}$. They are a lot less brittle than most other thermoplastics. The high glass temperature ($T_g = 147^\circ\text{C}$) allows for sterilization by heating. Polycarbonates are however less chemical inert to many substances, especially bases and organic solvents, than other polymers, but this can be influenced by different factors.¹²³ See Thakur and Thakur¹²³ for an overview of the chemical stability of PC under various conditions.

The quality of polycarbonate can be affected by different degradation mechanisms, Thakur and Thakur¹²³ lists some examples: 'thermolysis, thermal oxidation, hydrolysis, photolysis or photooxidation'.

Bio-compatibility

Polycarbonate based on bisphenol-A (BPA), has been used for a long time for medical instruments and cell culture inserts. Medical grades from Makrolon® from Bayer AG are biocompatible according to ISO 10993-1 test requirements, or some of them. However, BPA is known to leach from the bulk material under certain conditions such as higher temperatures or in neutral or alkaline pH. BPA is a xenoestrogen which has endocrine-disruptive effects at very low (nanomolar) concentrations. Different studies indicate that BPA is also cytotoxic. The effect of leached BPA from PC on the results of cell culture experiments is not known.¹²³

Fabrication methods

Polycarbonate structures can be directly fabricated using laser ablation or micromachining or indirectly by replication with injection molding or hot embossing. Becker and Heim¹³ fabricated channels with a width of 20 μm and a depth of 140 μm . The process parameters are given, but it is mentioned that these will vary slightly for every design. Using laser ablation structures with widths down to 50 μm and aspect ratios up to 10 can be fabricated.¹⁴⁴

Micromilling

Yen et al.¹⁴⁸ reported a precision of $< 28\mu\text{m}$ for micromilling channels with a width of 250 μm in polycarbonate, when using a 1/64" (379 μm) end mill. The diameter of the mill defines the minimum width of milled channels. The surface quality of the micromilled polycarbonate surface in the report of Yen et al.¹⁴⁸ was not sufficient for optical imaging. Yen et al.¹⁴⁸ therefore treated the surfaces first with sand paper, which reduced the average roughness R_a from $\sim 1.0000 - 1.7000\mu\text{m}$, depending on end mill size, to $\sim 0.2500\mu\text{m}$. In microchannels however, sand paper can not be used, so a different method should be used. After that, vapor-polishing using methylene chloride gas was performed which did not affect R_a significantly. However, where non vapor-polished surfaces had an average absorbance of visible light of $\sim 0.2 - 0.48$ the vapor-polish treatment turned the surface to 'almost completely transparent'. Chen et al.²⁸ minimized the surface roughness obtained with their micromilling machine, by investigating the role of spindle speed, the feed rate and the depth of cut. Spindle speed appeared to be the most influential factor. A surface roughness of 0.147 μm was obtained with a spindle speed of 20,000 rpm , a feed rate of 300 mm/min and depth of cut of 10 μm . The authors note that in a different micro milling machine, these parameters might lead to different results, since other parameters such as substrate grain size or tool edge geometry, might dominate the surface roughness.

Bonding

Ogonczyk et al.⁹⁶ summarize different bonding techniques used in literature: 'thermal, chemical, and adhesive methods'. Thermal bonding is used to bond slabs and to laminate thin foils. The material is heated to T_g and compressed⁹⁶, diffusion of polymer chains between the two surfaces leads to a strong bond, which could theoretically be as strong as the cohesive strength of the bulk material¹³⁰. Due to the compression at T_g , the microchannels could be deformed. Deformations can be diminished by heating to much higher temperatures than T_g and applying a much lower pressure than needed at T_g . Ogonczyk et al.⁹⁶ report a method where the PC parts are exposed to solvents (DCM, MEK and MMK) prior heating and compression to reduce channel deformations. Rupture strengths up to 0.6 MPa were reached. In chemical bonding the surfaces are treated with plasma or active surface groups are introduced, before the surfaces are brought together. A maximum bond strength of 6.8 MPa can be reached. In addition, glues or adhesives can be used.¹⁴⁴ However, Tsao and DeVoe¹³¹ note that only few successful examples of bonding using glue have been published, which is probably due to channel clogging. Also solvent bonding and lamination film bonding is used for bonding of PC.¹³¹

5.4.3 Cyclic Olefin Polymers

Cyclic olefin polymers are a class of amorphous thermoplastic polymers. Various brands offer COPs, which differ from each other depending on the cyclic monomer and polymerisation process used. Two

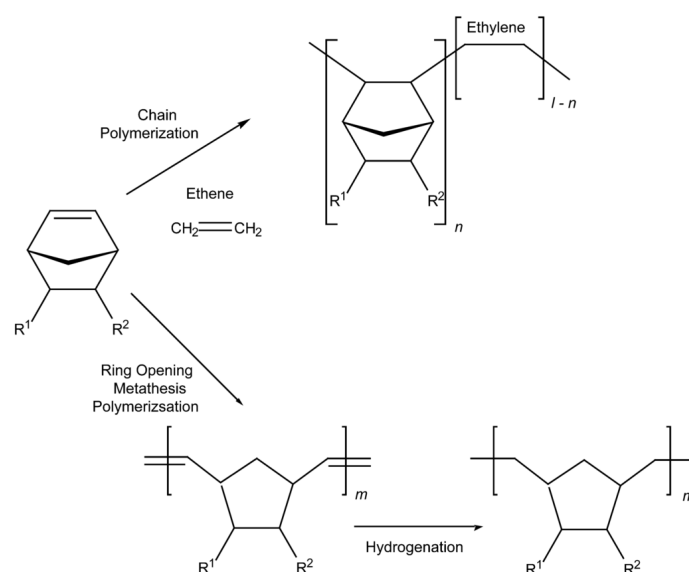


Figure 5.2: Two different polymerisation reactions for cyclic olefin polymer. Reproduced from ¹¹²

different methods are used: 'Chain polymerisation of cyclic monomers with ethene (Topas and Apel), and ring-opening metathesis polymerisation of cyclic monomers followed by hydrogenation (Arton, Zeonex and Zeonor)'⁹³, see fig. 5.2. The first process yields a material that is referred to as a cyclic olefin copolymer, since two different types of monomers are used. COP is available in pellet form, solution or in sheets.⁹³

Bio-compatibility

Various grades of COPs are biocompatible according to ISO 10993 tests. COPs are already used a lot for biomedical applications.¹¹⁹ Van Midwoud et al.¹³³ investigated the biocompatibility of different polymers (PDMS, PMMA, PC, PS and COC) by culturing HepG2 cells on these polymers coated with collagen after UV-ozone treatment. In terms of cell adherence and viability, COC performed as well as PDMS, PC and PS. Johansson et al.⁶¹ compared cell growth of HeLa cervix carcinoma cells on COPs (Zeonex® and Topas®), PMMA, styreneacrylonitrilecopolymer (SAN) and PS after different radiofrequency air plasma treatment intensities, with cell growth on commercial PS substrates. Where Zeonor, PS and SAN performed as good as commercial substrates, Topas performed worse. The difference between Topas and Zeonor could be explained by cytotoxic substances leaching from the surfaces originating from nonspecific additives Johansson et al.⁶¹.

Untreated COP is hydrophobic, which increases protein adsorption. The adsorption of proteins can be reduced by photografting poly(ethylene glycol) methacrylate or by means of a dynamic coating of hydroxyethyl cellulose.⁹³

Fabrication methods

One of the advantages of COP is the low water absorption (<0.01%), since absorption of water causes dimensional changes and could influence other mechanical and chemical properties.⁹³ The water vapor permeability is relatively low, which confines the evaporation of water from the culture medium. The optical quality of COP is high, since it has a high optical transparency from 300–1200nm, a high refractive index (n=1.53 for Topas5013), low birefringence and a large Abbe number (56.4 for Topas5013). The transmittance of UV light is higher than other polymers like PMMA, PC and PS. The autofluorescence is in the same order of magnitude as PMMA and PC.

The glass transition temperature T_g can be influenced by the fraction of norbornene molecules, COPs with T_g values between 30 and 180°C are available. A higher norbornene content makes the polymers

chains more rigid resulting in less chain entanglement, increasing T_g , but also making the polymer more brittle.¹⁵¹

COP structures can be obtained with replication techniques: injection molding, hot embossing, nanoimprint technology, soft lithography and even lamination have been used, or using direct structuring methods: milling and laser ablation.

Injection molding

Injection molding, which is not interesting for prototyping but for mass production, can be done using COP in pellet form. Because of the high mold temperatures, mostly metal molds are used. The quality of the replicated structure mainly depends on parameters as injection speed, mould wall temperature and structure depth. To avoid a skin-shear-core structures with different molecular structure higher temperatures in various parts of the injection molding machine can be applied. Structures of 600 nm wide and 200 nm in height have been replicated with high quality.⁹³

Hot embossing

For hot embossing COP in wafer or sheet form is used. Different mold materials are used like nickel/stainless steel, steel, silicon and SU-8, see Nunes et al.⁹³ for the different studies in which these mold materials are used. Typically SU-8 molds can only be used for less than 10 times and coatings are used to facilitate demolding.⁹³ Dhouib et al.³⁸ did not need an anti-stick layer on their laser machined steel mold to get replication results with 'good fidelity' of channels of 100 μm wide and 50 μm in depth.

Crazing or shear stress whitening, visible whitened areas on the polymer surface, can occur during the replication process. This is caused by localized yielding behaviour when the mold temperature is too high, the cooling rate is too high, the demolding temperature is too low and when stress is applied to the replicate during demolding.⁴⁶

Laser ablation

Nunes et al.⁹³ note that no intensive studies on laser ablation in COC have been published yet (2010). Sabbert et al.¹⁰⁵ experimented with a 193nm ArF laser and were able to produce flat structures up to 200 μm deep with smooth surfaces and almost no deposition debris. Since Nunes et al.⁹³'s review few studies on the cutting performance of different lasers in COC have been published. Leech⁷² investigated the norbornene content on the performance of a 248nm/5ns laser, McCann et al.⁸² experimented with a 1064nm/750ps laser, Suriano et al.¹²⁰ and Eaton et al.³⁹ with a 800nm and 40fs and 50fs laser respectively and Singaravelu et al.¹¹⁴ used a 343nm/200fs and 1064nm/15ns laser. Since the lasers used in these studies are all very different from the laser available at the department, they will only be useful to a small extent in tweaking the ablation parameters for the Talon 355-15 laser and in predicting if sufficient quality can be obtained.

Micromilling

Few studies have been published about micromilling in COPs. Bundgaard²³ investigated the process of micromilling in COC and fabricated channels with dimensions down to 25 μm .²³ reports that next to surface roughness control also burr formation is an important issue. Since COC is a ductile material relatively large burrs that remain attached to the material are formed. Mechanical polishing of the soft Topas²³ used appeared to be more difficult than polishing of metal and PMMA.

Other studies have used micromilling to fabricate channels in COC, but do not report on the surface quality explicitly^{95,118,52}.

Bonding

COC can be bonded using thermal fusion bonding, solvent bonding, surface treatment bonding and adhesive bonding.¹³¹ The possibility of tweaking the T_g of COCs allows to use a low T_g COC as a sealant. Layers with microchannels which are prone to deform during thermal bonding can be fabricated out of COC with a high T_g and a cover plate out of COC with a lower T_g . The thermal bonding temperature can now be higher than the T_g of the cover plate and lower than the T_g of the microchannel layer, such that the microchannels will not deform. Jena et al.⁵⁹ accomplished a burst strength of 3.2MPa for their device with two crossing channels of 100 μm wide and about 15 and 10mm long respectively.

Another significant advantage of COP is the experience already gained at the department.

5.5 Choice of material and fabrication method

The goal of this study is to fabricate a device, not to investigate the use and possibilities of a certain fabrication method. If possible, the use of methods about which only marginal information is available will therefore be avoided. The properties and manufacturing possibilities given above are summarized in table 5.2, on the basis of the list a choice will be made in terms of fabrication method and material.

Most literature on fabrication of microchannels was found about hot embossing. Structures of sufficient aspect ratio and resolution for this study have been accomplished. The surface quality depends mainly on the surface quality of the mold, so adequate mold fabrication techniques are yet to be chosen. Hot embossing has been done more often at the department successfully, which makes it a more convenient choice than PS and PC.

For laser ablation some literature was found on the fabrication of microchannels. However, for PS the results were not sufficient for this study and for all materials the lasers used are not comparable to the Talon 355 laser at the department. This implies experiments have to be performed to get to the right operating parameters first, which could be quite time consuming.

Not many studies have been published yet about milling. In these studies no sufficient surface quality for optical imaging has been reached for microchannels in PS. In the case of COP information on surface quality is not reported. Milling in combination with PS or COP will therefore not be used. PC microchannels have been fabricated with sufficient aspect ratio and resolution. To obtain a surface of optical quality, sandpapering and vapor polishing is needed, which adds an extra production step and is complex inside a microchannel.

Both PS and PC have been successfully used in conventional cell culture experiments for decades, which makes them the preferred materials among biologists, even though leaching of xenobiotic compounds has been signalled by human enzymes in the case of PD and the xenoestrogen BPA leaches from PC. Like PC and PC, COP meets the ISO 10993 standards for biocompatibility. The formula Zeonor® performed in experiments with HeLa cervix carcinoma cells as good as PS in terms of viability. However, the formula Topas® might leach cytotoxic additives affecting cell viability. For this reason Zeonor® would be preferred above Topas®.

One important shortcoming of PDMS is its tendency to absorb hydrophobic compounds into the bulk material. This property could influence cell culture experiments when for example signalling agents or drugs are absorbed from the medium. Thermoplastics are only subject to surface adsorption of hydrophobic compounds, which makes the interplay of the material with the cells in culture smaller. Indeed absorption of testosterone and some other compounds is shown to be significantly lower in PS, PC and COP than in PDMS.

Another problem that could arise when using PDMS is its high permeability to water vapor, which causes problems with medium osmolarity in especially static culture conditions. For all three alternative materials the water vapor permeability is a lot lower, especially for COP, which has a water vapor permeability 50× and 100× lower than PS and PC respectively.

The surfaces of the three thermoplastics are less hydrophobic (contact angles between 82° and 88°) than PDMS, but still need treatments to reduce the hydrophobicity to enhance cell adhesion and for bonding. Using UV-ozone treatment low hydrophobic recovery was found for all three materials, in contrast to PDMS.

An advantageous property of PDMS is its low Young's modulus, which is in the same order of magnitude as the stiffness of the basement membrane in vivo. The Young's moduli of the three alternative materials are four orders of magnitude higher, which makes the mutual differences (< 1.5x) negligible.

All materials have sufficient optical quality.

To conclude, COP has no major disadvantages to PS and PC, except for the wealth of experience with PS and PC present among biologists. The biggest disadvantage of COP (and PS and PC) to PDMS is the high stiffness. In a later stadium the use of gels for example could be investigated to overcome the high stiffness. Hot embossing appears to be the most researched microfabrication method in combination with PS, PC and COP. It comes with sufficient results in terms of aspect ratio and resolution. Sufficient surface quality can be accomplished by fabricating a mold with high surface quality. On top of that, a lot of experience on hot embossing in COP is present at the department. On the basis of these reasons it is determined to use hot embossing to fabricate a device out of COP.

The COP used at the department is Topas® grade 6013, from TOPAS Advanced Polymers. It was found that Zeonor® performed better in terms of cell viability. However, since Topas® 6013 and experience with Topas® 6013 are already present at the department, it is chosen to use this formula.

5.6 Mold fabrication

The next choice to be made is the mold fabrication procedure and mold material. The mold should have sufficient surface quality and should sustain high temperatures. The mold will be heated to a temperature around the glass temperature of the COP used. The TOPAS ® grades available and their glass transition temperatures are given in table 5.3. Jena et al.⁵⁹ studied the effect of embossing temperature, embossing load and embossing time on the formation of microchannels using Topas grades 6015 and 5013 and report an ideal temperature of 10 °C above the T_g of Topas. Most procedures used at the department to emboss Topas prescribe temperatures 20 °C below T_g . To start with, these procedures will be used because of the available experience.

Table 5.3: Glass transition temperature of different TOPAS grades

Grade	9903	9506	8007	7010	5013	6013	6015	6017
T_g	33°C	65°C	78°C	110°C	134°C	138°C	158°C	178°C

5.6.1 3D-printing

In 3D-printing a structure is built layer by layer. At the department two 3D-printers are available which could be used to fabricate the mold. Both use a different principle to built the layers. Especially in the direction of added layers the surface is not smooth, but the different layers remain present to a greater or lesser extend.

EnvisionTEC Micro Plus Hi-Res

The Micro Plus Hi-Res printer from EnvisionTEC produces the layers by curing a resin through UV exposure on the x-y-plane. The cured material is then lifted in z-direction, such that the next layer can be cured. The resolution in the xy-plane is 30 µm, in z direction 25-75 µm, depending on the material used. For high temperature molding EnvisionTEC has the material HTM140 M available for this printer. Properties of this material are given in table 5.4. The heat deflection temperature of HTM140 M is quite low compared to the T_g of half of the grades listed in table 5.4, so when using HTM140 M as mold material, it should be taken into account that the mold could deform during the embossing process when using Topas 5013 or a grade with an even higher T_g . Instead of turning to Topas® grades with low T_g , it is also possible to create a positive mold using 3D-printing and next using soft lithography to fabricate the negative mold out of PDMS, which is able to endure high temperatures.

Table 5.2: Properties and manufacturing possibilities of PDMS, PS, PC and COPs.

	PDMS	PS	PC	COC
Injection molding	PDMS is not well suited for injection molding because of the long curing times.	Injection molding is often used ¹⁵	Injection molding is often used ¹⁴⁴	Many studies report on injection molding of COC on microscale. ⁹³
Hot embossing	Together with injection molding the most used method for microfluidic device fabrication out of PS. ¹⁵ Molds are made of metals using CNC machining or laser ablation or made of PDMS or an epoxy cast on PDMS. Small structures in the order of tens of micrometers ^{50,129,84} have been produced and also 200 μm deep rectangular channels ⁸⁴ . Laser ablation of polystyrene is possible ⁷⁶ , but the results of the few studies found that report on the fabrication of microchannels in polystyrene are not sufficient for this study. ⁷³ Microchannels of $276 \pm 3 \mu\text{m}$ wide and $223 \pm 9 \mu\text{m}$ to $452 \mu\text{m}$ deep have been fabricated, but did not yield transparent surfaces. ³⁰	Becker and Heim ¹³ fabricated channels with a width of 20 μm and a depth of 140 μm . Process parameters are given, but vary slightly for every designs.		Many studies report on hot embossing of COC with different mold materials and different feature sizes, e.g. 100 μm wide, 50 μm deep channels. Good temperature control required to avoid crazing.
Laser ablation			Structures with widths down to $50 \mu\text{m}$ and aspect ratios up to 10 have been fabricated. ¹⁴⁴	Few studies performed, none for the available laser
Milling			Microchannels with widths down to 250 μm and a precision of $< 28 \mu\text{m}$ have been fabricated, but needed surface treatments, sandpapering and vapor polishing, to obtain surfaces suitable for optical imaging. ¹⁴⁸	Structures down to 25 μm have been fabricated. ²³ Marginal information available about surface quality. Issues with surface roughness and burr formation are reported ²³ .
Bonding	Many different bonding techniques are reported, also for bonding with different materials, based on surface treatments and chemical bonding. ¹⁰³	Solvent, thermal, lamination film and surface treatment bonding. Thermal fusion bonding is prone to result in deformed channels and increases autofluorescence. Solvent bonding requires adequate removal of solvents. ^{15,150}	Solvent, thermal, adhesive, surface treatment and lamination film bonding. The risk of adhesive bonding is channel clogging. Thermal bonding could result in channel deformation, which could be limited by using solvents in the process. ^{96,131}	Thermal bonding, solvent bonding and surface treatment bonding are possible techniques. Thermal bonding with lower glass temperature layer to avoid channel deformation has been demonstrated (3.2 Mpa burst strength)

	PDMS	PS	PC	COC
Biocompatibility	Leaching of uncrosslinked oligomers, which were found in cellmembranes of cells cultured on PDMS. ¹⁰⁰ Leaching of irritants ⁵⁵ strong acids, hydrocarbons	ISO 10993 standards Often used in lab equipment and culture wells Leaching of xenobiotic compounds is shown ⁸³	ISO 10993 standards Often used in lab equipment and culture wells Leaching of BPA (xenoestrogen) ¹²³	ISO 10993 standards Possible leaching of additives affecting cell viability from certain formulas (topas) ⁹³
Chemical inertia	not resistant	concentrated acids, ether, hydrocarbons, most organic solvents	Hydrocarbons, ketones, KOH, most organic solvents	
Adsorption and absorption hydrophobic substances	weak acids and bases Adsorption and absorption of small hydrophobic compounds, such as hormones and drugs, to an extent that could influence cell culture experiments ^{125,100,137} Significant adsorption or absorption of 7-ethoxycoumarin and the hormone testosterone and some of its metabolites. ¹³³ Treatments to reduce absorption of small molecules are available, but effects on cell cultures should be tested.	Bases, alcohols No significant adsorption or absorption of 7-ethoxycoumarin and the hormone testosterone and their metabolites. ¹³³	Alcohols, acids No significant adsorption or absorption of 7-ethoxycoumarin and the hormone testosterone and their metabolites. ¹³³	Acids, bases No significant adsorption or absorption of 7-ethoxycoumarin and the hormone testosterone and their metabolites. ¹³³
Water vapor permeability	3000-6000 $\mu\text{m}^2/\text{s}$ ⁵⁶	3.6 g mm/(m ² day) ⁹²	6 g mm/(m ² day) ⁹²	0.057 g mm/(m ² day) ⁹² 0.23-0.45g mm/(m ² day) (DIN 53 122 test) ¹²⁶ 0.01% ¹³¹ 0.09 $\mu\text{m}^2/(\text{s atm})$ ⁹²
Water absorption	0.03% ¹⁴⁴	0.02-0.15% ¹³¹	0.12-0.34% ¹³¹	
Gas permeability	O ₂ 3000 $\mu\text{m}^2/\text{s}$ ⁸¹ 4100 $\mu\text{m}^2/\text{s}$ (35°C) ²⁷ 2600 $\mu\text{m}^2/(\text{s atm})$ (35 °C) ²⁷	1.8 $\mu\text{m}^2/(\text{s atm})$ ⁹²	0.9 $\mu\text{m}^2/(\text{s atm})$ ⁹²	
CO ₂		8 $\mu\text{m}^3 \mu\text{m}/(\mu\text{m}^2 \text{s atm})$ (25 °C) ²	6 $\mu\text{m}^3 \mu\text{m}/(\mu\text{m}^2 \text{s atm})$ (25 °C) ²	

	PDMS	PS	PC	COC
Contact angle	114.41 ± 3.14° ⁷	87.4° ¹	82° ¹	88 ± 3° ⁵⁸
Hydrophobic re-covery	High hydrophobic recovery probably already in the first two hours after treatment. 60 minutes of treatment only resulted in a contact angle of 70 degrees, which re-covered to more than 80 degrees after 4 weeks.	Low hydrophobic recovery first 4 weeks after treatment	Low hydrophobic recovery first 4 weeks after treatment	Low hydrophobic recovery after 4 weeks after 15 min treatment Higher hydrophobic recovery after 30 min treatment, but still about 50 degrees contact angle after 4 weeks
oxygen-plasma	Almost complete hydrophobic recovery within one week after treatment	Much higher hydrophobic recovery than for UV-ozone treatment, but contact angle still below 50 degrees for 60-120 seconds of treatment four weeks after treatment	Higher hydrophobic recovery, especially between 1 hour and 1 week after treatment. Between 1 and 4 weeks low hydrophobic recovery, all treatment times yielded in about 60 degrees contact angle after 4 weeks.	Higher hydrophobic recovery, especially between 1 hour and 1 week after treatment. Between 1 and 4 weeks low hydrophobic recovery, all treatment times yielded in about 60 degrees contact angle after 4 weeks.
CTE	310 × 10 ⁻⁶ m/mC ¹³¹	10-150 × 10 ⁻⁶ m/mC ¹³¹	60-70 × 10 ⁻⁶ m/mC ¹³¹	60-80 × 10 ⁻⁶ m/mC ¹³¹
Youngs modulus	0.360-0.870 MPa ¹⁴⁴	3200 MPa (90 °C), 3600 MPa (20°C) ¹¹	3600 MPa ¹⁴⁴	3000 MPa ¹⁴⁴
Tensile strength	2.24 MPa ¹⁴⁴	~ 57 MPa ¹¹	65MPa ¹⁴⁴	60 MPa ¹⁴⁴
Glass temperature	-125°C ¹⁴⁴	92-100°C ¹³¹	145-148°C ¹³¹	70-155°C ¹³¹
Melting temperature	-40°C ¹⁴⁴	240-260°C ¹³¹	260-270°C ¹³¹	190-320°C ¹³¹
Heat distortion temperature	200°C ¹²	70°C ¹²	125°C ¹²	140-170°C ¹²
Transparency		~ 81% transmission for (4 mm thickness), low transmission for lower wavelengths ¹¹	87-90% transmission 400-1100 nm (4 mm thickness), high up to 1650 nm ^{123,32}	from high for 300-1200 nm ⁹³
Refractive index	1.40-1.42 ³¹	1.59 ¹¹	1.57-1.64 ³²	1.53 ⁹³
Birefringence				low ⁹³
Abbé number		31 ¹¹	30 ³²	56.4 ⁹³

Table 5.4: Properties of HTM 140 M

Tensile Strength	56 MPa
Elongation at Break	3.5%
Flexural Strength	115 MPa
Flexural Modulus	3350 MPa
HDT	140°C

Nanoscribe

The 3d-printer from Nanoscribe makes use of a nonlinear two-photon absorption process to fabricate structures. A structure is drawn with an ultra short pulse laser in a droplet of photoresist material on a substrate, for example silicon. The high intensity of the laser allows the molecules in the photoresist to take up two photons simultaneously. The energy of the two photons combined induces the polymerization process. The photoresist materials available for the Nanoscribe printer are thermosetting materials. Depolymerization temperatures are not given by the manufacturer, but the materials have been used for hot embossing at high temperatures (>165degree) already before at the department.

The resolution of the printing process is defined by the size of the laser spot and focal depth. One laser pulse induces the polymerization of a sphere, a voxel, with a diameter of 20nm, in practice this appears to be about 100 nm. Resolutions are thus high enough for our application. The range in which the laser can be moved in the xy-plane is 300 μm x 300 μm and about a centimeter in height. For larger structures, as in our case, moving the base plate on which the droplet is placed is needed. Different smaller objects are then stitched together. With previous models of the Nanoscribe this has been tried before, but performance in terms of accuracy and time efficiency were not sufficient. Therefore the Nanoscribe will only be used if other techniques fail.

5.6.2 Laser ablation

For the production of a mold using laser ablation, the same laser cutter as presented in section 5.3.3 is available. The performance of the laser cutter in terms of the surface quality has been studied at the department by Jia⁶⁰. Beams with a width of 70 μm were fabricated in 300 μm thick silicon wafers. Optimization of the parameters resulted in beams with a taper of 15.66σ degree and a surface roughness of the side walls of $R_a = 0.802 \mu\text{m}$. Since the grooves were completely cut through the material, the surface roughness of the bottom side of a groove is not available, which is important for optical imaging. However, it will be in the same order of magnitude, which is too high for optical applications.

5.6.3 Conclusion

The resulting quality of laser ablated silicon surfaces is assumed not to be good enough for optical applications, since the bottom side of a groove will have a surface roughness lower, but in the same order of magnitude as the sidewalls of the groove, which is too high for optical applications. The Nanoscribe has been used before at the department for embossing of small structures. The performance of the Nanoscribe is good enough for small structures (>300x300 μm), but becomes more time consuming and less accurate for larger structures, as in our case. Prints from the EnvisionTec have not been used yet at the department in combination with soft embossing and little can be found about the surface quality of the prints. However, the resolution is high enough and the process is less time- and labour consuming than with the Nanoscribe. It is assumed that the surface roughness will be low enough to yield transparent surfaces. Therefore the first devices will be embossed using PDMS molds, which in their turn are produced by soft lithography on molds printed with the EnvisionTEC. If the quality is not sufficient, soft embossing with molds directly from the Nanoscribe will be used.

Nr.	Process step	Illustration
1	Cleaned non-conductive TOPAS® substrate (light gray)	
2	Spin on of a thin, conductive PEDOT layer (black)	
3	One step hot embossing procedure to define microfluidics and electrode structures using a Al-stamp (dark grey)	
4	Sealing the system by thermal bonding of a TOPAS® lid	

Figure 5.3: Hot embossing of a TOPAS®substrate with a layer of PEDOT. At the edge with a 90degree angle the PEDOT is separated into two pieces. Reproduced from Kafka et al. ⁶².

5.7 Electrode fabrication by hot embossing COC with a conductive polymer layer

One of the requirements for the device is the possibility of performing TEER measurements. Hereto electrodes need to be incorporated. As stated in chapter 4 these electrodes need to be transparent to allow for optical imaging. In the following section it is described how the fabrication of these electrodes would be addressed. However, these steps will not be mentioned in the project proposal, since it is assumed that they will not fit in the timeframe of the project.

In only one of the devices discussed in section 2.2 transparent electrodes are used ¹³⁶. These electrodes are fabricated by sputter coating a thin layer of gold on a glass slide. The slot for the channel goes completely through a layer of PDMS, such that one side of the channel is formed by the coated glass slide. In section 5.3 the choice is made to construct the channels by making slots that do not run completely through the materials, such that less bonding steps are needed.

Technique

The choice is made to use a technique that has been used at the department more often by Chang ²⁶, Fanzio et al. ⁴³⁴⁴, either in combination with hot embossing or soft embossing. The electrodes are produced by applying a thin layer of conductive polymer before embossing. During the embossing process the layer of conductive polymer will be interrupted at edges with a slope above a certain degree, see fig. 5.3. Hot embossing of a polymeric substrate with a thin film layer of conductive polymer has been done before by Kafka et al. ⁶² and at the department by Chang ²⁶. In both studies COC is used as substrate and the conductive polymer poly_(3,4)-ethylenedioxythiophene (PEDOT). Chang ²⁶ explains in his thesis why the conductive polymer PEDOT is chosen in his study. For this, polypyrrole (PPy), polyaniline (PANI) and PEDOT were compared in terms of electrical conductivity, electrochemical stability and compatibility. In all three subjects PEDOT outperformed the other three. See Chang ²⁶ for a discussion on the characteristics of PPy and PANI. Below it will be clarified why PEDOT is a good material electrode candidate.

Biocompatibility of PEDOT

Hadjizadeh and Doillon ⁵⁴ give a summary of studies on biocompatibility of PEDOT: The biocompatibility of PEDOT with epithelial cells ³⁶ and NIH3T3 fibroblasts ⁷⁸ have been shown. In vivo implantation experiments in mice showed 'very low cytotoxicity and no inflammatory response'. ⁷⁸ 'Adhesion and proliferation of neuronal cells on PEDOT-coated PET' was found to be excellent ¹⁸ and in vitro L929 fibroblasts and human neuroblastoma SH-SY5Y cell cultures and in vivo mice studies with PEDOT-coated platinum electrodes suggest that these electrodes are non-cytotoxic and induce no aberrant immunological response compared to platinum electrodes. ⁷

Electrochemical stability of PEDOT

Kros et al.⁶⁸ characterised the electrochemical stability of PEDOT (and PPy) in a phosphate buffered saline solution (PBS) with a pH of 7.4, which has the same pH of blood and osmolarity of the human body. Over a period of two weeks no loss of DC-resistance of PEDOT was found, contrary to PPy. Using cyclic voltammetry it was shown that PEDOT remain electrochemically stable for at least two weeks, as opposed to PPy, which loses most of its electrochemical activity in the first day.

Conductivity of PEDOT

The conductivity of PEDOT depends on the processing method. Applying a thin film layer of PEDOT can be done by spin coating or spraying. In the report of Kafka et al.⁶² and the reports of Fanzio et al.⁴³ and Fanzio et al.⁴⁴, performed at the department, spin coating is used to produce the thin film on TOPAS®. In order to use spincoating to apply the PEDOT layer, the PEDOT is mixed with a compound to increase the water-solubility of PEDOT. The compound used in the work of Chang²⁶, Fanzio et al.^{43,44} is PSS. Mixing PEDOT with PSS results in a decreased conductivity. By using solvents with a high boiling point in the coating solution, Louwet et al.⁷⁷ were able to produce PEDOT electrodes with a sheet resistance of 350 Ω/cm^2 and a transparency of 80% to visual light.

6. Project proposal

Based on the literature study in this chapter a plan is proposed for the rest of the project. In the first place will be determined what exactly will be researched in this project by means of research questions. Next milestones and deliverables will be determined. After that the major activities to reach the deliverables and milestones are described and possible risks are evaluated. When needed, a plan B is proposed to mitigate risks. Finally, the time needed for these activities, milestones and deliverables determined and represented on a timeline.

6.1 Research question

The goal of this project is as follows:

To fabricate a bio-mimicking Blood-Brain Barrier on Chip device which can be efficiently produced in large quantities.

To reach this goal the following subquestions have been defined:

- Is it possible to to recreate the mechanical factors influencing the Blood-Brain Barrier in an Organ-on-Chip model?
- Is it possible to manufacture this BBB-on-Chip device using up-scalable methods as additive manufacturing and mold replication?
- Is it possible to integrate thin membranes by sandwiching the membrane between two TOPAS layers using thermal fusion bonding?

6.2 Milestones and deliverables

Milestones:

- Thermal fusion bonding protocol for the integration of a membrane
- Functional BBB-on-Chip

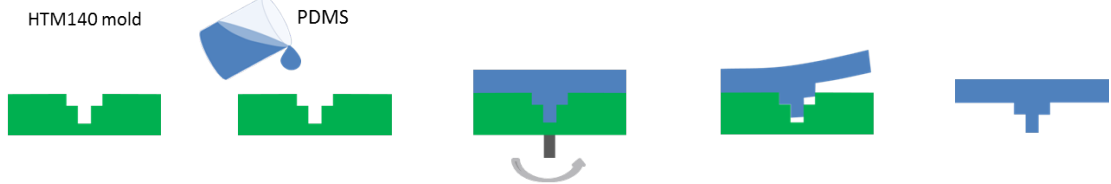
Deliverables:

- Design of the BBB-on-Chip and molds, implementing the mechanical factors influencing the Blood-Brain Barrier
- Optimal protocols for soft lithography, substrate preparation and soft embossing for the fabrication of the two separate layers of the device
- Optimal protocol to integrate a membrane in a TOPAS device using thermal fusion bonding
- Characterized BBB-on-Chip model

6.3 Activities and risk mitigation

To reach the set milestones and produce the deliverables a number of process steps are needed. These processes are discussed in this section. For every process possible risks are considered and a risk mitigation plan is written when needed. Figure 6.1 gives an overview of the processing steps.

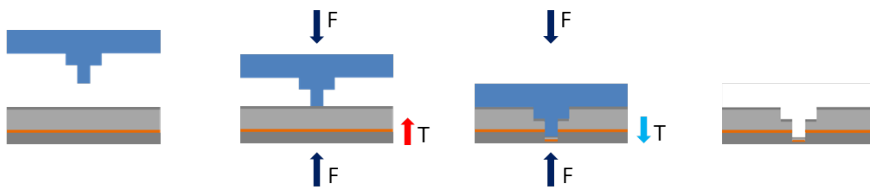
PDMS mold fabrication



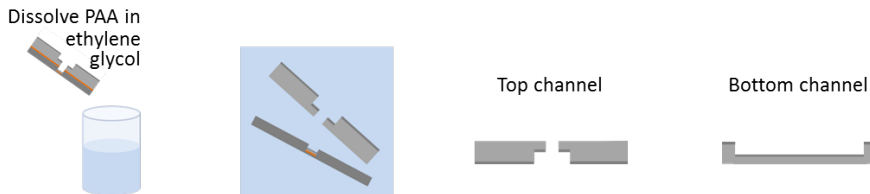
Adding thermal bonding and sacrificial layers



Soft embossing



Removing sacrificial layers



Thermal fusion bonding

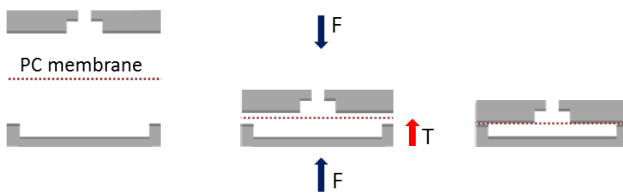


Figure 6.1: Process steps

6.3.1 Design and simulation

The requirements on dimensions and fluid flow will be taken into account to design a first concept of the BBB-on-Chip. The fabrication protocols will be optimized in order to fabricate this design. However, it can be adjusted during the rest of the project if needed to make the production feasible or more efficient. The design stage firstly consists of designing the BBB-on-Chip itself. Next, the soft embossing mold will be designed by taking into account the fabrication process. Lastly, the to be printed soft lithography mold will be designed. During the design stage the behaviour of the fluid and particles in the fluid need to be determined. This summarizes as the following actions in the design stage:

- Design passive device
- Design soft embossing mold
- Design soft lithography mold
- Simulate fluidics in the device

The risks in the design stage are not significant, since the design is not complex and the flow through rectangular channels and diffusion and convection through membranes is well described.

6.3.2 Mold fabrication

The fabrication of the soft embossing mold consists of two steps. First a mold will be made using the Micro Plus HiRes printer from EnvisionTEC with the material HTM140. Using this as a soft lithography mold, the soft embossing mold will be made.

Printing mold using UV-light induced polymerization

<i>Known</i>	Structures have been printed at the department with similar dimensions using the same material (HTM140) and printer. The surface quality of these structures is high at the fluid side of the structure, lower at the sides of the structure and the substrate side.
<i>Unknown</i>	The printed products have not been used yet to fabricate soft embossing molds out of PDMS to emboss COC. If the surface roughness of the prints is high, the surface roughness of the channels in COC will be high.
<i>Risks</i>	Low: Optical imaging becomes complicated or impossible and air bubbles might remain on the channel walls when a medium flow is applied.
<i>Mitigation</i>	Using the printer from Nanoscribe for mold fabrication or applying a vapor solvent treatment on the COC product of channel fabrication to smoothen the surface.

Soft lithography of soft embossing mold

<i>Known</i>	Soft lithography of PDMS with a HTM140 mold has been done before at the department. There are some problems with the surface roughness of the sidewalls of the molds, which cause the PDMS to stick to the mold.
<i>Unknown</i>	Soft lithography in combination with a HTM140 mold has not been used yet at the department to create standing structures in PDMS, but only for the fabrication of channels in PDMS.
<i>Risks</i>	Medium: Stiction of the sidewalls when peeling off the mold could be more problematic for standing structures than for the channels which have been produced so far. The structures could tear.
<i>Mitigation</i>	After printing the mold an anti-stiction coating could be applied on the mold. The coating could be either chemically attached or applied as a layer covering the surface. If this does not work, instead of HTM140 another material could be used to print the mold. For example, different ABS like materials are available for the Micro Plus Hi-Res printer.

6.3.3 Substrate preparation

Now the mold is ready, the substrate to be embossed should be produced. The base material is a TOPAS 6015 substrate. On top of this substrate a thin layer of TOPAS 5013 is needed as for the thermal fusion bonding step. A sacrificial layer is needed at the bottom side of the TOPAS substrate to make embossing through holes possible. A layer of water dissolvable poly(acrylic acid) (PAA) is hereto spincoated on the substrate. Since a layer of 2 μm maximum was reached in previous experiments at the department, a sheet of TOPAS is attached to this PAA layer to make sure the total sacrificial layer is thick enough to create through holes. Adhering a sheet of TOPAS to the PAA layer brings an insignificant risk and will therefore not be discussed. Next to the adhering of a TOPAS sheet to the PAA layer the substrate preparation step consists thus of the following actions:

Spincoating PAA on TOPAS 6015

Known Based on protocols in a publication of Linder et al.⁷⁴ the following protocol was used at the department before:

- PAA is used as sacrificial layer for soft embossing in TOPAS 5013 with a layer of PEDOT. Hereto PAA in powder form is mixed in DI water in a ratio of 3g:10 ml in a falcon tube and shaken until completely dissolved.
- The TOPAS 5013 substrate is treated with oxygen plasma for 30 second at 60 Watt. The solution is spin coated on TOPAS for 15 second at 3000 rpm
- The substrate with PAA layer is placed in an oven for 20 minute at 70 °C to harden the PAA.

Unknown In our case TOPAS 6015 will be used as substrate instead of TOPAS 5013. To begin with, the same procedure will be used. The oxygen plasma treatment might have to be altered since a different TOPAS grade is used.

Risks Low:

It is very unlikely that the procedure will be complicated a lot only by changing the TOPAS grade. The risks in this fabrication step are therefore low and a risk mitigation plan is not needed.

Spincoating 3-5 μm TOPAS 5013 on TOPAS 6015

Known Steigert et al.¹¹⁸ spin coated a 3-5 μm thick layer of TOPAS 8007 on a 500 μm thick TOPAS 6013 foil by dissolving 5% wt in toluene and spinning at 5000 rpm. The composite was annealed for 1 h at 75 ° to drive out the remaining solvent.

Bundgaard²³ reports the use of sec-butyl benzene instead of toluene as solvent, which has a higher boiling point, thus evaporating slower, but similar chemical structure. They found that toluene evaporated too quickly and resulted in inhomogeneities, which they account for by the fact that 'the evaporation from thin film areas takes place more rapidly than from thicker areas. The thin areas become gel-like and the liquid can not flow to level out, leaving thicker areas confined.'

The thickness (T) of a spin coated layer depends on the concentration (C) of the polymer in solvent (g/100 ml), the intrinsic viscosity (η) of the polymer, the rotational speed (ω in rpm) and some constants (α, β, γ, K) and can be calculated according to the empirical relation until the point centripetal forces exceed the surface tension at the edges:⁷⁹

$$T = \frac{K \cdot C^\beta \cdot \eta^\gamma}{\omega^\alpha} \quad (6.1)$$

However, the solvent mixture will cause swelling of the substrate and affect the obtained layer thickness. Bundgaard²³ performed experiments with TOPAS 8007 solved in sec-butyl benzene and found an empirical relation for the layer thickness of TOPAS 8007 on a TOPAS substrate for a wt% of 10-30:

$$T(C, \omega) = \frac{9.88 \cdot C^{3.78}}{\omega^{0.740}} - 165 \quad (6.2)$$

This expression gives a negative layer thickness for a 5wt% solution, but fits the experimental data of the other solutions well.

Unknown In our case the TOPAS 6013 foil in the report of Steigert et al.¹¹⁸ is replaced by a TOPAS 6015 substrate and a bonding layer of TOPAS 5013 instead of TOPAS 8007. An empirical relation for layer thickness or a published procedure on spin coating TOPAS 5013 has not been found.

Risks Low:

The solvent in the solution attacks the substrate. Bundgaard²³ writes that the solutions therefore needs to be applied to the substrate all at once, while spinning, in a continuous flow. In this way isolated drops are avoided, which would penetrate deeper into the substrate and cause a non-uniform layer.

At the department typically toluene has been used to dissolve TOPAS, this would therefore be the solvent of choice. However, although Steigert et al.¹¹⁸ were able to use toluene as solvent to spin coat the TOPAS 8007, Bundgaard²³ reports the toluene evaporated to quick to obtain homogeneous layers of TOPAS 8007. Therefore there is a chance a different solvent than toluene needs to be used. This will only bring a small risk, since Bundgaard²³ succesfully used a different solvent, sec-butyl benzene.

Since different TOPAS grades are used than the ones used before in literature, the optimum procedures will most likely differ from the ones in literature.

Mitigation Since experience is at the department, at first it will be attempted to spin coat TOPAS 5013 dissolved in toluene. The same procedure will be used as Steigert et al.¹¹⁸ used at first and will be adapted during experiments. If toluene indeed appears to evaporate too quick, sec-butyl benzene or another non-polar solvent with a higher boiling temperature could be used.

6.3.4 Soft embossing

Using the soft PDMS mold fabricated in section 6.3.2 the substrate obtained from the step in section 6.3.3 can be embossed. Some experience is already present at the department and in literature some studies can be found on soft embossing TOPAS. However, different TOPAS grades are used and different feature sizes are fabricated, which leads to medium-high risks:

Soft embossing in TOPAS 6015 with thermal bonding- and sacrificial layers

Known Soft embossing in COC with a PDMS mold has been done before by Lee et al.⁷¹, Narasimhan and Papautsky⁸⁹, Fanzio et al.⁴³. Narasimhan and Papautsky⁸⁹ produced 1 mm wide and 110 μm deep channels in PMMA using a PDMS mold. A force of 4.5 kN and an embossing temperature of 147 $^{\circ}\text{C}$, 40 $^{\circ}\text{C}$ above the T_g , was used. PMMA has a similar density and Young's modulus, see table 6.1, so the applied force needs to be in the same order for COC as for PMMA. The embossing temperature will be higher because of the higher T_g of TOPAS.

Lee et al.⁷¹ were able to produce channels of 100 μm wide and 40 μm deep in TOPAS 5013 and found that a lower force, complying with the fact that the density of COC is lower than that of PMMA. This also implies that in COC a larger area could be embossed than in PMMA. Lee et al.⁷¹ used a force in the range 2.4-4.5 kN and reported that for channels wider than 100 μm only a small force dependence of the replication accuracy was found. The lowest embossing temperature tested was 165 $^{\circ}\text{C}$ and appeared to be sufficiently high for 100 μm wide channels.

Applying the right force is important, since if the force will be too high, the PDMS molds gets compressed and replication accuracy decreases. If the force is too low, mold features will not penetrate the COC substrate.

Table 6.1: Mechanical properties of PMMA and COC. Adapted from Lee et al.⁷¹

	PMMA	COC
Density (g/m ³)	1.17-1.20	1.02
Youngs Modulus Gpa	2.2-3.1	3.1
Thermal Expansion Coefficient at 25°C (10 ⁻⁶ K ⁻¹)	20-30 < T_g , 60 > T_g	60
Thermal Conductivity(W/m K)	0.193	-
Tensile strength (Mpa)	48-76	66
Poissons Ratio	0.35	-
Refractive Index	1.49	1.53

Jena et al.⁵⁹ obtained excellent replication results by hot embossing 100 μm wide, 60 μm deep channels in COC using a silicon mold at 2.94 kN, 170°C and 180 s.

Since manufacturing channels of 1 mm wide and 110 μm deep was shown to be successful in PMMA and 100 μm wide and 40 μm deep channels in TOPAS 5013 using PDMS molds, it is expected that embossing the 500 - 1000 μm wide, 100 μm deep channels of the BBB-on-Chip device will be possible in COC 6015 by using higher embossing temperatures. This temperature will be higher for soft embossing than for hot embossing, so a temperature above 170°C will be needed, as used by Jena et al.⁵⁹. Lee et al.⁷⁰ fabricated 20 μm thick structures with an aspect ration of 2.00, but with high replication errors ($\sim 17.0\%$ change in width). These replication errors appeared to become higher with decreasing structure thickness. The microfluidic inlets and outlets will be manufactured by soft embossing through holes, with aspect ratios depending on the thickness of the TOPAS substrate.

Unknown The process parameters needed to soft emboss TOPAS 6015 with a PDMS mold are not known. Publications on soft embossing through-holes have not been found.

Risks Medium-high:
Fabricating through holes during embossing will be difficult if high aspect ratios need to be reached. The elastic PDMS could buckle or bend during the embossing process. Furthermore, the volume that needs to be displaced to create the through-holes is quite large. It could be difficult to apply enough force to displace all this volume without compressing or tearing the PDMS mold.

Mitigation It was shown that wide channels with low aspect ratios and small structures with aspect ratios up to 2.0, if a lower accuracy is allowed, can be fabricated. Replication errors decrease with increasing feature size. Since the diameter of the through-holes can be as large as the channel width, the feature size can be as large as 500 - 1000 μm . If through-holes will only be fabricated in the top layer, this layer can be very thin, for example 300 μm . Stiffness can then be obtained from a thick bottom layer which does not need through-holes.

If the volume to be displaced appears to large, the through-holes could be fabricated by milling.

6.3.5 Thermal fusion bonding

The embossed TOPAS substrates now need to be bonded while sandwiching a PC membrane. This will be done by using thermal fusion bonding. In this process different parts are pressed together under a determined force and heated to above the T_g of the to be bonded material.

Thermal fusion bonding

Known Thermal fusion bonding brings along the risk of channel deformation, since the polymers have to be heated above the glass temperature to induce bonding. However, a method published by ? will be used were the bonding is accomplished by heating a layer of TOPAS with a lower T_g than that of the TOPAS layer in which the channel is fabricated. In this way channel deformation will be limited.

The protocol published by Steigert et al.¹¹⁸ can be used as a base and is as follows:

- A TOPAS 5013 substrate with a microstructured channel is pressed on a TOPAS 6013 foil with a 3-5 μm thick TOPAS 8007 layer in a lamination machine.
- The two cylinders in the lamination machine are pressed together with a force of 5 bar and heated to 120 °.

A sealed cavity with a diameter of 2 mm was tested to withstand 4 bar, which is high enough for the BBB-on-Chip device. The channel geometry was not affected.

Unknown In our case a permeable polycarbonate membrane will be sandwiched between the two substrates with respectively the blood and brain channel and bonded to the TOPAS substrate by thermal fusion bonding. This has not been done before.

Risks High risk:
No experience at the department is present in thermal fusion bonding, but procedures are found in literature for thermal fusion bonding TOPAS.

The assembly is heated above the T_g of TOPAS 5013, so the bonding layer melts. If the bonding force and temperature are high enough the TOPAS 5013 could flow into the channels and clog the channels and membrane.

Mitigation It is possible that a strong bond will not be formed between TOPAS and polycarbonate. Clogging of the channels or membrane can be avoided by optimizing the bonding parameters. In the case the polycarbonate and TOPAS do not bond firmly, a TOPAS membrane could be used instead.

6.3.6 Characterization

In the characterization step the performance of the BBB-on-Chip device is determined. One important parameter is the wall shear stress exerted on the permeable membrane, where later endothelial cells will be cultured. The shear stress could be influenced by the surface roughness of the channels and membrane and by the edges of the membrane. To validate the shear stress calculation, the velocity profile in the channels will be visualised. The maximum hydrostatic pressure that can be withstood before leakage will be determined and transport of the nano-carriers across the permeable membrane will be evaluated. The usability of the device in terms of imaging is determined by imaging the membrane on luminal side and the brain channel at the location of the glioblastoma spheroid.

Imaging and applying pressure to the blood channel are both simple tests and do not need risk mitigation plans.

Flow characterization and permeability of the membrane

Known Babetski Holton et al.⁸ visualised the flow through their microfluidic channels by injecting fluorescently conjugated beads (Molecular Probes® FluoSpheres® beads, Life Technologies) in the channels. A concentration of 1×10^6 beads/mL was diluted in phosphate buffer and perfused through the microfluidic channel by using a peristaltic pump. The channel is 10 mm long, 600 μm wide and 125 μm in height. The flow was then visualised by recording the fluorescently conjugated beads with a fluorescence microscope. By using a long exposure time the velocity of the beads can be determined. The fluorescently labeled nano-carriers can be used both to visualize the flow inside the device and to test the permeability of the membrane to the nano-carriers. The flow will be visualised and velocity calculated as described by Babetski Holton et al.⁸. The permeability can be measured by adding a known concentration of nano-carriers to the input of the blood channel and perfusing the solution through the blood channel. The solution is collected from the output of the blood channel and after the experiment the medium from the brain channel is collected as well. The concentration of nano-carriers in the fluids can then be determined using a fluorimeter.

Unknown The tendency of the nano-carriers to clog the membrane is unknown, but assumed to be low since the nano-carriers are hydrophilic and small compared to the pore diameters.

Risks

Low risk:

The nano-carriers could clog the membrane, but the chance is small.

Mitigation

At the moment a research project is being performed at the department on preventing membrane fouling. If clogging of the membrane by the nano-carriers appears to be a problem the knowledge acquired in the membrane fouling project could be used to avoid fouling in the BBB-on-Chip project.

6.4 Timeline

To conclude this chapter the milestones, deliverables and activities are represented on a timeline. The red line defines the estimated time needed per activity. The coloured bars indicate the maximum scheduled time per activity, which should preferably not be exceeded to make sure the project will be finished within 50 ECTS.

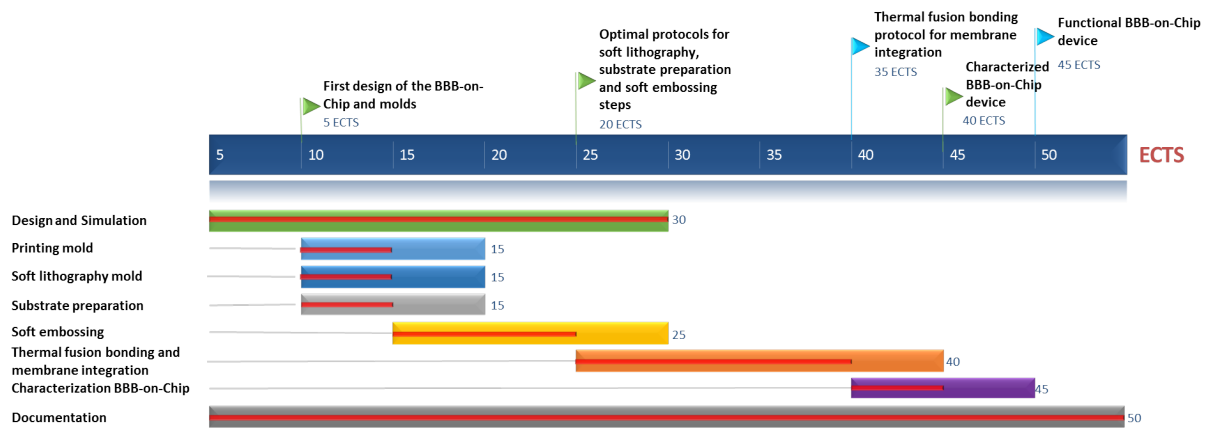


Figure 6.2: Timeline of the design, fabrication and characterization processes, with deliverables in green and milestones in blue.

Bibliography

- [1] Accu dyne test. URL https://www.accudynetest.com/polytable_03.html?sortby=contact_angle#branding.
- [2] Goodfellow catalogue. URL <http://www.goodfellow.com/catalogue/GFCatalogue.php?Language=E>.
- [3] Adam R. Abate, Daeyeon Lee, Thao Do, Christian Holtze, and David A. Weitz. Glass coating for PDMS microfluidic channels by solgel methods. *Lab on a Chip*, 8(4):516, 2008. ISSN 1473-0197. doi: 10.1039/b800001h. URL <http://xlink.rsc.org/?DOI=b800001h>.
- [4] N. Joan Abbott. Blood-brain barrier structure and function and the challenges for CNS drug delivery. *Journal of Inherited Metabolic Disease*, 36(3):437–449, 2013. ISSN 01418955. doi: 10.1007/s10545-013-9608-0.
- [5] N. Joan Abbott, Diana E.M. Dolman, Siti R. Yusof, and Andreas Reichel. In vitro models of CNS barriers. In Margareta Hammarlund-Udenaes, Elizabeth C.M. de Lange, and Robert G. Thorne, editors, *Drug Delivery to the Brain: Physiological Concepts, Methodologies and Approaches*, volume 10, chapter In Vitro M, pages 163–197. AAPS Advances in the Pharmaceutical Sciences Series, 2014. ISBN 978-1-4614-9104-0. doi: 10.1007/978-1-4614-9105-7. URL <http://link.springer.com/10.1007/978-1-4614-9105-7>.
- [6] Anil Kumar H. Achyuta, Amy J. Conway, Richard B. Crouse, Emilee C. Bannister, Robin N. Lee, Christopher P. Katnik, Adam a. Behensky, Javier Cuevas, and Shivshankar S. Sundaram. A modular approach to create a neurovascular unit-on-a-chip. *Lab on a Chip*, pages 542–553, 2013. ISSN 1473-0197. doi: 10.1039/c2lc41033h.
- [7] M Asplund, E Thaning, J Lundberg, A C Sandberg-Nordqvist, B Kostyszyn, O Inganäs, and H von Holst. Toxicity evaluation of PEDOT/biomolecular composites intended for neural communication electrodes. *Biomedical Materials*, 4(4):045009, 2009. ISSN 1748-6041. doi: 10.1088/1748-6041/4/4/045009. URL <http://stacks.iop.org/1748-605X/4/i=4/a=045009?key=crossref.71c6481d45d93c825e4139167dec446d>.
- [8] Angela Babetski Holton, Francy L. Sinatra, Jenny Kreamling, Amy J. Conway, David A. Landis, and Soner Altıok. Microfluidic Biopsy Trapping Device for the Real-Time Monitoring of Tumor Microenvironment - Supporting Information 1. *PLoS ONE*, 12(1), 2017. doi: 10.1371/journal.pone.0169797.
- [9] Kim M. Baeten and Katerina Akassoglou. Extracellular Matrix and Matrix Receptors in Blood-Brain Barrier Formation and Stroke. *Developmental Neurobiology*, 71(11):1018–1039, 2011. doi: 10.1002/dneu.20954.Extracellular.
- [10] B J Ballermann, a Dardik, E Eng, and a Liu. Shear stress and the endothelium. *Kidney international. Supplement*, 67:S100–S108, 1998. ISSN 0085-2538. doi: 10.1046/j.1523-1755.1998.06720.x.
- [11] BASF. Polystyrene and Styrolux, 2010.
- [12] Holger Becker and Claudia Gärtner. Polymer microfabrication technologies for microfluidic systems. *Analytical and Bioanalytical Chemistry*, 390(1):89–111, 2008. ISSN 16182642. doi: 10.1007/s00216-007-1692-2.
- [13] Holger Becker and Ulf Heim. Hot embossing as a method for the fabrication of polymer high aspect ratio structures. *Sensors and Actuators, A:Physical*, 83:130–135, 2000.

- [14] Kathrin Benson, Sandra Cramer, and Hans-joachim Galla. Impedance-based cell monitoring : barrier properties and beyond. *Fluids and Barriers of the CNS*, 10(5), 2013. doi: 10.1186/2045-8118-10-5.
- [15] Erwin Berthier, Edmond W. K. Young, and David Beebe. Engineers are from PDMS-land, Biologists are from Polystyrenia. *Lab on a Chip*, 12(7):1224, 2012. ISSN 1473-0197. doi: 10.1039/c2lc20982a. URL <http://xlink.rsc.org/?DOI=c2lc20982a>.
- [16] Joana Bicker, Gilberto Alves, Ana Fortuna, and Amílcar Falcao. Blood-brain barrier models and their relevance for a successful development of CNS drug delivery systems: A review. *European Journal of Pharmaceutics and Biopharmaceutics*, 87(3):409–432, 2014. ISSN 18733441. doi: 10.1016/j.ejpb.2014.03.012. URL <http://dx.doi.org/10.1016/j.ejpb.2014.03.012>.
- [17] L. F. Blume, M. Denker, F. Gieseler, and T. Kunze. Temperature corrected transepithelial electrical resistance (TEER) measurement to quantify rapid changes in paracellular permeability. *Pharmazie*, 65(1):19–24, 2010. ISSN 00317144. doi: 10.1691/ph.2010.9665.
- [18] Maria H. Bolin, Karl Svennersten, Xiangjun Wang, Ioannis S. Chronakis, Agneta Richter-Dahlfors, Edwin W H Jager, and Magnus Berggren. Nano-fiber scaffold electrodes based on PEDOT for cell stimulation. *Sensors and Actuators, B: Chemical*, 142(2):451–456, 2009. ISSN 09254005. doi: 10.1016/j.snb.2009.04.062.
- [19] Ross Booth and Hanseup Kim. Characterization of a microfluidic in vitro model of the blood-brain barrier (μ BBB). *Lab on a Chip*, 12(10):1784, 2012. ISSN 1473-0197. doi: 10.1039/c2lc40094d.
- [20] Ross Booth and Hanseup Kim. Permeability Analysis of Neuroactive Drugs Through a Dynamic Microfluidic In Vitro Blood-Brain Barrier Model. *Annals of Biomedical Engineering*, 42(12):2379–2391, 2014. ISSN 15739686. doi: 10.1007/s10439-014-1086-5.
- [21] Ross Booth, Seungbeom Noh, and Hanseup Kim. A high-throughput permeability assay platform for shear stress characterization of endothelial cells. *Proceedings of the IEEE International Conference on Micro Electro Mechanical Systems (MEMS)*, pages 238–241, 2014. ISSN 10846999. doi: 10.1109/MEMSYS.2014.6765619.
- [22] Jacquelyn A. Brown, Virginia Pensabene, Dmitry A. Markov, Vanessa Allwardt, M. Diana Neely, Mingjian Shi, Clayton M. Britt, Orlando S. Hoilett, Qing Yang, Bryson M. Brewer, Philip C. Samson, Lisa J. McCawley, James M. May, Donna J. Webb, Deyu Li, Aaron B. Bowman, Ronald S. Reiserer, and John P. Wikswo. Recreating blood-brain barrier physiology and structure on chip: A novel neurovascular microfluidic bioreactor. *Biomicrofluidics*, 9(5), 2015. ISSN 19321058. doi: 10.1063/1.4934713. URL <http://dx.doi.org/10.1063/1.4934713>.
- [23] Frederik Bundgaard. *Prototyping of Microfluidic Systems with Integrated Waveguides in Cyclic Olefin Copolymer (COC)*. PhD thesis, Technical University of Denmark, 2006.
- [24] Dean J. Campbell, Katie J. Beckman, Camilo E. Calderon, Patrick W. Doolan, Rebecca M. Ottosen, Arthur B. Ellis, and George C. Lisensky. Replication and Compression of Surface Structures with Polydimethylsiloxane Elastomer. *Journal of Chemical Education*, 76(4):537, 1999. ISSN 0021-9584. doi: 10.1021/ed076p537. URL <http://pubs.acs.org/doi/abs/10.1021/ed076p537>.
- [25] Filipa Lourenco Cardoso, Dora Brites, and Maria Alexandra Brito. Looking at the blood-brain barrier: Molecular anatomy and possible investigation approaches. *Brain Research Reviews*, 64(2):328–363, 2010. ISSN 01650173. doi: 10.1016/j.brainresrev.2010.05.003. URL <http://dx.doi.org/10.1016/j.brainresrev.2010.05.003>.
- [26] C T Chang. *Micromanufacturing of Conductive Polymer Electrodes for Sensing Microsystems*. PhD thesis, Delft University of Technology, 2017.
- [27] S. G. Charati and S. a. Stern. Diffusion of Gases in Silicone Polymers: Molecular Dynamics Simulations. *Macromolecules*, 31(98):5529–5535, 1998. ISSN 0024-9297. doi: 10.1021/ma980387e. URL <http://dx.doi.org/10.1021/ma980387e><http://pubs.acs.org/doi/abs/10.1021/ma980387e><http://pubs.acs.org/doi/full/10.1021/ma980387e><http://pubs.acs.org/doi/pdf/10.1021/ma980387e>.

- [28] Pin-chuan Chen, Chang-wei Pan, Wei-chen Lee, and Kuan-ming Li. Optimization of Micromilling Microchannels on a Polycarbonate Substrate. *International Journal of Precision Engineering and Manufacturing*, 15(1):149–154, 2014. doi: 10.1007/s12541-013-0318-1.
- [29] Caroline Cheng, Frank Helderma, Dennie Tempel, Dolf Segers, Beerend Hierck, Rob Poelmann, Arie van Tol, Dirk J. Duncker, Danielle Robbers-Visser, N. T C Ursem, Rien van Haperen, Jolanda J. Wentzel, Frank Gijzen, A. F W van der Steen, Rini de Crom, and Rob Krams. Large variations in absolute wall shear stress levels within one species and between species. *Atherosclerosis*, 195(2):225–235, 2007. ISSN 00219150. doi: 10.1016/j.atherosclerosis.2006.11.019.
- [30] Kv Christ, Bb Smith, Fe Pfefferkorn, and Kt Turner. Micro End Milling Polystyrene for Microfluidic Applications ICOMM/4M. *Core.Kmi.Open.Ac.Uk*, pages 423–430, 2010. URL <http://core.kmi.open.ac.uk/download/pdf/10597915.pdf>.
- [31] Dow Corning. Electronics Sylgard ® 184 Silicone Elastomer, 2013. ISSN 1098-6596.
- [32] Covestro Deutschland AG. Optical properties of Makrolon and apec for non-imaging optics, 2016.
- [33] Luca Cucullo, Mark S. McAllister, Kelly Kight, Ljiljana Krizanac-Bengez, Matteo Marroni, Marc R. Mayberg, Kathe A. Stanness, and Damir Janigro. A new dynamic in vitro model for the multidimensional study of astrocyte-endothelial cell interactions at the blood-brain barrier. *Brain Research*, 951(2):243–254, 2002. ISSN 00068993. doi: 10.1016/S0006-8993(02)03167-0.
- [34] Luca Cucullo, Nicola Marchi, Mohammed Hossain, and Damir Janigro. A dynamic in vitro BBB model for the study of immune cell trafficking into the central nervous system. *Journal of cerebral blood flow and metabolism : official journal of the International Society of Cerebral Blood Flow and Metabolism*, 31(2):767–777, 2011. ISSN 1559-7016. doi: 10.1038/jcbfm.2010.162. URL <http://dx.doi.org/10.1038/jcbfm.2010.162>.
- [35] Luca Cucullo, Mohammed Hossain, William Tierney, and Damir Janigro. A new dynamic in vitro modular capillaries-venules modular system: cerebrovascular physiology in a box. *BMC neuroscience*, 14(1):18, 2013. ISSN 1471-2202. doi: 10.1186/1471-2202-14-18. URL <http://www.pubmedcentral.nih.gov/articlerender.fcgi?artid=3598202&tool=pmcentrez&rendertype=abstract>.
- [36] L. J. del Valle, D. Aradilla, R. Oliver, F. Sepulcre, A. Gamez, E. Armelin, C. Alemán, and F. Estrany. Cellular adhesion and proliferation on poly(3,4-ethylenedioxythiophene): Benefits in the electroactivity of the conducting polymer. *European Polymer Journal*, 43(6):2342–2349, 2007. ISSN 00143057. doi: 10.1016/j.eurpolymj.2007.03.050.
- [37] Sudhir P. Deosarkar, Balabhaskar Prabhakarandian, Bin Wang, Joel B. Sheffield, Barbara Krynska, and Mohammad F. Kiani. A novel dynamic neonatal blood-brain barrier on a chip. *PLoS ONE*, 10(11):1–21, 2015. ISSN 19326203. doi: 10.1371/journal.pone.0142725.
- [38] Kaouthar Dhouib, Chantal Khan Malek, Wilhelm Pfleging, Bernard Gauthier-Manuel, Roland Duffait, Gaël Thuillier, Rosaria Ferrigno, Lilian Jacquamet, Jeremy Ohana, Jean-Luc Ferrer, Anne Théobald-Dietrich, Richard Giegé, Bernard Lorber, and Claude Sauter. Microfluidic chips for the crystallization of biomacromolecules by counter-diffusion and on-chip crystal X-ray analysis. *Lab Chip*, 9(10):1412–21, 2009. ISSN 1473-0197. doi: 10.1039/b819362b. URL <http://www.ncbi.nlm.nih.gov/pubmed/19417908>.
- [39] Shane M. Eaton, Carmela De Marco, Rebeca Martinez-Vazquez, Roberta Ramponi, Stefano Turri, Giulio Cerullo, and Roberto Osellame. Femtosecond laser microstructuring for polymeric lab-on-chips. *Journal of Biophotonics*, 5(8-9):687–702, 2012. ISSN 1864-0648. doi: 10.1002/jbio.201200048. URL <http://dx.doi.org/10.1002/jbio.201200048>.
- [40] G Eibl, H G Hotz, J Faulhaber, M Kirchengast, H J Buhr, and Th Foitzik. Effect of endothelin and endothelin receptor blockade on capillary permeability in experimental pancreatitis. *Gut*, 46:390–394, 2000. doi: 10.1136/gut.46.3.390.

- [41] A Ettinger and T Wittmann. Fluorescence Live Cell Imaging. *Methods in Cell Biology*, 123:77–94, 2015. doi: 10.1016/B978-0-12-420138-5.00005-7.Fluorescence.
- [42] EVOM2 Manual. EVOM2 Manual, 2015. URL <http://www.wpi-europe.com/products/cell-and-tissue/teer-measurement/evom2.aspx>.
- [43] Paola Fanzio, Alberto Cagliani, Kristof G. Peterffy, and Luigi Sasso. High throughput soft embossing process for micro-patterning of PEDOT thin films. *Microelectronic Engineering*, 176:15–21, 2017. ISSN 01679317. doi: 10.1016/j.mee.2017.01.011. URL <http://dx.doi.org/10.1016/j.mee.2017.01.011>.
- [44] Paola Fanzio, Chi-Tung Chang, Maciej Skolimowski, Simone Tanzi, and Luigi Sasso. Fully-Polymeric pH Sensor Realized by Means of a Single-Step Soft Embossing Technique. *Sensors*, 17(6):1169, 2017. ISSN 1424-8220. doi: 10.3390/s17051169. URL <http://www.mdpi.com/1424-8220/17/5/1169>.
- [45] Ronald L. Fournier. *Basic transport phenomena in biomedical engineering*. Francis & Taylor, 1999.
- [46] Carl K. Fredrickson, Zheng Xia, Champak Das, Ryan Ferguson, Fernando T. Tavares, and Z. Hugh Fan. Effects of fabrication process parameters on the properties of cyclic olefin copolymer microfluidic devices. *Journal of Microelectromechanical Systems*, 15(5):1060–1068, 2006. ISSN 10577157. doi: 10.1109/JMEMS.2006.880352.
- [47] Jennifer L. Fritz and Michael J. Owen. Hydrophobic Recovery of Plasma-Treated Polydimethylsiloxane. *The Journal of Adhesion*, 54(1-4):33–45, 1995. ISSN 0021-8464. doi: 10.1080/00218469508014379. URL <http://www.tandfonline.com/doi/abs/10.1080/00218469508014379>.
- [48] Pieter Jaap Gaillard and Albertus Gerrit De Boer. Relationship between permeability status of the blood-brain barrier and in vitro permeability coefficient of a drug. *European Journal of Pharmaceutical Sciences*, 12(2):95–102, 2000. ISSN 09280987. doi: 10.1016/S0928-0987(00)00152-4.
- [49] Rafael Gomez-Sjoberg, Anne A. Leyrat, Benjamin T. Houseman, Kevan Shokat, and Stephen R. Quake. Biocompatibility and reduced drug absorption of sol-gel-treated poly(dimethyl siloxane) for microfluidic cell culture applications. *Analytical Chemistry*, 82(21):8954–8960, 2010. ISSN 00032700. doi: 10.1021/ac101870s.
- [50] V.N. Goral, Y.-C. Hsieh, O.N. Petzold, R.A. Faris, and P.K. Yuen. Hot embossing of plastic microfluidic devices using poly (dimethylsiloxane) molds. In *14th International Conference on Miniaturized Systems for Chemistry and Life Sciences*, pages 1214–1216, 2010. ISBN 9780979806438. doi: 10.1088/0960-1317/21/1/017002. URL <http://iopscience.iop.org/0960-1317/21/1/017002>.
- [51] L. M. Griep, F. Wolbers, B. De Wagenaar, P. M. Ter Braak, Babette Weksler, Ignacio a Romero, Pierre Oliver Couraud, I. Vermes, Andries D van der Meer, and Albert van den Berg. BBB on CHIP: Microfluidic platform to mechanically and biochemically modulate blood-brain barrier function. *Biomedical Microdevices*, 15(1):145–150, 2013. ISSN 13872176. doi: 10.1007/s10544-012-9699-7.
- [52] M. Grumann, J. Steigert, L. Riegger, I. Moser, B. Enderle, K. Riebeseel, G. Urban, R. Zengerle, and J. Ducrée. Sensitivity enhancement for colorimetric glucose assays on whole blood by on-chip beam-guidance. *Biomedical Microdevices*, 8(3):209–214, 2006. ISSN 13872176. doi: 10.1007/s10544-006-8172-x.
- [53] David John Guckenberger, Theodorus de Groot, Alwin Ming-Doug Wan, David Beebe, and Edmond Young. Micromilling: A method for ultra-rapid prototyping of plastic microfluidic devices. *Lab Chip*, 15(11):2364–2378, 2015. ISSN 1473-0197. doi: 10.1039/C5LC00234F. URL <http://pubs.rsc.org/globalproxy.cvt.dk/en/content/articlehtml/2015/lc/c5lc00234f>.
- [54] Afra Hadjizadeh and Charles J Doillon. Directional migration of endothelial cells towards angiogenesis using polymer fibres in a 3D co-culture system. *Journal of tissue engineering and regenerative medicine*, 4(7):524–531, 2010. ISSN 1932-7005. doi: 10.1002/term.

- [55] Skarphedinn Halldorsson, Edinson Lucumi, Rafael Gómez-sjöberg, and Ronan M T Fleming. Biosensors and Bioelectronics Advantages and challenges of micro fluidic cell culture in polydimethylsiloxane devices. *Biosensors and Bioelectronics*, 63:218–231, 2015. ISSN 0956-5663. doi: 10.1016/j.bios.2014.07.029. URL <http://dx.doi.org/10.1016/j.bios.2014.07.029>.
- [56] Yun Seok Heo, Lourdes M. Cabrera, Jonathan W. Song, Nobuyuki Futai, Yi Chung Tung, Gary D. Smith, and Shuichi Takayama. Characterization and resolution of evaporation-mediated osmolality shifts that constrain microfluidic cell culture in poly(dimethylsiloxane) devices. *Analytical Chemistry*, 79(3):1126–1134, 2007. ISSN 00032700. doi: 10.1021/ac061990v.
- [57] Amy M. Hopkins, Elise DeSimone, Karolina Chwalek, and David L. Kaplan. 3D in vitro modeling of the central nervous system. *Progress in Neurobiology*, 125:1–25, 2015. ISSN 18735118. doi: 10.1016/j.pneurobio.2014.11.003. URL <http://dx.doi.org/10.1016/j.pneurobio.2014.11.003>.
- [58] Rajeeb K. Jena and C. Y. Yue. Cyclic olefin copolymer based microfluidic devices for biochip applications: Ultraviolet surface grafting using 2-methacryloyloxyethyl phosphorylcholine. *Biomicrofluidics*, 6(1):1–12, 2012. ISSN 19321058. doi: 10.1063/1.3682098.
- [59] Rajeeb K. Jena, C. Y. Yue, and Y. C. Lam. Micro fabrication of cyclic olefin copolymer (COC) based microfluidic devices. *Microsystem Technologies*, 18(2):159–166, 2012. ISSN 09467076. doi: 10.1007/s00542-011-1366-z.
- [60] Boran Jia. *Department of Precision and Microsystems Engineering*. PhD thesis, Delft University of Technology, 2017.
- [61] Bo Lennart Johansson, Anders Larsson, Anette Ocklind, and Åke Öhrlund. Characterization of air plasma-treated polymer surfaces by ESCA and contact angle measurements for optimization of surface stability and cell growth. *Journal of Applied Polymer Science*, 86(10):2618–2625, 2002. ISSN 00218995. doi: 10.1002/app.11209.
- [62] Jan Kafka, Niels B. Larsen, Steen Skaarup, and Oliver Geschke. Fabrication of an all-polymer electrochemical sensor by using a one-step hot embossing procedure. *Microelectronic Engineering*, 87(5-8):1239–1241, 2010. ISSN 01679317. doi: 10.1016/j.mee.2009.11.137. URL <http://dx.doi.org/10.1016/j.mee.2009.11.137>.
- [63] a Kamiya and T Togawa. Adaptive regulation of wall shear stress to flow change in the canine carotid artery. *The American journal of physiology*, 239(1):H14–H21, 1980. ISSN 0002-9513. doi: 7396013.
- [64] Akira Kamiya, Razaq Bukhari, and Tatsuo Togawa. Adaptive regulation of wall shear stress optimizing vascular tree function. *Bulletin of Mathematical Biology*, 46(1):127–137, 1984. ISSN 00928240. doi: 10.1007/BF02463726.
- [65] Aristotle G Koutsiaris. Un co rre cte d Au tho r P roo f Un co rre cte d Au tho r P roo f. doi: 10.3233/CH-151976.
- [66] Aristotle G Koutsiaris, Sophia V Tachmitzi, Nick Batis, Maria G Kotoula, Constantinos H Karabatsas, Evagelia Tsironi, and Dimitrios Z Chatzoulis. Volume flow and wall shear stress quantification in the human conjunctival capillaries and post-capillary venules in vivo. *Biorheology*, 44(5-6): 375–86, 2007. ISSN 0006-355X. URL <http://www.ncbi.nlm.nih.gov/pubmed/18401076>.
- [67] Aristotle G Koutsiaris, Sophia V. Tachmitzi, and Nick Batis. Wall shear stress quantification in the human conjunctival pre-capillary arterioles in vivo. *Microvascular Research*, 85(1):34–39, 2013. ISSN 00262862. doi: 10.1016/j.mvr.2012.11.003. URL <http://dx.doi.org/10.1016/j.mvr.2012.11.003>.
- [68] Alexander Kros, Nico A.J.M. Sommerdijk, and Roeland J.M. Nolte. Poly(pyrrole) versus poly(3,4-ethylenedioxythiophene): Implications for biosensor applications. *Sensors and Actuators, B: Chemical*, 106(1 SPEC. ISS.):289–295, 2005. ISSN 09254005. doi: 10.1016/j.snb.2004.08.011.

- [69] Véronique Lecault, Michael VanInsberghe, Sanja Sekulovic, David J H F Knapp, Stefan Wohrer, William Bowden, Francis Viel, Thomas McLaughlin, Asefeh Jarandehi, Michelle Miller, Didier Falconnet, Adam K White, David G Kent, Michael R Copley, Fariborz Taghipour, Connie J Eaves, R Keith Humphries, James M Piret, and Carl L Hansen. High-throughput analysis of single hematopoietic stem cell proliferation in microfluidic cell culture arrays. *Nature Methods*, 8(7):581–586, 2011. ISSN 1548-7091. doi: 10.1038/nmeth.1614. URL <http://www.nature.com/doi/10.1038/nmeth.1614>.
- [70] Jessamine Ng Lee, Cheolmin Park, and George M. Whitesides. Solvent Compatibility of Poly(dimethylsiloxane)-Based Microfluidic Devices. *Analytical Chemistry*, 75(23):6544–6554, 2003. ISSN 00032700. doi: 10.1021/ac0346712.
- [71] Jin-Hwan Lee, Erik T K Peterson, Gabriel Dagani, and Ian Papautsky. Rapid prototyping of plastic microfluidic devices in cyclic olefin copolymer (COC). *Proc. SPIE*, 5718:82–91, 2005. ISSN 0277786X. doi: 10.1117/12.591852. URL <http://dx.doi.org/10.1117/12.591852>.
- [72] Patrick W. Leech. Effect of norbornene content on laser ablation of cyclic olefin copolymers. *Materials & Design*, 31(10):4858 – 4861, 2010. ISSN 0261-3069. doi: <http://dx.doi.org/10.1016/j.matdes.2010.05.038>. URL <http://www.sciencedirect.com/science/article/pii/S0261306910003316>.
- [73] Huawei Li, Yiqiang Fan, Rimantas Kodzius, and Ian G. Foulds. Fabrication of polystyrene microfluidic devices using a pulsed CO2 laser system. *Microsystem Technologies*, 18(3):373–379, 2011. ISSN 0946-7076. doi: 10.1007/s00542-011-1410-z. URL <http://www.springerlink.com/index/10.1007/s00542-011-1410-z>.
- [74] Vincent Linder, Byron D. Gates, Declan Ryan, Babak A. Parviz, and George M. Whitesides. Water-soluble sacrificial layers for surface micromachining. *Small*, 1(7):730–736, 2005. ISSN 16136810. doi: 10.1002/sml.200400159.
- [75] Thomas Lippert. *UV Laser Ablation of Polymers: From Structuring to Thin Film Deposition*, pages 141–175. Springer Berlin Heidelberg, Berlin, Heidelberg, 2010. ISBN 978-3-642-03307-0. doi: 10.1007/978-3-642-03307-0_7. URL https://doi.org/10.1007/978-3-642-03307-0_7.
- [76] L E Locascio, D J Ross, P B Howell, and M Gaitan. Fabrication of polymer microfluidic systems by hot embossing and laser ablation. *Methods Mol Biol*, 339(1):37–46, 2006. ISSN 1064-3745. doi: 10.1385/1-59745-076-6:37. URL <http://www.ncbi.nlm.nih.gov/pubmed/16790865> <http://download.springer.com/static/pdf/651/chp/253A10.1385-252F1-59745-076-6-253A37.pdf?auth66=1406187205{ }ae134393429ee70c3496cd5bc576e5ec{ }ext=.pdf>.
- [77] F. Louwet, L. Groenendaal, J. Dhaen, J. Manca, J. Van Luppen, E. Verdonck, and L. Leenders. Pedot/pss: synthesis, characterization, properties and applications. *Synthetic Metals*, 135(Supplement C):115 – 117, 2003. ISSN 0379-6779. doi: [https://doi.org/10.1016/S0379-6779\(02\)00518-0](https://doi.org/10.1016/S0379-6779(02)00518-0). URL <http://www.sciencedirect.com/science/article/pii/S0379677902005180>. Proceedings of the International Conference on Science and Technology of Synthetic Metals.
- [78] Shyh-chyang Luo, Emril Mohamed Ali, Natalia C Tansil, Hsiao-hua Yu, Shujun Gao, Eric a B Kantchev, and Jackie Y Ying. Thin , Ultrasmooth , and Functionalized PEDOT Films with in Vitro and in Vivo Biocompatibility Ultrasmooth , and Functionalized PEDOT Films with in Vitro and in Vivo Biocompatibility. *Society*, (c):8071–8077, 2008. doi: 10.1021/la800333g.
- [79] Marc J. Madou. *Fundamentals of microfabrication : the science of miniaturization*. Boca Raton: CRC Press, 2 edition.
- [80] Elaine Nicpon Marieb, Katja Hoehn, Matt Hutchinson, and R.T. Hutchings. *Human anatomy & physiology*. Pearson Education, Inc., 9th edition, 2013.
- [81] Dmitry A. Markov, Elizabeth M. Lillie, Shawn P. Garbett, and Lisa J. McCawley. Variation in diffusion of gases through PDMS due to plasma surface treatment and storage conditions. *Biomedical Microdevices*, 16(1):91–96, 2014. ISSN 13872176. doi: 10.1007/s10544-013-9808-2.

- [82] R. McCann, K. Bagga, A. Stalcup, M. Vázquez, and D. Brabazon. Laser micro-engineering of functionalized cyclic olefin polymers for microfluidic applications. volume 9351, 2015. doi: 10.1117/12.2076916. URL <https://www.scopus.com/inward/record.uri?eid=2-s2.0-84930037823&doi=10.1117%2f12.2076916&partnerID=40&md5=dd61bfe94cf8885c463d7e0911a986cd>. cited By 0.
- [83] J C McDonald, D C Duffy, J R Anderson, D T Chiu, H Wu, O J Schueller, and G M Whitesides. Fabrication of microfluidic systems in poly(dimethylsiloxane). *Electrophoresis*, 21(1):27–40, 2000. ISSN 01730835 (ISSN). doi: 10.1002/(SICI)1522-2683(20000101)21:1<27::AID-ELPS27>3.0.CO;2-C.
- [84] G Mehta, J Lee, W Cha, Y C Tung, J J Linderman, and S Takayama. Hard top soft bottom microfluidic devices for cell culture and chemical analysis. *Anal Chem*, 81(10):3714–3722, 2009. ISSN 1520-6882. doi: 10.1021/ac802178u[doi].
- [85] Sukriti Nag. The Blood-Brain Barrier. In Sukriti Nag, editor, *The Blood-Brain Barrier - Biology and Research Protocols*, chapter Morphology, pages 3–36. Humana Press, Totowa, New Jersey, 2003. ISBN 978-1-58829-073-1. doi: 10.1385/1-59259-419-0:385. URL <http://dx.doi.org/10.1385/1-59259-419-0:385>.
- [86] Pooja Naik and Luca Cucullo. In vitro blood-brain barrier models: Current and perspective technologies. *Journal of Pharmaceutical Sciences*, 101(4):1337–1354, 2012. ISSN 00223549. doi: 10.1002/jps.23022. URL <http://dx.doi.org/10.1002/jps.23022>.
- [87] Shinsuke Nakagawa, M??ria A. Deli, Hiroko Kawaguchi, Takeshi Shimizudani, Takanori Shimono, ??gnes Kittel, Kunihiro Tanaka, and Masami Niwa. A new blood-brain barrier model using primary rat brain endothelial cells, pericytes and astrocytes. *Neurochemistry International*, 54(3-4):253–263, 2009. ISSN 01970186. doi: 10.1016/j.neuint.2008.12.002.
- [88] NanoAnalytics. cellZscope - How It Works.
- [89] Jagannathan Narasimhan and Ian Papautsky. Polymer embossing tools for rapid prototyping of plastic microfluidic devices. *Journal of Micromechanics and Microengineering*, 14:96–103, 2003. ISSN 0960-1317. doi: 10.1088/0960-1317/14/1/013.
- [90] Robert J Naumann. *PHYSICS and CHEMISTRY of MATERIALS*. CRC Press - Taylor & Francis Group, 2008. ISBN 9781420061345.
- [91] Winfried Neuhaus, Regina Lauer, Silvester Oelzant, Urs P. Fringeli, Gerhard F. Ecker, and Christian R. Noe. A novel flow based hollow-fiber blood-brain barrier in vitro model with immortalised cell line PBMEC/C1-2. *Journal of Biotechnology*, 125(1):127–141, 2006. ISSN 01681656. doi: 10.1016/j.jbiotec.2006.02.019.
- [92] Walter D. Niles and Peter J. Coassin. Cyclic Olefin Polymers: Innovative Materials for High-Density Multiwell Plates. *ASSAY and Drug Development Technologies*, 6(4):577–590, 2008. ISSN 1540-658X. doi: 10.1089/adt.2008.134. URL <http://www.liebertonline.com/doi/abs/10.1089/adt.2008.134>.
- [93] Pedro S. Nunes, Pelle D. Ohlsson, Olga Ordeig, and Jörg P. Kutter. Cyclic olefin polymers: Emerging materials for lab-on-a-chip applications. *Microfluidics and Nanofluidics*, 9(2-3):145–161, 2010. ISSN 16134982. doi: 10.1007/s10404-010-0605-4.
- [94] Mathieu Odijk, Andries D van der Meer, Daniel Levner, Hyun Jung Kim, Marinke van der Helm, Loes I Segerink, Jean-Phillipe Frimat, Geraldine A Hamilton, Donald E Ingber, and Albert van den Berg. Measuring direct current trans-epithelial electrical resistance in organ-on-a-chip microsystems. *Lab on a chip*, 15(3):745–52, 2015. ISSN 1473-0189. doi: 10.1039/c4lc01219d. URL <http://pubs.rsc.org/en/content/articlehtml/2015/1c/c4lc01219d>.
- [95] I R G Ogilvie, V J Sieben, C F a Floquet, R Zmijan, M C Mowlem, and H Morgan. Solvent processing of PMMA and COC chips for bonding devices with optical quality surfaces. *14th International Conference on Miniaturized Systems for Chemistry and Life Sciences*, (October):1244–1246, 2010. ISSN 0960-1317. doi: 10.1088/0960-1317/20/6/065016.

- [96] D. Ogonczyk, J. Wegrzyn, P Jankowski, B Dabrowski, and P Garstecki. Bonding of microfluidic devices fabricated in polycarbonate. *Lab on a Chip*, 10:1324–1327, 2010. doi: 10.1039/b924439e.
- [97] J. B. Orhan, V. K. Parashar, J. Flueckiger, and M. A M Gijs. Internal modification of poly(dimethylsiloxane) microchannels with a borosilicate glass coating. *Langmuir*, 24(16):9154–9161, 2008. ISSN 07437463. doi: 10.1021/la801317x.
- [98] Aigars Piruska, Irena Nikcevic, Se Hwan Lee, Chong Ahn, William R. Heineman, Patrick A. Limbach, and Carl J. Seliskar. The autofluorescence of plastic materials and chips measured under laser irradiation. *Lab on a Chip*, 5(12):1348, 2005. ISSN 1473-0197. doi: 10.1039/b508288a. URL <http://xlink.rsc.org/?DOI=b508288a>.
- [99] Balabhaskar Prabhakarandian, Ming-Che Shen, Joseph B Nichols, Ivy R Mills, Marta Sidoryk-Wegrzynowicz, Michael Aschner, and Kapil Pant. SyM-BBB: a microfluidic blood brain barrier model. *Lab on a Chip*, 13(6):1093–1101, 2013. ISSN 1473-0189 (Electronic). doi: 10.1039/c2lc41208j. URL <http://dx.doi.org/10.1039/C2LC41208J>.
- [100] Keil J Regehr, Maribella Domenech, Justin T Koepsel, Kristopher C Carver, J Ellison-zelski, William L Murphy, Linda A Schuler, Elaine T Alarid, and J David. Biological implications of polydimethylsiloxane-based microfluidic cell culture. *Lab on a chip*, 9(15):2132–2139, 2009. doi: 10.1039/b903043c.Biological.
- [101] Adam Reinitz, Jackson DeStefano, Mao Ye, Andrew D. Wong, and Peter C. Searson. Human brain microvascular endothelial cells resist elongation due to shear stress. *Microvascular Research*, 99: 8–18, 2015. ISSN 10959319. doi: 10.1016/j.mvr.2015.02.008. URL <http://dx.doi.org/10.1016/j.mvr.2015.02.008>.
- [102] Robert S. Reneman, Hans Vink, and Arnold P G Hoeks. Wall shear stress revisited. *Artery Research*, 3(2):73–78, 2009. ISSN 18729312. doi: 10.1016/j.artres.2009.02.005. URL <http://dx.doi.org/10.1016/j.artres.2009.02.005>.
- [103] Pouya Rezai, P Ravi Selvaganapathy, and Gregory R Wohl. Plasma enhanced bonding of polydimethylsiloxane with parylene and its optimization. *Journal of Micromechanics and Microengineering*, 21(6):065024, 2011. ISSN 0960-1317. doi: 10.1088/0960-1317/21/6/065024. URL <http://stacks.iop.org/0960-1317/21/i=6/a=065024?key=crossref.dd813fcaf523f2a33f02d8cd4f9c12d8>.
- [104] Stephen J Royle. The cellular functions of clathrin Clathrin genes. *Cellular and molecular life sciences*, 63(16):1823–1832, 2006. doi: 10.1007/s00018-005-5587-0.The.
- [105] Dirk Sabbert, Jörg Landsiedel, Hans Dieter Bauer, and Wolfgang Ehrfeld. ArF-excimer laser ablation experiments on Cycloolefin Copolymer (COC). *Applied Surface Science*, 150(1):185–189, 1999. ISSN 01694332. doi: 10.1016/S0169-4332(98)00334-1.
- [106] Eric K. Sackmann, Anna L. Fulton, and David J. Beebe. The present and future role of microfluidics in biomedical research. *Nature*, 507(7491):181–189, 2014. ISSN 0028-0836. doi: 10.1038/nature13118. URL <http://www.nature.com/doi/10.1038/nature13118>.
- [107] Vinny R. Sastri. Chapter 6 - commodity thermoplastics: Polyvinyl chloride, polyolefins, and polystyrene. In Vinny R. Sastri, editor, *Plastics in Medical Devices*, Plastics Design Library, pages 73 – 119. William Andrew Publishing, Boston, 2010. ISBN 978-0-8155-2027-6. doi: <https://doi.org/10.1016/B978-0-8155-2027-6.10006-6>. URL <http://www.sciencedirect.com/science/article/pii/B9780815520276100066>.
- [108] M Sato and Toshiro Ohashi. Biorheological views of endothelial cell responses to mechanical stimuli. *Biorheology*, 42(6):421–441, 2005. ISSN 0006-355X.
- [109] Masaaki Sato, Murina J Levesque, and Robert M Nerem. Micropipette Aspiration of Cultured Bovine Aortic Endothelial Cells Exposed to Shear Stress. *Arteriosclerosis, Thrombosis, and Vascular Biology*, 7:276–286, 1987. doi: <http://dx.doi.org/10.1161/01.ATV.7.3.276>.

- [110] Norman R Saunders, Jean-jacques Dreifuss, Katarzyna M Dziegielewska, Pia A Johansson, Mark D Habgood, Kjeld Møllgård, and Hans-christian Bauer. The rights and wrongs of blood-brain barrier permeability studies : a walk through 100 years of history. *Frontiers in neuroscience*, 8(December): 1–26, 2014. doi: 10.3389/fnins.2014.00404.
- [111] Katelyn L. Sellgren, Brian T. Hawkins, and Sonia Grego. An optically transparent membrane supports shear stress studies in a three-dimensional microfluidic neurovascular unit model. *Biomedical microfluidics*, 9(6):48–52, 2015. ISSN 19321058. doi: 10.1063/1.4935594. URL <http://dx.doi.org/10.1063/1.4935594>.
- [112] Ju Young Shin, Ji Yong Park, Chenyang Liu, Jiasong He, and Sung Chul Kim. Chemical structure and physical properties of cyclic olefin copolymers. *Pure and Applied Chemistry*, 77(5):801–814, 2005. ISSN 0033-4545. doi: 10.1351/pac200577050801. URL <http://www.degruyter.com/dg/viewarticle.fullcontentlink:pdfeventlink/{\protect\T1\textdollar}002fj{\protect\T1\textdollar}002fpac.2005.77.issue-5{\protect\T1\textdollar}002fpac200577050801{\protect\T1\textdollar}002fpac200577050801.pdf?t:ac=j{\protect\T1\textdollar}002fpac.2005.77.issue-5{\protect\T1\textdollar}002fpac200577050801{\protect\T1\textdollar}002fpac200577050801.xml>.
- [113] A C Shore, D D Sandeman, and J E Tooke. Capillary pressure , pulse pressure and pressure waveform in healthy amplitude , volunteers. *American Journal of Physiology*, 268(1 PT 2):H147–54, 1995.
- [114] S. Singaravelu, J. M. Klopff, K. E. Schriver, H. K. Park, M. J. Kelley, and R. F. Haglund. Resonant infrared pulsed laser deposition of cyclic olefin copolymer films. *Applied Physics A*, 114(4):1285–1293, Mar 2014. ISSN 1432-0630. doi: 10.1007/s00339-013-7933-7. URL <https://doi.org/10.1007/s00339-013-7933-7>.
- [115] Younggon Son. Determination of shear viscosity and shear rate from pressure drop and flow rate relationship in a rectangular channel. 48:632–637, 2007. doi: 10.1016/j.polymer.2006.11.048.
- [116] Spectra Physics. Disruptive cost-performance uv and green lasers, 2016. URL <http://www.spectra-physics.com/products/q-switched-lasers/talon>.
- [117] Balaji Srinivasan, Aditya Reddy Kolli, Mandy Brigitte Esch, Hasan Erbil Abaci, Michael L Shuler, and James J Hickman. TEER Measurement Techniques for In Vitro Barrier Model Systems. *Journal of Laboratory Automation*, 20(2):107–126, 2015. doi: 10.1177/2211068214561025.
- [118] J Steigert, S Haeberle, T Brenner, C Müller, C P Steinert, P Koltay, N Gottschlich, H Reinecke, J Rühle, R Zengerle, and J Ducrée. Rapid prototyping of microfluidic chips in COC. *Journal of Micromechanics and Microengineering*, 17(2):333–341, 2007. ISSN 0960-1317. doi: 10.1088/0960-1317/17/2/020.
- [119] Serguei Stoukatch. Low-Temperature Microassembly Methods and Integration Techniques for Biomedical Application. In *Wireless Medical Systems and Algorithms*, pages 21–42. 2016.
- [120] Raffaella Suriano, Arseniy Kuznetsov, Shane M. Eaton, Roman Kiyan, Giulio Cerullo, Roberto Osellame, Boris N. Chichkov, Marinella Levi, and Stefano Turri. Femtosecond laser ablation of polymeric substrates for the fabrication of microfluidic channels. *Applied Surface Science*, 257(14): 6243 – 6250, 2011. ISSN 0169-4332. doi: <http://dx.doi.org/10.1016/j.apsusc.2011.02.053>. URL <http://www.sciencedirect.com/science/article/pii/S0169433211002443>.
- [121] Marta Tajés, Eva Ramos-Fernández, Xian Weng-Jiang, Mònica Bosch-Morató, Biuse Guivernau, Abel Eraso-Pichot, Bertrán Salvador, Xavier Fernández-Busquets, Jaume Roquer, and Francisco J Muñoz. The blood-brain barrier: Structure, function and therapeutic approaches to cross it. *Molecular membrane biology*, 31(5):152–67, 2014. ISSN 1464-5203. doi: 10.3109/09687688.2014.937468. URL <http://www.ncbi.nlm.nih.gov/pubmed/25046533>.
- [122] G J Tangelder, D W Slaaf, a M Muijtjens, T Arts, M G oude Egbrink, and R S Reneman. Velocity profiles of blood platelets and red blood cells flowing in arterioles of the rabbit mesentery. *Circulation Research*, 59(5):505–514, 1986. ISSN 0009-7330. doi: 10.1161/01.RES.59.5.505.

- [123] Vijay Kumar Thakur and Kumari Manju Thakur. *Handbook of Polymers for Pharmaceutical Technologies Volume 2 Processing and Applications*. Wiley Scrivener, 2015. ISBN 9781119041382.
- [124] T Tilling, D Korte, D Hoheisel, and H J Galla. Basement membrane proteins influence brain capillary endothelial barrier function in vitro. *Journal of neurochemistry*, 71(3):1151–1157, 1998. ISSN 0022-3042. doi: 10.1046/j.1471-4159.1998.71031151.x.
- [125] Michael W. Toepke and David J. Beebe. PDMS absorption of small molecules and consequences in microfluidic applications. *Lab on a Chip*, 6(12):1484, 2006. ISSN 1473-0197. doi: 10.1039/b612140c. URL <http://xlink.rsc.org/?DOI=b612140c>.
- [126] Topas Advanced Polymers. TOPAS- Cyclic Olefin Copolymers, 2015. URL [http://www.topas.com/sites/default/files/files/TOPAS{}_Brochure{}_E{}_2014{}_06\(1\).pdf](http://www.topas.com/sites/default/files/files/TOPAS{}_Brochure{}_E{}_2014{}_06(1).pdf).
- [127] Erica Tornabene and Birger Brodin. Stroke and Drug Delivery - In Vitro Models of the Ischemic Blood-Brain Barrier. *Journal of Pharmaceutical Sciences*, 105(2):398–405, 2016. ISSN 0022-3549. doi: 10.1016/j.xphs.2015.11.041. URL <http://dx.doi.org/10.1016/j.xphs.2015.11.041>.
- [128] Rafael Torres, Luciano Pizarro, Attila Csendes, Carlos García, and Néstor Lagos. GTX 2/3 epimers permeate the intestine through a paracellular pathway. *The Journal of toxicological sciences*, 32(3):241–8, 2007. ISSN 0388-1350. doi: 10.2131/jts.32.241. URL <http://www.ncbi.nlm.nih.gov/pubmed/17785941>.
- [129] Reginald Tran, Byungwook Ahn, David R Myers, Yongzhi Qiu, Yumiko Sakurai, Robert Moot, Emma Mihevc, H Trent Spencer, Christopher Doering, and Wilbur A Lam. Simplified prototyping of perfusable polystyrene microfluidics. *Biomicrofluidics*, 8(4):046501, 2014. ISSN 1932-1058. doi: 10.1063/1.4892035. URL <http://www.ncbi.nlm.nih.gov/pubmed/25379106>{%}5Cn<http://www.pubmedcentral.nih.gov/articlerender.fcgi?artid=PMC4189295>.
- [130] Chia Wen Tsao. Polymer microfluidics: Simple, low-cost fabrication process bridging academic lab research to commercialized production. *Micromachines*, 7(12), 2016. ISSN 2072666X. doi: 10.3390/mi7120225.
- [131] Chia-Wen Tsao and Don L. DeVoe. Bonding of thermoplastic polymer microfluidics. *Microfluidics Nanofluidics*, 6(1):1–16, 2009. doi: 10.1007/s10404-008-0361-x.
- [132] Marinke van der Helm, Andries van der Meer, Jan Eijkel, Albert van den Berg, and Loes Segerink. Microfluidic organ-on-chip technology for blood-brain barrier research. *Tissue Barriers*, 8370(May):00–00, 2016. ISSN 2168-8370. doi: 10.1080/21688370.2016.1142493. URL <http://www.tandfonline.com/doi/full/10.1080/21688370.2016.1142493>.
- [133] P.M. Van Midwoud, A. Janse, M.T. Merema, G.M.M. Groothuis, and E. Verpoorte. Comparison of biocompatibility and adsorption properties of different plastics for advanced microfluidic cell and tissue culture models. *Analytical Chemistry*, 84(9), 2012. ISSN 00032700. doi: 10.1021/ac300771z.
- [134] S A Vanapalli, D van den Ende, M H G Duits, and F Mugele. Scaling of interface displacement in a microfluidic comparator. *Applied Physics Letters*, 90(114109):1–4, 2007. doi: 10.1063/1.2713800.
- [135] Federico Vozzi, Francesca Bianchi, Arti Ahluwalia, and Claudio Domenici. Hydrostatic pressure and shear stress affect endothelin-1 and nitric oxide release by endothelial cells in bioreactors. *Biotechnology Journal*, 9(1):146–154, 2014. ISSN 18606768. doi: 10.1002/biot.201300016.
- [136] Fruzsina R. Walter, Sándor Valkai, András Kincses, András Petneházi, Tamás Czeller, Szilvia Veszelka, Pál Ormos, Mária A. Deli, and András Dr. A versatile lab-on-a-chip tool for modeling biological barriers. *Sensors and Actuators, B: Chemical*, 222:1209–1219, 2016. ISSN 09254005. doi: 10.1016/j.snb.2015.07.110. URL <http://dx.doi.org/10.1016/j.snb.2015.07.110>.
- [137] Jack D. Wang, Nicholas J. Douville, Shuichi Takayama, and Mohamed Elsayed. Quantitative analysis of molecular absorption into PDMS microfluidic channels. *Annals of Biomedical Engineering*, 40(9):1862–1873, 2012. ISSN 00906964. doi: 10.1007/s10439-012-0562-z.

- [138] Imola Wilhelm and Istvan A. Krizbai. In vitro models of the blood-brain barrier for the study of drug delivery to the brain. *Molecular Pharmaceutics*, 11(7):1949–1963, 2014. ISSN 15438392. doi: 10.1021/mp500046f.
- [139] Imola Wilhelm, C Fazakas, and I A Krizbai. In vitro models of the blood-brain barrier. *Acta Neurobiol Exp (Wars)*, 71(1):113–128, 2011. ISSN 00651400. doi: 10.1007/978-1-4939-0320-7_34. URL <http://www.ncbi.nlm.nih.gov/entrez/query.fcgi?cmd=Retrieve{&}db=PubMed{&}dopt=Citation{&}list{&}uids=21499332>.
- [140] S A Williams, S Wasserman, D W Rawlinson, R I Kitnef, L H Smaje, and J E Too. Dynamic measurement of human capillary blood pressure. *Clinical Science*, 74(5):507–512, 1988.
- [141] Anette Wolff, Maria Antfolk, Birger Brodin, and Maria Tenje. In Vitro Blood-Brain Barrier Models-An Overview of Established Models and New Microfluidic Approaches. *Journal of Pharmaceutical Sciences*, 104(9):2727–2746, 2015. ISSN 15206017. doi: 10.1002/jps.24329. URL <http://dx.doi.org/10.1002/jps.24329>.
- [142] Andrew D. Wong, Mao Ye, Amanda F. Levy, Jeffrey D. Rothstein, Dwight E. Bergles, and Peter C. Searson. The blood-brain barrier: an engineering perspective. *Frontiers in Neuroengineering*, 6 (August):1–22, 2013. ISSN 1662-6443. doi: 10.3389/fneng.2013.00007. URL <http://journal.frontiersin.org/article/10.3389/fneng.2013.00007/abstract>.
- [143] Matthias Worgull. *Hot Embossing*.
- [144] W.I. Wu, P. Rezai, H.H. Hsu, and P.R. Selvaganapathy. *Materials and methods for the microfabrication of microfluidic biomedical devices*. 2013. ISBN 9780857096975. doi: 10.1533/9780857097040.1.3. URL <http://linkinghub.elsevier.com/retrieve/pii/B9780857096975500013>.
- [145] Diane M. Wuest, Allison M. Wing, and Kelvin H. Lee. Membrane configuration optimization for a murine in vitro blood-brain barrier model. *Journal of Neuroscience Methods*, 212(2):211–221, 2013. ISSN 01650270. doi: 10.1016/j.jneumeth.2012.10.016. URL <http://dx.doi.org/10.1016/j.jneumeth.2012.10.016>.
- [146] Yao Yao, Zu-lin Chen, Erin H Norris, and Sidney Strickland. NIH Public Access. pages 1–26, 2014. doi: 10.1038/ncomms4413.Astrocytic.
- [147] Mao Ye, Henry M. Sanchez, Margot Hultz, Zhen Yang, Max Bogorad, Andrew D. Wong, and Peter C. Searson. Human brain microvascular endothelial cells resist elongation due to curvature and shear stress. *Scientific Reports*, (4), 2014. ISSN 10959319. doi: 10.1016/j.mvr.2015.02.008.
- [148] Daniel P Yen, Yuta Ando, and Keyue Shen. A cost-effective micromilling platform for rapid prototyping of microdevices. *Technology*, 4(4), 2016. doi: 10.1142/S2339547816200041.
- [149] Ju Hun Yeon, Dokyun Na, Kyungsun Choi, Seung Wook Ryu, Chulhee Choi, and Je Kyun Park. Reliable permeability assay system in a microfluidic device mimicking cerebral vasculatures. *Biomedical Microdevices*, 14(6):1141–1148, 2012. ISSN 13872176. doi: 10.1007/s10544-012-9680-5.
- [150] Edmond W K Young, Erwin Berthier, and David J. Beebe. Assessment of enhanced autofluorescence and impact on cell microscopy for microfabricated thermoplastic devices. *Analytical Chemistry*, 85 (1):44–49, 2013. ISSN 00032700. doi: 10.1021/ac3034773.
- [151] Seung Tack Yu, Sung Jae Na, Tae Sun Lim, and Bun Yeoul Lee. Preparation of a bulky cycloolefin/ethylene copolymer and its tensile properties. *Macromolecules*, 43(2):725–730, 2010. ISSN 00249297. doi: 10.1021/ma902334d.
- [152] Rigor RR Yuan SY. *Regulation of Endothelial Barrier Function*.

B

Procedures

All procedures used in this thesis are documented in this appendix. Procedures that can not be found elsewhere in e.g. a manual are documented step by step, for other procedures the reader is referred to the source.

B.1. Mold fabrication

3D printed mold

A positive mold is fabricated out of a negative photoresist (HTM140 M V2, Envisiontec) using the Micro Plus Hi-Res printer from EnvisionTEC, which makes use of UV photopolymerization. The resolution in the xy-plane is $30\ \mu\text{m}$, in z direction 25. Around the mold a container is printed, such that the mold can be used for soft lithography directly.

Printing and curing is performed following the operation manual from the department. Particularities are noted below:

The printed layers are produced by curing a resin through UV exposure in the x-y-plane from below. The cured material is then lifted in z-direction to let in new resin and pushed back to touch the bottom of the resin container again, such that the next layer can be cured from below. The open side of the container is facing down during printing, to avoid trapping of liquid resin by the up and down movements during printing, see figure B.1. Trapped air can escape via holes in the walls of the container. See Appendix E.2 for a drawing of the printed part.

At the beginning of the project the Envisiontec printer was new and the mold could be printed horizontally without any problems. However, with time the prints seemed to cure to a lesser degree. The mold would bend under the weight of the resin which flows between the support structure between every step. To avoid this bending the bottom of the mold is tilted, see Figure B.3.

After printing and before curing in the UV curing machine, the print is sandwiched between two microscope slides. The two slides are taped together to apply stress. The print is cured in the UV curing machine in between the microscope slides. This prevents the print from warping, see Figure B.2, during the curing process.



Figure B.1: Direction of writing and movement during printing of the mold. Holes for air escape in light grey.



Figure B.2: HTM140 warps if not fixed straight during UV curing



Figure B.3: Model of the printed mold. The bottom is tilted with 15° to advance drainage of the resin to the side.

PDMS mold

After the positive mold has been produced the PDMS mold is fabricated. Base and curing agent are mixed in a 5:1 ratio (SYLGARD™ 184, Dow), poured in the HTM140M molds, degassed and cured overnight at 60 °C. The cured PDMS molds are released using a scalpel and 99.9% ethanol, dried and stored between Scotch tape.

B.2. Spin coating

In this section first the preparation of the spin coating solutions is described and next the spin coating procedure itself. Some substrates are sputter coated before spin coating, the sputter coating procedure is described next. Lastly the reflectance of the sputter coated layer is approximated, to determine the visibility of this layer using white light interferometry after spin coating.

B.2.1. Spin coating solution

In the spin coating experiments different solvents and weight percentages are used for the spin coating solution. The preparation of these spin coating solutions are described below. The solvents and weight percentages used are given in Table B.1.

Note: Toluene and sec-butylbenzene are both strong solvents. Take care when selecting lab ware, since many plastics are not resistant to these solvents.

Materials

Chemicals

1. TOPAS® 5013 granulate
2. Solvent: toluene $\geq 99.8\%$ or sec-butylbenzene $\geq 99\%$
3. Liquinox 1%
4. Isopropanol $\geq 99.9\%$
5. Deionized water

Equipment

1. Pipetting balloon
2. Precision balance
3. Balance
4. Orbital shaker

Glass ware

1. Glass bottle with a PTFE cap or a PTFE film to line the inside of the cap, to prevent interaction between cap and solvent.
2. Small beaker
3. Disposable glass pipette of 5 ml

Consumables

1. Small funnel
2. Pipette tip
3. Aluminium foil

Procedure

Cleaning

1. Clean the glass bottle, beaker and a glass pipette using Liquinox, DI water and isopropanol consecutively. Let evaporate until completely dry.
2. Clean TOPAS granulate in a clean glass bottle consecutively with Liquinox and isopropanol in an ultrasound bath for 15 and 10 minutes respectively. Rinse with DI water after both cleaning steps. Drain and dry using a clean, dry airstream. Let evaporate in an oven at elevated temperature to dry the granulate completely.

Weighing

The weight percentages of the solutions used are listed in Table B.1.

1. Weigh the TOPAS granulate on the precision balance in a cup folded from aluminium foil
2. Pour approximately the corresponding weight of solvent in the cleaned beaker glass using the balance in the fume hood.

Table B.1: Solvent and weight percentages of the solutions used for spin coating

Solvent	Weight percentage (wt%)
Toluene $\geq 99.8\%$	12.5
	20.0
Sec-butylbenzene $\geq 99\%$	15.0
	25.0

- Place the glass bottle on the balance in the fume hood and transfer the precise amount of solvent from the beaker to the glass bottle using the glass pipette.

Mixing

- Using a funnel or folded piece of weighing paper, add the TOPAS granulate slowly to the glass bottle with the solvent while shaking the bottle carefully to prevent the granulates from clumping together. Close the bottle with the PTFE cap or PTFE lined cap.
- Leave the glass bottle on an orbital shaker until the granulate is completely dissolved. Depending on the solvent, weight percentage and degree of clumping of the granulates in the previous step, this could take a couple of hours to days.
- Store the solution in a lab-safe refrigerator.

B.2.2. Spincoating

The programs as entered in the spin coater and as used for the spin coating experiments are given in Table B.2. The steps taken in the preparation and execution of the spin coating experiments follow below.

Table B.2: Spin coating program used in spin coating experiments 1-5. All spin coating parameters are kept constant as indicated in this table, except for the spin speed in step 1, ω_1 , which is varied between 1000 and 5000 rpm. To obtain the desired 10 μm layer thickness the spin speed of the first step is set to ω_1 2355 rpm and a solution of 15.0 wt% of TOPAS® in sec-butylbenzene is used.

	spin speed (rpm)	acceleration (rpm/s)	time (s)
Step 1	1000-5000	250	50
Step 2	100	250	30

Materials

Substrates

One of the following substrate materials:

- TOPAS 6015 sheet, $t = 1.0$ mm
- Glass microscope slides, 26x76x1 mm
- Glass petridishes, $\varnothing 54$ mm

Chemicals

- Spin coating solution as produced in Appendix B.2.1
- Solvent: toluene $\geq 99.8\%$ or sec-butylbenzene $\geq 99\%$, choose the same as used for the spin coating solution
- Liquinox 1%
- Isopropanol $\geq 99.9\%$
- Deionized water

Equipment

- Lab support stand
- Spin coater (Polos spin150i)
- Pipettor 100-1000 μl
- Metal ruler
- Razor blade
- Glass cutter
- Marker pen

8. Tweezers

Glass ware

1. 2 glass bottles
2. Small beaker or petridish
3. Large petridish
4. Disposable glass pipette of 5 ml

Consumables

1. Pipetting tip 1 ml
2. Syringe 20 ml
3. Duct tape
4. PET process chamber liner set for spin coater
5. Double sided tape
6. Aluminium foil

Procedures

Prepare substrates

1. When needed, cut substrates to size using the glass cutter (glass substrates) or the razor blade (TOPAS substrates) and the ruler.
2. Clean the glass substrates: Place the substrates in a holder in a beaker that keeps the individual substrates separated. Clean consecutively with Liquinox and isopropanol in an ultrasonic bath for respectively 15 and 10 minutes. Drain, and rinse with DI water after both cleaning steps and switch. Use a second beaker to facilitate draining and rinsing. Let evaporate (to speed up the process in an oven) until completely dry.
3. Store in clean and closed petridish.

Prepare equipment

1. Clean two glass bottles and the glass pipette, using Liquinox, DI water and isopropanol consecutively and dry.
2. Add DI water to a clean small petridish. Using a pipettor and the DI water measure 3 ml with step of 0.5 ml on the glass pipette with a marker pen.
3. Attach a 20 ml syringe to the glass pipette, using duct tape to seal properly.
4. Cover the insides of a PET process chamber liner set from the spin coater with aluminium foil using double sided tape.
5. Cover the two chucks with aluminium foil. Remove foil covering the O-rings.
6. Cover the chuck holder with a 'skirt' of aluminium foil such that it can still rotate.
7. Assemble all parts of the spin coater while making sure that all part exposed to the spin coating solution during spin coating are covered with aluminium foil.
8. Add a slightly larger amount of spin coating solution than needed for spin coating to one of the glass bottles.
9. Add approximately 50 ml of solvent to the second glass bottle.
10. Cover the glass bottles with aluminium foil and punch a hole for the glass pipette.
11. Place the spin coater, air outlet of the vacuum pump, lab stand, the two glass bottles in the fume hood. Hang the pipette with syringe in the lab stand such that it hangs just above the fluids in the glass bottles.

Spin coating

1. Place a sample in the center of the vacuum chuck using tweezers. In case of TOPAS samples: remove protective foil first.
2. Apply vacuum
3. Using the glass pipette and syringe apply 0.5 - 1.5 ml solution to the substrate while spreading the solution evenly over the surface of the substrate. Prevent the ejection of air bubbles.
4. Close the lid of the spin coater promptly and start the spin coating program.
5. Empty the glass pipette in the glass bottle with the solution. Rinse the pipette with solvent from the second glass bottle and empty meticulously to ensure a constant weight percentage.
6. Remove the sample using tweezers and place in an aluminium foil covered large petridish in the fume hood.
7. Repeat step 1-6 for the next samples.
8. Let the samples evaporate in the fume hood for 3 days.

Cleaning

Remove the liners and aluminium foil directly from the spin coater to prevent the solvent to damage the spin coater. Let the liners and aluminium foil evaporate in the fume hood.

B.2.3. Sputter coating

The sputter coating procedure is performed using PDMS masks. The PDMS masks are cut from a sheet of PDMS produced by pouring a layer of PDMS (SYLGARD™ 184, Dow, 10:1 mixing ratio) of about 0.5 mm in a clean petridish (PS, \varnothing 180 mm). The masks, see Figure B.4, are cut using a scalpel for the straight edges and a needle (Microlance 1.2x40 mm) for the dot shape.

Materials

1. Substrates (36x15x1 mm)
2. 4 PDMS masks
3. Scotch tape
4. Sputter coater

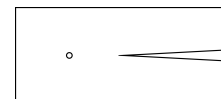


Figure B.4: PDMS mask for sputter coating (37x16mm)

Procedure

1. Remove protecting foil from 4
2. Clean PDMS masks using Scotch tape if necessary
3. Cover all 4 substrates with a PDMS mask
4. Place the substrates with PDMS masks in the sputter coater ordered in a rosette
5. Sputter coat the substrates according to the manual from the sputter coater for 180 s at 25 mA with the Au/Pd target
6. Repeat until the desired amount of substrates is sputter coated

B.2.4. Thin film reflectance

Reflectance due to thin film interactions of the combination of thin films of TOPAS® and gold or palladium is calculated using the Spectral Reflectance Calculator from Filmetrics[19], which uses calculations based on the complex-matrix form of the Fresnel equations. The entries used in the calculator are given in table B.3 and table B.4. At $\lambda = 550\text{nm}$ a reflectance of 0.832 and 0.059 is found when using respectively gold and palladium as second layer material.

Table B.3: Layer build-up entered in the Spectral Reflectance Calculator of Filmetrics[19]

	Material type	Thickness (μm)
Medium	Air	
Layer 1	TOPAS	10
Layer 2	Au or Pd	0.1
Substrate	TOPAS	

Table B.4: Reflective indices selected or entered in the Spectral Reflectance Calculator of filmetrics [19]. For Pd and TOPAS® $n(550\text{ nm})$ is used.

	Reflective index
Air	from calculator
Au	from calculator
Pd	1.6175
TOPAS®	1.53

B.3. Soft embossing

The steps to be taken to perform the soft embossing experiments is described in the procedure below. The embossing process itself is described in Table B.6 and Figure B.5. The parameters used in the different embossing experiments with the PDMS mold are given in Table B.5.

Materials

1. TOPAS 6015 substrates (36x15x1 mm)
2. PDMS mold
3. Kapton foil (\approx 45x120 mm)
4. Wafer tweezers
5. Scotch tape
6. Clean room wipes

7. Isopropanol $\geq 99.9\%$
8. PreheatPress.vi
9. EmbossingProcess.vi
10. Hand press with connected thermocouples, fan, DAQ device and computer

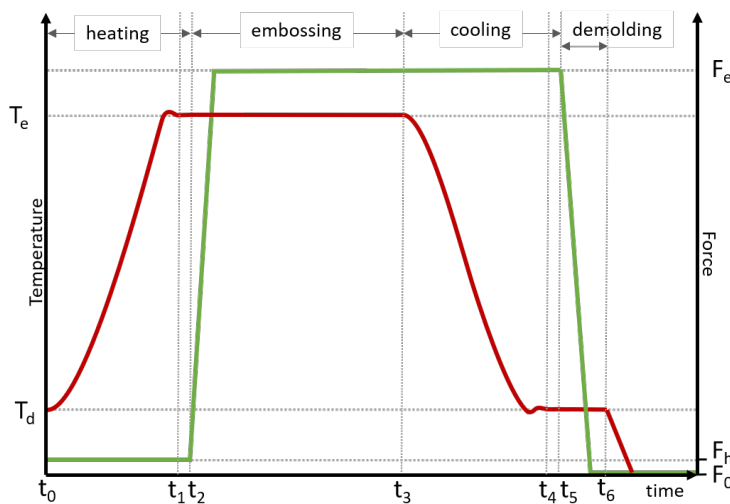
Procedure

Preparation

1. Open EmbossingProcess.vi and set the desired temperatures and times in the embossing process.
2. Preheat the press to the desired starting temperature using PreheatPress.vi.

Embossing process

1. Clean the Kapton foil with isopropanol and a clean room wipe if necessary and fold in half along the short axis.
2. Clean the PDMS mold by applying Scotch tape, picking up dust, and removing the tape again.
3. Remove the protecting foil from both sides of one substrate.
4. Place the PDMS mold on top of the substrate with the features facing the substrate and place in between the folded Kapton foil.
5. Using tweezers place the package in the press with the substrate facing down and the fold in the Kapton foil facing backwards. Apply a minimum compression force to hold the package in place.
6. Stop PreheatPress.vi and run EmbossingProcess.vi to start the embossing process (or click continue in EmbossingProcess.vi after the first experiment.)
7. Wait until the press is heated to the molding temperature, indicated by a single beep and the burning red 'Molding' sign in the VI.
8. Apply the molding force by screwing down the sliding plate until the deflection (indicated by the caliper) corresponding to the desired molding force is reached. Apply the force slowly and smoothly, avoiding any jerk.
9. Wait until the molding step and cooling step are finished, indicated by two beeps and the burning green 'Waiting' sign in the VI.
10. Slowly remove the compression force and remove the package of foil, mold and substrate using tweezers. Separate mold from substrate and store the embossed substrate.
11. Repeat step 1-11 until finished.



Set	t_e (min)	T_e (°C)	F_e (N)	Mold
1	10	170	400	C
2	10	175	400	B
3	10	180	400	B
4	20	175	200	A
5	10	175	200	A

Figure B.5: Schematic of temperature (red) and force (green) during embossing as a function of time.

Table B.5: Embossing parameters used per sample set, with $t_e = t_3 - t_2$

Table B.6: Description of the embossing process

t	T	F	Actions
t_0	T_d	0	Mold and substrate are aligned by hand and placed on the bottom plate with the substrate facing down. A small holding force F_h is applied to hold mold and substrate in place.
t_1	T_d	F_h	Mold and substrate are heated to embossing temperature T_e .
t_2	T_e	F_e	Embossing force F_e is applied.
t_3	T_e	F_e	Mold and substrate are cooled down to demolding temperature T_d . Substrate and mold are removed from the press and separated from each other.
t_4	T_d	0	The temperature of the substrate drops quickly to room temperature, since it is not in contact any more with a heated element.

B.4. Benchtop press

Working drawings of the hand press are given in Appendix E. Particularities for the fabrication of the individual parts are given below:

B.4.1. Machining of the separate parts

1. Mill the four stainless steel plates (parts 1, 2, 14 and 22) to size in length and width, preferably all at the same time while clamped together.
2. Flatten one side of the large surfaces of the stainless steel plates to size. Make multiple strokes with a relatively small mill, such that any error in the vertical alignment of the milling head are minimized.
3. Mill the stainless steel plates to size in thickness one at a time, again using multiple strokes with a small mill. Keep the workpiece clamped and drill the holes. In this way the axis of the hole and the surface will be as close to perpendicular as the alignment of the milling machine allows. For the two plates sandwiching the substrates, the last surface to be face milled are the ones in contact with the substrate. For the top and spring plate it is not important which surface is face milled last, but it is chosen to take the bottom surface and top surface respectively.
4. Machine the bushes for the sliding axis (parts 5 and 9).
5. Press the bushes in place, to make sure these do not stick out of the surface in the final product after sanding and polishing.
6. Sand and polish the surfaces in contact with the substrates, since the surface profile will be transmitted to the substrates.
7. Protect the surfaces from dust, chemicals and fingerprints to avoid scratching and etching.

B.4.2. Assembly of the parts

1. Assemble parts 15 and 16 by welding
2. Assemble parts 1, 14 and 7 and drill the dowel holes through parts 1 and 7, and 14 and 7.
3. Pressed all bushes into place, use a hand press for parts 5 and 9 when necessary.
4. Assemble parts 1, 5, 7-9, 11, 13-19 and 20 and drill the dowel hole through parts 8 and 15, and 20 and 15.
5. Assemble parts 1-20 22, and 24-26 and clamp the assembly in a milling machine to drill the dowel holes and the holes for caliper attachment. The holes in the caliper are drilled separately in a milling machine and drilled larger than the bolts that will be used to attach the caliper, to allow for some play and circumvent minor misalignment of the plates, which would block the caliper.
6. Disassemble the press and deburr all holes drilled in steps 2-5.
7. Assembly parts 1-27. The plates will most probably not slide smoothly along the axes right away, some misalignment is inevitable. Sliding the plates a few hundred times up and down will wear out the bronze bushes and make the sliding smoother. Alignment of the four plates would be better if all holes would be drilled simultaneously while clamping the plates together. However, in this way is would not be possible to reach as much perpendicularity between the sandwiching surfaces and the axes.

B.4.3. Calibration of force control

Equipment

1. Hand press with connected thermocouples and DAQ device

2. Futek LCM300 loadcell 2 kN
3. Strain gauge analogue signal conditioner CPJ
4. Computer to run LabView
5. Force Displacement Temperature.vi
6. 2 pieces of flattened steel (30x50x10 mm) with a perpendicular, tapped hole in the center (M6x1)
7. 2 strips of rubber ($\approx 40 \times 50 \times 1$ mm) resistant to a maximum temperature of 80 °C

Procedure

1. Screw the pieces of steel on the load cell, avoiding contact between the steel and the large cylinder of the load cell.
2. Cover the bottom and sliding plate of the press with the strips of rubber and place the load cell in between.
3. Connect the load cell, strain gauge conditioner, DAQ device and connection of the hand press and run the VI.
4. Tighten the hand press and save the deflection indicated by the caliper for three different loads equally spaced along the working range of the spring.
5. Completely unscrew the press and move the spring around to simulate interchanging the spring.
6. Repeat step 4-5 two times
7. Repeat step 4-6 at 45°C and 70°C by setting the desired temperature in the VI.

B.4.4. Calibration of temperature control

Determination of K_c , T_i and T_d

Materials

1. Hand press with connected thermocouples, fan, DAQ device and computer
2. StepResponse.vi
3. PreHeat.vi
4. Substrate
5. Piece of PDMS simulating mold

Procedure

Tuning K_c , T_i and T_d

1. Open StepResponse.vi
2. Set T_{max} heater, the maximum temperature of the heater, to 200 °C.
3. Set PWM duty cycle to 0.05 for a duty cycle of 5%.
4. Place a substrate on the bottom plate and the PDMS on top of the substrate
5. Apply a force in the order of magnitude of the force that will be used in the experiments for which the press is calibrated
6. Run StepResponse.vi
7. Click *Stop heater* and *Stop program* when the temperature chart clearly shows that the slope of the temperature deflects again.
8. Determine K_c , T_i and T_d for PID control as indicated in Figure B.6 and Table B.7 and as explained by [3]
9. Fine-tune K_c , T_i and T_d further if necessary.

Filling out look-up table

1. Open PreHeat.vi and set the PID Gains as determined in step 6
2. Run PreHeat.vi and change the *Set point* to a temperature which is going to be used as set point in the embossing process
3. Wait until the temperature is settled. Note the value of u_I . Add the set point and corresponding value for u_I in the look-up table.
4. Repeat for all temperatures settings needed in the embossing process. Skip temperatures that vary less than 10 °C from previous examined values since adding will not increase the settling time significantly.

B.4.5. Emissivity of Kapton foil

The emissivity of Kapton foil is needed to obtain accurate temperature measurements with a heat camera, FLIR E75 from FLIR®. The emissivity of Kapton foil could not be found in literature and is therefore, based on the FLIR E75 manual[71], determined as follows:

1. The reflected apparent temperature is determined by placing crumpled aluminium foil on top of the bottom embossing plate of the press, while the emissivity is set to $\epsilon = 1.0$.

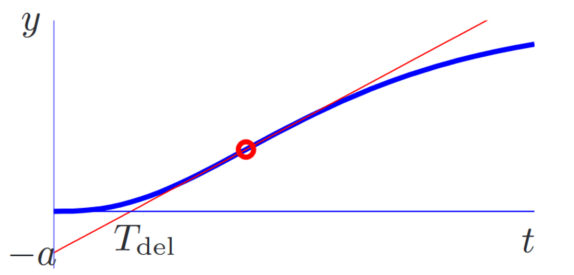


Figure B.6: Extracting the parameters L (here T_{del}), the delay time of the system, and a from the step response to obtain good starting values for the PID parameters. The circle indicates the point of inflection, with the tangent line in red. Figure reproduced from [3].

Controller	K_c	T_i	T_d
P	$\frac{1}{a}$		
PI	$\frac{0.9}{a}$	$3L$	
PID	$\frac{1.2}{a}$	$2L$	$0.5L$

Table B.7: PID parameters obtained with the Ziegler-Nichols step response method. Table modified from Åström and Murray [3].

2. The bottom embossing plate is masked with Kapton foil and partly with electrical tape with a known emissivity of $\epsilon = 0.97$.
3. The embossing plate is heated to $T \approx 50^\circ\text{C}$.
4. The average temperature of the area covered with electrical tape is measured with the settings $\epsilon = 0.97$ and the reflected temperature as measured in step 1.
5. The average temperature of the area with Kapton foil is measured. The reflected temperature is kept constant at the measured temperature in step 1. The emissivity is adjusted until the average temperature of the Kapton foil equals the measured temperature of the electrical tape in step 4.
6. Repeat step 2-5 but now switch the location of the electrical tape to cancel out differences in temperature and reflections between the two locations.
7. Average the emissivities found in step 5. and 6.

C

LabView control layout

Temperature control of the hand press is implemented using LabView. The graphical user interface and the block diagrams of the program used to control the temperature during a series of embossing experiments is shown in figures C.1 to C.6.

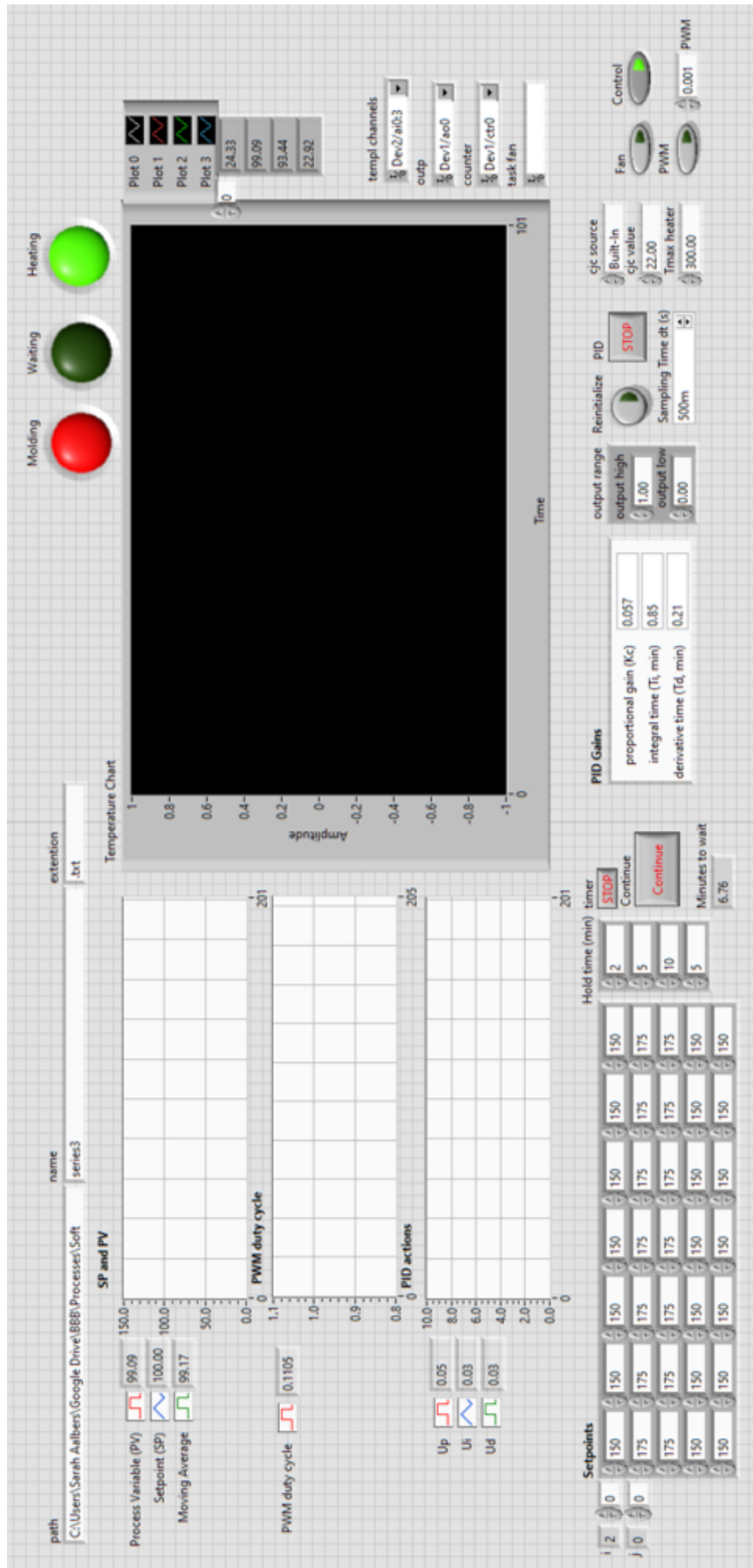
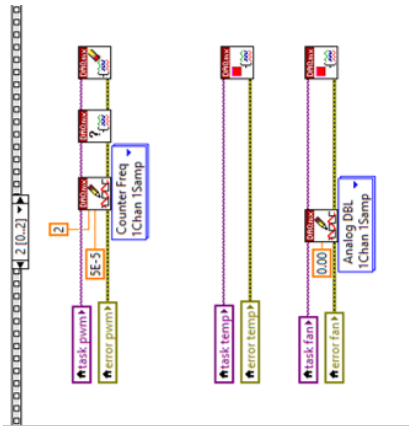


Figure C.1: GUI. The programs runs through the listed set points from top to bottom starting with the left column. Per row the hold time of the set points can be set in the column *Hold time (min)*. The bottom set point is held until the button *continue* is clicked to proceed with the next column.



See next page

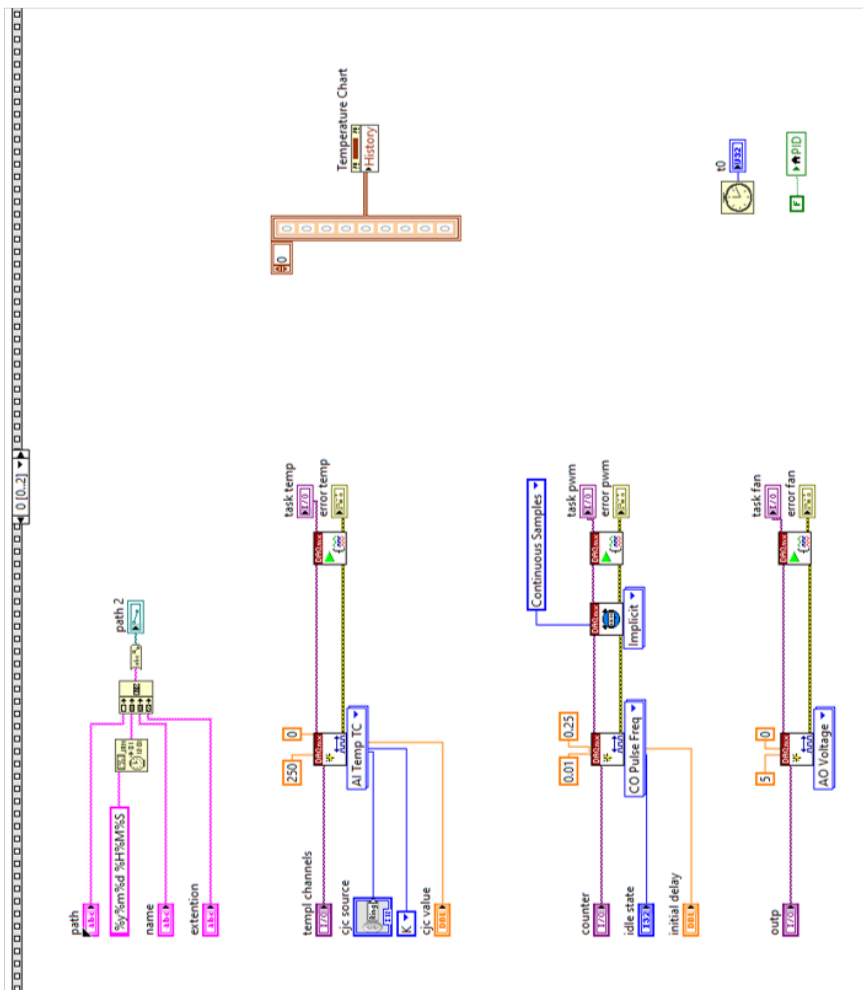


Figure C.2: Frame 0/2 and 2/2 of the program.

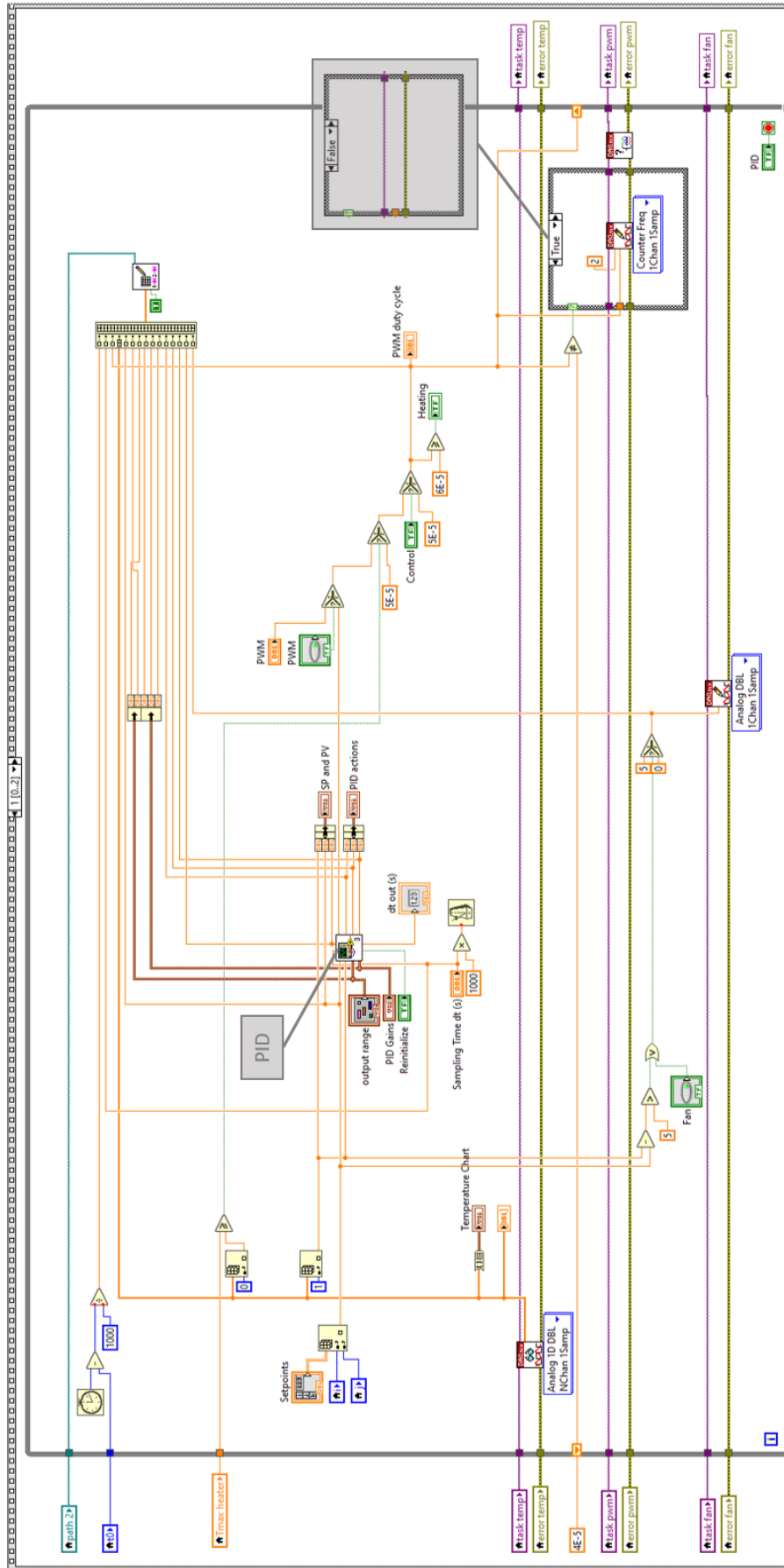


Figure C.3: While loop 1 in frame 1/2 of the program in which temperature is measured and the PWM duty cycle and fan activity is determined.

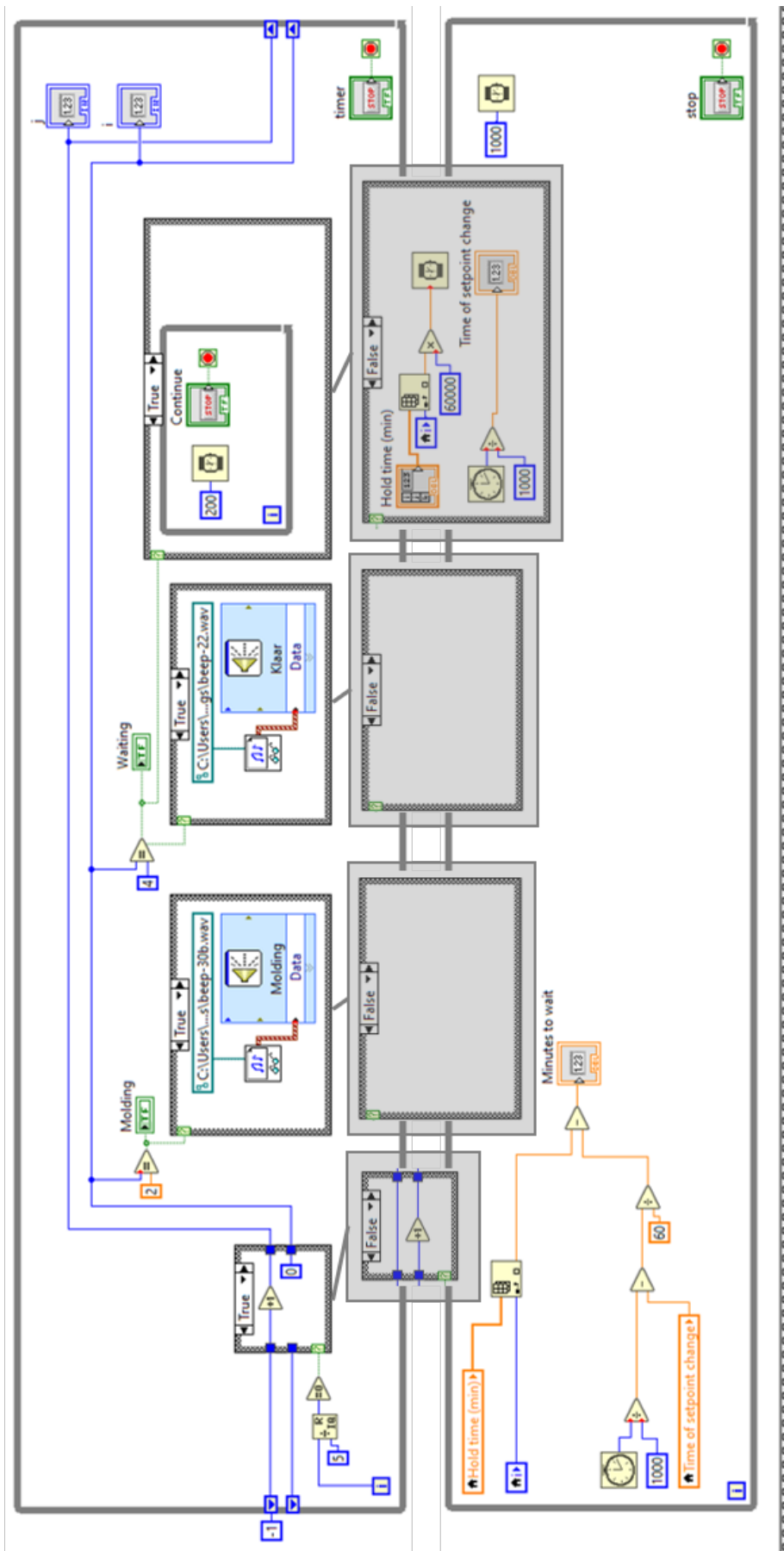


Figure C.4: While loop 2 and 3 in frame 1/2 of the program in which the process steps are respectively timed and displayed.

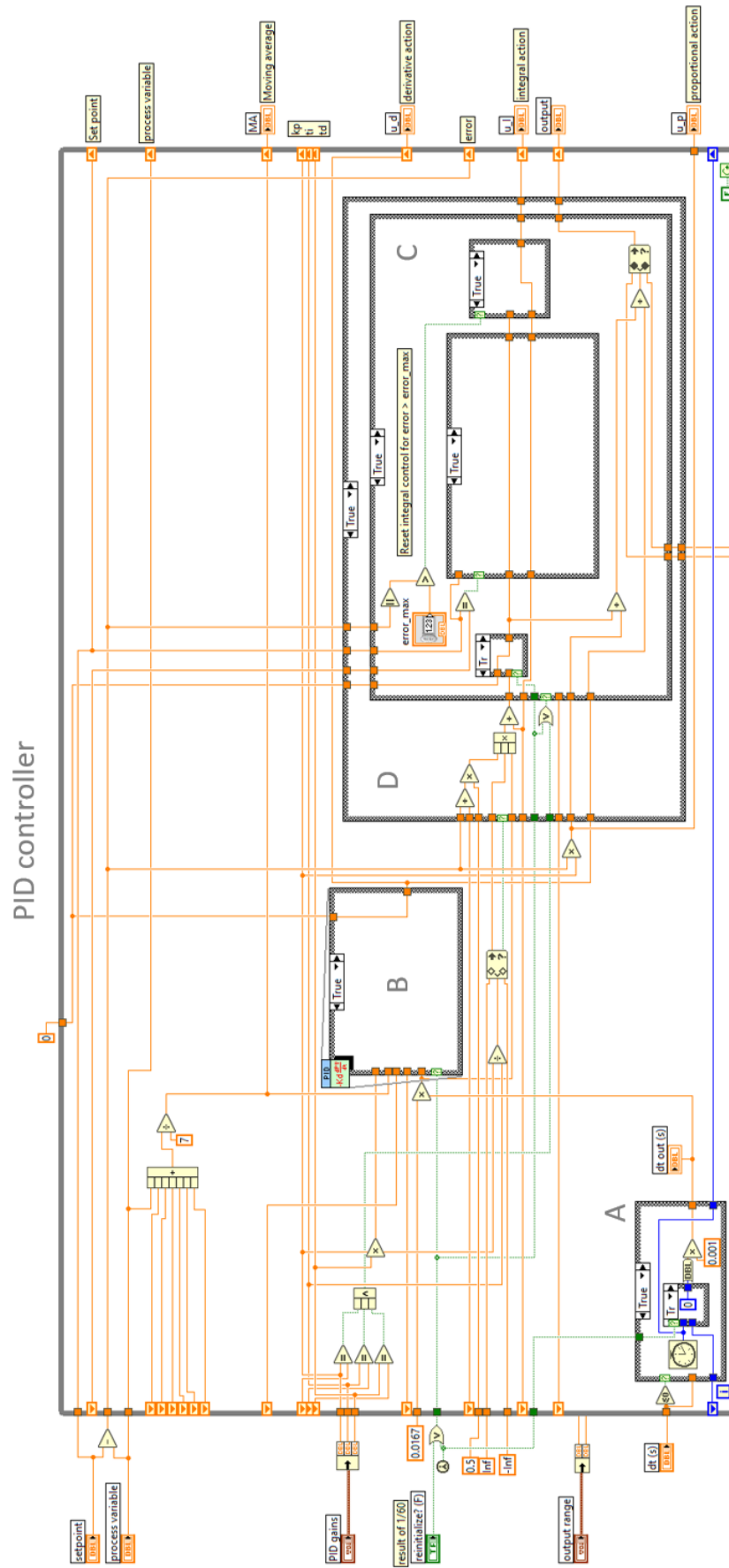


Figure C.5: PID controller adapted from the standard PID controller from LabView. False cases are shown in figure C.6.

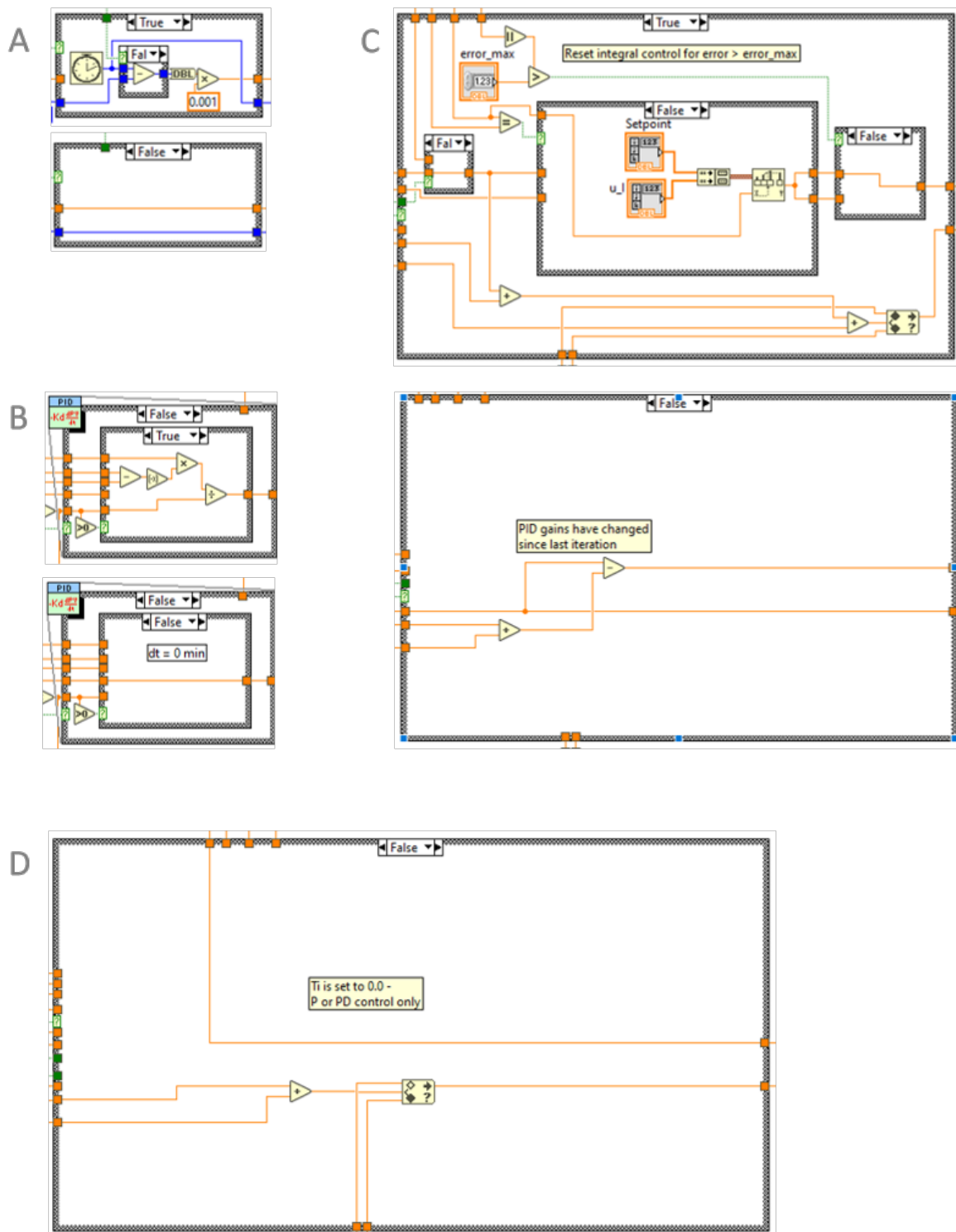


Figure C.6: Details of the PID controller. A. Loop cycle time determination (unaltered from the standard LabView PID controller) B. Derivative control (unaltered from the standard LabView PID controller). C. Reset integral control to $u_I = f(\text{setpoint})$ from the lookup table when the error is larger than the set value. D. Integral control



Measurement data

D.1. Calibration of embossing tool

D.1.1. Force calibration using torque wrench

In the first attempt to control the compression force a torque wrench was used. The torque wrench used can be set with steps of minimally 0.1 Nm. During calibration the accuracy and precision of this method appeared insufficient, see Figure D.1.

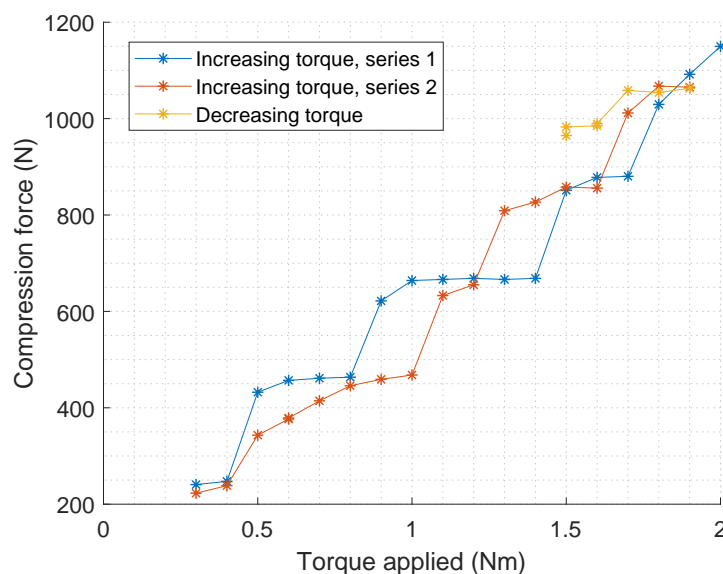


Figure D.1: Measured compression force for applied torque. Two series of increasing torque values are measured and partly a decreasing torque value.

D.1.2. Calibration of blue spring before and after experiments

The blue spring is used in the embossing press during the embossing experiments with the PMDS mold and MD700 mold. The embossing press in combination with the blue spring is calibrated before and after the experiments to ensure constant behaviour of the combination. No significant changes were observed, see Figure D.2 for the results.

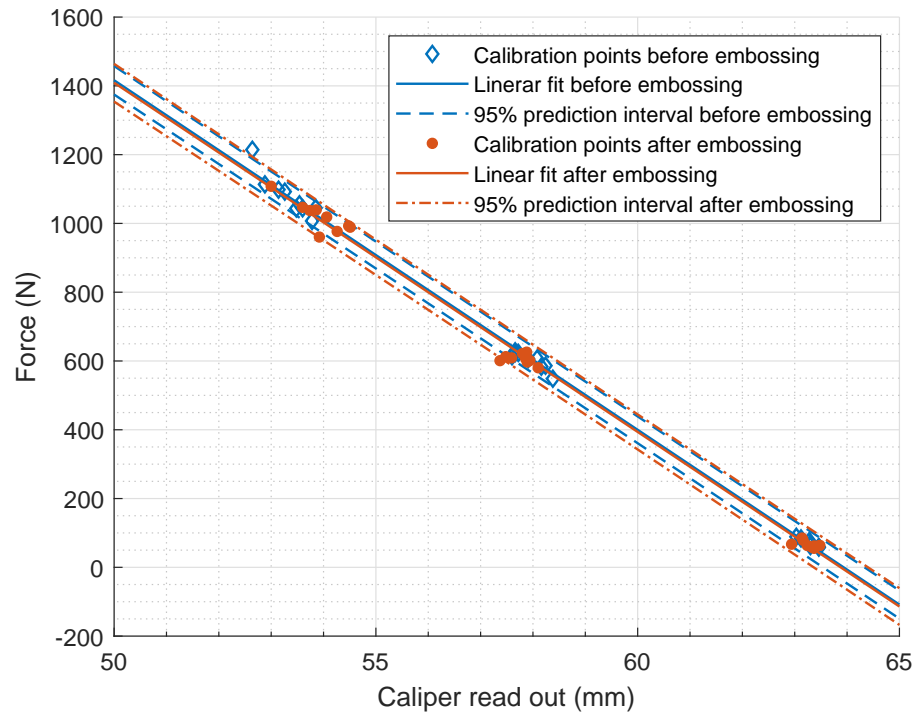


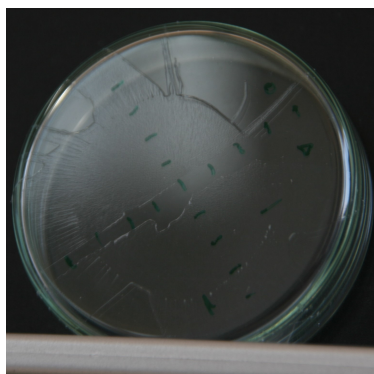
Figure D.2: Calibration results for the blue spring before and after all embossing experiments reported in the paper. The linear fit and the 95% prediction interval for new observations is plotted for both calibration series. At a small, medium and large indentation of the spring and at three different temperatures (room temperature, 45°C and 60°C) three measurements are taken per calibration series, resulting in 27 measurement points per calibration series.

D.1.3. Emissivity of Kapton foil

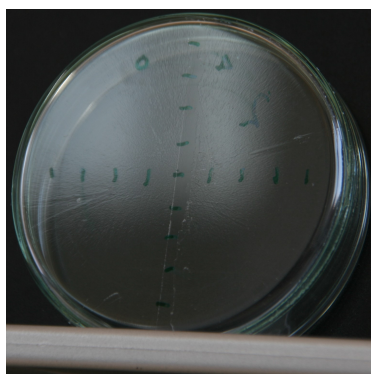
Table D.1: Determination of the emissivity of Kapton foil. See Appendix B.4.5 for the procedure followed to obtain these values.

Measurement	$T_{\text{electrical tape}}$ (°C)	$T_{\text{Kapton foil}}$ (°C)	ϵ setting (-)
1 a	48.6 ± 0.4		0.970
1 b		48.6 ± 0.3	0.935
2 a	48.8 ± 0.2		0.970
2 b		48.8 ± 0.2	0.915

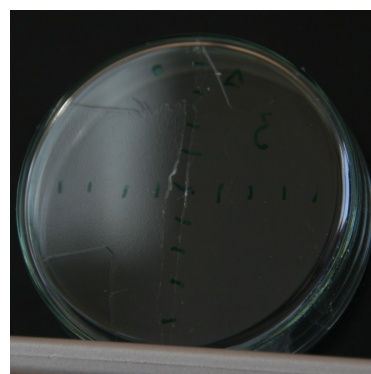
D.2. Substrate preparation



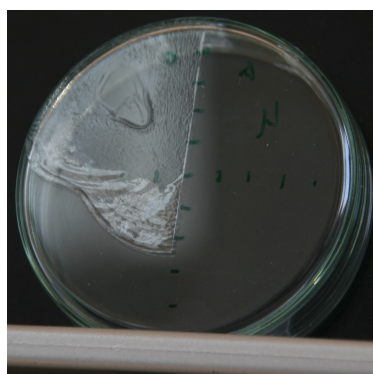
(a) 12.5 % Topas 5013 in Toluene, $\omega_1=3900$ rpm, $\alpha_1=250$ rpm/s, $t=50$ s, long waiting time between dispense and first spincoating step



(b) 20 % Topas 5013 in Toluene, $\omega_1=3900$ rpm, $\alpha_1=250$ rpm/s, $t=50$ s



(c) 12.5 % Topas 5013 in Toluene, $\omega_1=3900$ rpm, $\alpha_1=250$ rpm/s, $t=50$ s



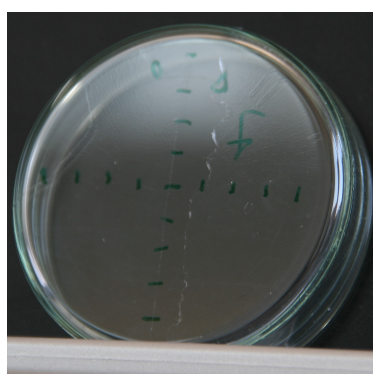
(d) 12.5 % Topas 5013 in Toluene, $\omega_1=100$ rpm, $\alpha_1=20$ rpm/s, $t=50$ s



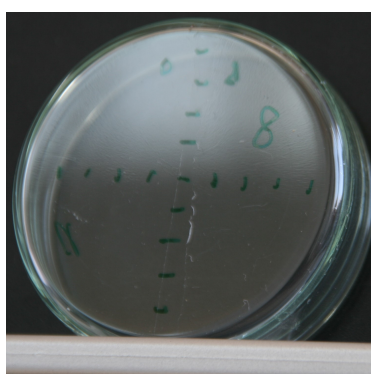
(e) 12.5 % Topas 5013 in Toluene, $\omega_1=5000$ rpm, $\alpha_1=400$ rpm/s, $t=50$ s



(f) 12.5 % Topas 5013 in Toluene, $\omega_1=3900$ rpm, $\alpha_1=250$ rpm/s, $t=50$ s



(g) 12.5 % Topas 5013 in Toluene, $\omega_1=3000$ rpm, $\alpha_1=250$ rpm/s, $t=50$ s



(h) 12.5 % Topas 5013 in Toluene, $\omega_1=2000$ rpm, $\alpha_1=250$ rpm/s, $t=50$ s

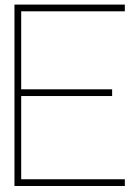


(i) 12.5 % Topas 5013 in Toluene, $\omega_1=2000$ rpm, $\alpha_1=100$ rpm/s, $t=50$ s

Figure D.3: Spincoating results of dissolved Topas 5013 in toluene. Along the center of the petridish the Topas film is scratched away to allow for thickness measurements. Speed and acceleration of the first spincoating step and weight percentage of the solution have been varied. The second spincoating step has been kept constant at $\omega_2=100$ rpm and $\alpha_2=250$ rpm/s

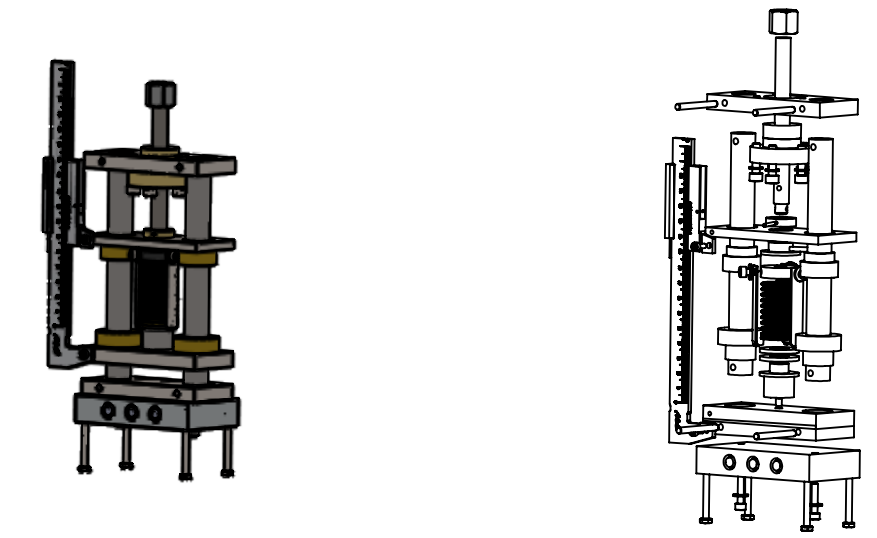
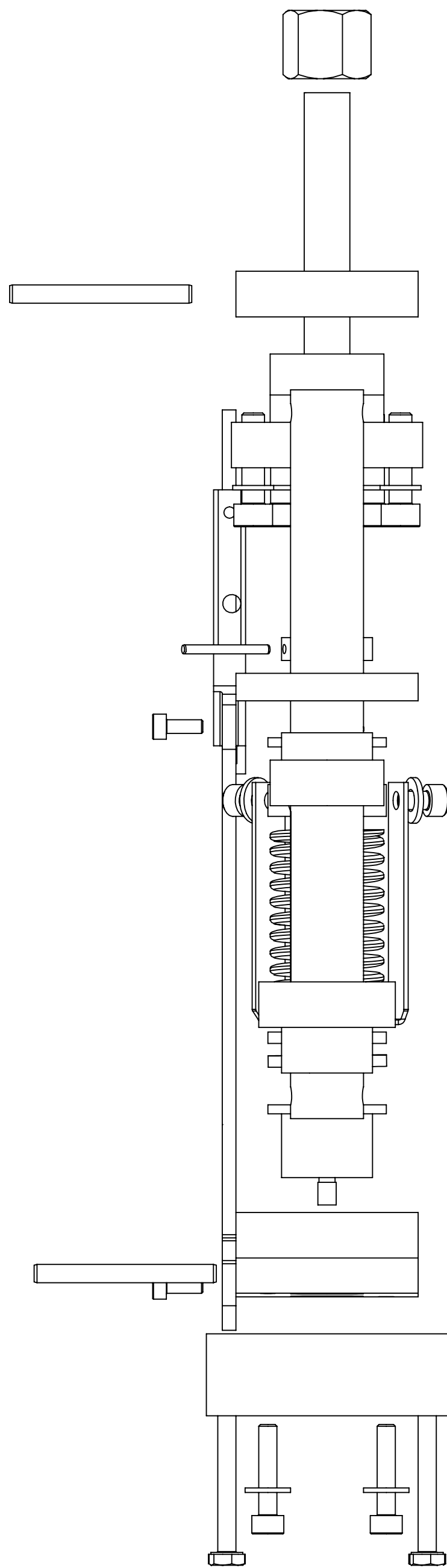
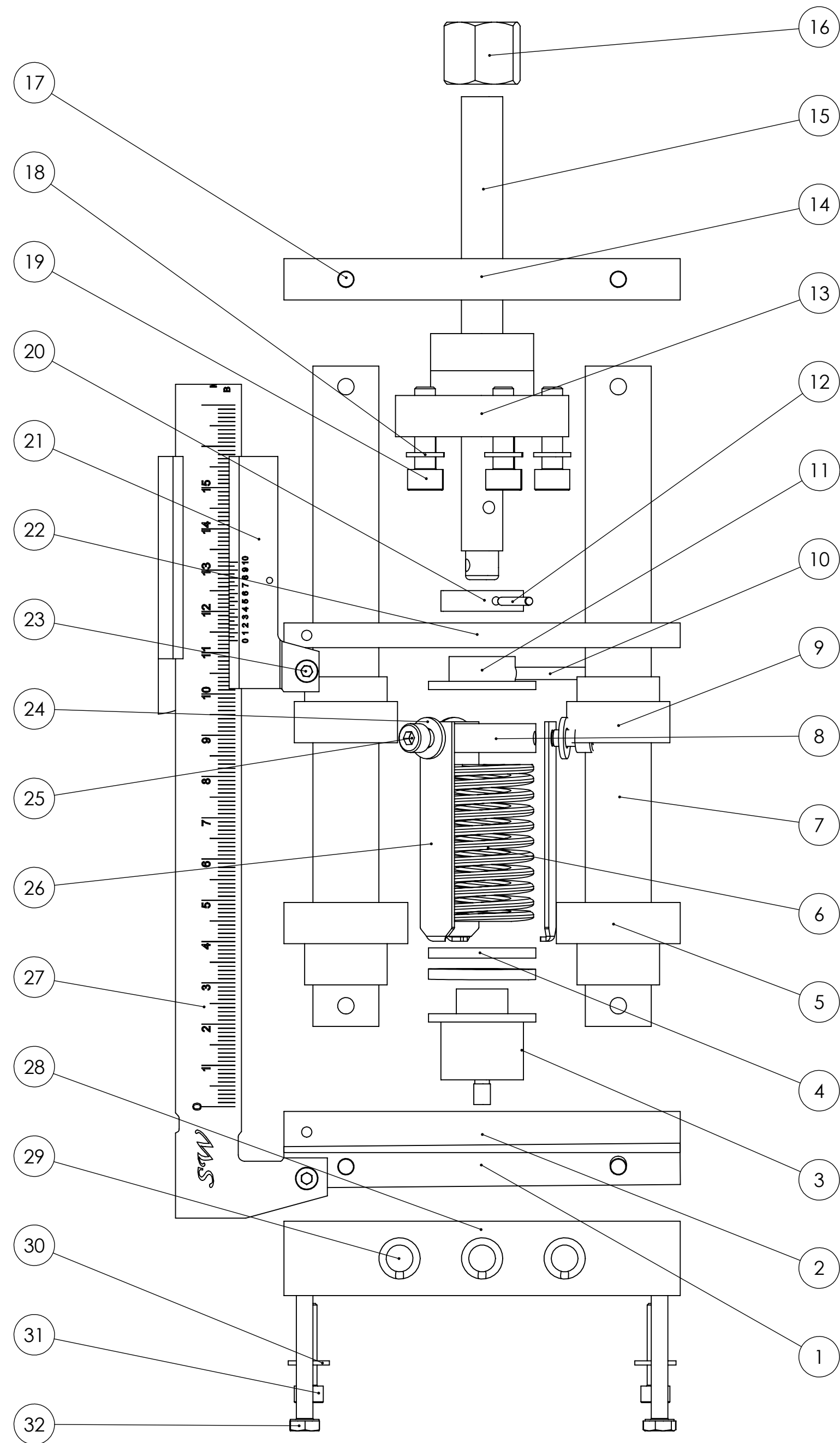


Figure D.4: Spincoating results of dissolved 25wt% Topas 5013 in sec-butylbenzene. Along the center of the microscope slides the Topas film is scratched away to allow for thickness measurements. Velocity of the first spincoating step is varied, acceleration is kept constant at $\alpha_1 = 250$ rpm/s. The second spincoating step has been kept constant at $\omega_2 = 100$ rpm and $\alpha_2 = 250$ rpm/s

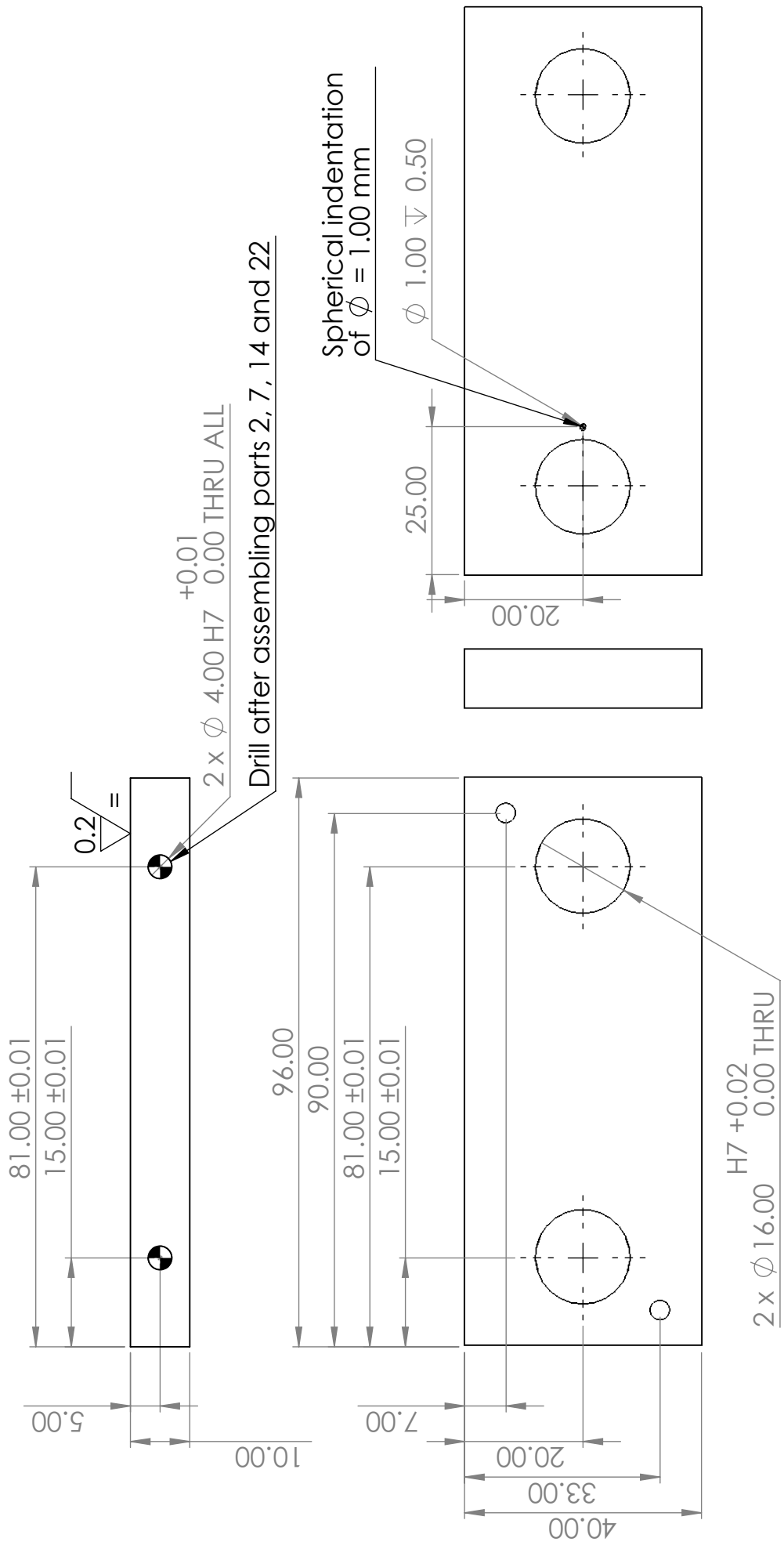


Design drawings

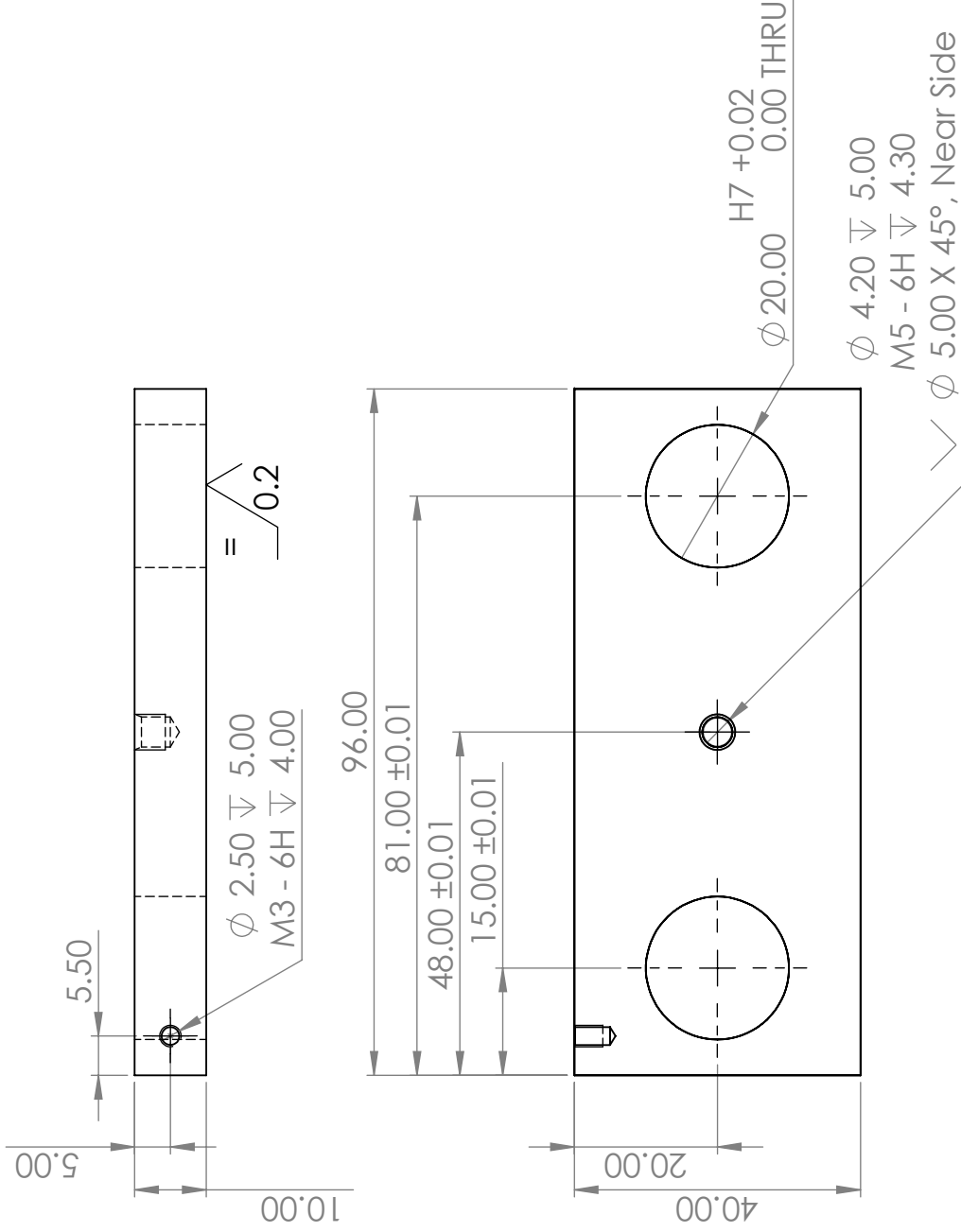
E.1. Embossing and bonding press



ITEM NO.	QTY.	PART NAME	Material	DESCRIPTION
1	1	Bottom Plate	AISI 316L	See drawing no. 1
2	1	Sliding Plate	AISI 316L	See drawing no. 2
3	1	Stop	S235JRG2+C/SH	See drawing no. 7
4	2	Washer large	CuZn39Pb3	See drawing no. 9
5	2	Bush for Sliding Plate	CuZn39Pb3	See drawing no. 10
6	1	Die Spring		Amatec 203-506
7	2	Sliding Axis	AISI Type A2 Tool Steel	See drawing no. 5
8	1	Flange	S235JRG2+C/SH	See drawing no. 8
9	2	Bush for Measuring Plate	CuZn39Pb3	See drawing no. 11
10	1	Dowel pin 3 mm		ISO 8734 - 3 x 20 - A - St
11	1	Bush for Spindle	CuZn39Pb3	See drawing no. 12
12	1	Dowel pin 2 mm		ISO 8734 - 2 x 20 - A - St
13	1	Spindle flange nut		Motedis - EBFM 10x2
14	1	Top Plate	AISI 316L	See drawing no. 4
15	1	Spindle	C35E / C45E	See drawing no. 6
16	1	Spindle nut - hexagonal		Motedis - ESKM TR10x2
17	4	Dowel pin 4 mm		ISO 8734 - 4 x 40 - A - St
18	5	Washer - Spindle flange nut		ISO 10673-4.55-S
19	5	Bolt - Spindle flange nut		ISO 4762 M5 x 20 - 20N
20	1	Ring for Measuring Plate	CuZn39Pb3	See drawing no. 13
21	1	Caliper Nonius scale		See drawing no. 15
22	1	Measuring Plate	AISI 316L	See drawing no. 3
23	2	Bolt - Caliper		ISO 4762 M3 x 8 - 8N
24	3	Washer - Pull-up rod		ANSI B18.22M - Plain washer, 4 mm, narrow
25	3	Bolt - Pull-up rod		ANSI B18.3.1M - 4 x 0.7 x 6 Hex SHCS -- 6NHX
26	3	Pull-up rod	EN AW-1050A H14	See drawing no. 16
27	1	Caliper main scale		See drawing no. 14
28	1	Heater Block	EN AW-6082T6	See drawing no. 17
29	3	Cartridge heater		Acim Jouanin - standard cartridge heater, 6.5x50mm, 150W, 230V
30	2	Washer - Heater Block		ISO 10669-4-N
31	2	Bolt - Heater Block		ISO 4762 M4 x 20 - 20N
32	4	Bolt - Heater Block legs		ISO 4014 - M4 x 40 x 14-N

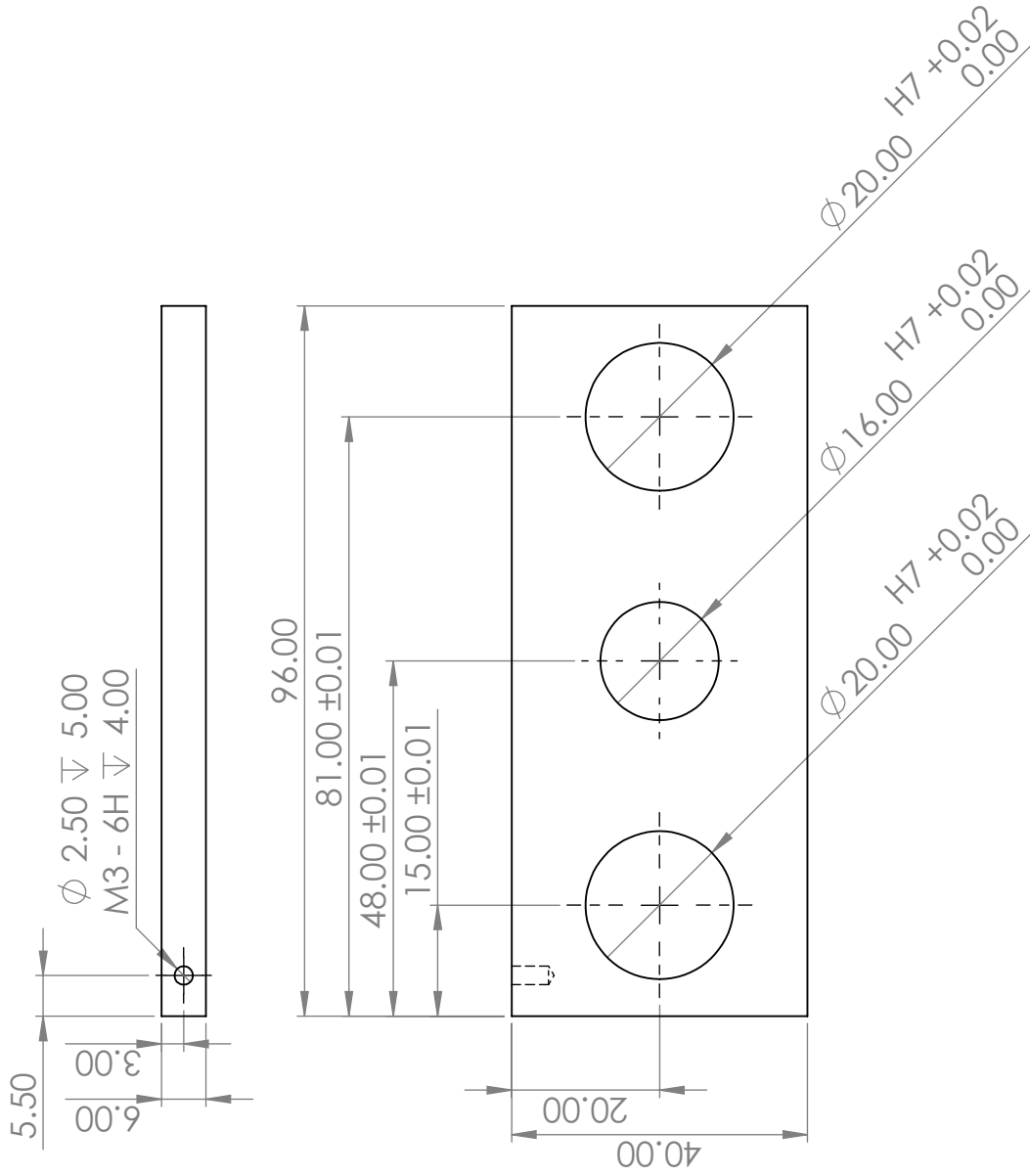


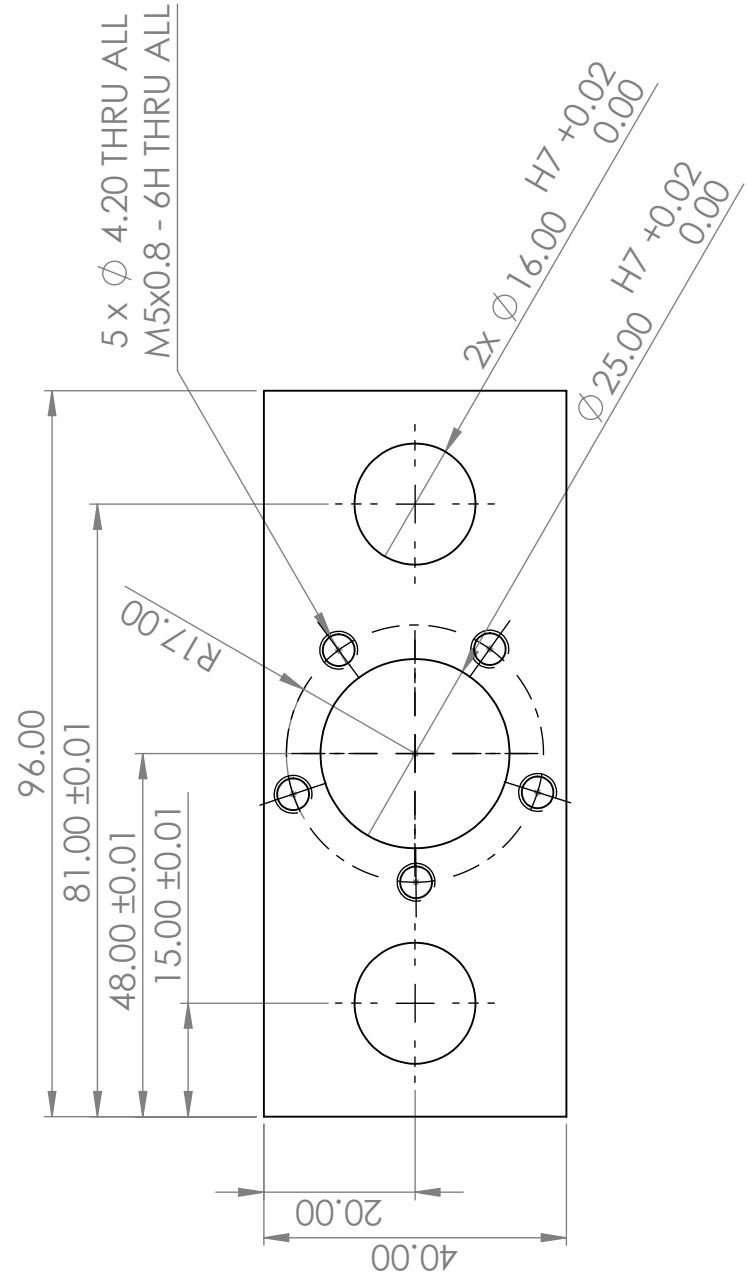
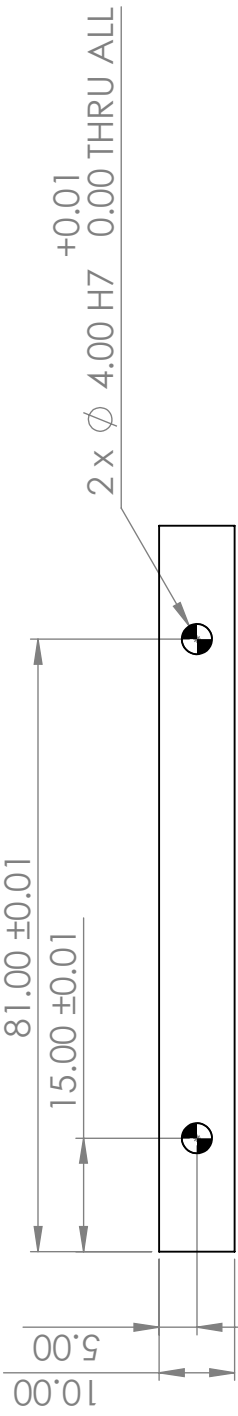
TU Delft Mechanical Engineering Precision and Microsystem Engineering	Bottom Plate		Material: AISI 316L	Drawn: Sarah Aalbers	18/09/2020
	Title		Tolerances: ISO 2768 - M unless otherwise specified	Scale: 1:1	Unit of measurement: mm
Finishing: As machined unless otherwise specified		Weight: 270 g	Drawing number: 1	Size: A4	Drawing number: 1
Deburr and file sharp edges		Quantity: 1	Quantity: 1	Sheet 1 / 1	Sheet 1 / 1



Material	AISI 316L
Tolerances	ISO 2768 - M unless otherwise specified
Finishing	As machined unless otherwise specified
Deburr and file sharp edges	

Drawn	Sarah Aalbers	18/09/2020
Scale	1:1	Unit of measurement mm
Weight	257 g	Drawing number 2
Quantity	1	Sheet 1 / 1





Material	AISI 316L
Tolerances	ISO 2768 -M unless otherwise specified
Finishing	As machined unless otherwise specified
Deburr and file sharp edges	

Drawn	Sarah Aalbers	18/09/2020
	Scale	1:1
	Unit of measurement	mm
Weight	226 g	Drawing number
Quantity	1	4
		Sheet 1 / 1

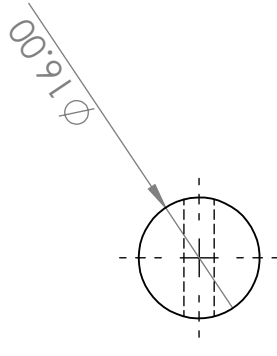
2 x \varnothing 4.00 H7 $\begin{matrix} +0.01 \\ 0.00 \end{matrix}$ THRU ALL

Drill and ream after assembly
with Top Plate and Bottom Plate.
Disassemble for deburring

160.00

5.00

5.00



Material DIN 115 Cr V 3

Tolerances ISO 2768 - M unless otherwise specified

Finishing As machined unless otherwise specified

Deburr and file sharp edges

Drawn

Sarah Aalbers

18/09/2020



Weight 250 g

Quantity 1

Scale
1:1

Size
5

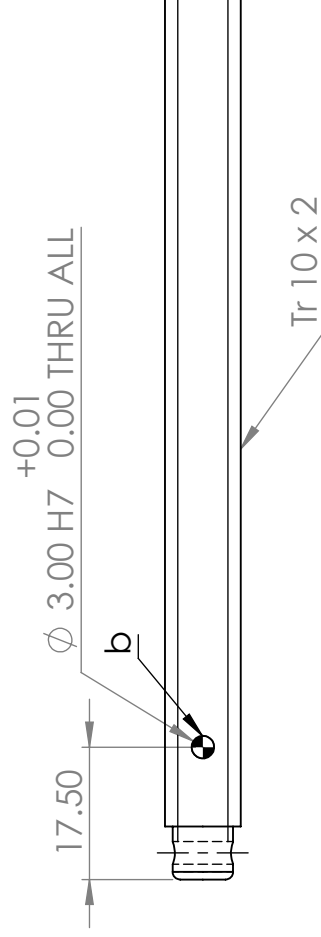
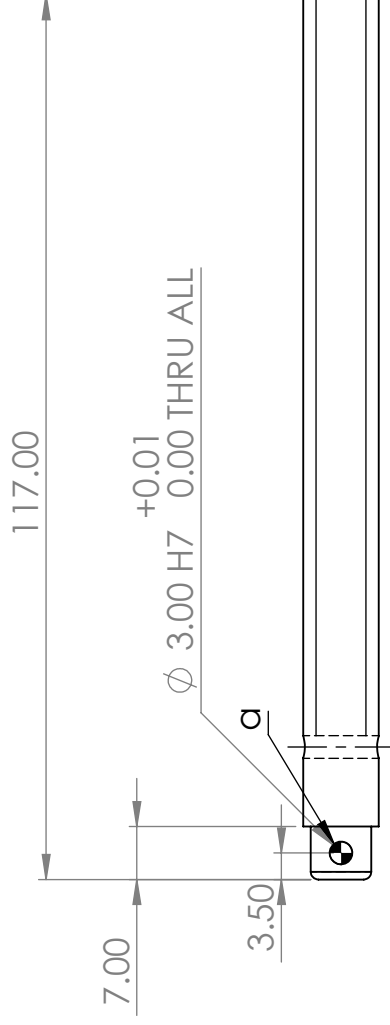
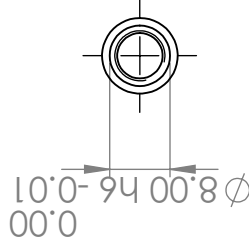
A4

Unit of measurement
mm

Drawing number
5

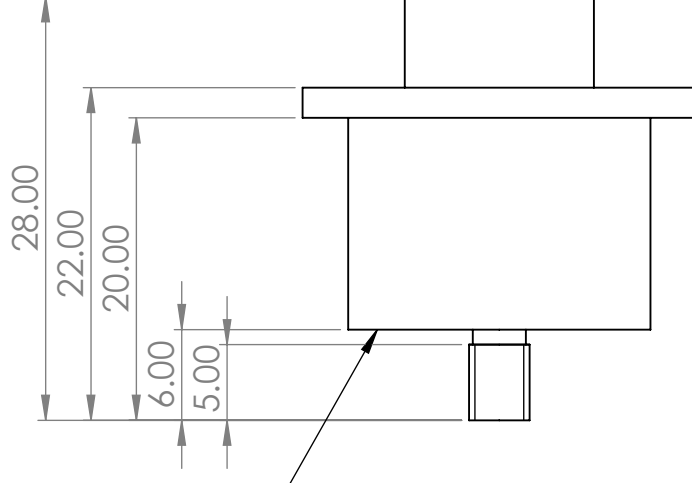
Sheet 1 / 1

1. Drill and ream dowel hole (a) in assembly with Bush for Spindle. 2. Drill and ream dowel hole (b) after assembling parts 8, 11, 15, 21 and 22. Do not compress parts 8, 11 and 21 too tight in axial direction: Rotational movement should still be possible.
3. Disassemble for deburring.

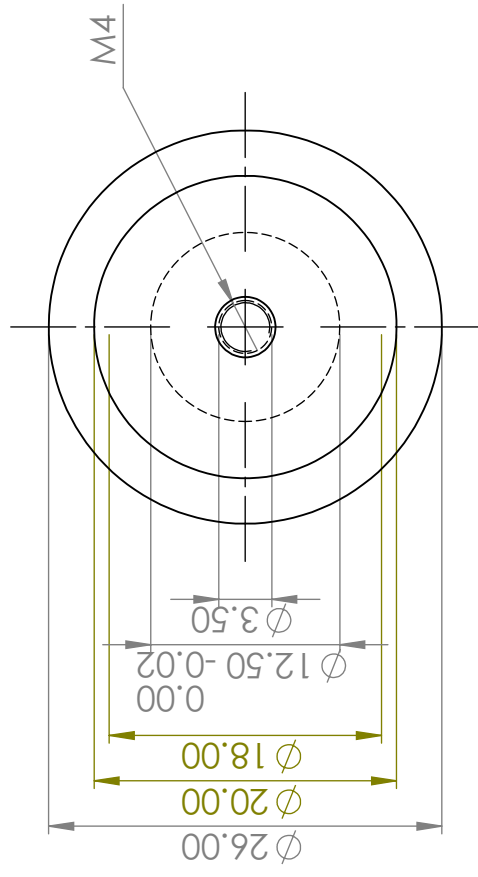


ITEM NO.	QTY.	MATERIAL	PART NUMBER	DESCRIPTION
1	1	C35E/C45E	Spindle	Motedis - RPTS TR 10x2 right, rolled. According to ISO 2901/2903 and DIN 103 tolerance 7e

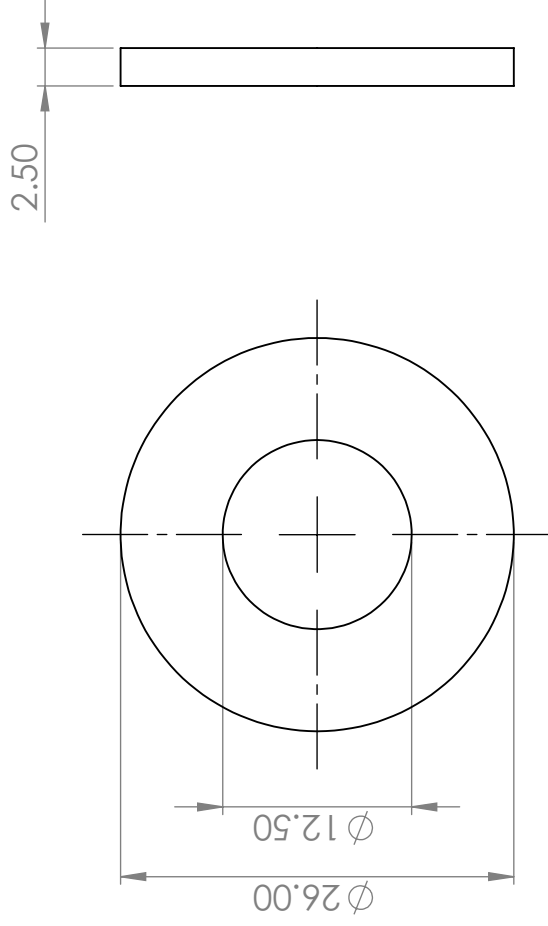
TU Delft Mechanical Engineering Precision and Microsystem Engineering	Title <h1>Spindle</h1>		Material C35E / C45E	Drawn Sarah Aalbers	18/09/2020	
	Tolerances ISO 2768 - M unless otherwise specified	Scale 1:1	Unit of measurement mm			
	Finishing As machined unless otherwise specified	Weight 70 g	Size 6	Drawing number 6		
	Deburr and file sharp edges	Quantity 1	Size A4	Sheet 1 / 1		



Mill 0,20 mm deep at ϕ 18,00 to avoid friction when tightening to Plate 2 and to leave space for adhesive



Material	S235JRC+C/SH	Drawn	Sarah Aalbers	10/03/2021
Tolerances	ISO 2768-M unless otherwise specified	Scale	2:1	Unit of measurement mm
Finishing	As machined unless otherwise specified	Weight	50 g	Drawing number 7
Deburr and file sharp edges		Quantity	1	Size A4 Sheet 1 / 1



Material CuZn39Pb3

Tolerances ISO 2768 - M unless otherwise specified

Finishing As machined unless otherwise specified

Deburr and file sharp edges

Drawn

Sarah Aalbers

30/03/2021



Scale
2:1

Unit of measurement
mm

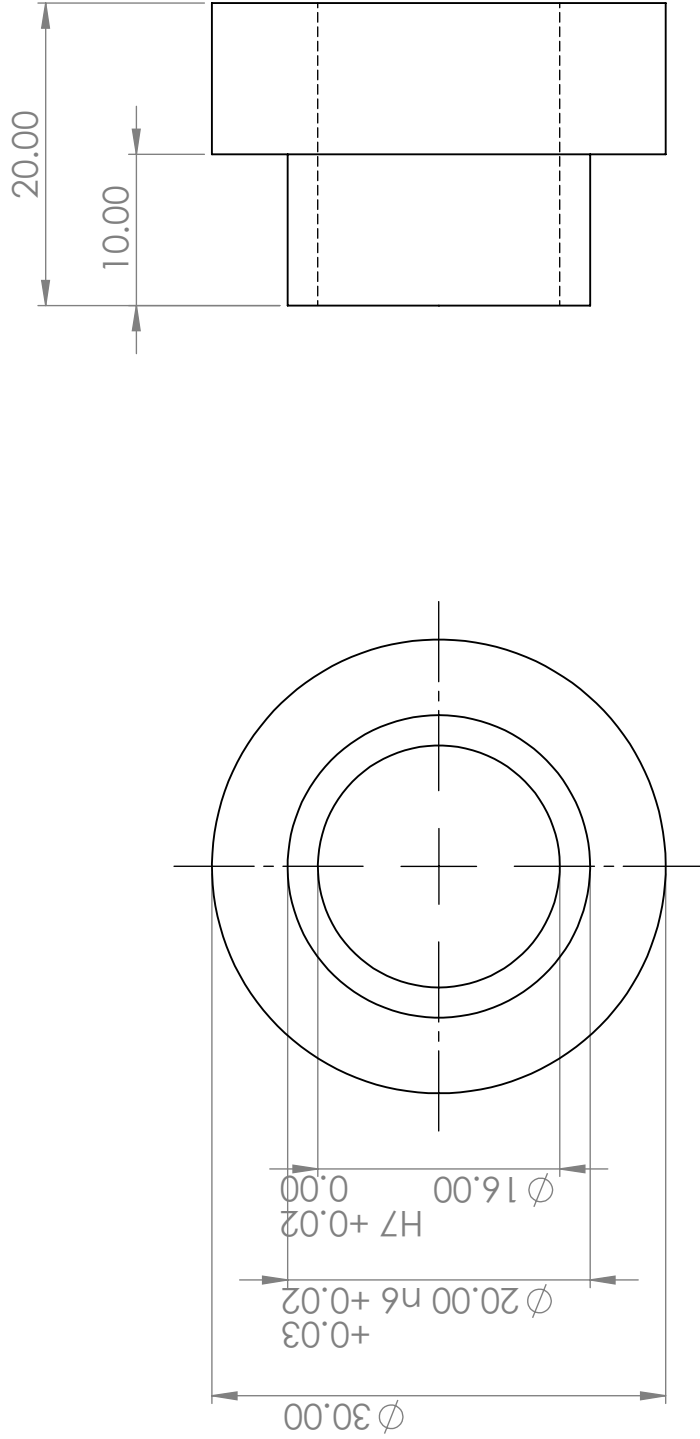
Weight 9 g

Drawing number
9

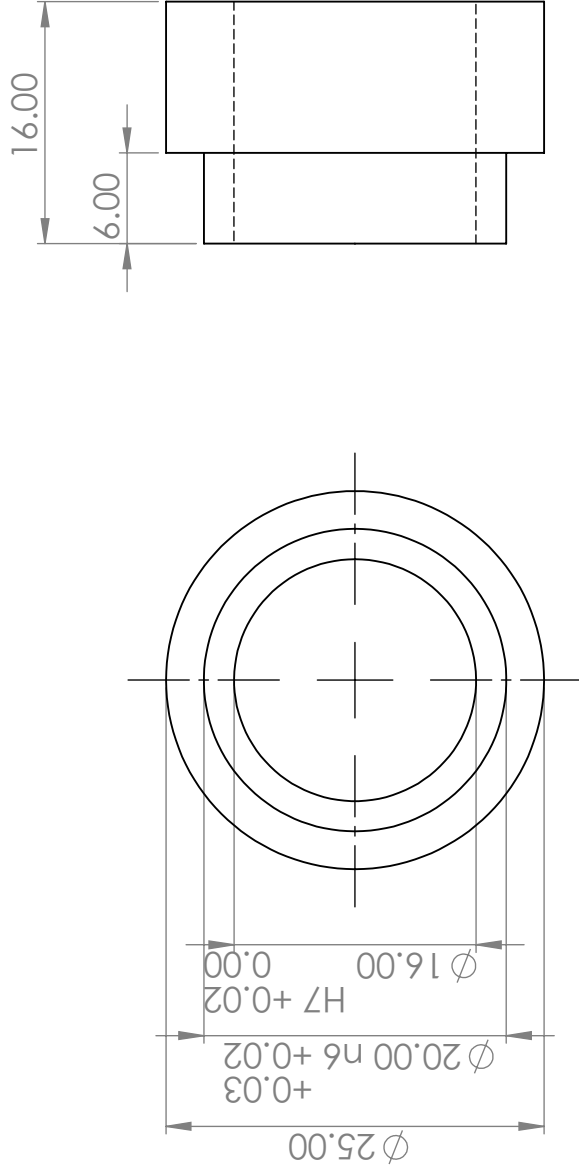
Quantity 2

Size
A4

Sheet 1 / 1



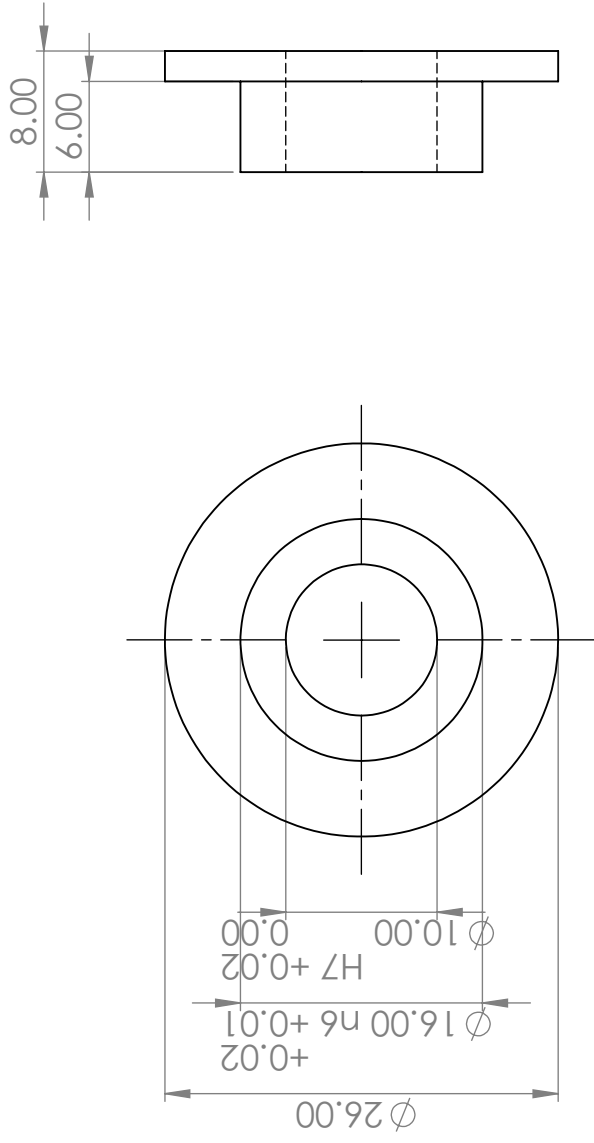
Material	CuZn39Pb3	Drawn	Sarah Aalbers	30/03/2021
Tolerances	ISO 2768-M unless otherwise specified	Scale		Unit of measurement
Finishing	As machined unless otherwise specified	2:1		mm
Deburr and file sharp edges		Weight	53 g	Drawing number
		Quantity	2	10
		Size		Sheet 1 / 1
		A4		



Material	CuZn39Pb3
Tolerances	ISO 2768 - M unless otherwise specified
Finishing	As machined unless otherwise specified
Deburr and file sharp edges	

Drawn	Sarah Aalbers	Scale	2:1
Weight	30 g	Size	A4
		Quantity	1

30/03/2021	Unit of measurement	mm
	Drawing number	11
	Sheet 1 / 1	



Material CuZn39Pb3

Tolerances ISO 2768 - M unless otherwise specified

Finishing As machined unless otherwise specified

Deburr and file sharp edges

Drawn Sarah Aalbers

Scale 2:1

Size A4

30/03/2021

Unit of measurement
mm

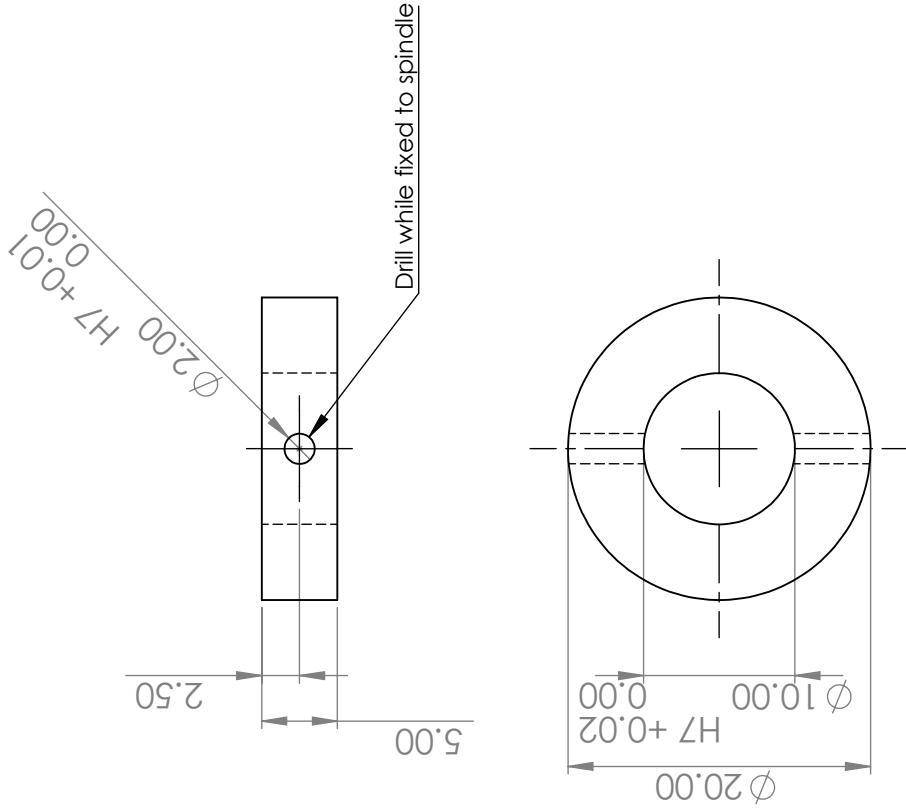
Drawing number
12

Sheet 1 / 1

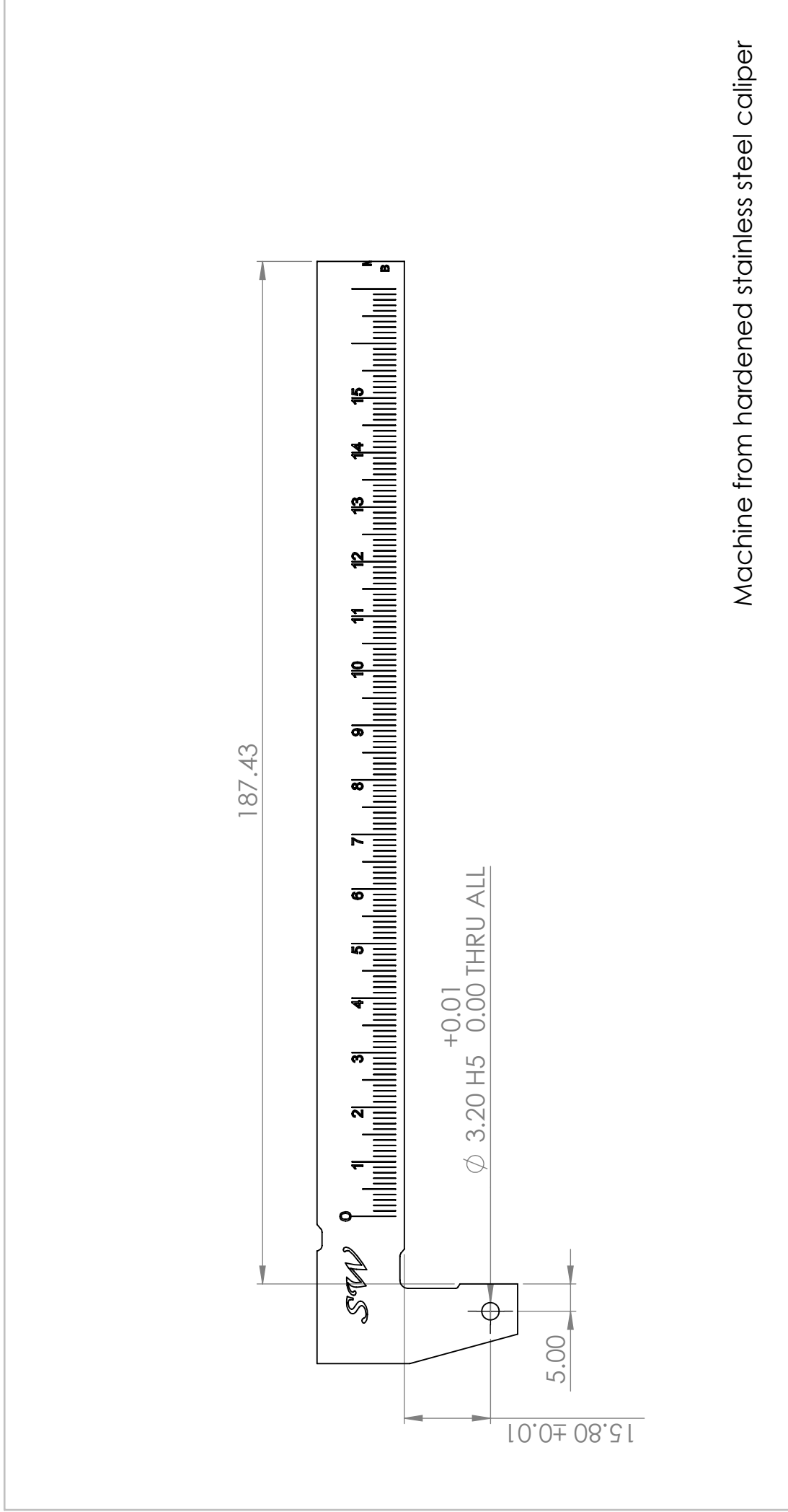


Weight 14 g

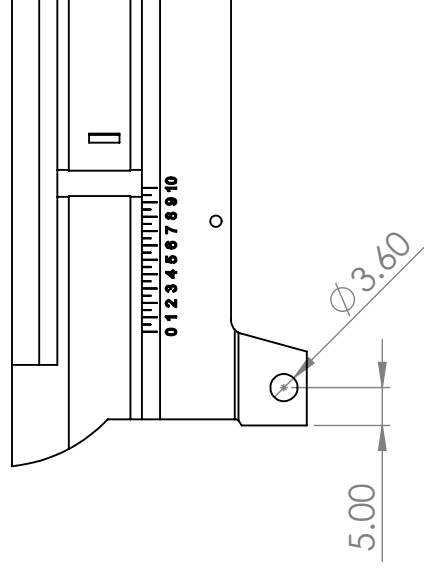
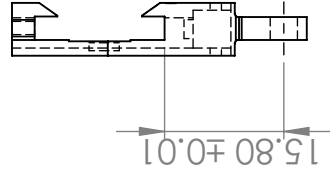
Quantity 1



Material	CuZn39Pb3	Drawn	Sarah Aalbers	30/03/2021
Tolerances	ISO 2768 - M unless otherwise specified		Scale	Unit of measurement
Finishing	As machined unless otherwise specified		2:1	mm
Deburr and file sharp edges		Weight	10 g	Drawing number
		Quantity	1	13
				Sheet 1 / 1

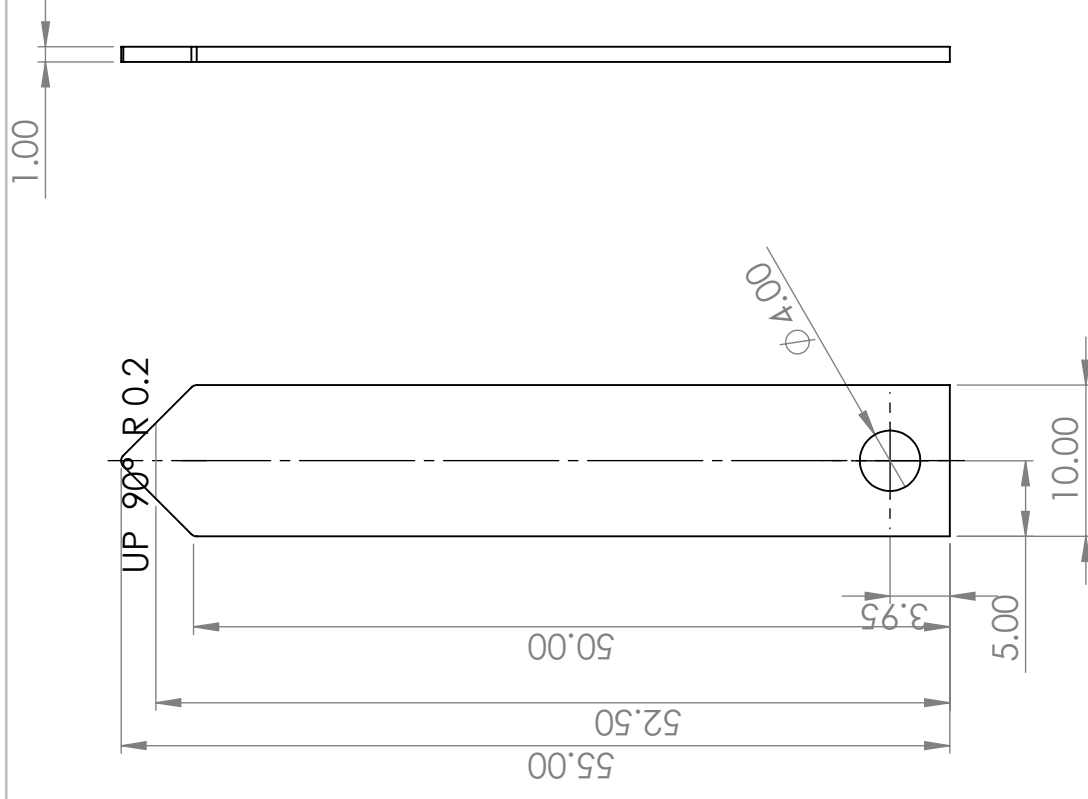


TU Delft Mechanical Engineering Precision and Microsystem Engineering	Title <h1>Caliper Main Scale</h1>		Material ISO 2768 - M unless otherwise specified	Drawn Sarah Aalbers	18/09/2020	
			Tolerances ISO 2768 - M unless otherwise specified		Scale 1:1	
			Finishing As machined unless otherwise specified	Weight g	Size 14	Unit of measurement mm
			Deburr and file sharp edges	Quantity 1	A4	Drawing number 14 Sheet 1 / 1

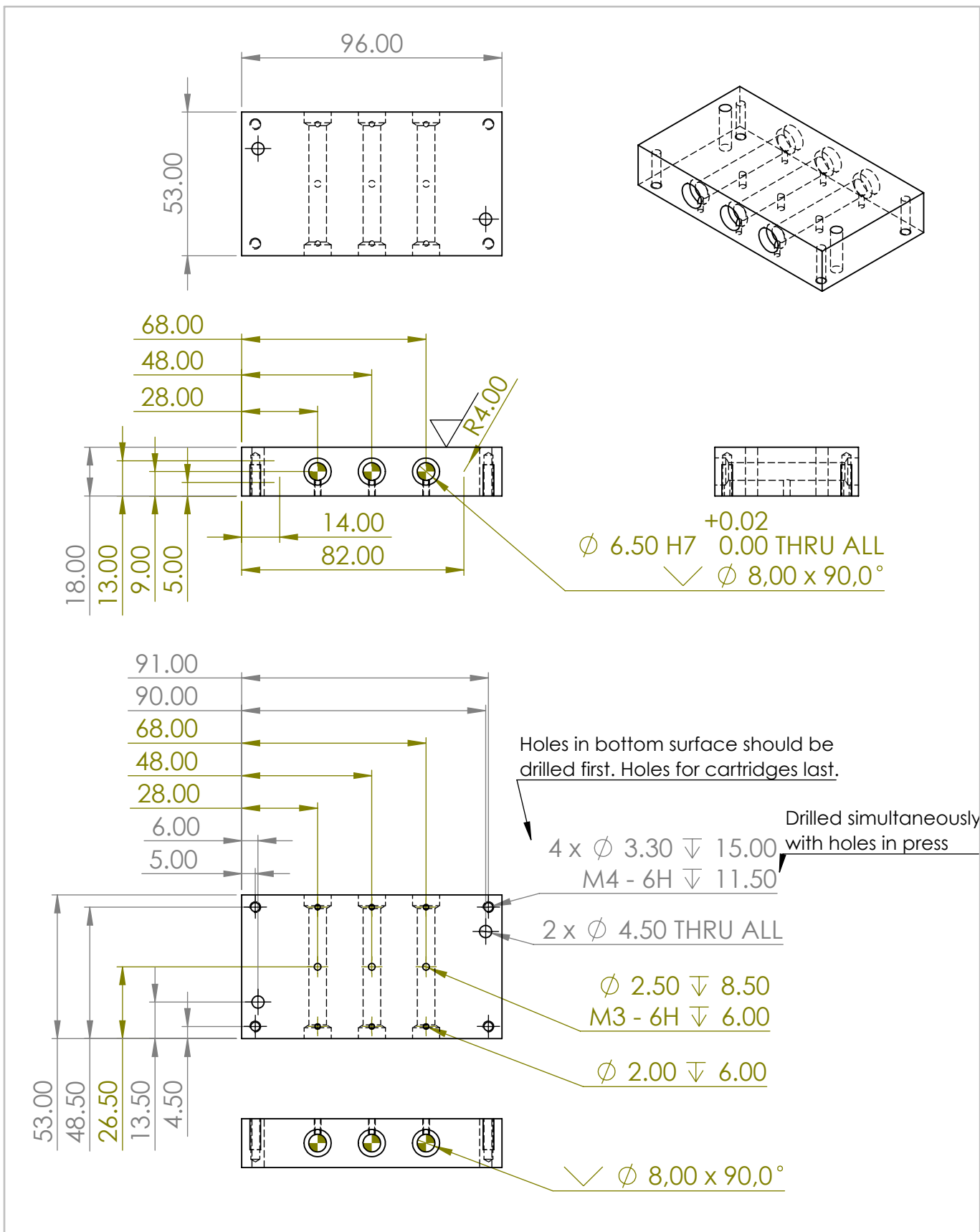


Material	ISO 2768 - M unless otherwise specified
Tolerances	As machined unless otherwise specified
Finishing	Deburr and file sharp edges

Drawn	Sarah Aalbers	18/09/2020
Scale	1:1	Unit of measurement mm
Weight	g	Drawing number 15
Quantity	1	Sheet 1 / 1

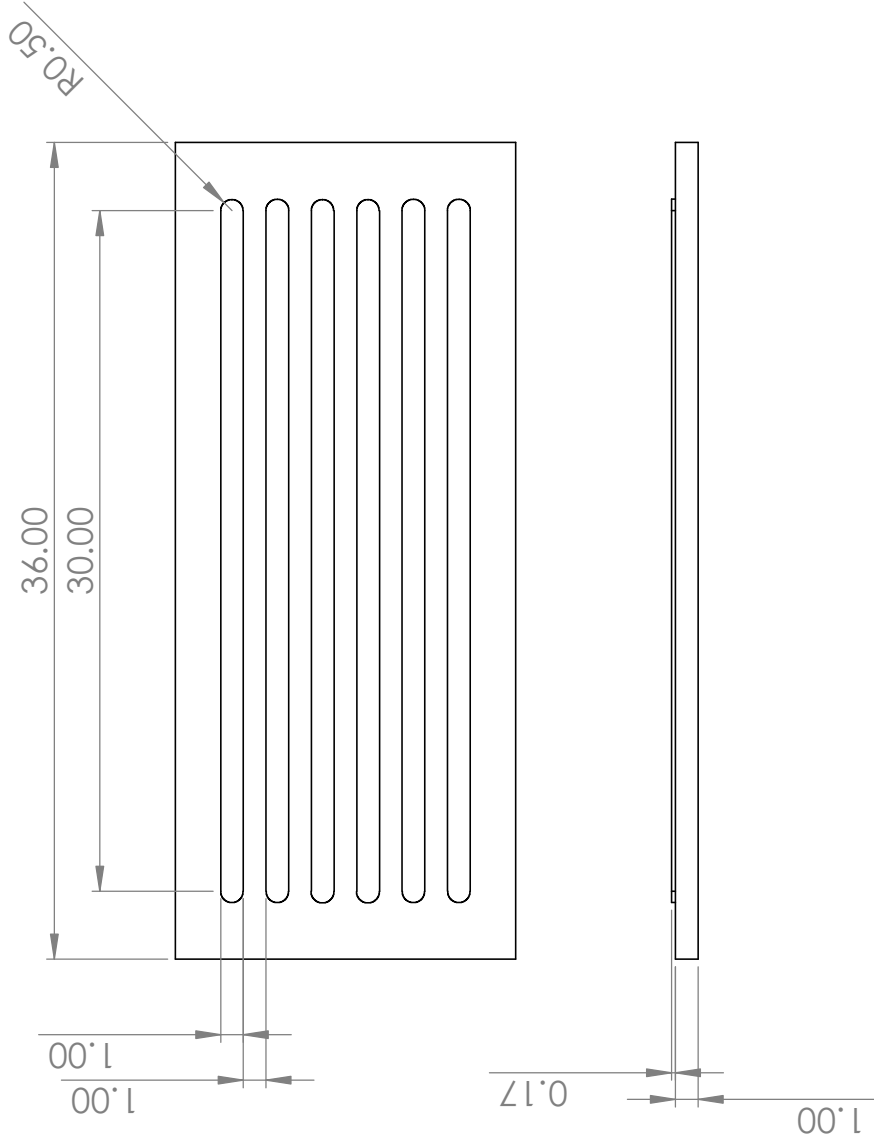


TU Delft Mechanical Engineering Precision and Microsystem Engineering	Title <h1>Pull-up rod</h1>		Material EN AW-1050A H14	Drawn Sarah Aalbers	18/09/2020
	Tolerances ISO 2768 - C unless otherwise specified	Scale 2:1	Unit of measurement mm	Weight 4 g	Drawing number 16
	Finishing As machined unless otherwise specified	Quantity 1	Size A4	Quantity 1	Sheet 1 / 1
	Deburr and file sharp edges				



<p>TU Delft Mechanical Engineering Precision and Microsystem Engineering</p>		Title Heater Block	
		Material EN AW-6082T6	Drawn Sarah Aalbers 18/09/2020
	Tolerances ISO 2768 - F unless otherwise specified	Scale 1:2	Unit of measurement mm
	Finishing As machined unless otherwise specified	Weight g	Size 17
	Deburr and file sharp edges	Quantity 1	A4

E.2. Soft lithography and soft embossing molds



Scale
 3:1

Unit of measurement
 mm

Weight
 g
 9

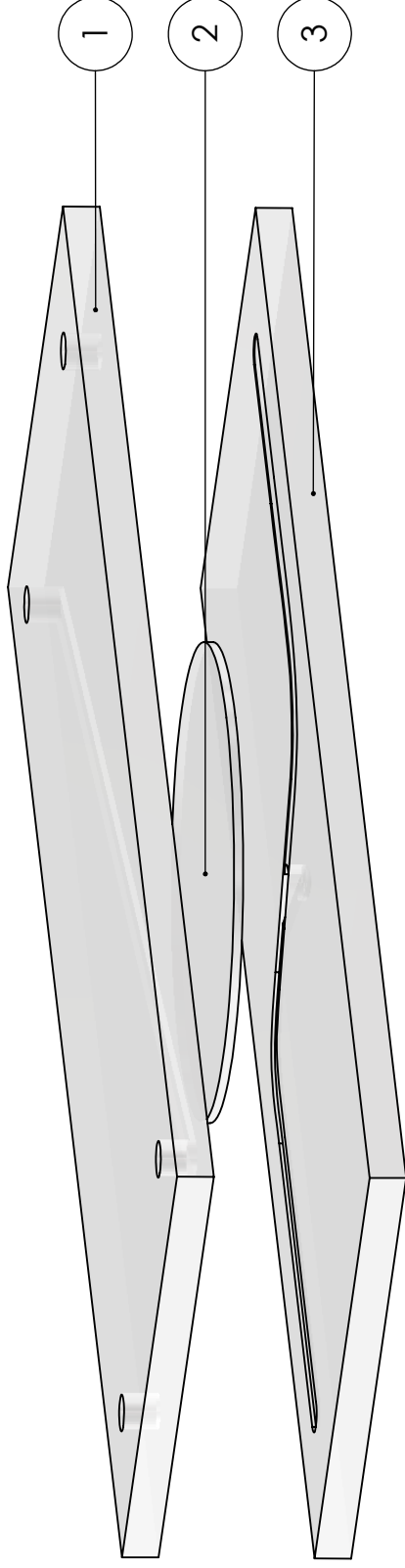
Drawing number
 1

Quantity
 1

Sheet 1 / 1

A4

E.3. BBB-on-Chip



ITEM NO.	PART NAME	Material	Description	QTY.
1	Blood channel	TOPAS 6015 + TOPAS 5013	See drawing no. 1	1
2	Membrane	PET	\varnothing 13mmx0.25mm, 0.4 μ m pores	1
3	Brain channel	TOPAS 6015 + TOPAS 5013	See drawing no. 2	1

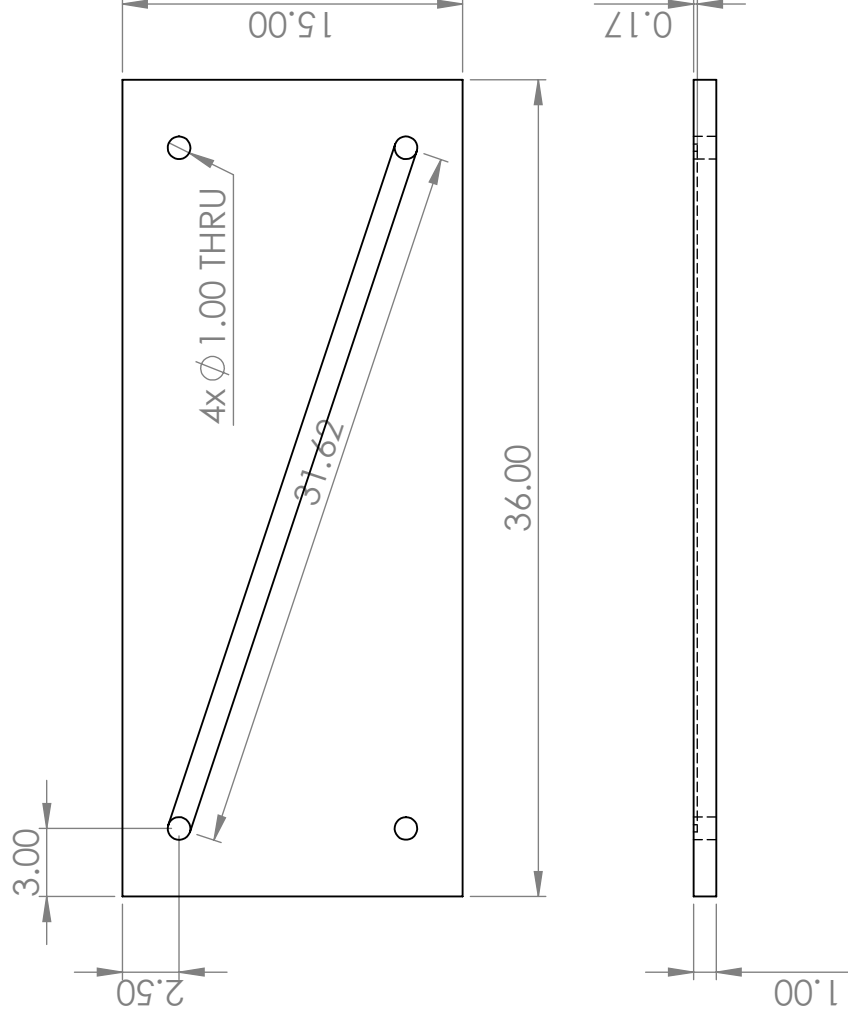
Title

Drawn Sarah Aalbers 24/09/2020

TU Delft
 Mechanical Engineering
 Precision and Microsystem
 Engineering

BBB-on-Chip

	Scale 2:1	Unit of measurement mm
Weight g	Size 0	Drawing number
Quantity 1	A4	Sheet 1 / 1



τ_{wss} (Pa)	Q (μ /s) [1]
1.5	0.81
6.4	3.44

w (μ m)	1000
h (μ m)	100
h/w	0.1
f* [2]	0.882
μ (mPa.s)	5.2

$$1 \quad Q = \frac{\tau_{wss} w h}{6\mu} \frac{f(1+h/w)}{h} \quad [2]$$

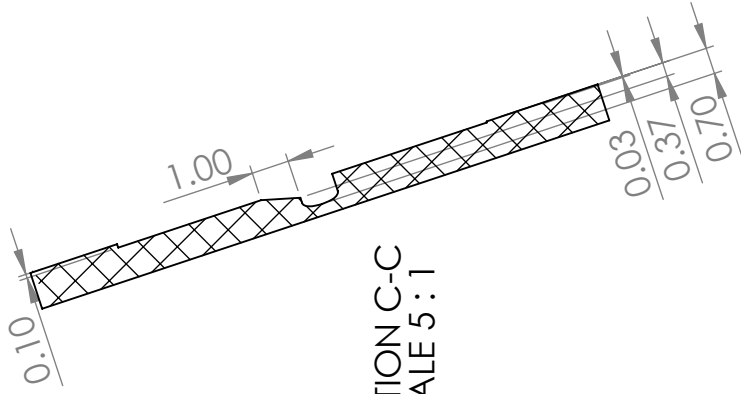
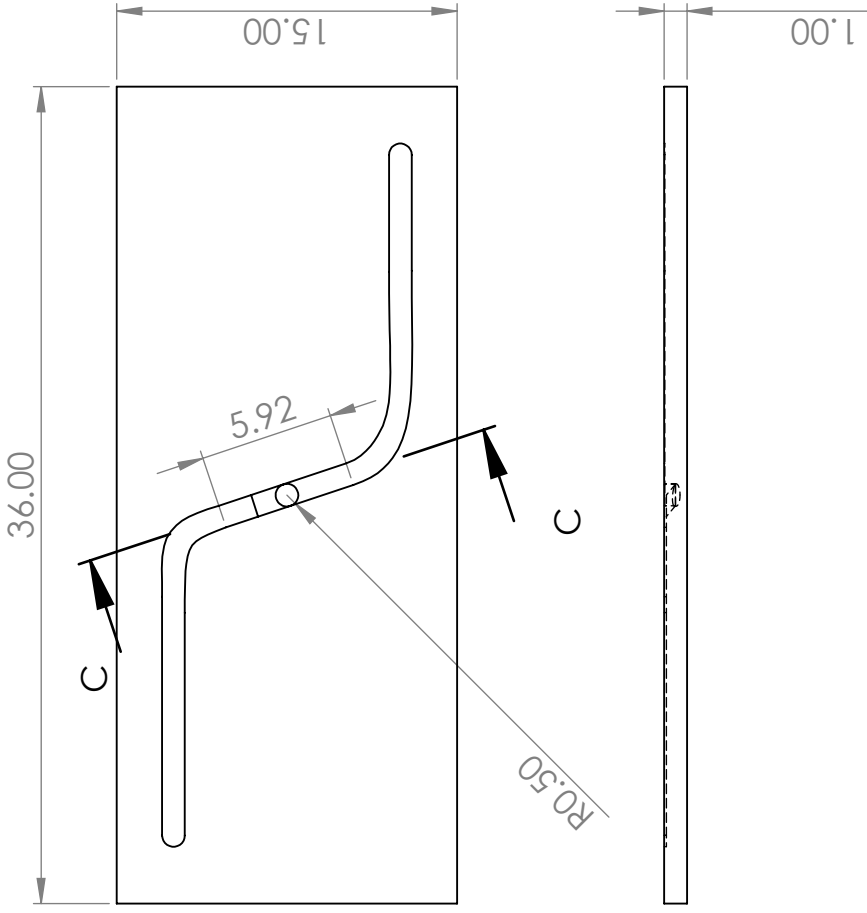
2 Sorin, Y. (2007). Determination of shear viscosity and shear rate from pressure drop and flow rate relationship in a rectangular channel, 48, 632-637. <https://doi.org/10.1016/j.polymer.2006.11.048>

TU Delft
 Mechanical Engineering
 Precision and Microsystem Engineering

Title
Blood channel

Material	TOPAS 6015 + TOPAS 5013	Drawn	Sarah Aalbers	24/09/2020
Scale	3:1	Weight	1 g	Unit of measurement
Quantity	1	Size	1	mm
		Quantity	1	Drawing number
				1
				Sheet 1 / 1

A4



SECTION C-C
SCALE 5 : 1



II

Part 2

F

BioDay Poster

Blood-Brain Barrier on Chip for the Development of Glioblastoma Therapeutics

Sarah Aalbers, Antonia Denkova, Luigi Sasso

The blood-brain barrier (BBB) is a highly restrictive barrier in the capillaries of the brain, formed by endothelial cells. It protects the brain from harmful substances in the blood and at the same time allows nutrients, oxygen and waste products to cross. Therapeutics to treat glioblastoma (brain tumor) need to be specially designed to be able to reach the brain via the BBB.

Goal: Developing a BBB-on-chip to test the ability of glioblastoma therapeutics to 1) cross the BBB and 2) treat a glioblastoma spheroid.

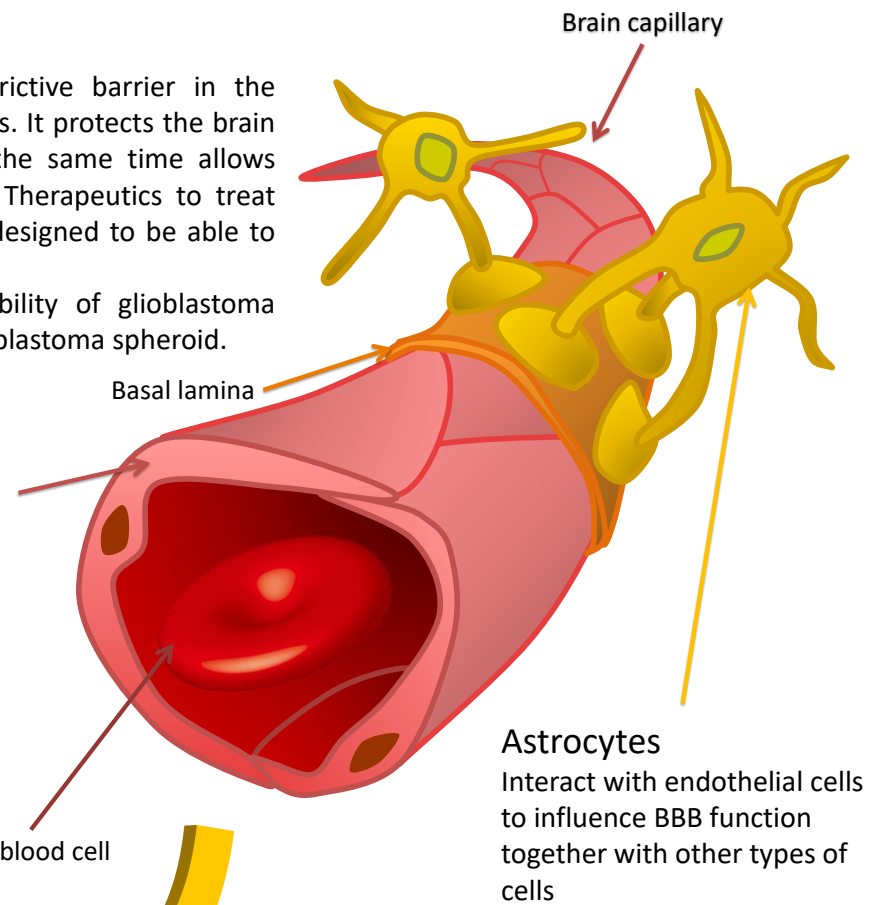
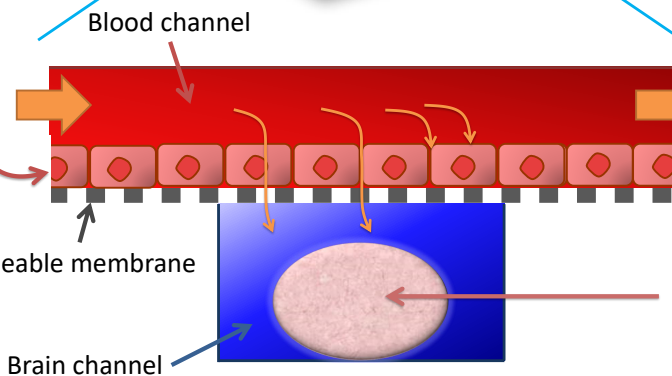
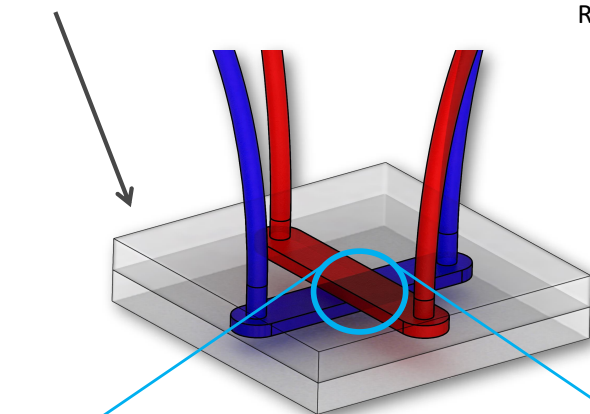
Endothelial cells

Sealed to each other with tight junctions to form a tight barrier.

Mimic in vivo situation of endothelial cells as good as possible to obtain a well functioning BBB.

Microfluidic device

A blood channel and a brain channel are fabricated in polymer. In between the channels a permeable membrane is placed. In the blood channel endothelial cells are cultured.



Astrocytes
Interact with endothelial cells to influence BBB function together with other types of cells

Testing of BBB:

- Permeability assays of known substances
- Electrical resistance of endothelial cells
- Staining junction proteins

Flow

Flow induces in vivo levels of shear stress on the cells which stimulates the formation of a tight BBB

Glioblastoma spheroid

Study uptake of and response to therapeutics administered in blood channel



Risk mitigation plan

All steps planned to reach the milestones of this thesis are analysed. Risks involving the steps are considered and a risk mitigation plan is proposed when needed.

Easily-manufacturable table-top hand press The delivery of the press consists of designing and manufacturing the press and next calibrating the force and temperature control.

Design and fabrication

Known A list of requirements is set up in Section 1.4 already. Worgull [88] extensively discusses requirements on hot embossing machines. Chen et al. [16] fabricated a hand press for embossing before, which is however not very convenient to use: the embossing force is applied with a separate device, during which the press cannot be heated.

Unknown Risks Medium:
Manufacturing the press could be too difficult or time consuming for a person not experienced in metalworking.
Fabrication of the parts of the press could be not precise enough, obstructing parallel movement of the embossing plates.
A straightforward design consists of plates sliding along two or four axes, which is enabled by brass or bronze bushings press fitted in the plates. Temperature cycles could cause stress relaxation in the bushings, which could result in the bushings coming loose from the plates or clamping the axes. Both obstruct smooth and parallel movement of the embossing plates.

Mitigation A commercial die press, whose plates' parallelism is sufficient could be ordered and adapted to be able to manually apply a controlled force and temperature.
Caution has to be taken when designing and manufacturing the bushings and housings. An intermediate fitting should be selected. Loose bushings can be fastened with high temperature resistant glue or by clamping the bushings to the plates in axial direction.

Force calibration

Known Load cells with sufficient accuracy and load capacity are available at the department to calibrate the force control.

Unknown The temperature dependent behaviour of the press and its influence on the exerted force is unknown and the force control can only be calibrated within a small temperature range.

Risks Low:
The influence of temperature on the exerted force could be significant and non-linear.

Mitigation Consider thermal expansion and its influence on the exerted force in the design stage. When the influence of temperature appears to be not sufficiently mitigated an experimental setup needs to be designed to measure the embossing force at high temperatures.

Temperature control

<i>Known</i>	Some embossing experiments have been performed at the department using an oven to control the temperature. Also [16] placed their press in an oven.
<i>Unknown</i>	The above mentioned experiments were performed to obtain one functioning embossed device, not to study the influence of temperature on embossing results. The accuracy of the temperature of the mold and substrate using the oven at the department is unknown.
<i>Risks</i>	High: The accuracy of the temperature when using an oven could be insufficient.
<i>Mitigation</i>	Use a hot plate or integrate a heating element with temperature control in the press.

Design of the chip and molds The design stage firstly consists of designing the BBB-on-Chip itself. Next to that, the soft embossing mold and soft lithography molds will be designed by taking into account the fabrication process. During the design stage the behaviour of the fluid and particles in the fluid need to be determined. This results into the following actions in the design stage:

- Design of device
- Design of soft embossing mold
- Design of soft lithography mold
- Simulate fluidics in the device

The risks in the design stage are not significant, since the design is not complex and the flow through rectangular channels and diffusion and convection through membranes is well described.

Mold fabrication The fabrication of the soft embossing mold consists of fabricating a soft lithography mold using the Micro Plus HiRes printer from EnvisionTEC with the material HTM140, and making the soft embossing mold using soft lithography.

Printing mold using UV-light induced polymerization

<i>Known</i>	Structures have been printed at the department with similar dimensions using the same material (HTM140) and printer. The surface quality of these structures is high at the bottom side, when printed exactly orthogonal to the print direction, and lower at the sides and top of the structure.
<i>Unknown</i>	The printed products have not been used yet to fabricate soft embossing molds out of PDMS to emboss COC. If the surface roughness of the prints is high, the surface roughness of the channels in COC will be high.
<i>Risks</i>	Low: Optical imaging becomes complicated or impossible and air bubbles might remain on the walls of the channels when a medium flow is applied and the wall surface is too rough.
<i>Mitigation</i>	Using the printer from Nanoscribe for mold fabrication or applying a vapor solvent treatment on the COC product of channel fabrication to smooth the surface.

Soft lithography of soft embossing mold

<i>Known</i>	Soft lithography of PDMS with a HTM140 mold has been done before at the department to produce channels in PDMS. There are some problems with the surface roughness of the sidewalls of the molds, which cause the PDMS to stick to the mold.
<i>Unknown</i>	Soft lithography in combination with a HTM140 mold has not been used yet at the department to create standing structures in PDMS, but only for the fabrication of channels in PDMS.
<i>Risks</i>	Medium: Stiction of the sidewalls when peeling off the mold could be more problematic for standing structures than for the channels which have been produced so far. The structures could tear.

Mitigation After printing the mold an anti-stiction coating could be applied on the mold. The coating could be either chemically attached or applied as a layer covering the surface. If this does not work, instead of HTM140 another material could be used to print the mold. For example, different ABS like materials are available for the Micro Plus Hi-Res printer.

Substrate preparation The substrate to be embossed consists of two materials. The base material is a TOPAS® 6015 substrate. On top of this substrate a thin layer of TOPAS® 5013 is needed for the thermal fusion bonding step.

Spincoating 10 µm TOPAS® 5013 on TOPAS® 6015

Known Steigert et al. [68] spin coated a 3-5 µm thick layer of TOPAS® 8007 on a 500 µm thick TOPAS® 6013 foil by dissolving 5% wt in toluene and spinning at 5000 rpm. The composite was annealed for 1 h at 75 ° to drive out the remaining solvent. Bundgaard [15] reports the use of sec-butyl benzene instead of toluene as solvent, which has a similar chemical structure and a higher boiling point, thus evaporating slower. They found that toluene evaporated too quickly and resulted in inhomogeneities, which they account for by the fact that 'the evaporation from thin film areas takes place more rapidly than from thicker areas. The thin areas become gel-like and the liquid can not flow to level out, leaving thicker areas confined.' The thickness (T) of a spin coated layer depends on the concentration (C) of the polymer in solvent (g/100ml), the intrinsic viscosity (η) of the polymer, the rotational speed (ω in rpm) and some constants (α , β , γ , K), until centripetal forces exceed the surface tension at the edges, according to the empirical relation :[45]

$$T = \frac{K \cdot C^\beta \cdot \eta^\gamma}{\omega^\alpha} \quad (\text{G.1})$$

The solvent mixture will cause swelling of the substrate and affect the obtained layer thickness. Bundgaard [15] performed experiments with TOPAS® 8007 dissolved in sec-butyl benzene and reported layer thickness - spin speed relations of TOPAS® 8007 on a TOPAS® substrate for a wt% of 10-30.

Unknown In our case the TOPAS® 6013 foil in the report of Steigert et al. [68] is replaced by a TOPAS® 6015 substrate and a bonding layer of TOPAS® 5013 instead of TOPAS® 8007. An empirical relation for layer thickness or a published procedure on spin coating TOPAS® 5013 has not been found.

Risks Low: The solvent in the solution attacks the substrate. Bundgaard [15] writes that the solutions therefore needs to be applied to the substrate all at once, while spinning, in a continuous flow. In this way isolated drops are avoided, which would penetrate deeper into the substrate and cause a non-uniform layer.

At the department typically toluene has been used to dissolve TOPAS, this would therefore be the solvent of choice. Steigert et al. [68] were able to use toluene as solvent to spin coat the TOPAS® 8007, but Bundgaard [15] reports the toluene evaporated too quick to obtain homogeneous layers of TOPAS® 8007. A different solvent than toluene might be needed. This brings a small risk only, since Bundgaard [15] successfully used sec-butyl benzene as alternative.

The TOPAS® grades in different than the ones used before in literature, so the optimum procedures will differ as well.

Mitigation Since experience is at the department, at first it will be attempted to spin coat TOPAS® 5013 dissolved in toluene. The same procedure will be used as Steigert et al. [68] used at first and will be adapted during experiments. If toluene indeed appears to evaporate too quickly, sec-butyl benzene or another non-polar solvent with a higher boiling temperature could be used.

Soft embossing Using the soft PDMS mold fabricated in Appendix G the substrate obtained from the step in Appendix G can be embossed. Some experience is already present at the department and in literature some

studies can be found on soft embossing TOPAS:

Soft embossing in TOPAS® 6015 with thermal bonding layer

<i>Known</i>	<p>Soft embossing in COC with a PDMS mold has been done before in a few studies [12, 26, 41]), hot embossing COC has been reported more often, see Niles and Coassin [54] for a summary. Narasimhan and Papautsky [51] produced 1 mm wide and 110 μm deep channels in PMMA using a PDMS mold, a force of 4.5 kN and an embossing temperature of 147 $^{\circ}\text{C}$, 40 $^{\circ}\text{C}$ above the T_g. PMMA has a similar density and Young's modulus, see table 6.1 of Appendix A, so the applied force needs to be in the same order for COC as for PMMA. The embossing temperature will be higher because of the higher T_g of TOPAS. Lee et al. [41] produced channels of 100 μm wide and 40 μm deep in TOPAS® 5013 using a force in the range 2.4-4.5 kN and 165 $^{\circ}\text{C}$ or higher. For channels wider than 100 μm only a small force dependence of the replication accuracy was found. Jena et al. [36] obtained excellent replication results by hot embossing 100 μm wide, 60 μm deep channels in COC using a silicon mold at 2.94 kN, 170$^{\circ}\text{C}$ and 180 s. It is expected that embossing the 500 - 1000 μm wide, 100 μm deep channels of the BBB-on-Chip device will be possible in COC 6015 by using higher embossing temperatures. This temperature will be higher for soft embossing than for hot embossing, so a temperature above 170$^{\circ}\text{C}$ will be needed, as used by Jena et al. [36]. Lee et al. [40] fabricated 20 μm thick structures with an aspect ratio of 2.00, but with high replication errors ($\sim 17.0\%$ change in width). These replication errors appeared to become higher with decreasing structure thickness.</p>
<i>Unknown</i>	<p>Soft embossing the exact same material and grade, TOPAS® 6015 with a PDMS mold, has not been reported.</p>
<i>Risks</i>	<p>Medium: Air bubbles between mold and substrate could negatively affect the replication accuracy and surface quality of the substrate when not performed in vacuum. Medium: The PDMS mold could deform under the pressure needed to emboss in TOPAS, which would leave a deformed imprint in the substrate.</p>
<i>Mitigation</i>	<p>Mold and substrate could be placed on a convex surface to drive out air pockets from the centre of the substrate. Deformations could be anticipated on by altering the design of the mold, aiming to obtain the intended mold shape after deformation. Alternatively the mold could be placed in a stiff container during embossing to obstruct deformation of the mold, or could be completely fabricated out of a stiff material, like an epoxy.</p>